米
日

U.S. - JAPAN COORDINATED PROGRAM
FOR
MASONRY BUILDING RESEARCH

REPORT NO. 5.1-1

PB93-214633

PLANK DIAPHRAGM CHARACTERISTICS

by

MAX L. PORTER
AZIZ A. SABRI

JULY 1990

supported by:

NATIONAL SCIENCE FOUNDATION
GRANT NO. CES-8517028
FORMERLY GRANT NO. ECE-8517028

College of
Engineering
Iowa State University

Disclaimer

This report presents the results of a research project which was part of the U.S. Coordinated Program for Masonry Building Research. The program constitutes the United States part of the United States - Japan Coordinated Masonry Research Program conducted under the auspices of the Panel on Wind and Seismic Effects of the U.S.-Japan Natural Resources Development Program (UJNR).

This material is based on work supported by the National Science Foundation under the direction of Program Director, Dr. S.C. Liu.

Engineering data, designs, details, and suggested specifications presented in this publication have been delineated in accordance with recognized professional principles and practices and are for general information only. The date, designs, details, and suggested conclusions should not, therefore, be used without first securing competent advice with respect to their suitability for any given application. The responsibility for the use of the information in this report remains with the user. Since additional analysis and subsequent journal publications are ongoing, this report is for information purposes and is made available with the understanding that it will not be cited or reproduced without the permission of the authors.

The contents of this report do not represent a warranty of the products used on behalf of the State of Iowa, Iowa State University, or the authors. Any opinions, findings, and conclusions or recommendations expressed in this publication are those of the authors and do not necessarily reflect the views of the National Science Foundation and/or the United States Government. The authors do not guarantee the accuracy or completeness of any of the information published herein and will not be responsible for any errors, omissions, or damages arising out of the use of this information.

PB93-214633

REPORT NO. 5.1-1

PLANK DIAPHRAGM CHARACTERISTICS

BY

MAX L. PORTER
PROFESSOR
CIVIL AND CONSTRUCTION ENGINEERING DEPARTMENT
IOWA STATE UNIVERSITY
AMES, IOWA 50011

AND

AZIZ A. SABRI
PRE-DOCTORAL RESEARCH ASSOCIATE
CIVIL AND CONSTRUCTION ENGINEERING DEPARTMENT
IOWA STATE UNIVERSITY
AMES, IOWA 50011

ib

Table of Contents

LIST OF TABLES

LIST OF FIGURES

1. INTRODUCTION

1.1 General Remarks

Many of today's masonry buildings are constructed with precast, prestressed concrete planks. These concrete planks are used for both floors and walls. In the past several decades, hollow-core slab production has increased sharply and is now the single most used product in the precast, prestressed concrete industry [20]. A typical building floor construction utilizing precast, prestressed planks is shown in Figure 1.

Hollow-core floor systems maintain several advantages over other more traditional building material systems [33]. Precasting offers improved quality control, higher strength concrete, accelerated curing techniques and better opportunities for standardization. These factors, in turn, allow for compressed construction time schedules. Prestressing permits the use of shallower depths, longer spans, more controllable performance in terms of cracking and deflections and less material usage. The use of masonry and concrete offer increased fire resistance and durability over other materials such as timber and steel.

As expected, precast, prestressed concrete floor panels also possess several disadvantages. Precasting requires closer tolerances in casting; there is less margin for error. Creep strains are greater in prestressed concrete because of the compression introduced with the prestressing strands. Compared to steel, concrete floor systems are heavier and bulkier. In seismic areas, this additional mass can cause an increase in the lateral forces within a structure. Therefore, further study of the lateral forces within a precast structure must be undertaken.

Lateral forces, typically produced by earthquakes or winds, are resisted by the use of a space frame system and/or shear walls. In either case, the lateral loads are transmitted from one wall to another through the floor system, as shown in Figure 2. For seismic design, one the essential components in a structure is the slab or horizontal diaphragm. This type of system is often referred to as a "box" system since each component serves the function of transferring the lateral force.

The distribution of the horizontal forces to the shear wall or space frame system depends on the properties of the diaphragm slab and the resisting system. In the case of a shear wall building, the diaphragm can be considered to be a horizontal beam with the roof or the floor system acting as the web of the beam. With simple, transverse lateral loads, the forces flow out to the shear walls as is shown in the force distribution diagram given in Figure 3. In order to optimize the performance of the floor system, the in-plane stiffness of the diaphragm should exceed that of their respective vertical subsystems. Diaphragms of this type are categorized as rigid [4,40] (refer to Figure 4 for a conceptual sketch). In this instance, the diaphragms act as a flat plate that transmits lateral loads to the vertical bracing elements in proportion to their relative rigidities. Conversely, with flexible diaphragms, loads are distributed to vertical subsystems as a continuous beam using tributary areas. Regardless, both rigid and flexible systems should be able to retain a sufficient amount of in-plane stiffness or strength in order to prevent collapse, well beyond the elastic range.

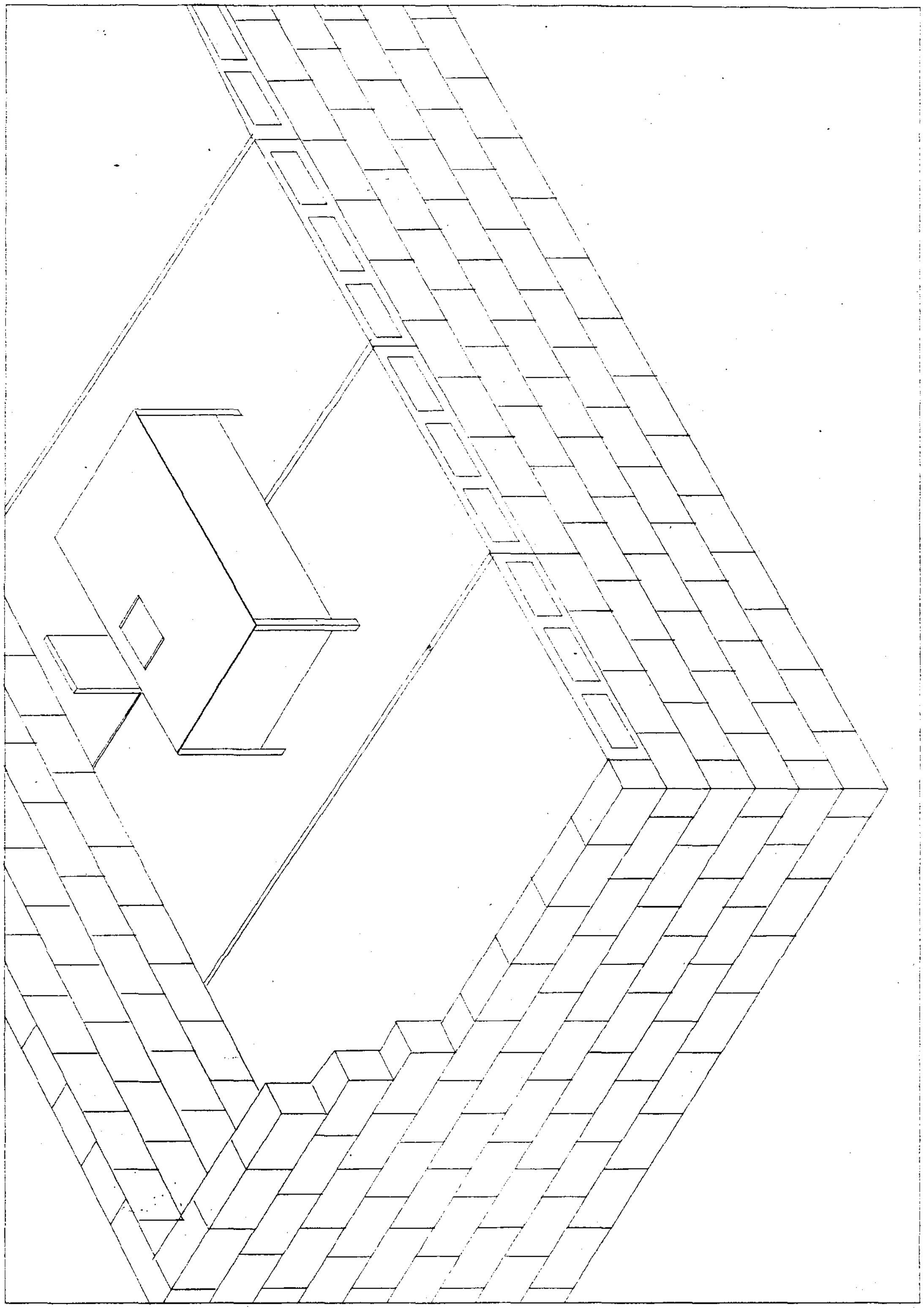

Figure 1. Typical building floor construction utilizing hollow-core planks

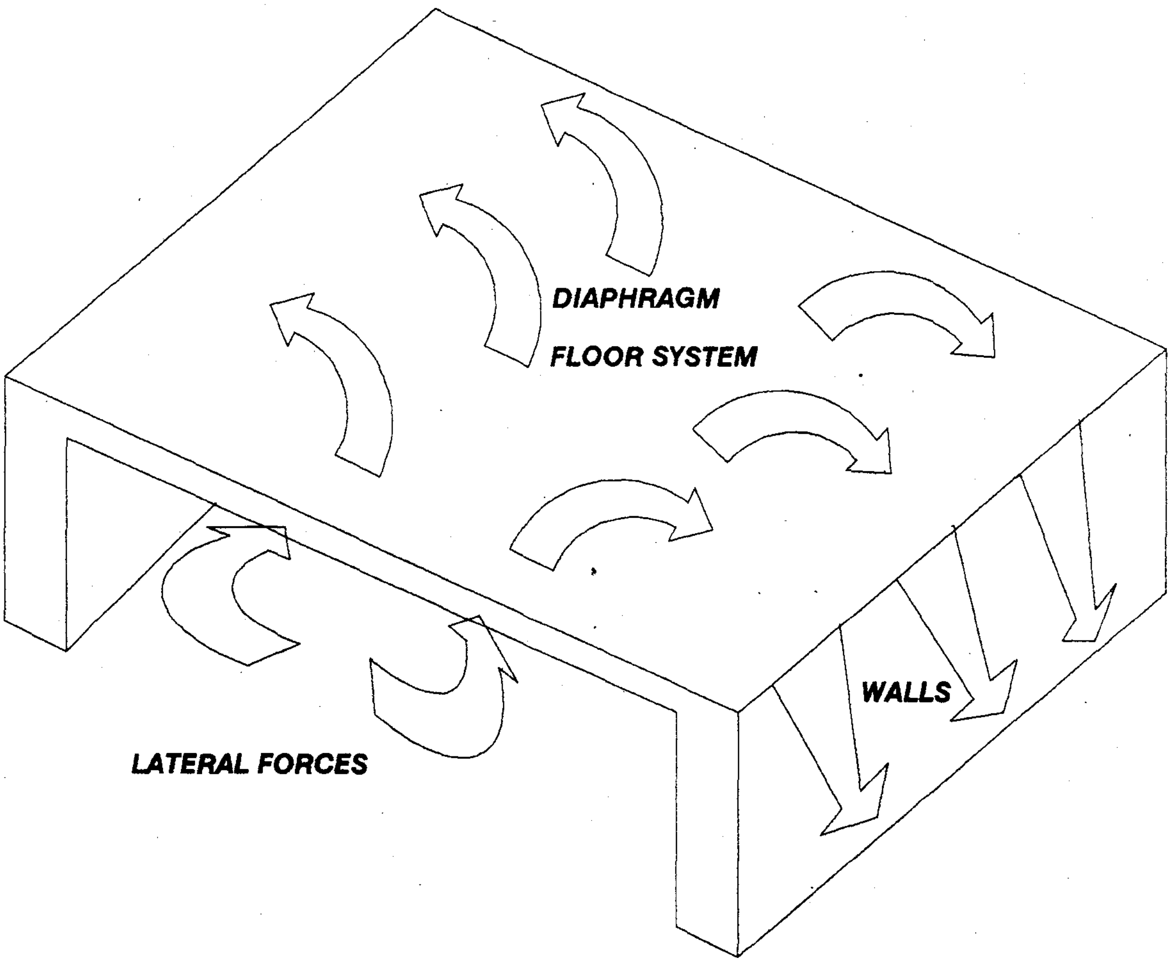

Figure 2. Lateral force distribution

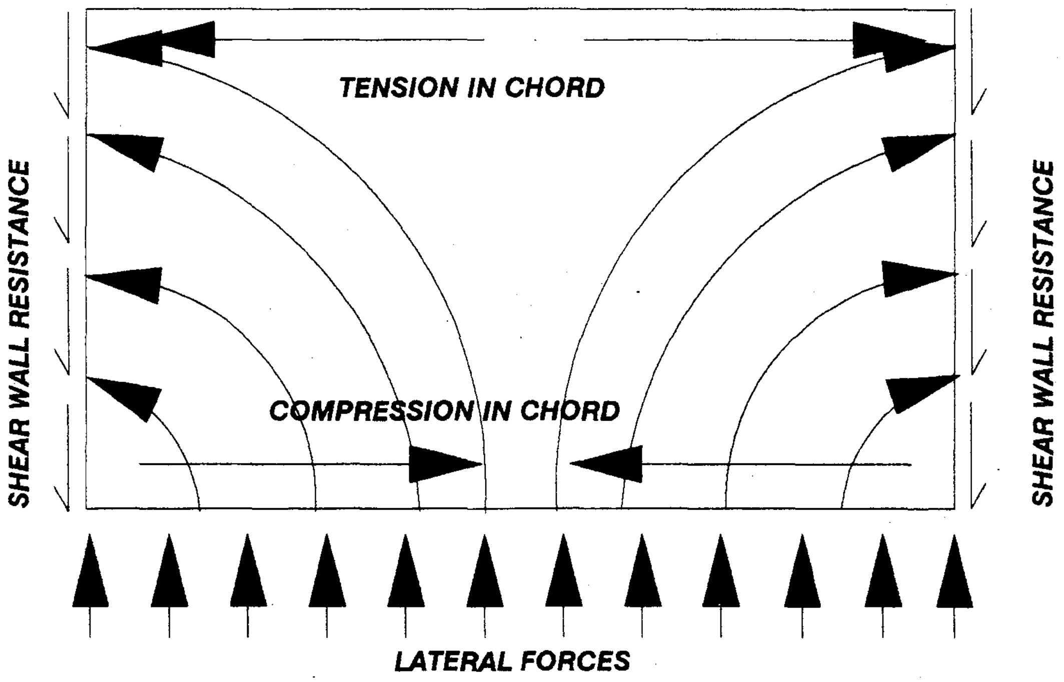

Figure 3. Schematic force distribution diagram

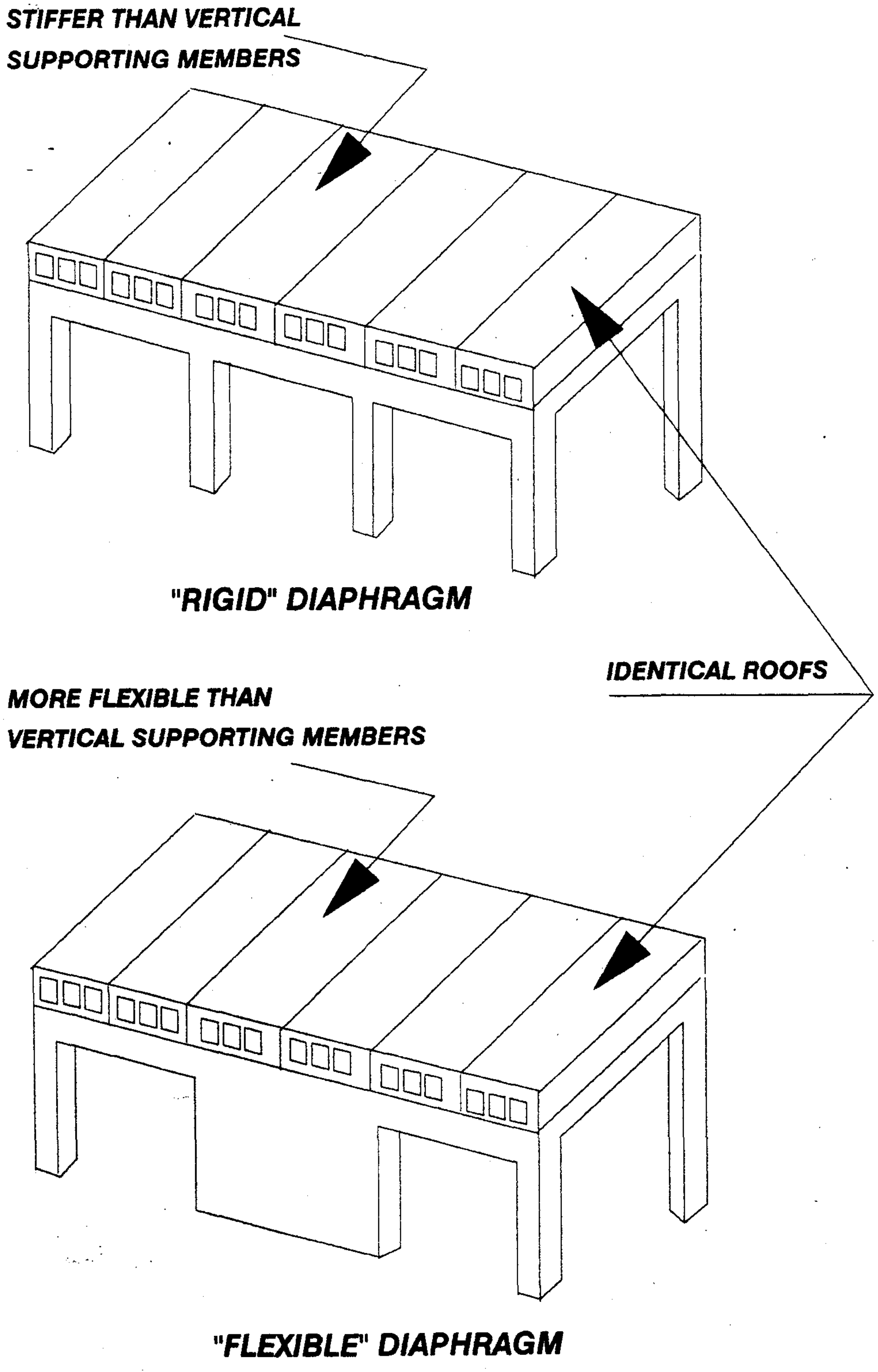

Figure 4. Diaphragm stiffness classification

1.2 Objective of the Overall Research Program

The research undertaken for this project is part of the U.S.-Japan Coordinated Program for Masonry Building Research. Each category of this program is conducted under the supervision of the Technical Coordinating Committee for Masonry Research (TCCMAR). The TCCMAR committee was organized to function under the auspices of the Panel of Wind and Seismic Effects of the U.S.-Japan Cooperative Program in Natural Resources (UJNR). Study of floor diaphragms, which is the objective of this project, is the fifth research task. Additional information on the organization of the Masonry Building Research Program is available in Reference 25.

The objective of the overall research program is to elevate masonry structural analyses, design, and construction practice to a level comparable to structural steel and reinforced concrete technology [25].

1.3 Scope of Task 5

The study of concrete diaphragm characteristics was divided into two separate tasks. Task 5.1 involved the experimental and analytical investigation of precast horizontal diaphragms subjected to in-plane loading. Task 5.2 focused on the collection of existing literature and data generated from the discussion and testing of horizontal diaphragms. This report is devoted to the findings on Task 5.1. A separate report will be issued for Task 5.2.

The objectives of this research project were to determine the basic failure modes, ascertain behavioral characteristics, and investigate analytical properties for the full-scale testing of precast, prestressed hollow-core plank diaphragms subjected to in-plane shear.

Diaphragm strengths were characterized by 1) First Major Event (FME) strength, 2) limit state strength, and 3) ultimate strength. The FME strength is the load associated with the initial diaphragm breakdown. The cause for this breakdown may be due to a major crack at the seam between adjacent planks, a diagonal tension crack propagating across the diaphragm, or any other event that results in a change in stiffness and eventual transformation of the diaphragm into the inelastic range. In this report, the limit state strength is defined as the peak stabilized strength, whereas the ultimate load refers to the peak virgin strength. Displacements associated with these peak strengths may or may not necessarily coincide. Achievement of a specific limit state strength for a particular diaphragm is more likely to be reproducible, since this strength is attained during stabilization cycles. On the other hand, the ultimate strength occurs during the virgin cycle (first time incremental displacement), and represents a load that may not be counted on under similar circumstances.

The effects of various parameters were investigated. These parameters included:

- boundary condition (number of sides connected to the loading frame)
- orientation (placement of the planks with respect to the direction of the applied lateral load)
- slab thickness (plank depth of six, eight and twelve inches)

- aspect ratio (geometric configuration of the diaphragm)
- topping (addition of a two-inch cast-in-place concrete slab)
- seam connectors (variation in the number of seam connectors to verify the implications of attaining an alternate failure mode for the untopped tests).

Table 1 summarizes the relationship of these parameters to the individual diaphragm tests.

In order to determine the behavioral characteristics of a precast, prestressed concrete floor system, the following items were completed:

1) Collecting previous experimental data on both hollow-core diaphragms and hysteretic models and condensing into summary form.
2) Testing sixteen full-scale prestressed, precast plank diaphragms employing the stated parameters.
3) Conducting sixty-six elemental tests, fifty-four under direct shear and twelve elemental tension tests.
4) Comparing the behavior of the diaphragm tests with the various parameters.
5) Developing a method of predicting initial stiffness, FME limit state strength, and ultimate limit state strength.
6) Defining hysteretic model for the plank diaphragms.

This document will include the procedure used and the results obtained from each of the items listed above.

The second phase of the project entailed gathering and reviewing existing literature and data on horizontal diaphragms. The information collected from both phases of the project is to be combined and used in other task areas of the Masonry Building Research Program which culminates with the eventual construction and testing of a full-scale masonry building.

Table 1. Summary of Parameters for Diaphragm Tests

Test No.	Plank depth (in.)	Number of sides connected	Orientation	Topping	Weld ties per seam
1	8	2	T	NO	3
2	8	2	P	NO	3
3	8	2	T	NO	3
4	8	2	T	NO	3
5	8	4	T	NO	3
6	8	4	P	NO	3
7	8	3	P	NO	3
8	8	2	P	NO	3
8B	8	2	P	YES	0
9	6	2	T	NO	3
10	6	4	P	NO	3
11	12	2	T	NO	3
12	8	2	P	YES	0
13	8	4	T	YES	0
14	8	4	P	YES	0
15	8	4	T	NO	15

Notes:

All two-sided tests, with the exception of Test #2, are connected to the loading beam and the restrained support.

The orientation refers to the direction of the applied load, i.e. P means parallel to the applied load (EW), T means transverse to the applied load (NS).

2. REVIEW OF PREVIOUS RESEARCH

A well designed diaphragm is essential for the structural integrity of a building during earthquake or wind induced motions. Shear force is distributed to the various elements of the lateral load resisting system in proportion to their rigidities relative to that of the diaphragm. Thus, knowledge of the behavioral characteristics of a diaphragm is necessary to perform a lateral load (seismic) analysis of a multi-story building.

Diaphragms may be categorized according to their composition into the following common types: cold-formed steel, composite steel deck, timber, reinforced concrete, and precast concrete. Each of these groups are similar in that they provide in-plane shear resistance, but they exhibit unique behavioral characteristics. A brief listing of the diaphragm system type, along with the history [11] follows:

System	Background
1. Wood Boards (straight laid)	Non-engineered; pre-1930
2. Structural Steel Bracing	First used in the late 1900's
3. Wood Boards (diagonally laid)	Used in construction, 1930's
4. Cast-in-place Concrete	First utilized in construction 1920's, Methods of analysis developed 1900-1950
5. Plywood Sheathing	First utilized 1940-1950, Diaphragm tests 1950's
6. Metal Deck Systems	Used in construction 1950's, Diaphragm tests 1950-1960
7. Precast, Prestressed Concrete Units	First used 1950's, Diaphragm tests 1950-1960
8. Composite steel deck and reinforced concrete	Diaphragm tests 1960-present

The seismic performance of each of these systems is different and depends on the characteristics of the diaphragm and the event.

Earthquakes are the physical manifestations of energy stored in a passive state beneath the earth's surface [5]. Energy is defined as the capacity to do work; and depends upon the duration, intensity, and characteristics of the event. A considerable number of uncertainties are evident in estimating these parameters; therefore, sufficient strength, durability and stability must be provided [12]. The net energy input must be dissipated either through damping or inelastic action. The inelastic action of the superstructure is represented by a stiffness degrading hysteresis model [17,26].

During previous seismic events, the performance of precast concrete units without topping has been poor, while the precast concrete units with topping have exhibited variable to good performance [12]. Martin and Korkosz [20] stated that the absence of continuity and redundancy (between the precast slabs) has caused some designers to question the stability (of precast structures) under high lateral loads. This statement is echoed in most references on this subject [2,4,5,16,20,42,43].

Energy will always take the route of least resistance. Because the panel connections of untopped systems are weaker than the adjacent elements, these seam joints normally fail first. Most of the pertinent information available states that the prestressed components perform excellently as individual units, however, the connections between the panels do not perform as well. To the author's knowledge, no full-scale tests have been conducted on hollow-core plank diaphragms with the periphery fastened to a supporting system. The connections between the precast panels and the walls are also a possible failure location and this is the subject of another of the TCCMAR investigations.

2.1 Hollow-core Planks

Hollow-core planks are most commonly used as structural floor or roof elements, but may also be used as wall panels for load bearing or non-load bearing purposes. Typical spans for hollow-core planks range from 16 to 42 feet with possible depths of 6-, 8- 10- and 12-inches. Presently, six types of hollow-core plank products are commercially available, as listed in Reference [28].

•Dynaspan:	Made in 4- or 8-foot widths by a slip forming process with low-slump concrete. Each slab has 14 cores.
•Flexicore:	A wet cast product poured in 2-foot widths and 60-foot long spans. Voids are formed with deflatable rubber tubes.
•Span-Deck:	A wet cast product poured in two sequential operations with the second being a slip cast procedure. The planks are 4- or 8-foot wide with rectangular voids.
•Spancrete:	Made in 40-inch wide units by tamping an extremely dry mix with three sequential sets of tampers in order to compact the mix around the slip forms.
•Spiroll:	An extruded product made in 4-foot wide units with round voids formed by augers which are part of the casting machine.
•Dy-Core:	An extruded 4-foot wide product made by compressing zero slump concrete into a solid mass by a set of screw-conveyors in the extruder. High frequency vibration combined with compression around a set of dies in the forming chamber of the machine produces the planks with oblate, or octagonal shaped voids.

Due to the close proximity of the manufacturing plant and several other factors, the Span-Deck planks were used exclusively in the diaphragm tests conducted as part of this investigation.

2.2 Seam Connections

Four methods of connections are currently being utilized [6]. These are cast-in-place topping, welded hardware, projecting reinforcement, and shear friction with grouted joints.

Specimens with the cast-in-place topping provide the best lateral force resisting system. The two-inch minimum topping, shown in Figure 5, has performed well. The topping mandates that all of the individual panels act as a single

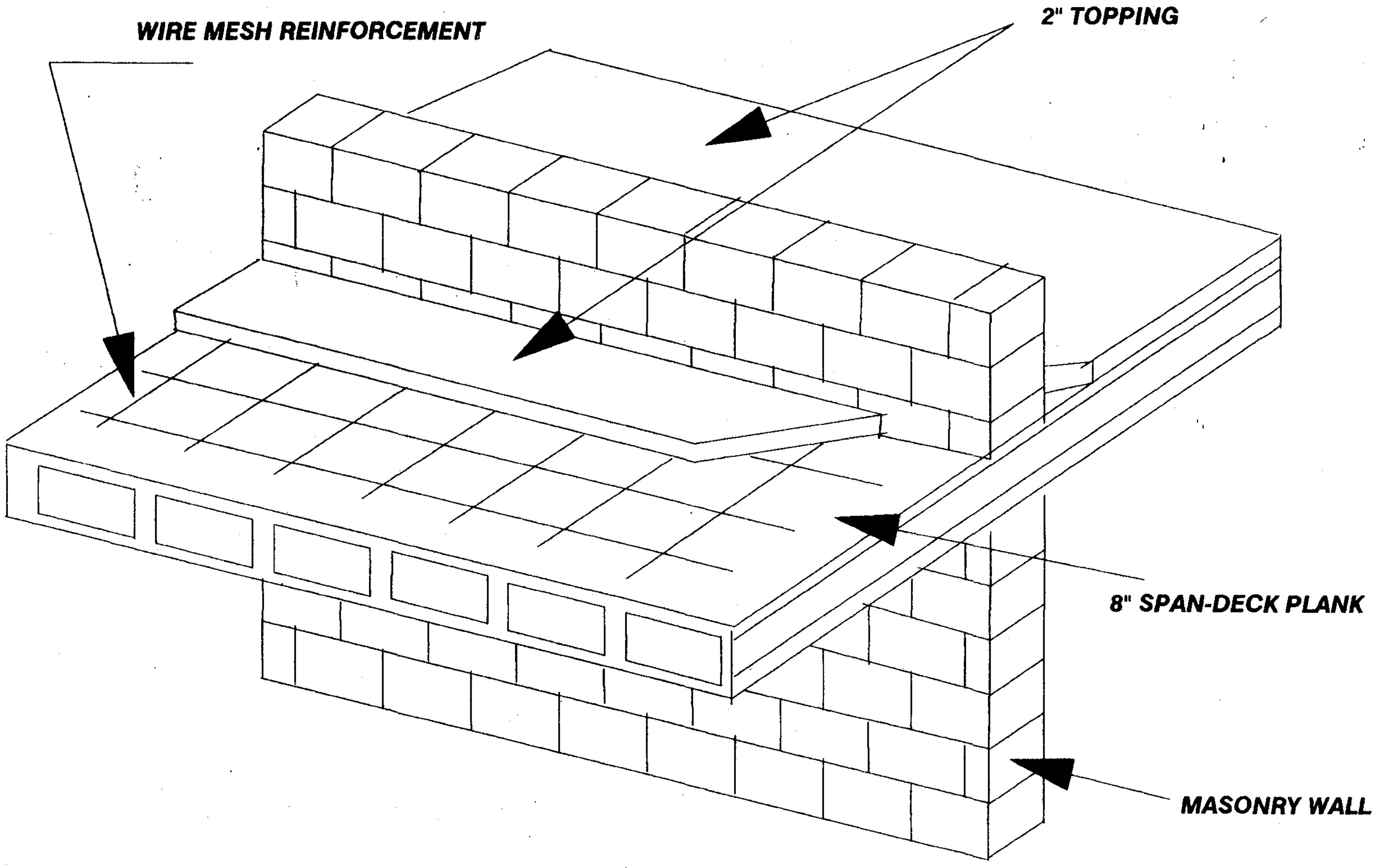

Figure 5. Plank system with topping

rigid unit. The American Concrete Institute (ACI318-83) Building Code contains a section which may be adopted for use in topping design.

Welded hardware connections comprise the second category of hollow-core connections. The Japanese Prestressed Concrete Association has stated the weld joints are suitable for seismic resistance provided that the parts to be welded are suitably doweled in the concrete to create the necessary bond [32]. This connection, shown in Figure 6, is quite common for precast members. The Prestressed Concrete Institute (PCI) Design Handbook [33] defines a method of strength prediction based on the angle, length and type of reinforcing bar. Values are presented in many texts and papers on this subject for different types of connection ties [7,36]. A value of approximately 10 kips in shear is referenced for a generic weld tie similar to those used in the diaphragm tests [33]. Elemental tests are recommended in order to determine the exact strength of any particular unit [2].

Untopped, grouted systems utilizing splicing of projecting reinforcement are the third type of connection. Figure 7 is an example of this type of joint connection. There are only a few code provisions and analysis techniques related to this design.

The most popular type of connection is the untopped, grouted-reinforced joint. This design employs reinforcement parallel and perpendicular to the joint at the extremes of each plank unit as is shown in Figure 8. The seam, however, is only filled with grout. Experimental observations have shown that the coefficient of friction in the seam after the initial crack approaches a value of 1.0 [6]. A conservative value of 80 psi is given for grout shear strength in several sources [2,33]. Some references list actual experimental values for various types of planks and seams [7,36,48].

Walker's article [48] "Summary of Basic Information on Precast Concrete Connections", alluded to information concerning shear strength tests of Spancrete slabs with grouted joints. These eight tests, which investigated various slab thicknesses, were performed for Arizona Sand and Rock Company, Phoenix, Arizona (1964). The grouted seams were subjected to a static, monotonic direct shear load applied on the center of the three slabs of the test specimen.

Proprietary tests were conducted by Tanner Prestressed and Architectural Company [13], which investigated the shear strength of the grouted horizontal shear joint in eight-inch Span-Deck planks. As in the previously discussed tests, a force was applied to the center of three sections, so that the load was equally transmitted to the five-foot long seams. The failure mode for each of the three tests was a longitudinal shear crack propagating along the grout-plank interface.

An experimental investigation of the shear diaphragm capacity was undertaken by Concrete Technology Corporation in February 1972 [6]. The objectives of this test were to measure and evaluate the ability of 8-inch Spiroll Corefloor slabs to transfer horizontal shear through the grouted longitudinal joints without shear keys, as well as to determine the coefficient of friction, which served as a direct measure of the effectiveness of shear friction reinforcement in the end beams. The longitudinal joints were subjected to pure shear as the load was

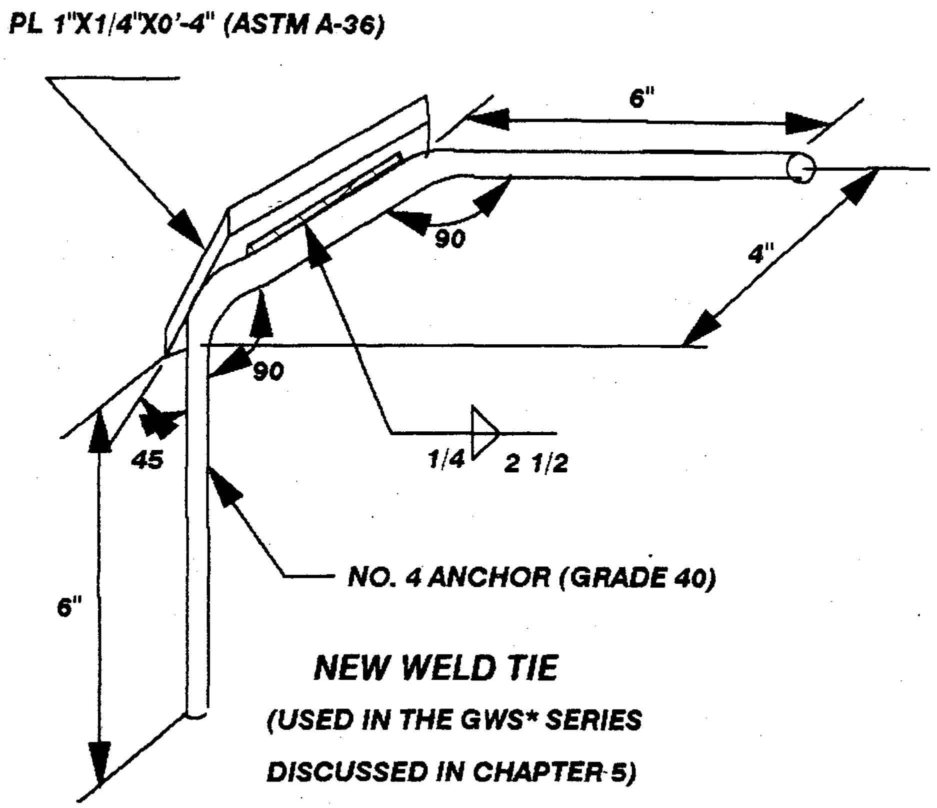

NEW WELD TIE

(USED IN THE GWS* SERIES
DISCUSSED IN CHAPTER 5)

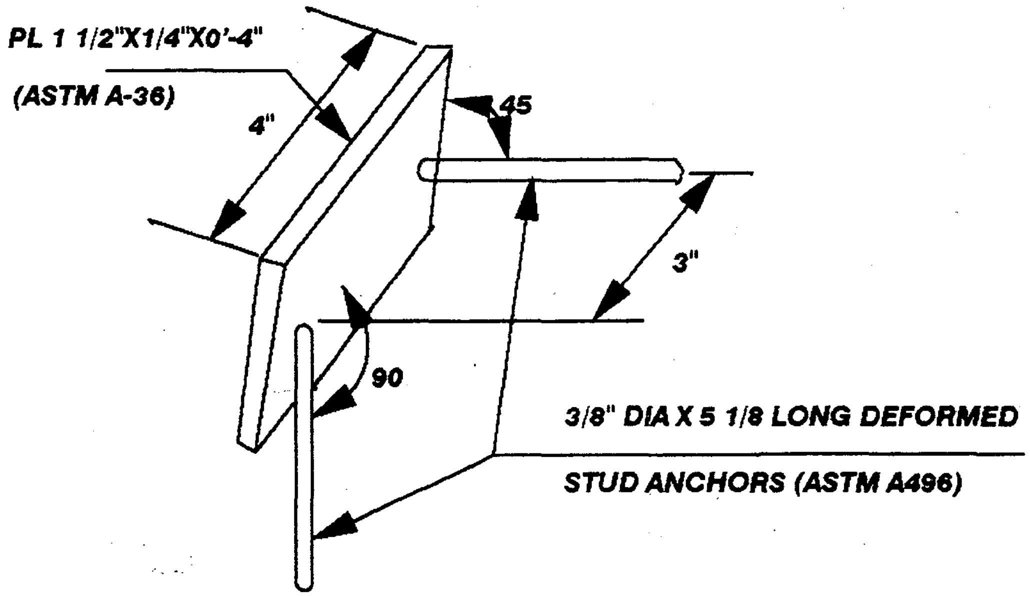

STANDARD WELD TIE

Figure 6. Weld tie details

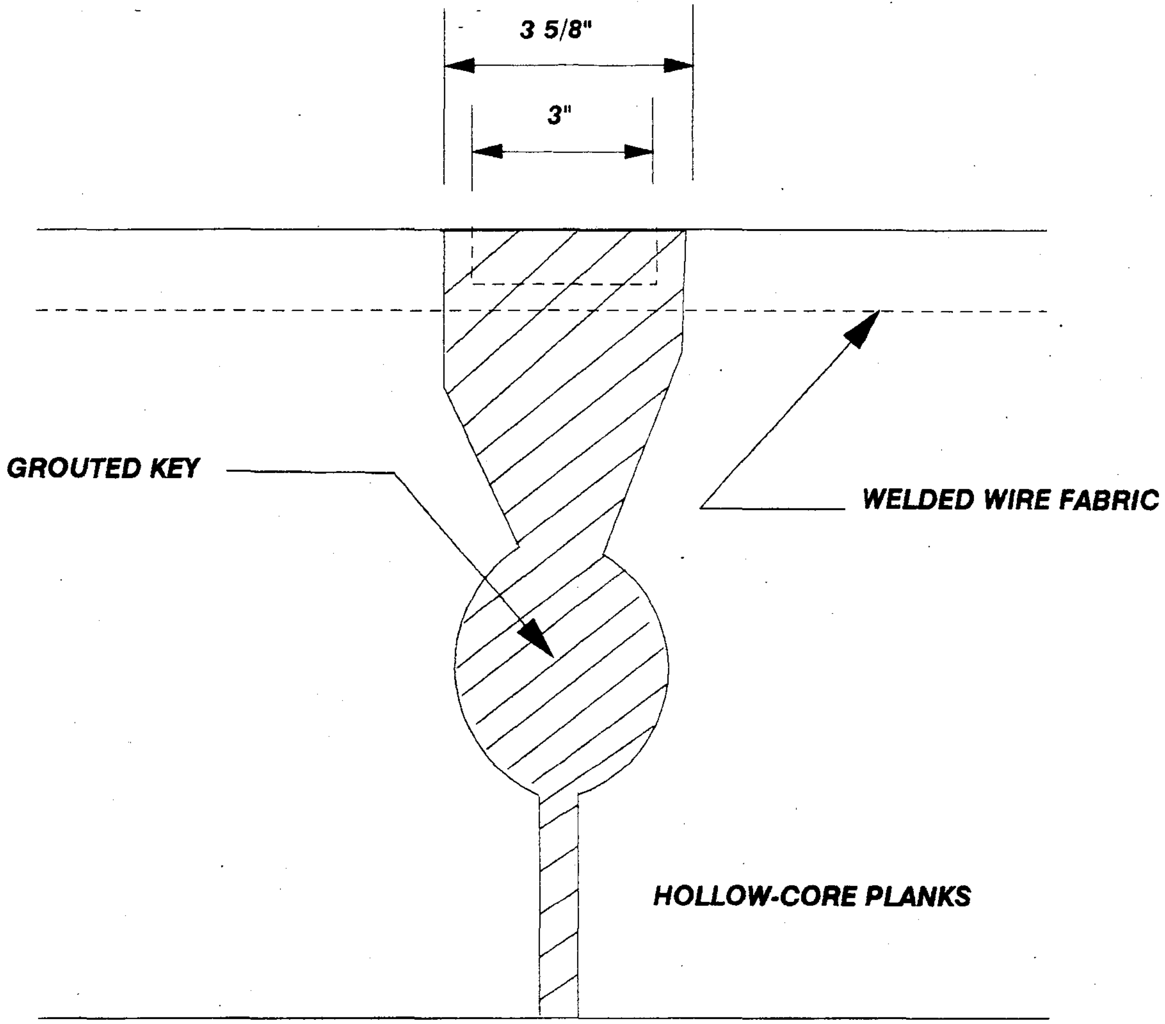

Figure 7. Typical mesh joint detail [17]

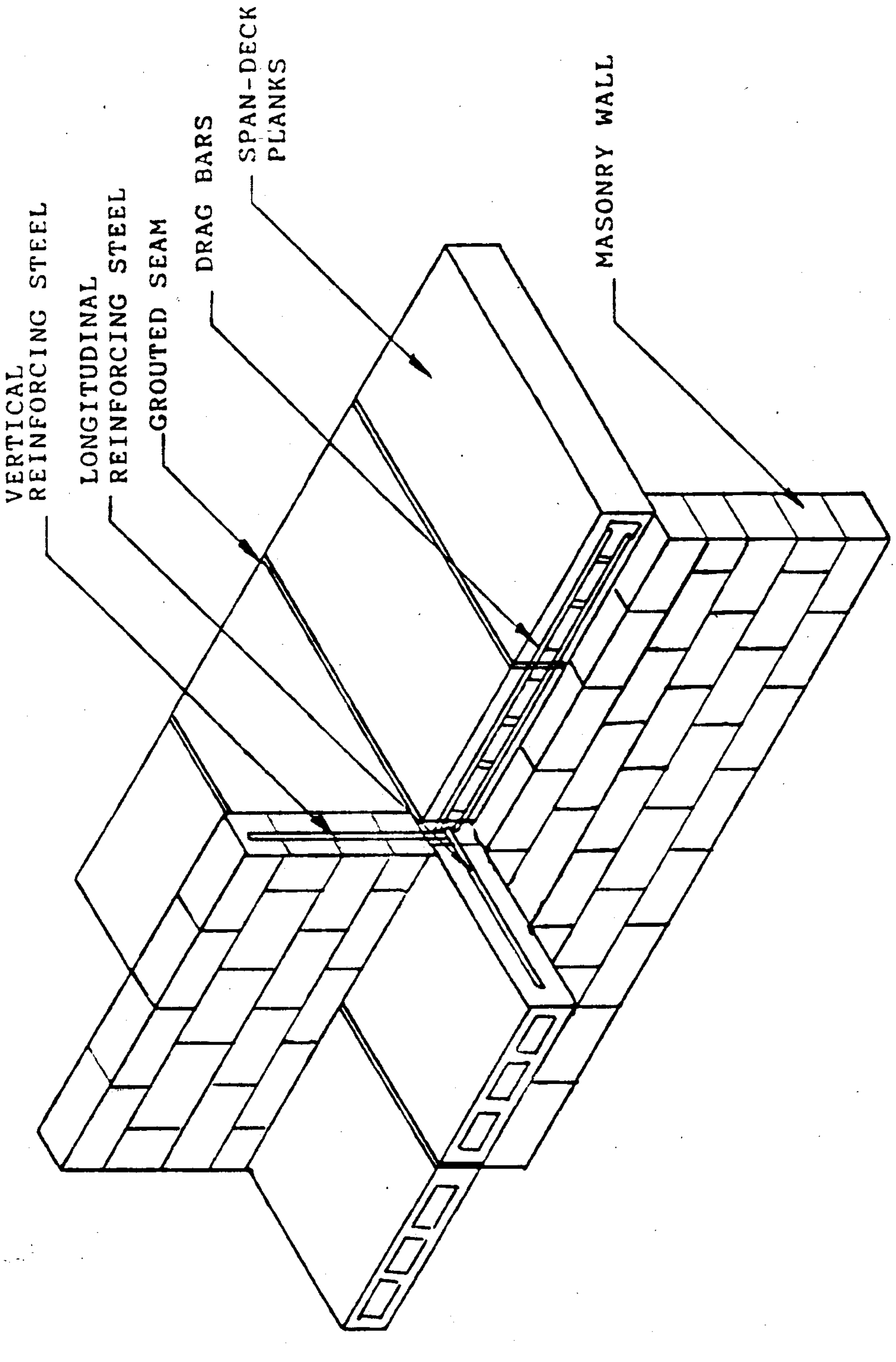

Figure 8. Schematic of shear friction joint

applied to the center slab while the exterior slabs were held in place. The shear strength was not tested to ultimate capacity, since a measure of the shear friction effectiveness was one of the desired objectives. After the joints were artificially cracked, the coefficient of friction was measured and was found to vary between 1.3 and 2.0. These values indicated that the reinforcement had performed satisfactorily and that the 1.0 value was conservative for planks with extruded edges.

A publication of the Concrete Technology Associates by Cosper, et.al. [7] reviewed hollow-core diaphragm test results for the shear strength of the grouted keyway between adjacent 12-inch Dy-Core panels. Longitudinal shear loading was accomplished by applying a load against sixteen 1/2-inch prestressing strands, which were in an "X" arrangement across the seam. Parameters researched included the following: 1) the shear capacity of an uncracked grouted joint, 2) the effectiveness of shear-friction reinforcement in transferring shear across a joint, 3) the ductility of the system after the bond between panels had fractured, and 4) the effect of cyclic loading on the system. The uncracked grouted seam demonstrated a high capacity in resisting lateral shear loads. Shear-friction steel placed in the edge beam supplied adequate clamping forces once the seam had fractured. Ductility demands were satisfied as well, since the shear strength continued to rise after joint displacement. Finally, the diaphragm exhibited sufficient resistance to cyclic loading by maintaining a stabilized strength after repeated cycles above design requirements.

Another experimental study, by Reinhardt [36], tested the joint between hollow-core planks under shear loading while subjected simultaneously to a normal force. Variable strengths of mortar and lengths of the grouted connection (0.3 to 2.1 meters) were accommodated for the single seam. Joint length was found to have a significant influence upon shear stress at fracture for their particular testing configuration. Failures were characterized by brittle fractures of the bond at the mortar and grout interface. Each of these tests used a slightly different testing frame two of which are shown in Figure 9. With such testing arrangements, however, the actual maximum shear is not simply the load divided by the contact area. A correction factor which accounts for the non-uniformity of the shear stresses must be used. Chow, Conway, and Winter state that the distribution of shear stresses in deep beams (beams whose depths are comparable to their spans) depart radically from that given by the ordinary, simple formulas [3]. Using finite difference, strain-gage measurements, and photoelastic measurements, Roark and Young have tabulated the correction factor for various testing arrangements [37]. The values for one such arrangement are shown in Figure 10.

2.3 Analysis of a Precast Diaphragm

The current design practice for diaphragms is based on the seam connection capacity. Therefore, with estimates of the strength of the seam connections, the analysis of the diaphragm is possible. In order to simplify the analysis procedures the following assumptions are generally made [47]:

- the panels initially remain in the linear range,
- all the nonlinear deformations occur first in the edge zone connections, and

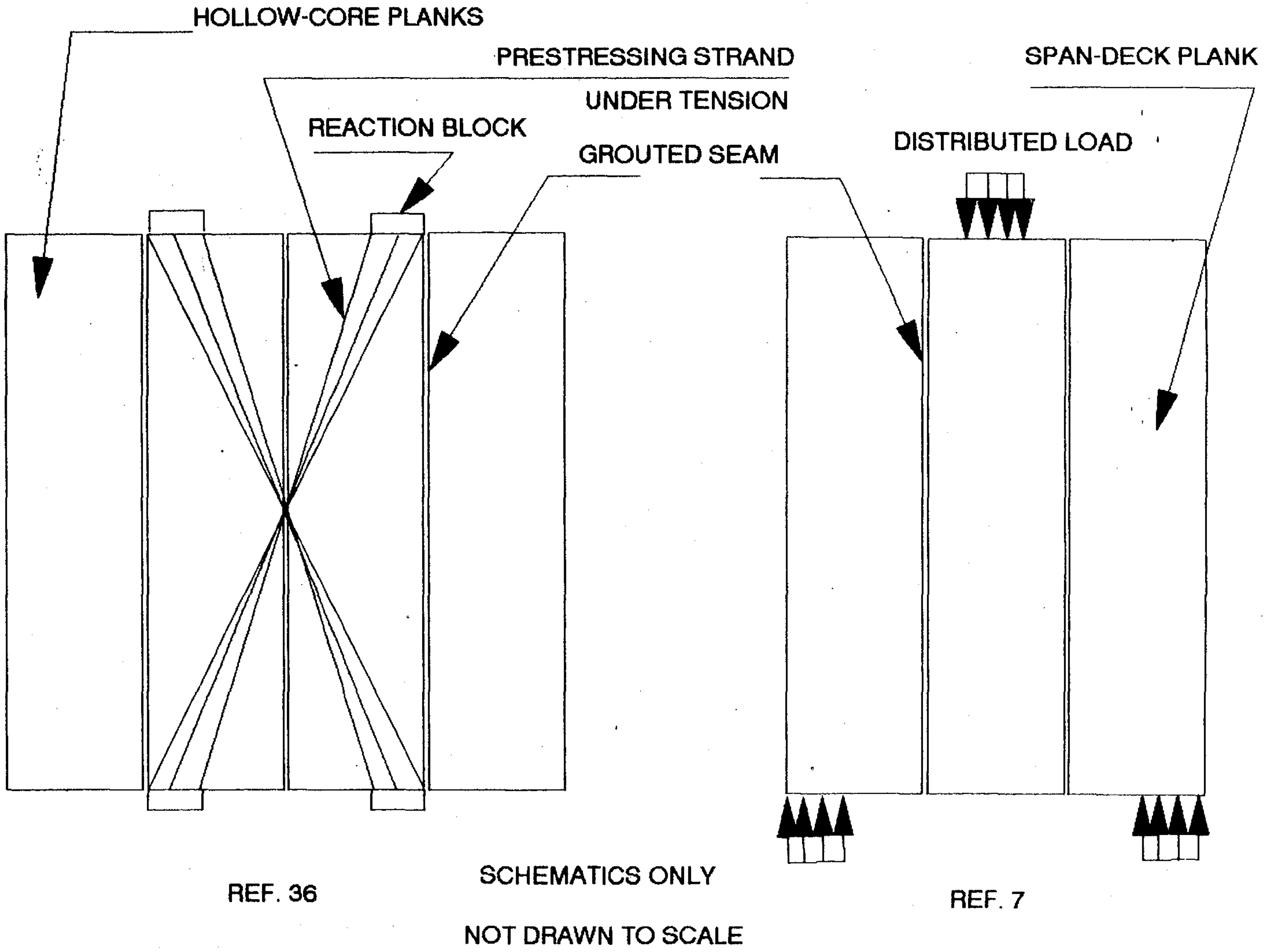

Figure 9. Sample elemental shear testing arrangements

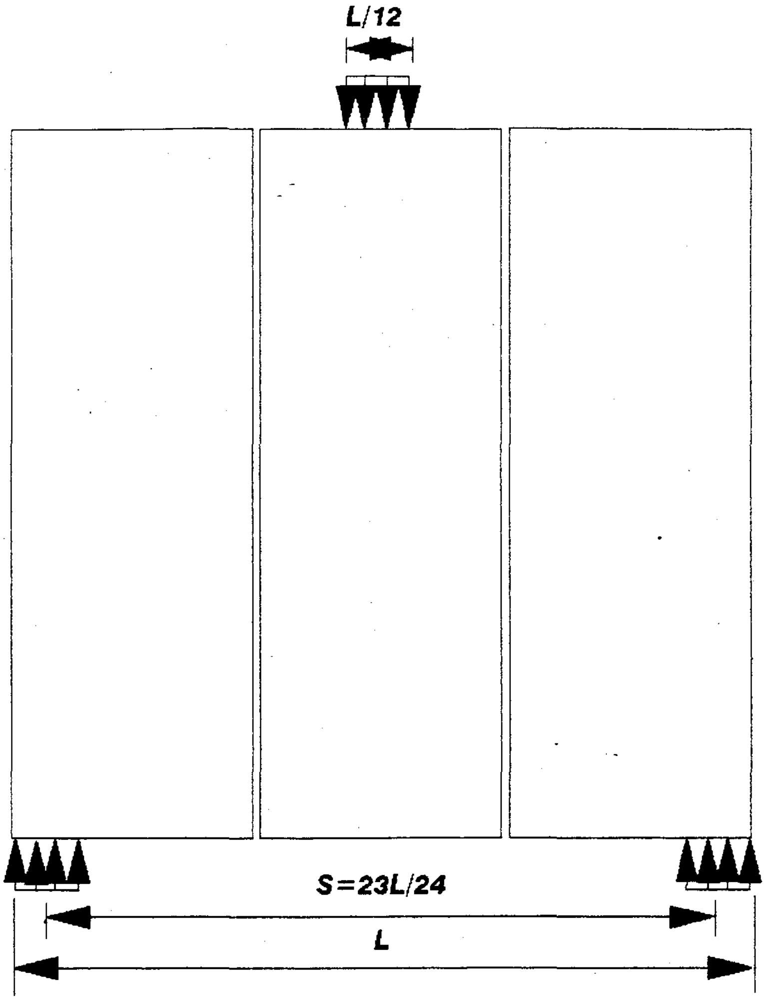

RATIO L/d	RATIO Span/d	MAX Mc/I	MAX Mc/I	MAX V/D
3	2.875	0.970	1.655	1.57
2	1.915	0.960	1.965	1.60
1	0.958	1.513	6.140	2.39
1/2	0.479	5.460	15.73	3.78

(From Reference 37)

Figure 10. Influence of s/d ratio on maximum shear stress and maximum fiber stress

- the horizontal panel systems (slabs) are usually rigid.

The magnitude of the horizontal unit in-plane shear force, V_u, is calculated according to the shear stress formula [7,17]:

$$V_u = VQ/I \tag{2-1}$$

where:
V_u= in-plane shear stress, Kips/in
V = applied shear, kips
Q = first moment of area, in.^{3}
I = first moment of inertia, in.^{4}

or

$$V_u = 1.5\ M / sh \tag{2-2}$$

where:
M = service load moment, kip-in.
h = thickness of diaphragm, in.
s = diaphragm span, in.

The allowable unit shear force is then calculated by the following formula based on a recommended shear stress of 80 psi from References 2 and 33:

$$V_n = 0.08(t) \tag{2-3}$$

where:
t = effective seam thickness, in.

A strength reduction factor of 0.85 is normally multiplied by the allowable unit shear force. Load factors are then multiplied by the calculated unit shear force values to obtain a controlling equation. For example, using the recommended load factor of 1.3 from Reference 2, the following equation results:

$$1.3\ V_u = 0.85\ V_n \tag{2-4}$$

The foregoing analysis procedure reflects the current practice which will be replaced later on with the proposed analysis and design recommendations.

2.4 Effect of Vertical Load

Most of the previous in-plane diaphragm tests have been conducted without the presence of vertical load. A comparison of tests with and without vertical load showed that the behavior of the systems was approximately the same [22]. Nakashima, Huang and Le-Wu Lu state that the crack pattern, failure mode and stiffness degradation were similar for tests with and without vertical load. In addition, the ultimate loads were within fifteen percent of each other. A study employing composite deck diaphragms was also performed and similar results were obtained [23]. The behavior of a floor slab under in-plane load is therefore assumed to be two-dimensional problem and hence vertical load effects were ignored in this study.

2.5 Finite Element Analysis of Hollow-core Plank Diaphragms

Research conducted by the United States Steel Corporations [19] focused on a finite element stress analysis of staggered-truss framing system with the horizontal diaphragm consisting of precast prestressed hollow-core planks. Several cases involving different parameters were studied: both cored and solid planks, the addition and exclusion of spandrel shear attachments, and whether or not the joints between adjacent floor planks were cracked. A shear force of 1000 kips was applied to each truss and stresses determined. (This assumed wind-shear was equivalent to applying a high wind pressure of 40 psf to a 40 story structure.) The procedure undertaken for the finite element model and results obtained were discussed.

The stress diagrams indicated that a shear diaphragm accurately described the majority of the behavior of the plank assembly with respect to the manner in which loads were transferred. However, locally high principal tensile stresses were noted in opposite corners of the floor. These were reduced with the shear attachment of the spandrels to the planks. Also, the substitution of the solid planks at the edges of the floor was not effective in reducing corner stresses. Adversely high stresses resulted when the joints were assumed to be cracked, thereby causing individual plank rotation. Finally, for tall structures, sufficiently high diagonal tension stresses existed, and therefore, must be considered in the design of the horizontal diaphragm.

2.6 Hysteretic Models

A complete description of the behavioral characteristics of a structure throughout the plastic and elastic ranges can be obtained with a hysteretic model. This type of model predicts, the force-displacement relation for a system utilizing stiffness and strength information discussed earlier. Riddell and Newmark described a set of desirable characteristics for a hysteretic model. These features can be summarized as follows [35]:

1. Reality: The selection of model parameters that are directly associated with known physical characteristics.
2. Accuracy: The model must portray the measured results as closely as possible.
3. Simplicity: The prediction should be completed with the simplest method possible.
4. Consistency: The relationship between the response variable and any specific parameter should be consistent.

Many different models have been developed in the past. Each successive model has improved upon the first effort in some way. The characteristics of any reinforced or prestressed concrete model have become more refined and can be briefly stated as follows [26,41]:

1. The stiffness must change with the cracking of the concrete and the yielding of longitudinal reinforcement.
2. The loading stiffness in the second cycle is lower than the that of the first.
3. The average peak to peak stiffness decreases with the increase of the maximum displacement amplitude.
4. There is a tendency for very low incremental stiffness near the origin followed by a stiffening region (pinching effect).
5. The load deflection curve for any cycle can be represented ideally by a series of linear segments or characteristics slopes. These slopes are the initial slope, fully cracked slope, slope after yielding, and the return slope.
6. The hysteretic curve for a prestressed structure has relatively small residual curvature.

A classification of the hysteretic models in three families was presented by Wakabayashi [49]. The first family is termed Massing type family which is characterized by having hysteresis curves geometrically similar to its envelope curves. Some examples of this family are the bilinear model, trilinear model, and Jennings model [18]. The next is called degrading type family. This type allows for the effect of stiffness degradation caused by load reversals in inelastic ranges. Many models of this type have been proposed such as Clough model [50], Takeda model [51], Sina model [38], etc. The third is the Slip-type family. This family is often used to represent bolt connection in a steel structure, bracing members with significant buckling effect, and also reinforced concrete members with shear distortion as dominating behavior. Some examples of this type are the double bilinear model [52], and Iwan model [53]. The following subsections present a brief description of the most relevant models for each family.

2.6.1 Massing Type Models

The most popular model of the massing type family is the bilinear hysteretic model [49]. An example of this model is shown in Figure 11. The elasto-plastic model is a special case defined for zero slope of the second branch. This model is often used to predict the force-displacement characteristics of a steel frame. When used for reinforced concrete systems, this model provides only a rough estimate.

The trilinear model [49] has no degradation characteristics. The skeleton curve is formed with three lines (see Figure 11b). Only few rules are necessary to define this model. This model is sometimes used for composite steel and reinforced concrete systems, but the trilinear model with degradation properties is preferred.

The Jennings model [18] was developed in the early 1960's. This model uses closed formed mathematical formulas with smooth rounded curves which are general enough to describe the behavior of systems ranging from linear to elasto-plastic. The skeleton curve uses a formula similar to that first proposed by Ramberg and Osgood [21] to describe relations between stress and strain (see Figure 11c).

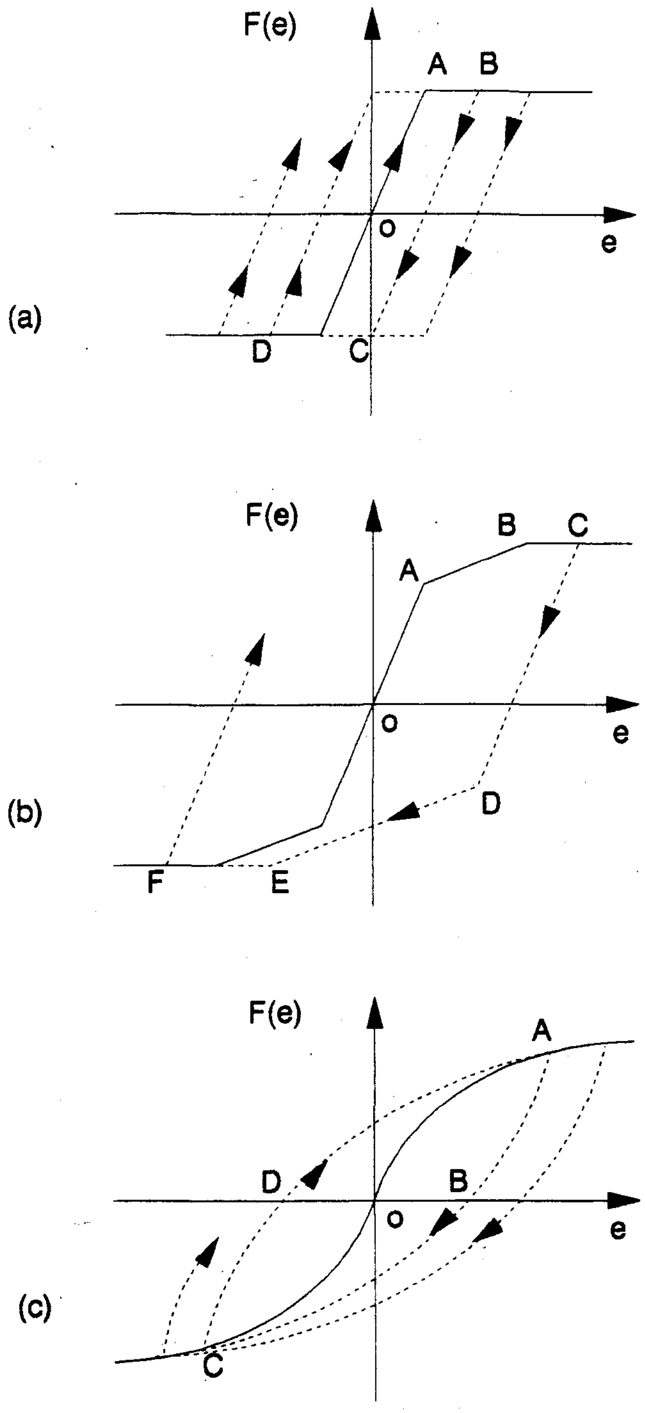

Figure 11. **Massing type models [52] (a) Bilinear model (b) Trilinear model (c) Jennings model.**

The skeleton curve is defined by the following equation:

$$x/x_y = p/p_y + \alpha(p/p_y)^r \qquad (2\text{-}5)$$

where
x = the displacement of the structure
x_y = the calculated yield displacement
p = the restoring force
p_y = the yield force
α, r = empirical constants controlling the skeleton curve shape

The ascending and descending branches of the hysteresis loop are defined respectively by:

$$(x/x_0)/2x_y = (p+p_0)/2p_y + \alpha[(p+p_0)/2p_y]^r \qquad (2\text{-}6)$$

where
x_0 = the displacement at the point where the loading is reversed
p_0 = the load at the point where the loading is reversed

2.6.2 Degrading Type Models

Clough and Johnston [50] proposed a degrading bilinear model, improving the elasto- plastic model by accounting for the stiffness degradation observed during the cycling loading of reinforced concrete components. By handling the stiffness degradation in different ways, several versions of the Clough model have been defined. For example, Otani [26] presented a modification to include the degradation in unloading stiffness using the following expression:

$$K_r = K_y \left|(D_y/D_m)^a\right| \qquad (2\text{-}7)$$

where
K_r = the unloading stiffness
K_y = the initial yield stiffness
D_y = the yield displacement
D_m = the maximum displacement
a = the unloading stiffness degradation index (ranging from 0.0 to 0.5)

One of the most popular degrading models is the degrading trilinear model proposed by Takeda, Sozen, and Nielsen [51]. A series of rules are stated to develop realistic force-displacement relationships many of them for low-amplitude cycles contained between large amplitude cycles previously reached. These rules determine different stiffness characteristics for reinforced concrete elements at different load levels as cracking, yielding, unloading, and reloading in successive cycle. A description of this model is shown in Figure 12.

Emori and Schnobrich [12] used a modified Takeda model which takes account of the pinching action and bond deterioration in beam-columns joints. See Reference 12 for the rules on loading, unloading, and load reversals.

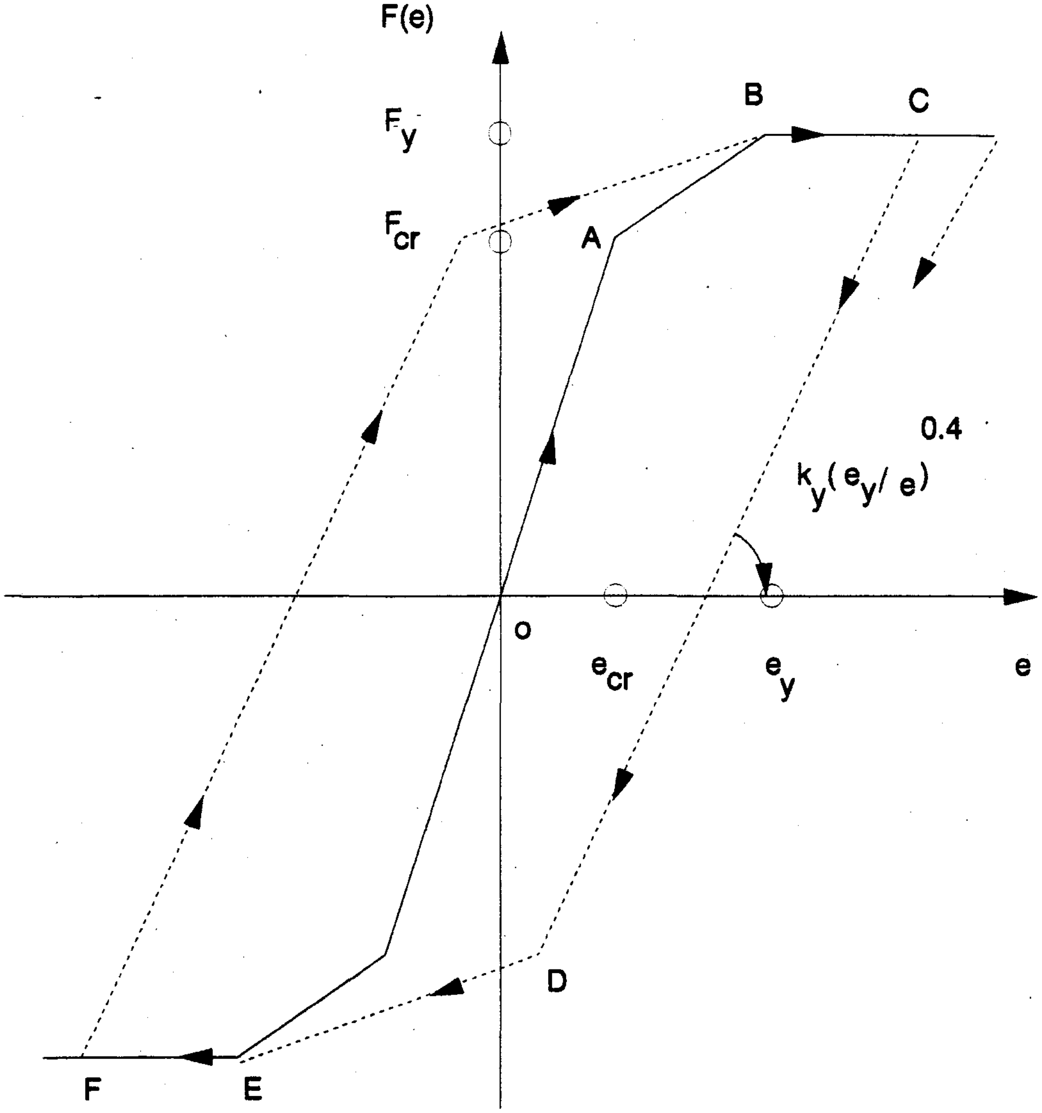

Figure 12. Takeda model

Saiidi and Sozen [38] developed the "Sina" model to simplify the rules associated with the Takeda model and to account for the effects of pinching. The skeleton curve consists of three parts as in the Takeda model and is defined by nine rules.

Otani [53] proposed a modified version of Takeda model to represent the stiffness variation of a joint spring in conjunction with a flexural spring. The skeleton curve used was bilinear with the yield as a break-point in the envelope. This model had less rules than those of Takeda model due to the fact that the cracking point was not recognized, therefore all the rules related to cracking points were eliminated. Eleven rules were associated with this model, as a result, it continued being complicated.

The Q-Hyst model, developed by Saiidi and Sozen [38], is a modified version of the bilinear hysteresis model. The objective of this model was to provide softened hysteresis loops specially for unloading and load reversal stages. Four rules define the model making it easy to use. As the Otani and simple bilinear models, the Q-Hyst model does not provide energy dissipation unless the system yields, therefore, an unreal condition is given when these models are applied to reinforced concrete elements subjected to displacements lower than yield displacement.

In the late 1980's, Ewing, Kariotis, and El-Mustapha [14], developed an hysteretic model employing many of the characteristics associated with the model techniques previously described. This model is part of the Lumped Parameter Model Program, LPM/1 and is named EKEH model. It has nonlinear, inelastic, degrading and pinching capabilities as is shown in Figure 13. This model was specifically designed to predict the nonlinear, hysteretic behavior of reinforced masonry cantilever shear walls. Later research done at Iowa State University by Tremel [54], and Meyer [55] showed that the same model can be used on precast prestressed hollow-core diaphragms. The skeleton curve consisted of a second order function and two linear segments. Key parameters for the envelope are the initial stiffness, peak strength, deformation at peak strength, and post peak degradation factor. The analytical expressions for the envelope curve are as follows:

$$F(e) = F_p e/(F_p/K_i + \alpha|e|) \qquad -e_p < e < e_p \tag{2-8}$$

$$F(e) = F_p(e_m - |e|)/(e_m - e_p)*\mathrm{sign}(e) \qquad e_p < |e| < e_t \tag{2-9}$$

$$F(e) = \beta F_p*\mathrm{sign}(e) \qquad -e_t > e > e_t \tag{2-10}$$

where

$F(e)$ = spring deformation force

e = spring deformation

e_p = deformation at peak strength

e_m = intersection of the post peak strength envelope line equation (2-9) with the deformation axis

β = post peak strength lower limit factor

F_p = peak strength

K_i = initial stiffness

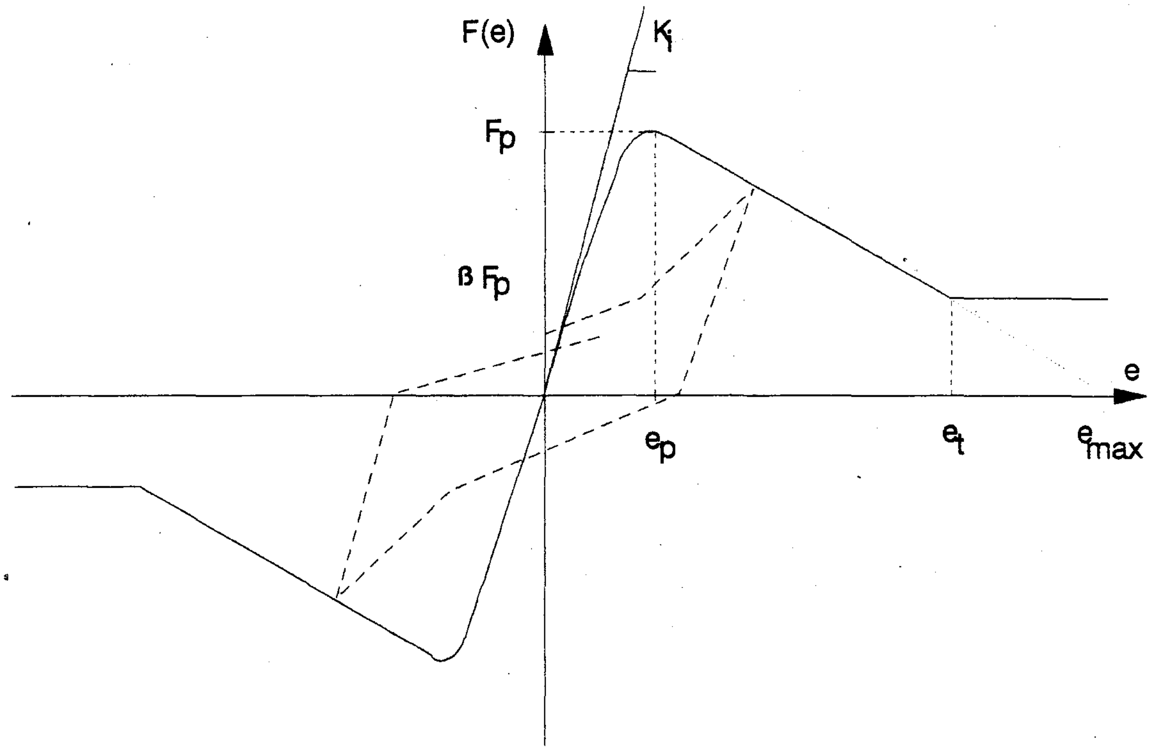

Figure 13. EKEH hysteresis model [14]

e_t = deformation that defines the separation between the two post peak straight line envelope curves given by equations (2-9) and (2-10)

The post-peak strength factor β, is defined as the load after the usable strength has been achieved. Loading and unloading in either tension and compression follow the same rules. For displacements not reached in previous cycles loading follows the envelope curve. Unloading occurs along a degrading stiffness slope defined by:

$$K_u = K_1(F_p/K_1 e_{max})^{\gamma} \tag{2-11}$$

where
K_u = unloading stiffness
e_{max} = maximum deformation reached in all prior load paths
γ = a degradation stiffness constant

The latter constant, γ, is defined from experimental test results and acceptable values range between 0.5 and 0.8. Values above 0.8 lead to nonconservative hysteresis loops.

Rules for reloading are described by straight line paths, which are a function of the pinch force, F_0, and the maximum deformation reached in all prior load paths. Noncycling reloading follows a path directed to point "a". Cyclic reloading is described by a path starting at the point of zero force and continues through the pinch force until it intersects and follows the straight line connecting the origin and a point "a". The location of point "a" is defined by one of the following conditions:

1. If the peak strength has not been exceeded in all previous cycles, point "a" is defined as the point on the envelope that corresponds to the maximum displacement, e_{max}.
2. If the peak strength has been exceeded in a previous cycle, point "a" is defined by the deformation equal to the maximum deformation, e_{max}, and a force equal to 0.8 times the force on the envelope curve that corresponds to e_{max}.

The first version of this model, showed a constant value for the pinch force. Tremel [55], and Meyer [54] suggested a pinch force expression similar to that proposed by Emori and Schnobrich [12].

2.6.3 Slip-Type Models

In the early and middle 1960's this family of models was extensively studied [52,53]. Iwan [53] in his study about the steady-state response of the double bilinear hysteretic model stated that the higher hysteretic energy loss was due to marked rounding of the hysteresis loop or to a pinching effect in the loop near the origin. Therefore, Iwan proposed the use of the double bilinear model with a hysteretic energy loss exactly half that of the usual bilinear model for the same amplitude of response. A typical cycle for this model, showed two rhombes in opposite quadrants joined at the origin by their vertexes. Generally, this model, when applied to reinforced concrete elements, provides only a rough estimate of the system behavior.

Many hysteretic models have been developed over time. Improvements in concrete models have been to allow for stiffness degradation and pinching action. The Takeda model, and its subsequent improved versions, as well as the EKEH model, represent the most comprehensive models currently in use.

3. EXPERIMENTAL PROGRAM

3.1 Full-Scale Tests

As part of the concrete plank diaphragm project underway at Iowa State University, sixteen full-scale diaphragms have been tested under in-plane loading. The fabrication of the specimens, type of frame and testing procedures used during the experiments will be discussed in the following sections.

3.1.1. Hollow-core plank specimens

Each diaphragm test, with the exception of Pilot Test #3, consisted of four precast planks. Pilot Test #3 differed in that it was made up of two planks. Span-Deck planks were used in this project because of the similarity of these units to most precast planks and the close proximity of the fabrication plant. All of the planks were constructed of normal weight, high strength concrete.

The test specimens were manufactured according to conventional procedures at Prestressed Concreted Operations (PCO), Des Moines, Iowa. The first step was to prestress the 1/2-inch or 7/16-inch diameter strands to a typical stress of 200 ksi. Strand elongation was approximately 30 inches in the 400-foot bed length with an applied force of 30 kips. The number of stands varied (either six or four). During the casting process, two separate machines were employed. The first laid down a 1 1/4 inch thick concrete layer, just covering the prestressing strands. The second machine deposited the remainder of the concrete to form the plank, while simultaneously dropping the pea gravel necessary to create the rectangular voids via a slip form. Figure 14 reveals the final cross-sections of the three depths of planks tested.

In order to allow for the fastening of the planks to the testing frame with steel studs, 4" by 10" voids were fabricated in the planks at the appropriate locations. This procedure involved adding a styrofoam insert into the bottom wythe prior to casting and removing the concrete in the vicinity of the void in the top wythe after the second layer was placed. Minimal additional reinforcement was placed around the voids. A schematic of the typical additional plank reinforcement is shown in Figures 15 and 16. Weld tie inserts (Figure 6) were placed in all the untopped tests. These inserts were placed five-foot on center and three-foot from the end.

The surface of the planks was then finished. All of the untopped specimens received a smooth finish, while those planks which were used in the topped tests had a raked or unsmoothed surface. The planks were cured for approximately 12 hours with hot oil then sawed to their appropriate lengths. The planks were then hung on end to allow for the removal of the pea gravel.

3.1.2 Diaphragm Test Preparation

The planks were connected to the testing frame with 5" x 3/4" diameter Nelson studs. Two studs were placed within each void for most of the tests. For Tests #11 through #14, three studs were placed in each void. U-shaped reinforcing bars (#3) were placed around the studs at the ends in order to

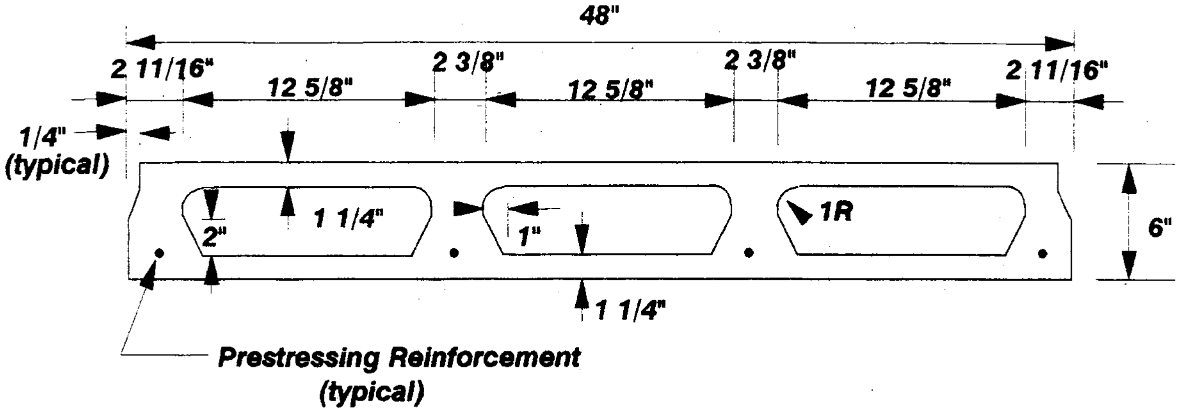

6" Plank

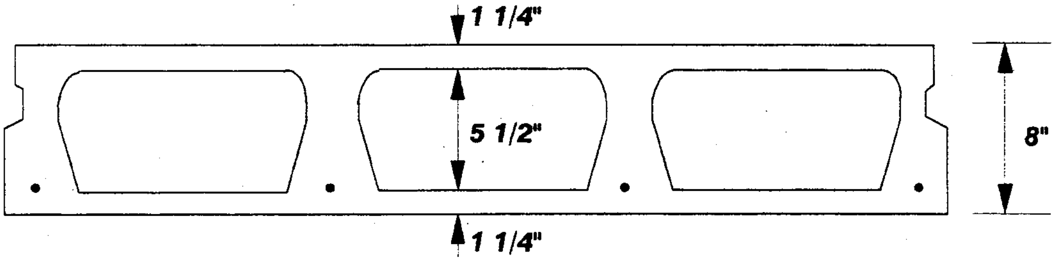

8" Plank

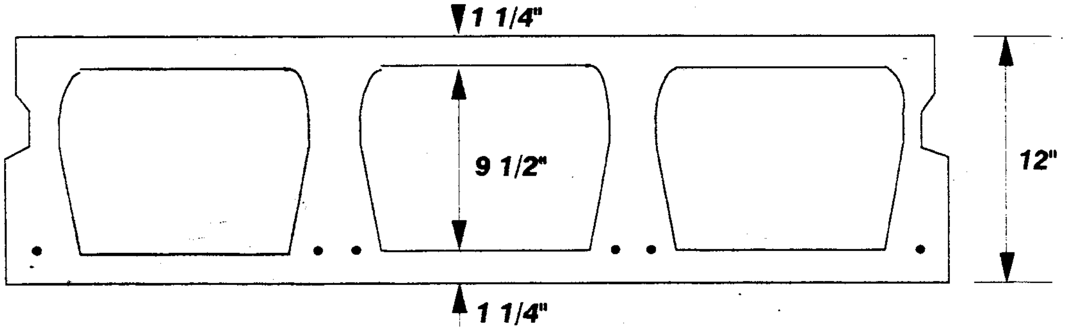

12" Plank

Not drawn to scale

Figure 14. Cross-sectional views of 6-, 8-, and 12-inch Span-deck planks

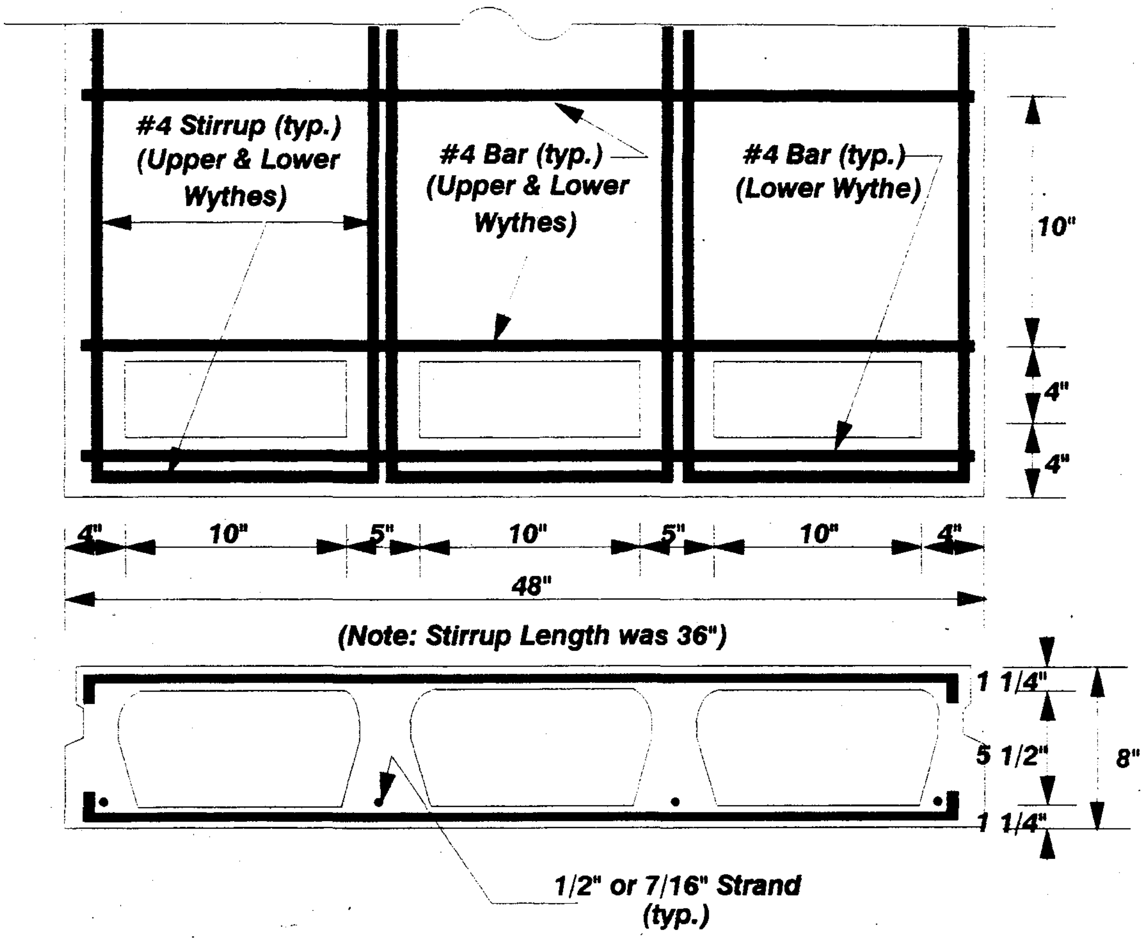

Figure 15. Span-deck reinforcement for voids along plank ends

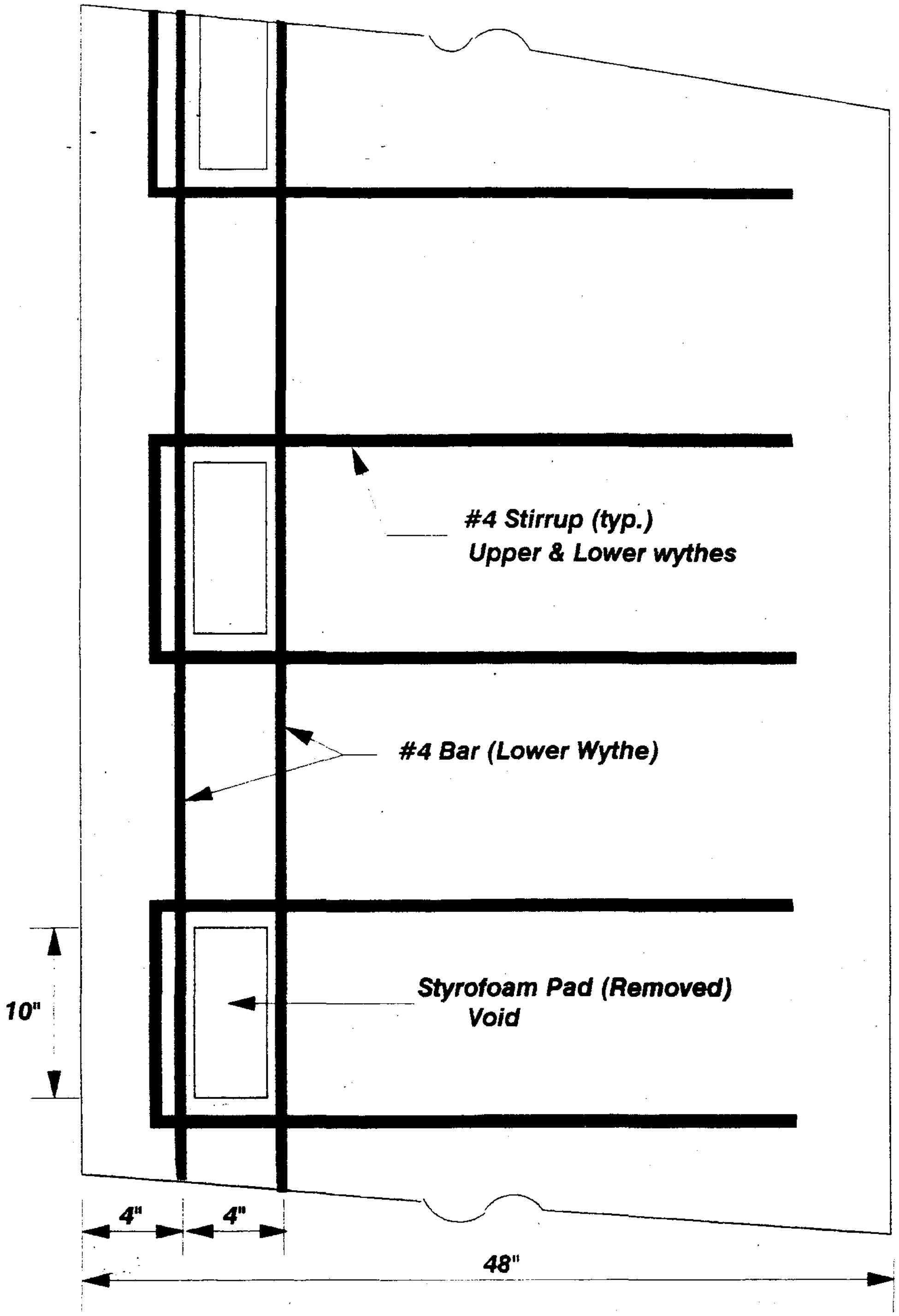

Figure 16. Span-deck reinforcement for voids along longitudinal edge

to minimize edge zone breakdown. The cores were then grouted back a distance of eighteen inches around the studs. These studs, when combined with the high-strength grout in the perimeter, acted as the anchoring mechanism of the diaphragm to the test frame. Although hollow-core diaphragms are not normally connected to the supporting members in this fashion, the objective of this project was to test the diaphragm and not the connections. The edge connection was therefore designed to remain intact throughout the test, allowing only the diaphragm to reach its limit state. A summary of pertinent pre-test data for each the diaphragm tests can be found in Table 2 and schematic drawings of the plank configurations are shown in Figures 17 and 18.

3.1.3 Laboratory Testing Facility

A cantilever diaphragm test frame with a fixed edge was selected as the final design for testing. The free edge modeled a masonry shear wall subjected to the horizontal (in-plane) drift induced by an earthquake. The fixed edge simulated either a stiff adjoining panel or another shear wall. The edge beam modeled interior or exterior masonry bearing walls. Requirements of the ASTM E455-76 (Reference 1) were reviewed prior to testing commencement but the two-point load system was chosen over the one-point load.

The cantilever testing frame is shown in Figure 19. The frame dimensions were fifteen feet square for all the tests. The system was designed for a working load of approximately 400 kips and a maximum displacement of ± 5 inches [9,10,30,34].

The fixed end of the testing frame was formed with three large concrete reaction blocks anchored to the laboratory floor with two-inch diameter high-strength bolts post-tensioned to 240 kips. A steel plate was embedded into the reaction blocks to facilitate placement of the studs. The remaining sides of the testing frame were composed of W24X76 wide flange steel framing beams. These beams were connected using flexible T-shaped elements.

The load was applied to the frame along the front beam through two double-acting hydraulic cylinders. Specially fabricated 240 kip load cells were attached in series to measure the load applied by the hydraulic actuators. Each of the hydraulic cylinders was mounted within two C15X40 channels connected to wide flange sections anchored to the floor with four high strength bolts post-tensioned to 240 kips. A closed-loop MTS control system was used to control the displacement during the test. A direct current differential transducer (DCDT) was mounted on the loading beam as shown in Figure 20 and served to deliver the feedback signal. The loop was completed by a servo-valve which controlled the hydraulic actuators. Loop stability could be maintained within 0.001 inches [9,10,30,34].

3.1.4 Data Acquisition System and Test Instrumentation

Many types of instrumentation were used to measure the behavior of the diaphragm throughout the test. Instrumentation was used to monitor the loading beam displacement and applied loads, in-plane and out-of-plane plank

Table 2. Summary of Parameters for Diaphragm Tests #1-15

Test No.	Orientation of planks	Thickness of planks (in.)	Compressive Strength of Seams (psi)	Compressive Strength of Cores (psi)	Compressive Strength of Planks (psi)	Compressive Strength of Topping (psi)
1	NS	8	3800	7800	7400	N/A
2	EW	8	6500	6500	7400	N/A
3	NS	8	5700	5700	7400	N/A
4	NS	8	6116	6652	7782	N/A
5	NS	8	5600	7700	6300	N/A
6	EW	8	5591	6301	8300[a]	N/A
7	EW	8	2879	6007	8300[a]	N/A
8	EW	8	2425	6100	8300[a]	N/A
8b	EW	8	N/A	6100	8300[a]	7000
9	NS	6	4216	6136	8300[a]	N/A
10	EW	6	4192	4539	8000	N/A
11	NS	12	3487	5835	8603	N/A
12	EW	8	N/A	5500	8300[a]	3500
13	NS	8	4246	5109	8300[a]	4246
14	NS	8	4895	6547	8300[a]	4000
15	EW	8	4000	6500	8300[a]	N/A

Notes:

[a] Plank strength not available, this value is assumed

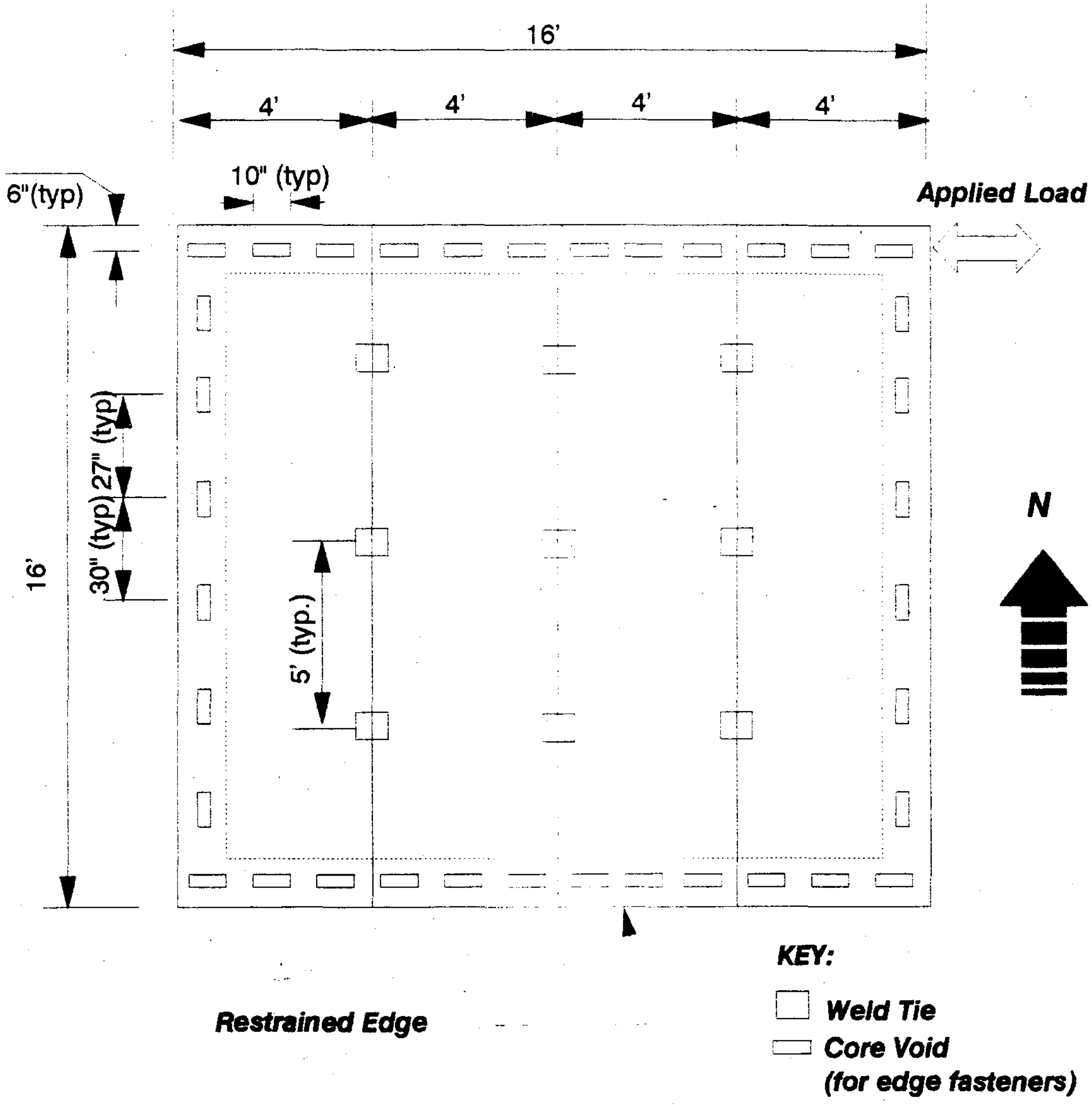

Figure 17. Typical dimensions for all diaphragms (except Test #3)

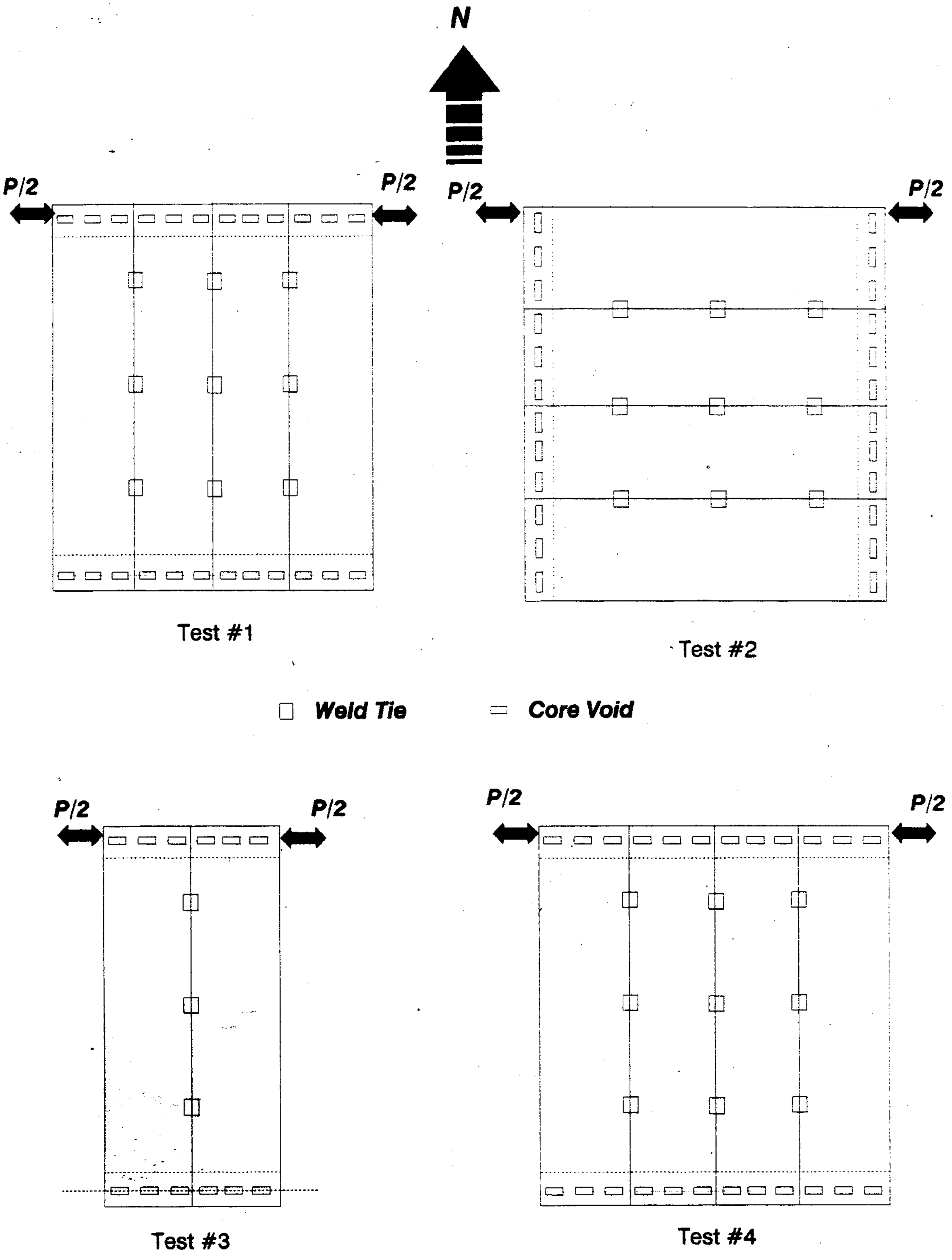

Figure 18a. Schematic of plank configurations for Tests #1-4

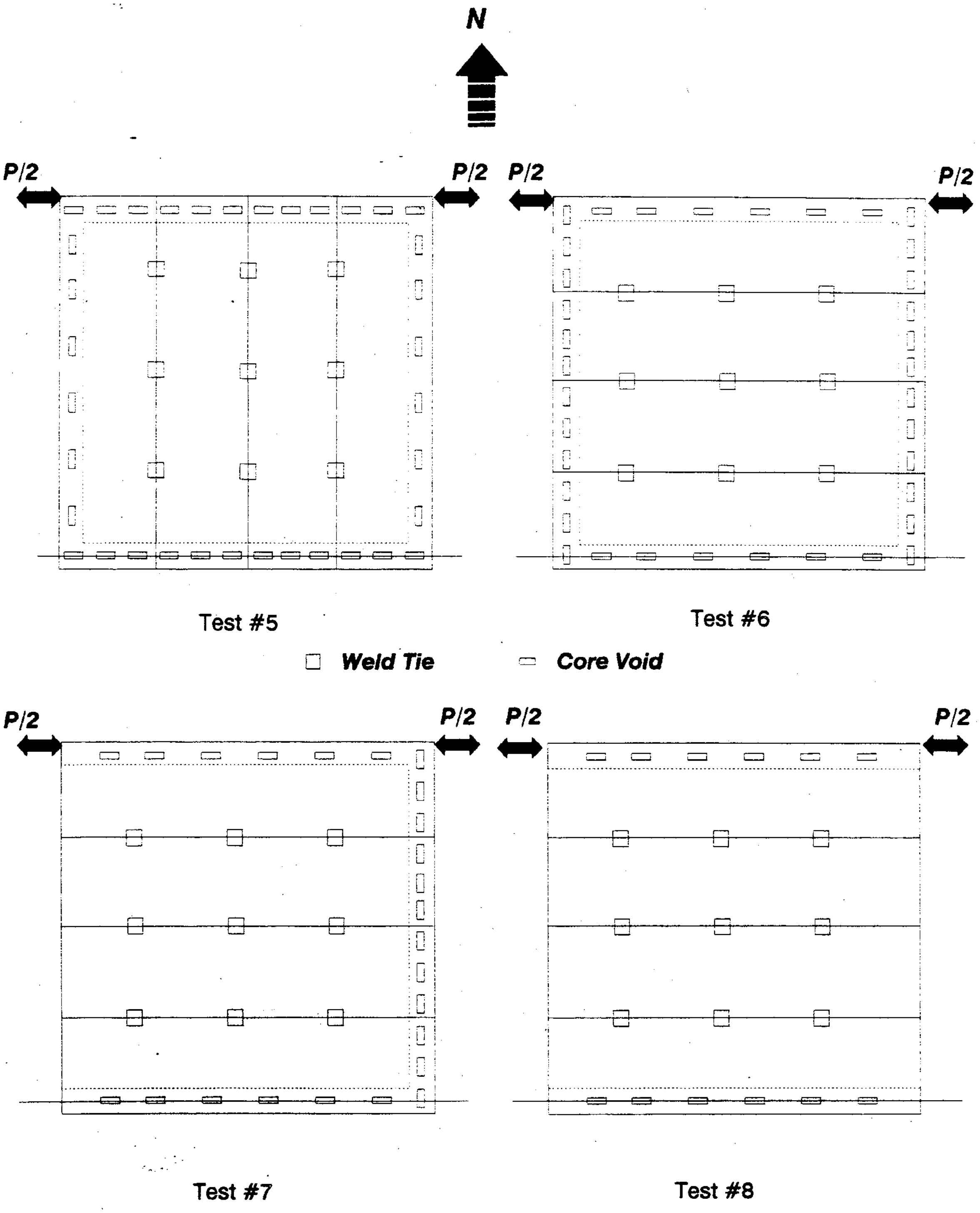

Test #5

Test #6

Test #7

Test #8

Figure 18b. Schematic of plank configurations for Tests #5-8

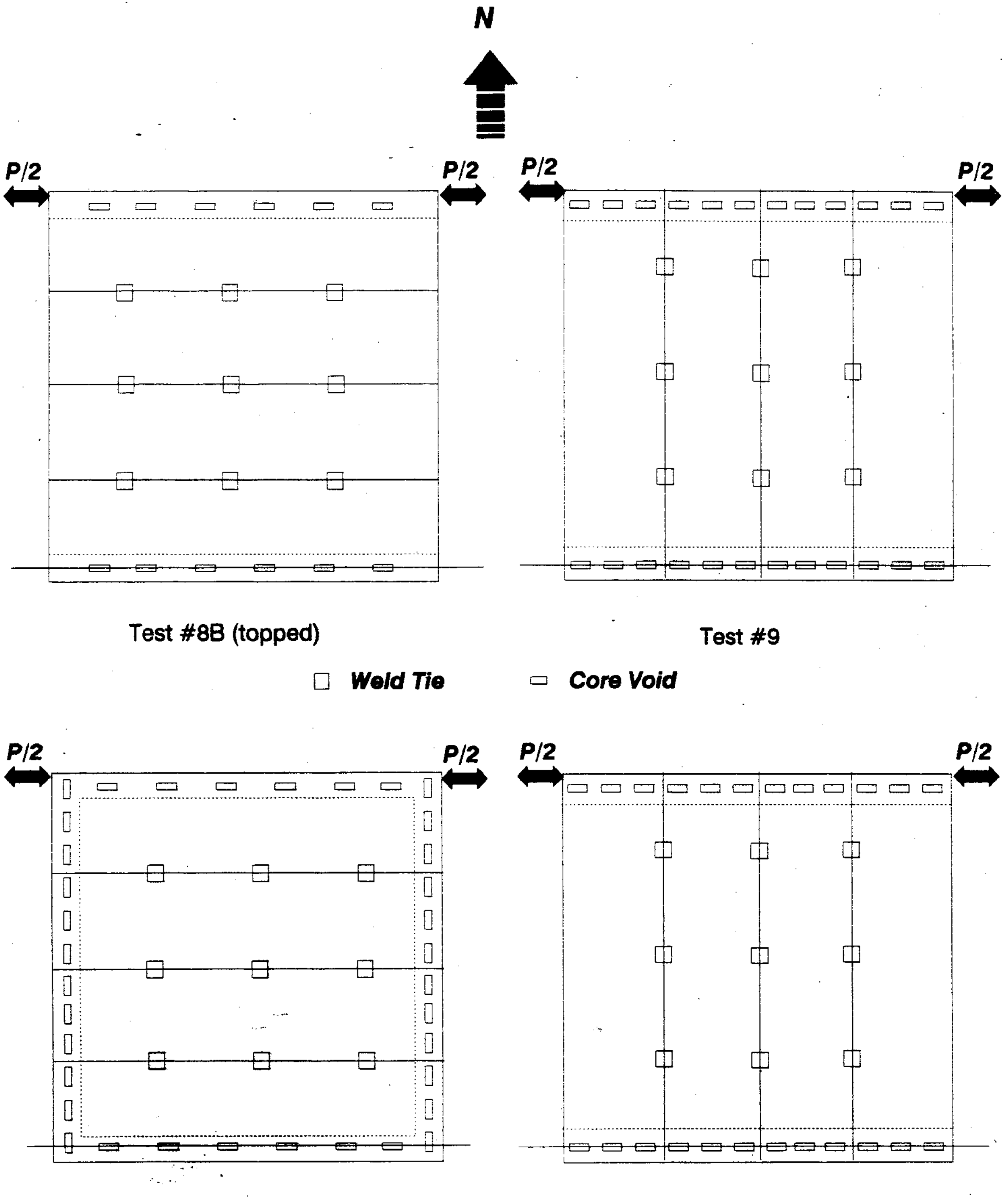

Test #8B (topped)

Test #9

Test #10

Test #11

Figure 18c. Schematic of plank configurations for Tests #8B-11

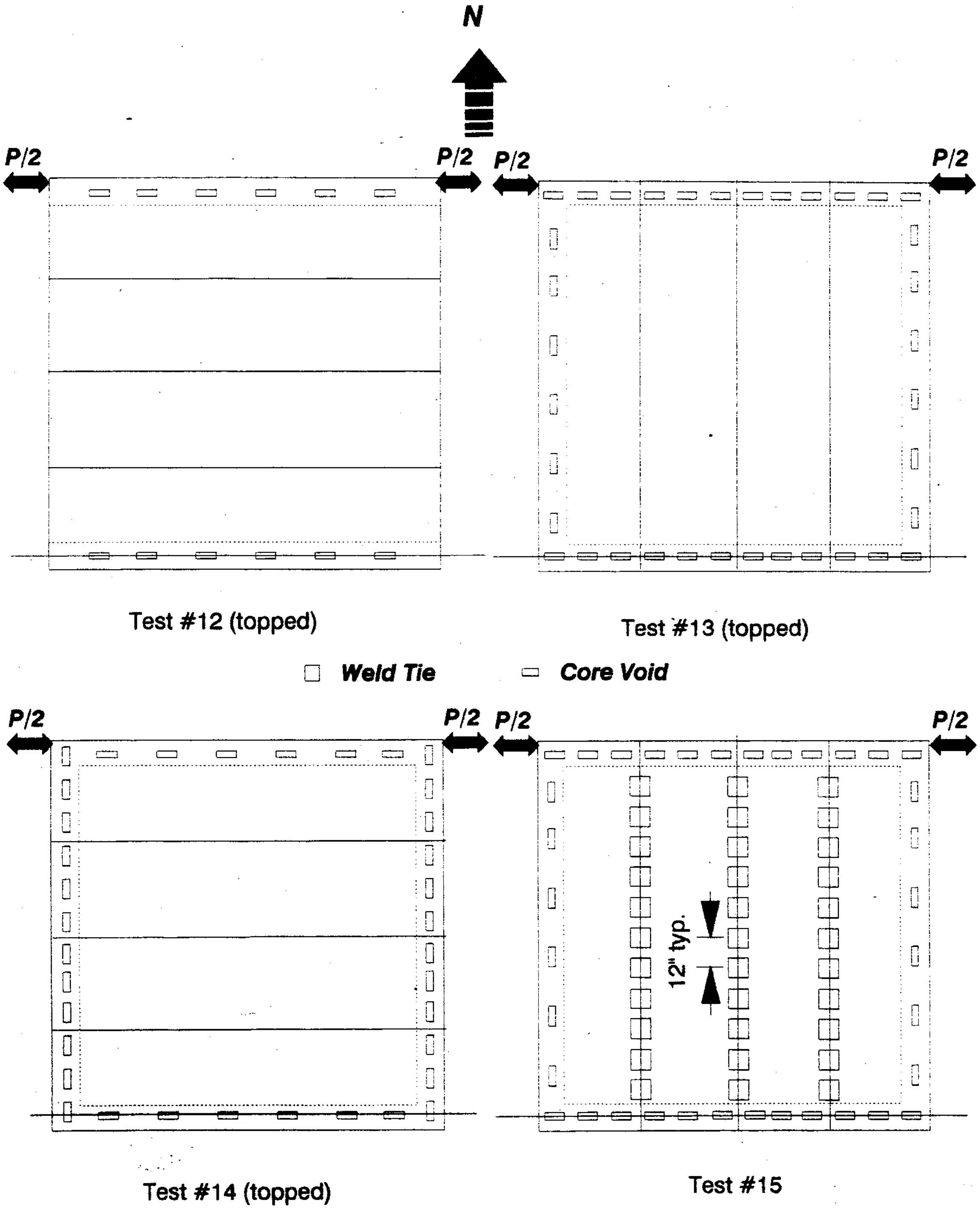

Figure 18d. Schematic of plank configurations for Tests #12-15

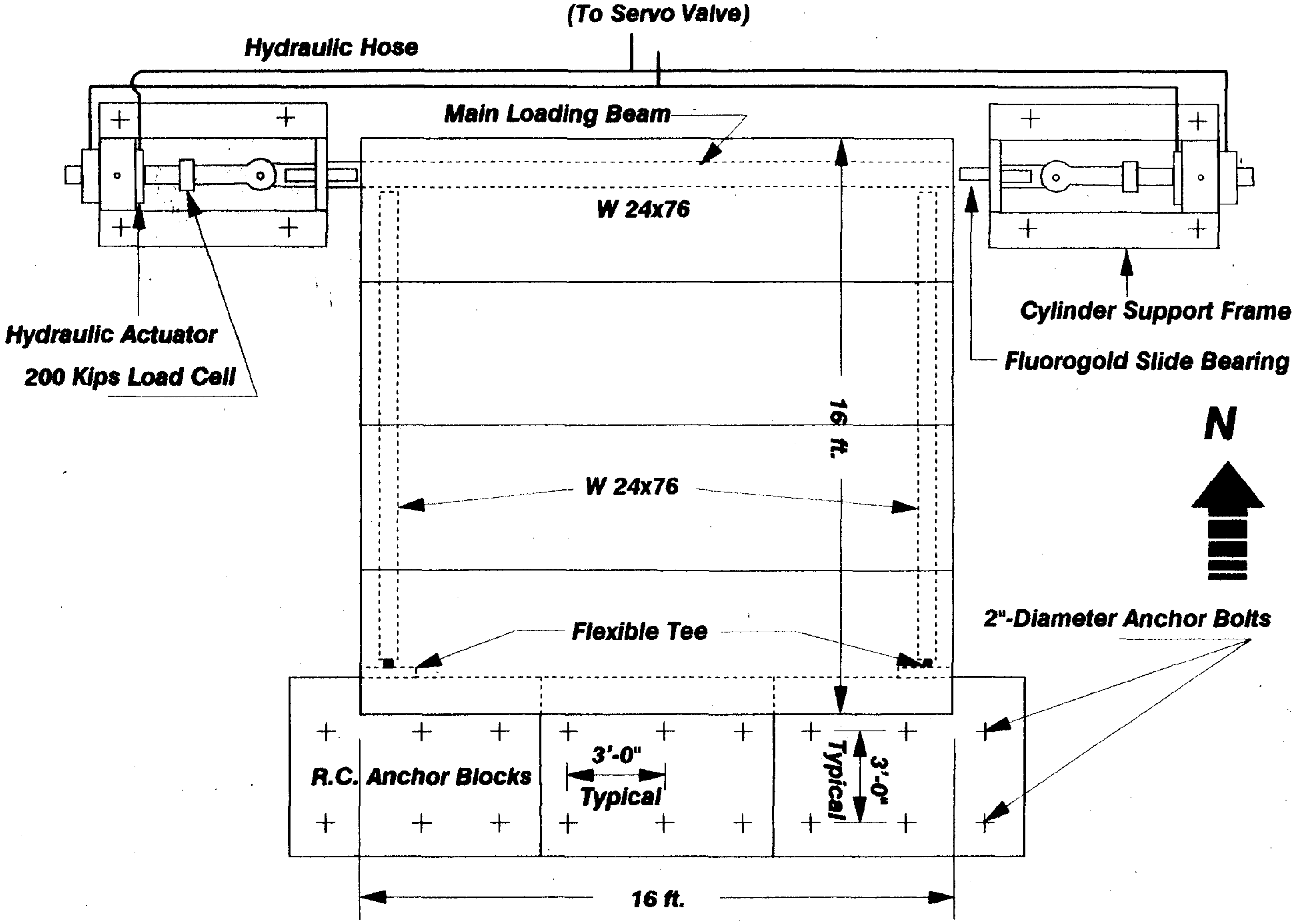

Figure 19a. Diaphragm test frame schematic for east-west orientation

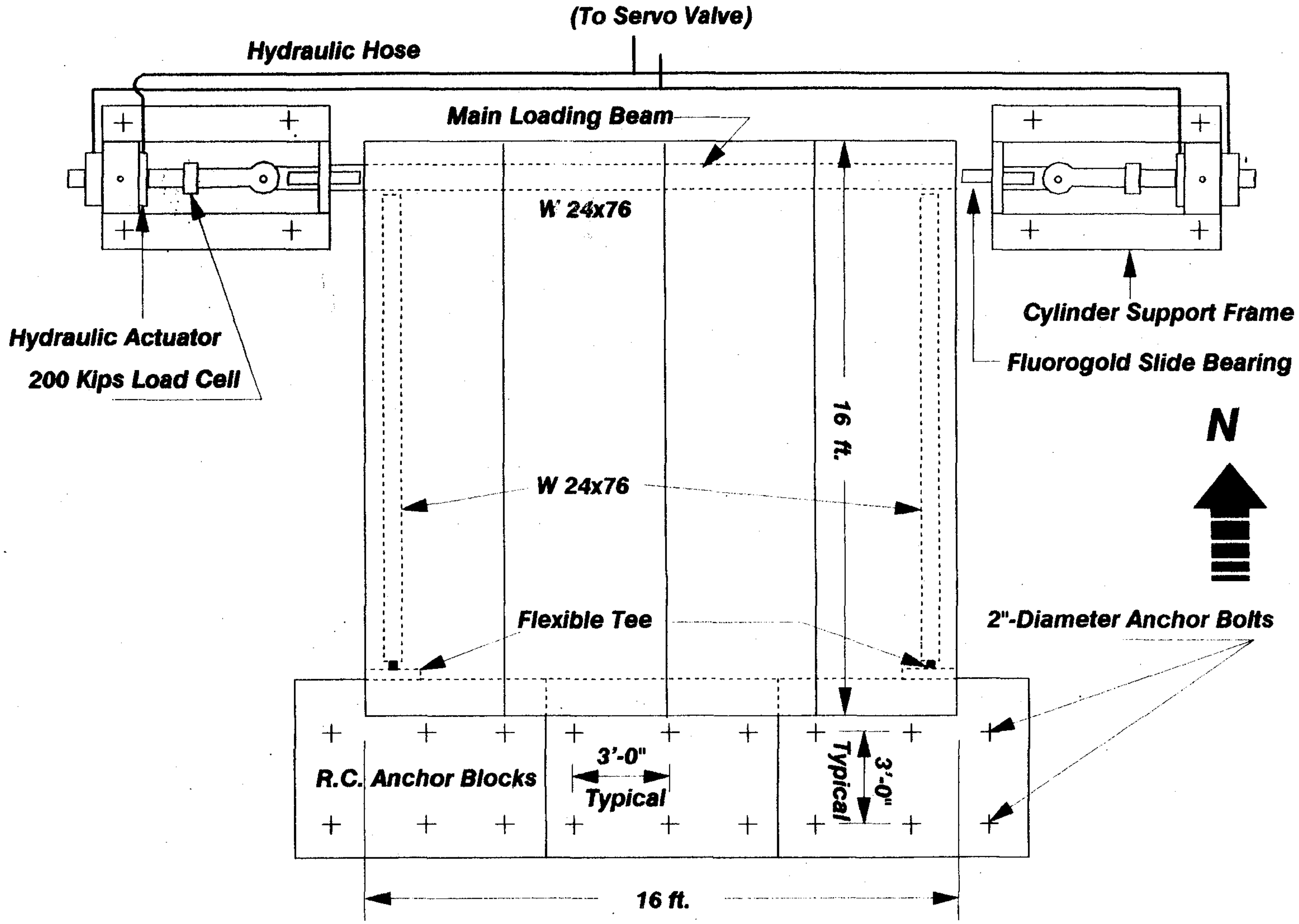

Figure 19b. Diaphragm test frame schematic for north-south orientation

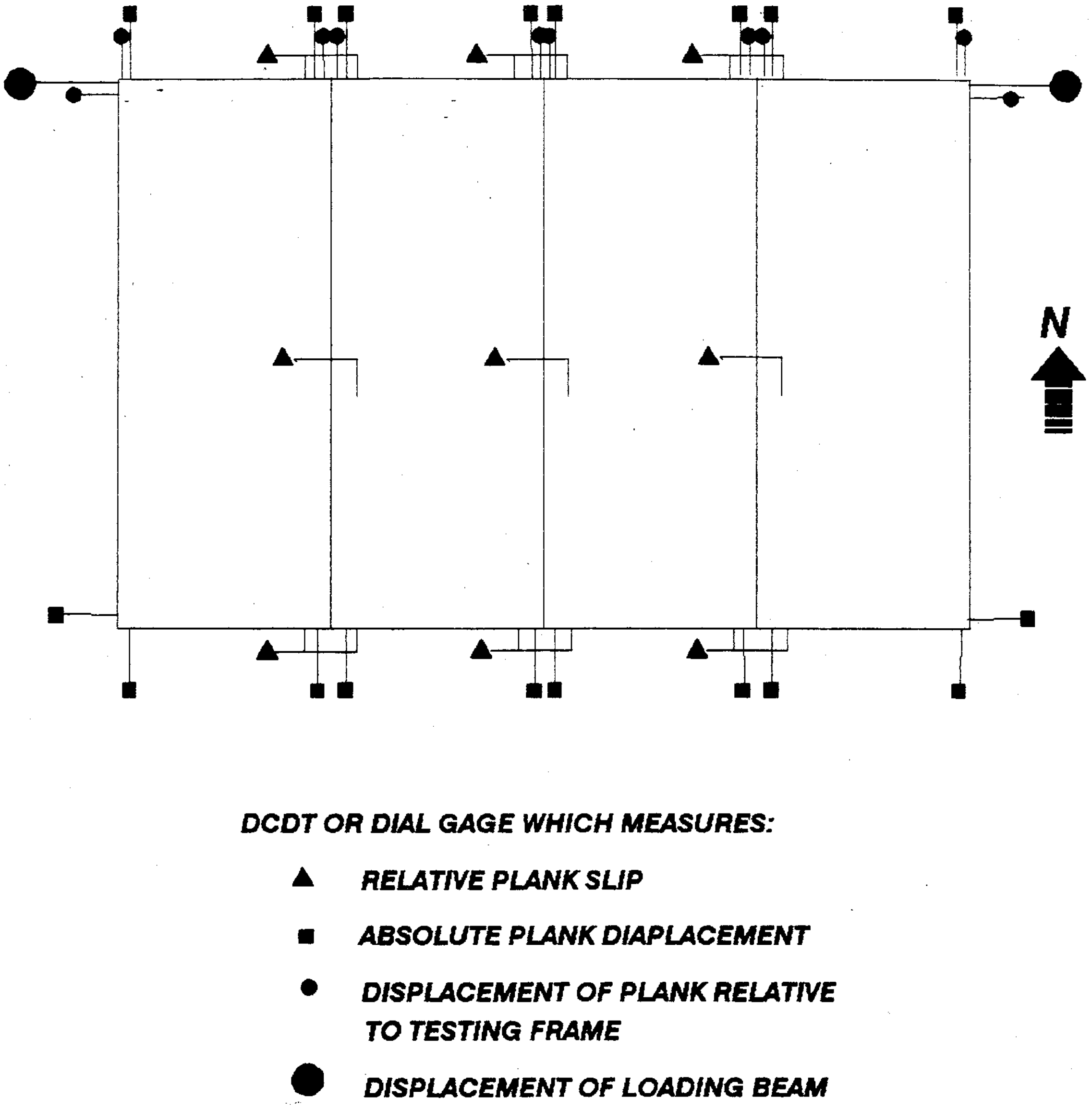

Figure 20. Typical diaphragm test instrumentation

displacements, relative slip and split between the planks, relative slip between the diaphragm and framing beams, and strains in the loading beams.

In-plane and vertical displacements were measured with direct current differential transducers (DCDT) or mechanical dial gauges. A DCDT located near the northeast corner of the diaphragm was connected to the loading beam and served to provide feedback to the MTS servo-controller, as was discussed earlier. Dial gages and DCDTs were placed at each corner of each of the planks to measure edge displacement relative to both the floor and the framing beams. Relative seam slip was measured with a DCDT on each end and at the center of every seam. Figure 20 shows typical placement of the dial gages and DCDTs.

Strain gages were attached to the webs of the framing beams to measure the strains along these edge beams. On the first and second pilot tests, uniaxial and rosette strain gages were mounted on the northeast quadrant of the diaphragm, however, accurate readings were not obtained due to the cores within the planks.

All of the DCDTs, strain gages and loading cells were monitored by the data acquisition system (DAS). The DAS consisted of a 150-channel Hewlett Packard (HP) model 3497A data acquisition control unit interfaced with an HP model 85 microcomputer. These units were in turn interfaced with two disk drives, a digital plotter and a high speed printer. At each load point, the DAS recorded all readings on both a magnetic disk and a printout. Between readings, the DAS constantly monitored and plotted the in-plane load and the in-plane displacement. In order to create this plot, the DAS recorded load and displacement readings at the rate of one reading per second during the entire time the displacement was being applied. The plot program also had the capability of integrating the area under the hysteretic plot, which represents the energy between load point readings. Figure 21 is an example of a plot produced during Test 5.

The concrete surface of the test specimen was painted with a soluble white latex paint to help distinguish cracks. The surface was also marked with a rectangular grid, as is shown in Figure 22, to aid in monitoring crack locations. After most load points, a search of the surface was conducted. The interstices were traced with a black marker and the load point was written next to it. The location of these cracks was noted on a tape recorder for future reference. A camera mounted thirty feet above the specimen was also used to document surface deformation. In addition, many close-up photographs were taken during each test.

During the first two diaphragm tests, a video camera was placed underneath the diaphragm before casting. The VHS camera and spotlights were mounted on a moveable cart in order to provide a constant view of the under side of the planks. Throughout these first two tests, however, no major cracks formed on the bottom surface. Due to this lack of success, and the danger of falling pieces of concrete, the camera was not used for the remaining tests.

After the first several tests, a record of the condition of each stud throughout the test was deemed necessary. A wire was therefore attached to the top of each stud before grouting. The wires for all the studs were then connected to a switching box and this box was attached to an ohmmeter. A ground wire was put on the loading beam to complete the circuit. Thus, when a stud

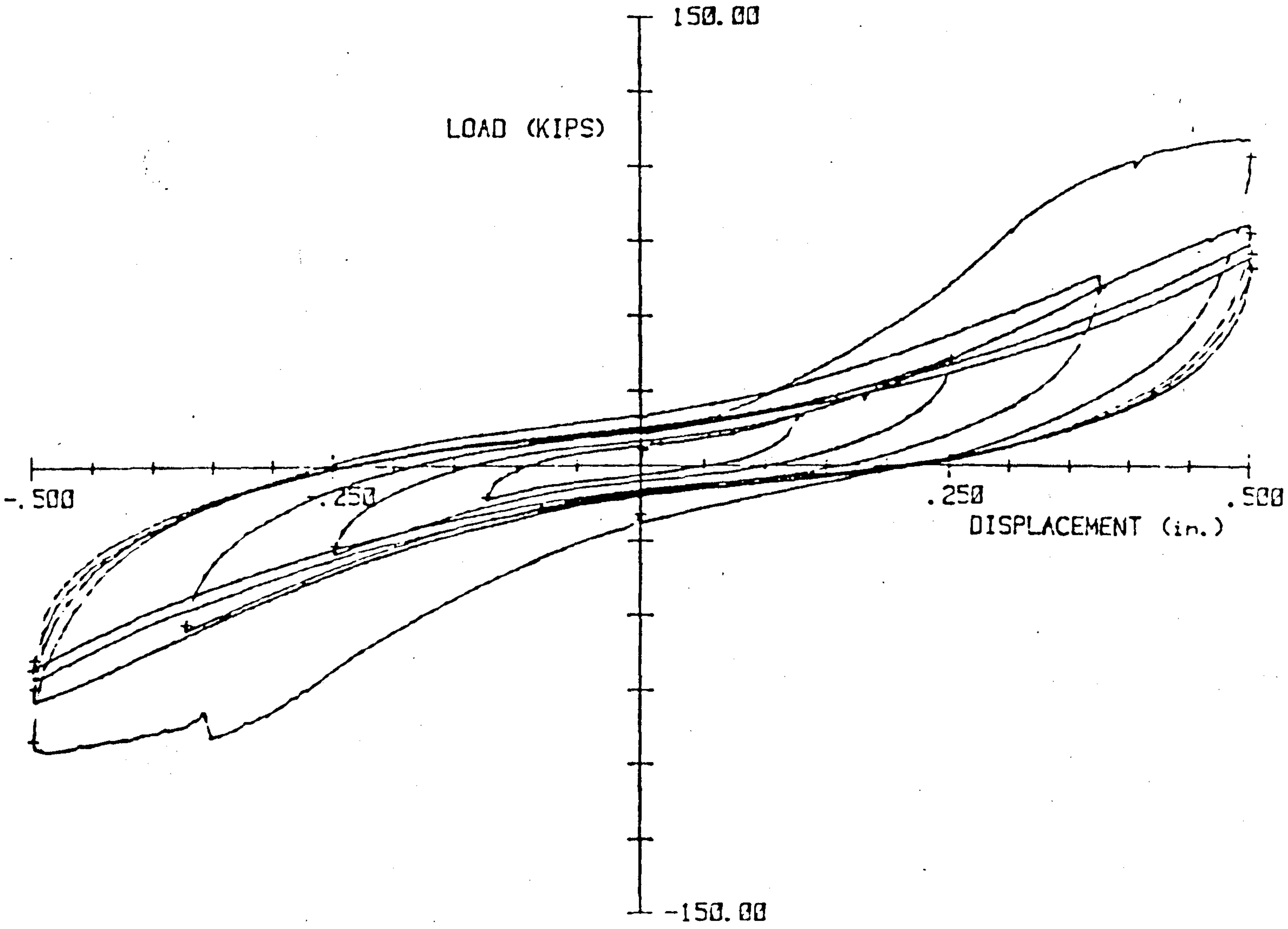

Figure 21. Example of hysteretic plot for Test #5

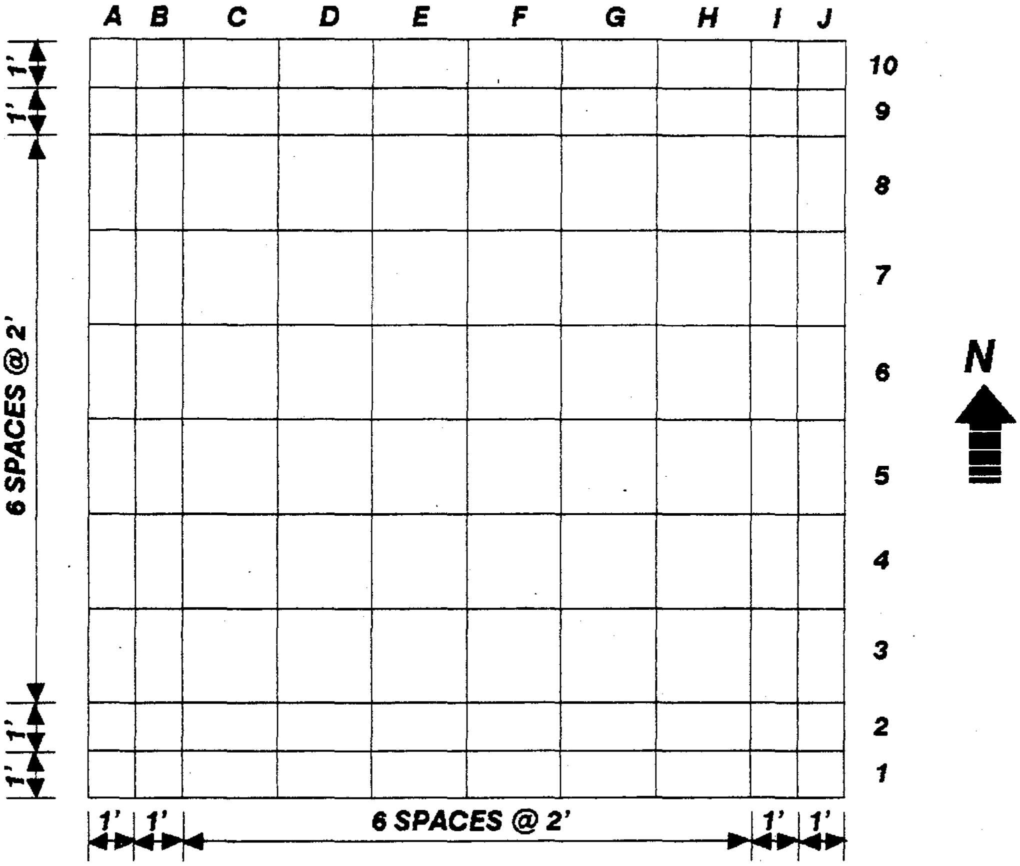

Figure 22. Plank grid schematic

broke, the ohmmeter measured infinite resistance. This data was recorded at the end of each of the stabilization cycles.

3.1.5 Load Program

The sequential phased displacement, SPD, loading program was used for each of the tests. The SPD procedure was conceived as a technique that could be utilized throughout various segments of the overall TCCMAR research and serve as a comparison basis. This program employed standard stabilization cycles beginning at approximately 0.0125 inches of displacement. In addition to these cycles, this technique utilized decaying displacement cycles to better define the hysteretic behavior. These degradation loops assisted in the establishment of the correlation between demand and capacity for inelastic deformations [31].

The procedure for the SPD program involved executing progressively larger increments of displacement for each cycle prior to the first major event (FME). In each of the diaphragm tests, the FME was either a seam or diagonal tension crack . Once the FME occurred, a sequential phased displacement loading procedure was followed. At every new increment of loading, both decay cycles and stabilization cycles were completed. The decay intervals were one-quarter the original displacement and were followed by at least three stabilization cycles. More than three stabilization cycles were required if the strength of the final cycle was less than ninety-five percent that of the previous cycle. Figure 23 is a schematic of a typical loading plot.

The SPD procedure was used because it more accurately represents the earthquake excitation pattern than the usual monotonic or simple reversed cyclic loading patterns do. Most seismic events contain many low-energy points between the major spikes as shown in the typical earthquake ground motion record in Figure 24. Saatcuglu, et. al. [39] noted that in many instances the maximum deformation can occur early in the excitation response with few inelastic cycles proceeding it. Thus, by using degradation cycles, the lower bound within a given hysteretic curve can be identified. The stabilization cycles are also essential in order to calculate the "stabilized" energy. Additional details on the SPD procedure and rationale can be found in Reference 31.

3.2 Elemental Tests

The primary failure mode for untopped plank diaphragms involved the breakdown of the seam connection between panels; thus, further investigation of this mode was undertaken in a series of elemental tests. For diaphragm tests with the seams oriented transverse to the applied load, the shear-bond failure mode predominated. After initial fracture of the seams, the weld tie assemblages acted to restrict slippage and provide ductility. Diaphragm action usually peaked prior to the failure of the first weld tie. The ties typically failed in one of the following three fashions: 1) exposure of the horizontal bar, 2) shearing of the vertical/horizontal bar at the weld or 3) weld breakage on the two-inch long angle connecting the plates. The greater the number of seams free to slip (within broken ties), the weaker the diaphragm action. Therefore, the

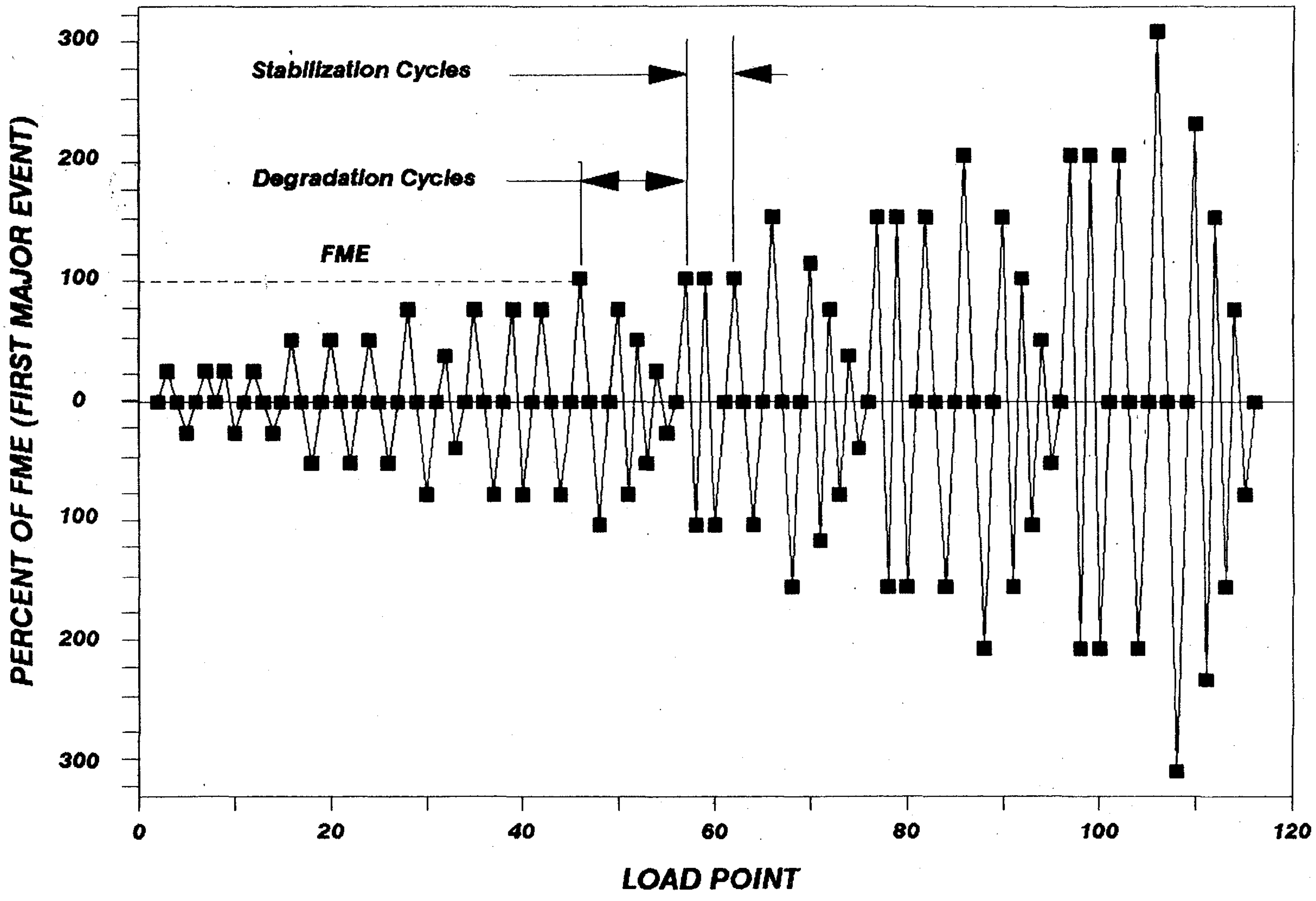

Figure 23. Sample SPD loading program

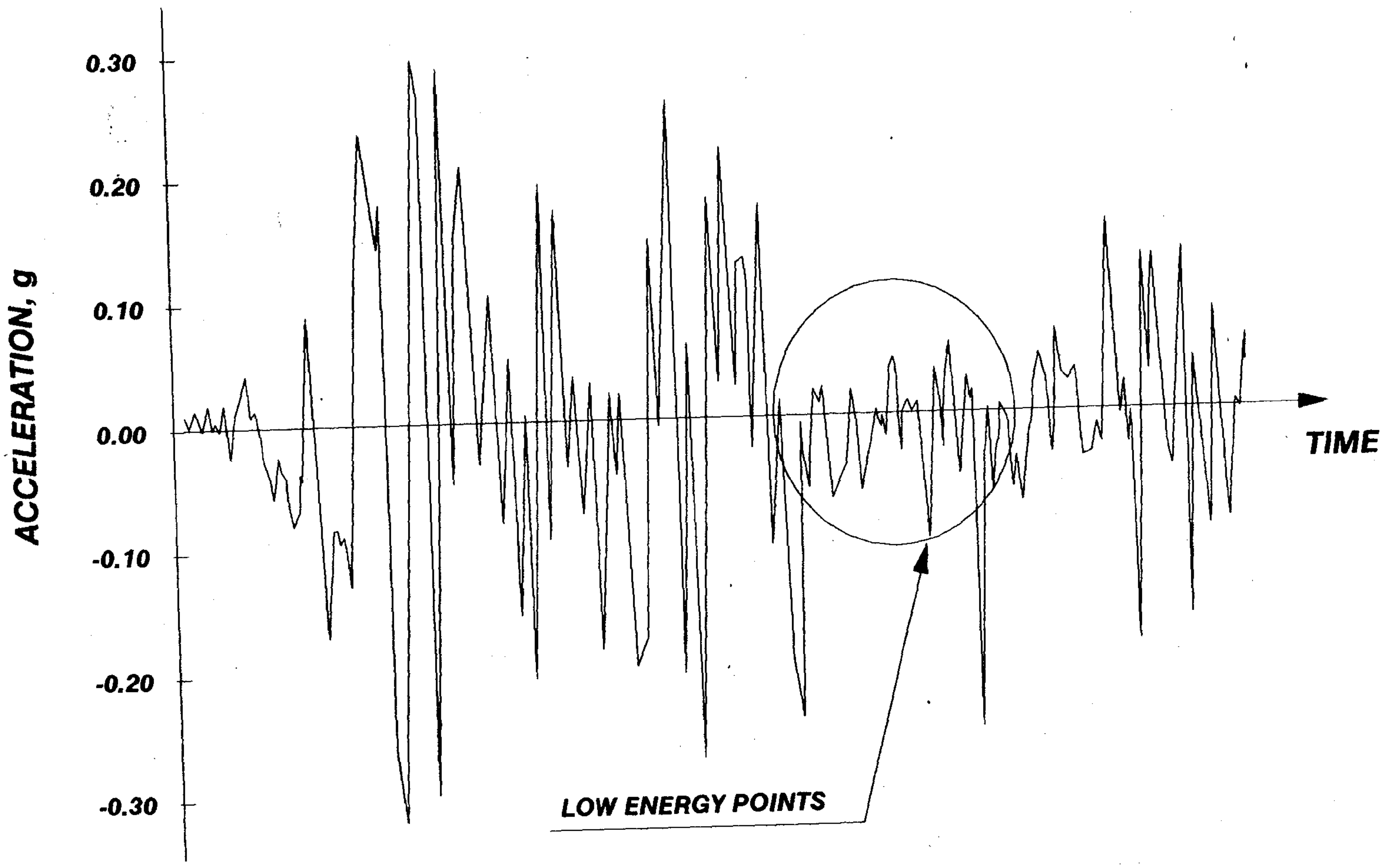

Figure 24. Typical earthquake ground motion record

limit state strength associated with the peak load is assumed to correlate with the failure of the first weld tie during a test.

A preliminary elemental shear test was first conducted. This test utilized short segments of actual Span-deck hollow-core planks. The peak load required to produce seam slip was measured. However, due to the cost and availability factors associated with these specimens, smaller elemental tests were used for additional experimentation.

Sixty-six small elemental seam strength tests were performed in conjunction with the hollow-core diaphragm research project. Fifty-four of these specimens were tested under direct shear and twelve were tension tests. The elemental shear tests were separated into series which were designed to study the following seam parameters:

1) Grout only
2) Grouted seam bonded to smooth edges with weld tie
3) Grouted seam (unbonded) with weld tie
4) Grouted seam bonded to rough edges with weld tie
5) Topping monolithically bonded with seams
6) Topping non-monolithically bonded with the seams
7) Specimen thickness
8) Grouted seam bonded to smooth edges and special continuous bar weld tie
9) Cyclic versus monotonic loading.

The parameters for the elemental tension tests included:

1) Grout only
2) Grouted seams bonded to smooth edges with weld tie
3) Specimen thickness (6" verses 8").

3.2.1 Elemental Test Specimens

Two sets of elemental tests were performed: the large Span-deck specimens and the smaller solid concrete units. The preliminary large shear test was conducted with three Span-Deck planks, each five feet long, four feet wide and eight inches thick. The planks were connected together with grout and a weld tie insert which was centered in the seam. The grout mix, by volume, consisted of three parts masonry sand and one part Type 1 Portland cement. The water/ cement ratio was set at 0.6 by weight. The average compressive strength of the grout was approximately 3,400 psi.

Each of the small elemental tests consisted of three solid concrete planks cast in the Structural Engineering Laboratory at Iowa State University. A schematic of these specimens is presented in Figure 25. The dimensions of the center slab were 14" X 24" and the two exterior components were 7" X 24". The thicknesses of the slabs were six and eight inches. The interior edges of the slabs were formed with contours similar to those used on the edges of the Span-Deck hollow-core planks in order to make them as realistic as possible. Note that wooden forms were used for the elemental tests, whereas the planks were

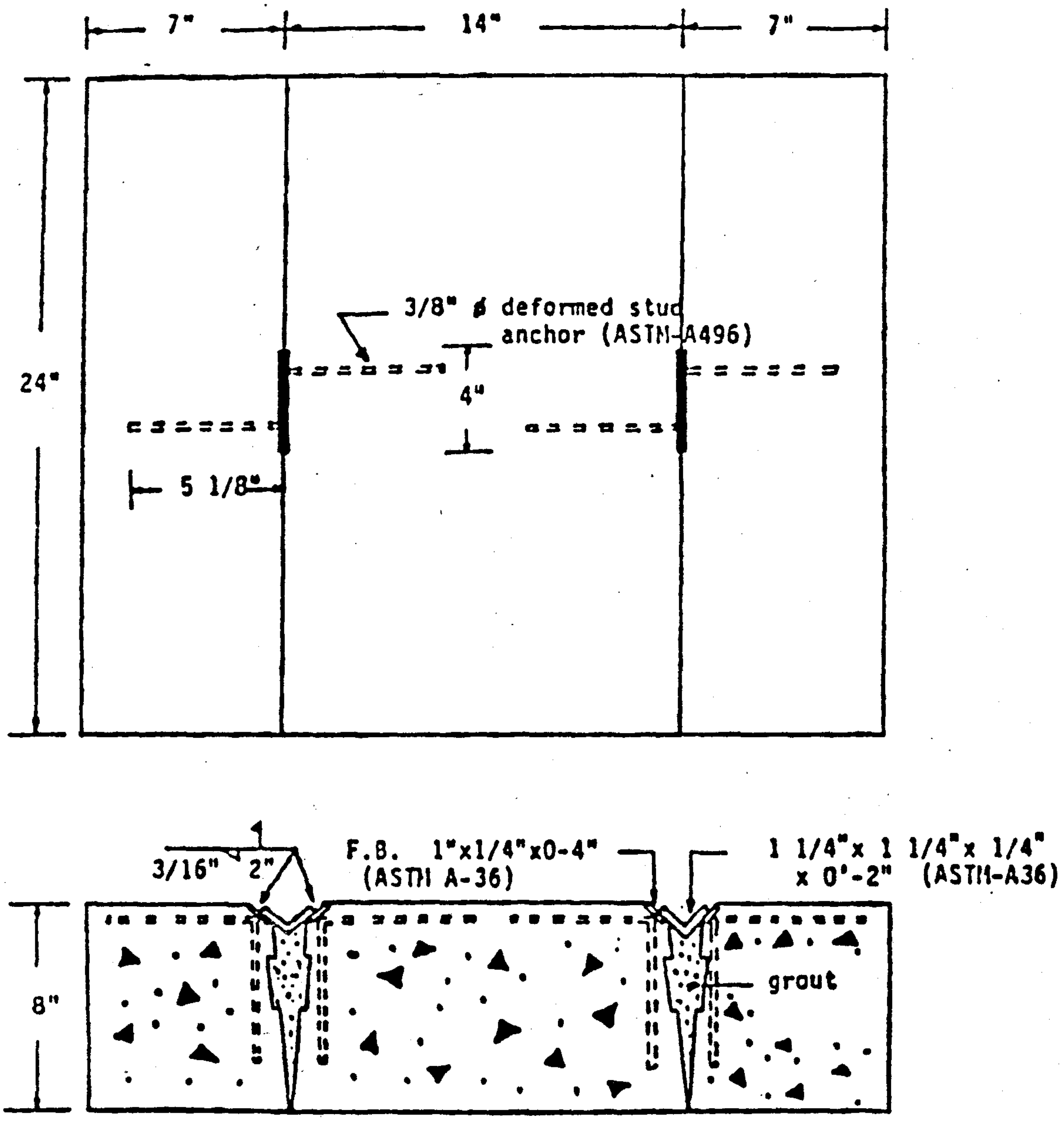

Figure 25. Schematic of elemental test specimen

produced with steel forms. This difference may have caused the elemental tests to have a slightly higher coefficient of friction.

Weld tie inserts were placed in the center of each of the seams. Figure 6 shows both types of weld ties used in these tests. The standard weld tie at the bottom of the figure was used in each of the untopped diaphragm tests and all of the elemental tests with the exception of the test series used to study the other type of ties. The standard weld tie is the unit that is currently being marketed, and was therefore tested.

After each group of concrete slabs had reached a strength comparable to the compressive strength of the actual hollow-core planks, (approximately 8,000 psi.) the slabs were connected. A professional welder completed the weld-tie insert by welding a 1-1/4" X 2" angle between the adjacent ties. The seams were subsequently filled with grout. The seam grout mixture was produced in the Structures Laboratory and consisted of masonry sands, Type 1 Portland cement and water in the following proportion:

masonry sand - 3 parts by volume
Type 1 cement - 1 part by volume
water/cement ratio - 0.6

Water was added until the grout mixture attained a flowable state. Grout samples were collected in 2" X 2" brass cubes and 3" X 6" brass cylinders in order to measure the compressive strength on the day of testing. The strengths actually recorded varied from 2,900 to 5,600 psi.

The reinforcing steel used in the elemental specimens varied. The shear tests contained no reinforcement, whereas the elemental specimens tested in tension contained a substantial amount of reinforcement as is shown in Figure 26. Due to the transfer of forces into the exterior seven-inch wide slabs, localized concrete failure occurred near the concrete anchor bolts in the preliminary tension tests. For this reason, two layers of #3 reinforcing bar were placed around the perimeter of each of the components. Pieces of reinforcing bar were also placed vertically in order to support the upper layer loops. A summary of the parameters of each of the elemental tests is included in Table 3.

3.2.2 Test Frames

Four different testing frames were used for the elemental tests. Three of these frames were used for the shear tests and one for the tension tests. These are described below.

3.2.2.1 Preliminary Shear Testing Frame

The large pilot elemental tests were tested in a frame anchored to the laboratory testing floor. The frame consisted of four channel irons post-tensioned to the floor. Three Span-Deck planks were placed between these beams and the center plank was pushed with respect to the outer two using a hydraulic ram. Reverse loading was applied in a similar fashion until specimen degradation occurred.

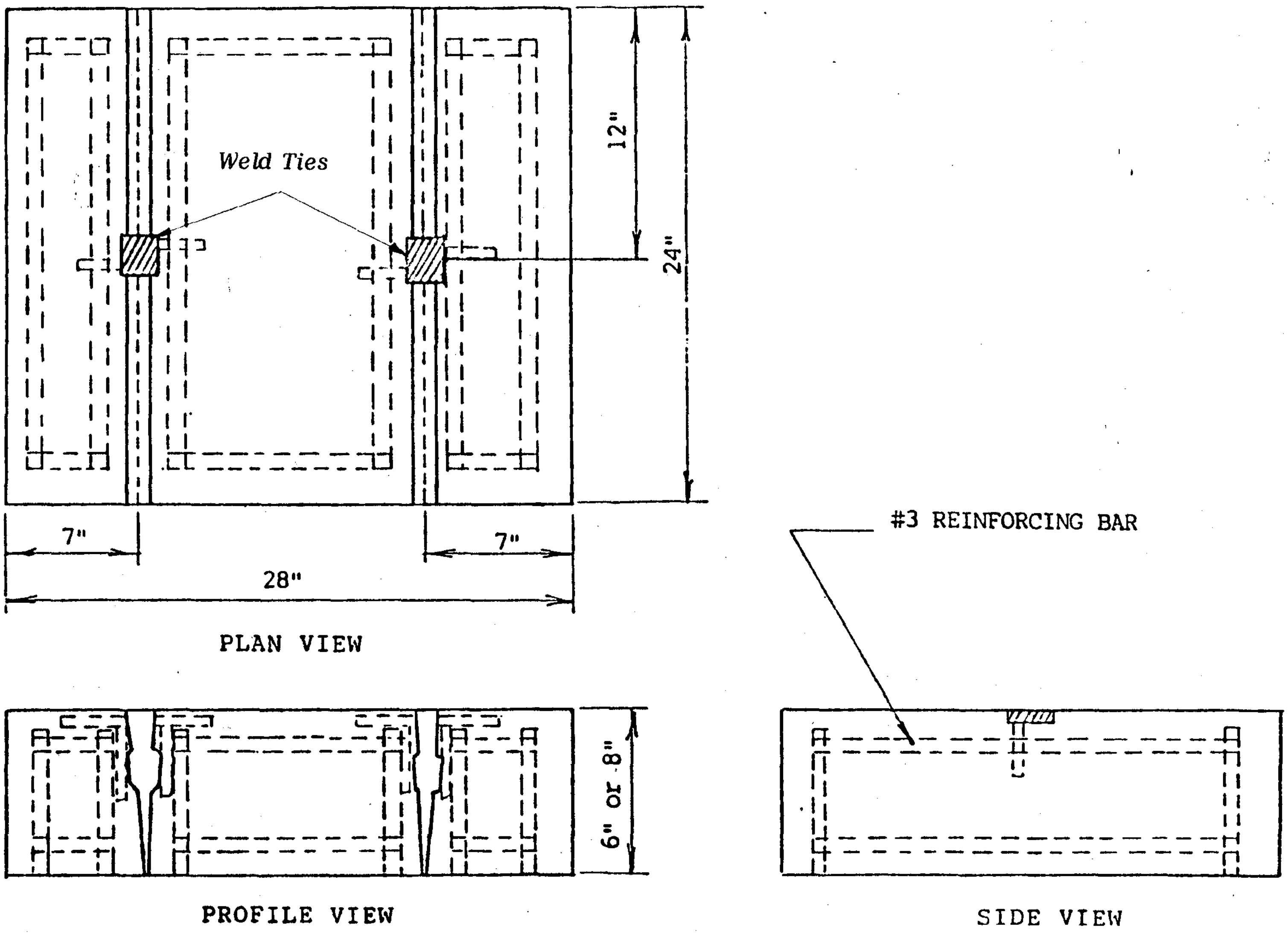

Figure 26. Reinforcement in elemental tension tests

Table 3. Summary of Parameters for Elemental Tests

Elemental Test #	Specimen name	Compressive seam strength (psi)	Average grout penetration (in.)	Weld ties used
1	GWSM 1	2961	7.000	YES
2	GWSM 2	2852	7.500	YES
3	GWSM 3	2852	6.500	YES
4	GWSM 4	3630	7.500	YES
5	GWSM 5	3630	7.500	YES
6	GWSM 6	3630	7.500	YES
7	GOSM 1	5178	7.500	NO
8	GOSM 2	5178	7.500	NO
9	GOSM 3	5178	5.000	NO
10	GOSM 4	5178	6.500	NO
11	GOSM 5	5633	7.500	NO
12	GOSM 6	5633	6.000	NO
13	GWSC 1	2933	7.000	YES
14	GWSC 2	2933	5.000	YES
15	GWSC 3	2933	5.500	YES
16	GWSC 4	4086	5.000	YES
17	GWSC 5	4086	5.500	YES
18	GWSC 6	4086	6.000	YES
19	GWUM 1	3630	-----	YES
20	GWUM 2	3630	-----	YES
21	GWUM 3	3630	-----	YES
22	GWUC 1	4190	6.000	YES
23	GWUC 2	4190	6.500	YES
24	GWUC 4	4190	6.500	YES
25	TOPW 1	4419	6.000	NO
26	TOPW 2	4419	7.785	NO
27	TOP 1	4419	5.250	NO
28	TOP 2	4419	4.785	NO
29	TOP 3	4419	5.625	NO
30	TOP 4	4419	6.500	NO
31	GORM 1	3867	5.750	NO
32	GORM 2	3867	4.250	NO
33	GORM 3	3867	6.125	NO
34	GORM 4	3867	6.375	NO
35	GORM 5	3867	5.375	NO
36	GORM 6	3867	5.375	NO
37	GOSM 7	4176	5.250	NO
38	GOSM 8	4176	7.250	NO
39	GOSM 9	4176	6.500	NO
40	TOPNM 1	4176	6.000	NO
41	TOPNM 2	4176	6.750	NO
42	TOPNM 3	4176	6.500	NO

Table 3. (Continued)

Elemental Test #	Specimen name	Compressive seam strength (psi)	Average grout penetration (in.)	Weld ties used
43	GO6SM 1	3015	5.750	NO
44	GO6SM 2	3120	5.750	NO
45	GO6SM 3	3437	5.750	NO
44	GO6SM2	3120	5.750	NO
45	GO6SM3	3437	5.750	NO
46	GW6SC1	3543	5.750	YES
47	GW6SC2	3754	5.750	YES
48	GW6SC3	3859	5.750	YES
49	GWSM*7	3203	8.000	YES
50	GWSM*8	3203	8.000	YES
51	GWSM*9	3203	8.000	YES
52	GWSC*7	3203	8.000	YES
53	GWSC*8	3203	8.000	YES
54	GWSC*9	3203	8.000	YES
55	TGO6S1	3821	5.000	NO
56	TGO6S2	3821	5.500	NO
57	TGO6S3	3821	5.000	NO
58	TGOS1	3821	6.500	NO
59	TGOS2	3821	6.000	NO
60	TGOS3	3821	7.000	NO
61	TGW6S1	3821	5.000	YES
62	TGW6S2	3821	5.250	YES
63	TGW6S3	3821	5.500	YES
64	TGWS1	3821	6.000	YES
65	TGWS2	3821	7.000	YES
66	TGWS3	3821	5.500	YES

Name Key:

G	Grout
M	Monotonic testing
S	Smooth bond
C	Cyclic testing
O	Only
R	Roughed edges
U	Unbonded
TOP	Monolithically cast topping
TOPW	Same as TOP but with weld wire mesh
6	6" specimen (as opposed to 8")
TOPNM	Non-monolithically cast topping
*	Different style of weld ties
W	Weld ties
T	Tension test

3.2.2.2 Shear Testing Frames

The first small elemental testing frame was designed to allow the specimens to be tested horizontally. These tests were conducted by restraining the outer planks from movement while forcing the center plank to displace relative to the others. Unlike the previous series of tests, this smaller specimens allowed the frame to be a single isolated unit. A schematic of this testing frame is shown in Figure 27. This frame was used for all the shear tests with the exception of the topped (TOP and TOPW) and grout-bonded-to-roughed-edge (GORM) series.

The shear testing frame consisted of two-69 inch W24X76 steel I-beams connected along the top flanges with a steel spacer plate. Six smaller sections protruded vertically out of these sections to serve as reaction blocks. Three of these reaction blocks were placed on each side of the testing platform to facilitate reversed cyclic testing.

The load was applied to the center plank with two 25-ton rams. Each of these rams was mounted on the center reaction block. The ram pushed against a neoprene pad. These pads were also placed at each of the four corners in order to compensate for any rough or uneven surfaces.

Three series of shear tests were performed in a different but comparable manner. The TOP, TOPW and GORM series of elemental tests were tested in an upright position in the 400,000 pound SATEC universal testing machine. The rationale behind using the machine was threefold.. First, the failure of these specimens was quite sudden in nature, and this testing machine was safer and more efficient to use. Second, these specimens were only loaded monotonically because weld ties were not used. The reversed cyclic loading capability of the other testing frame was not needed. Finally, the universal testing frame provided the capacity, with a factor of safety, to fail these specimens safely.

Although the tests were conducted in an upright position, the test setup was basically the same. Steel spacer plates and neoprene pads were placed under the exterior slabs, as well as under the compression (loading) head. The universal testing machine was used to apply the limit state force utilizing load rate control.

3.2.2.3 Tension Testing Frames

Tensile loading of the specimens was accomplished by a anchoring a steel channel section to the two outer planks and applying forces between these sections. This testing setup is shown in Figure 28. The testing frame consisted of two C15X40 channel sections attached with 4"X3/4" concrete anchor bolts to the small end sections of the specimens. Hydraulic rams (10 ton capacity) were then placed on each side near the centroid of the specimen. Failure of these specimens was quite sudden, so a safety chain was secured around the entire specimen.

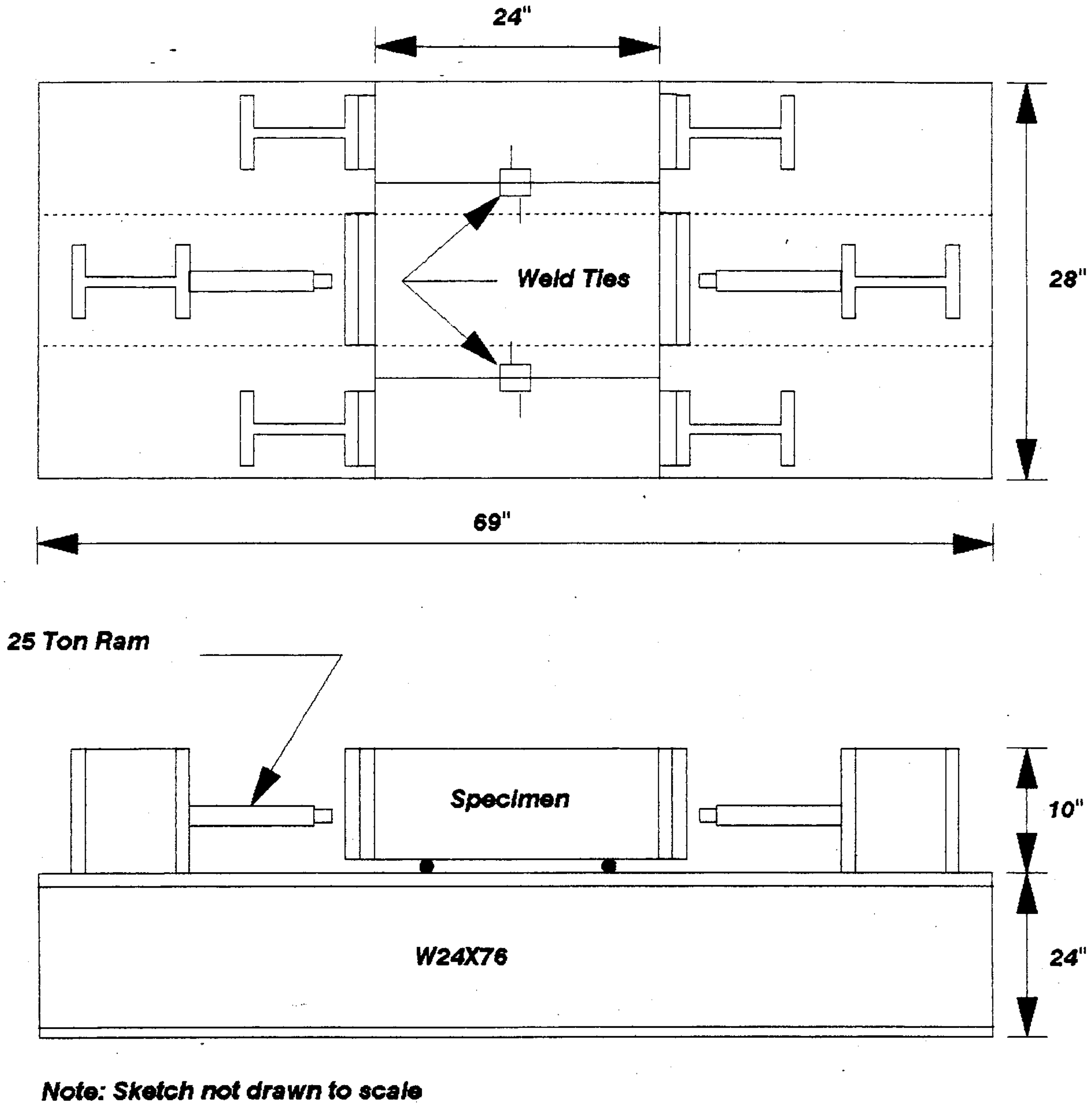

Figure 27. Elemental shear testing frame

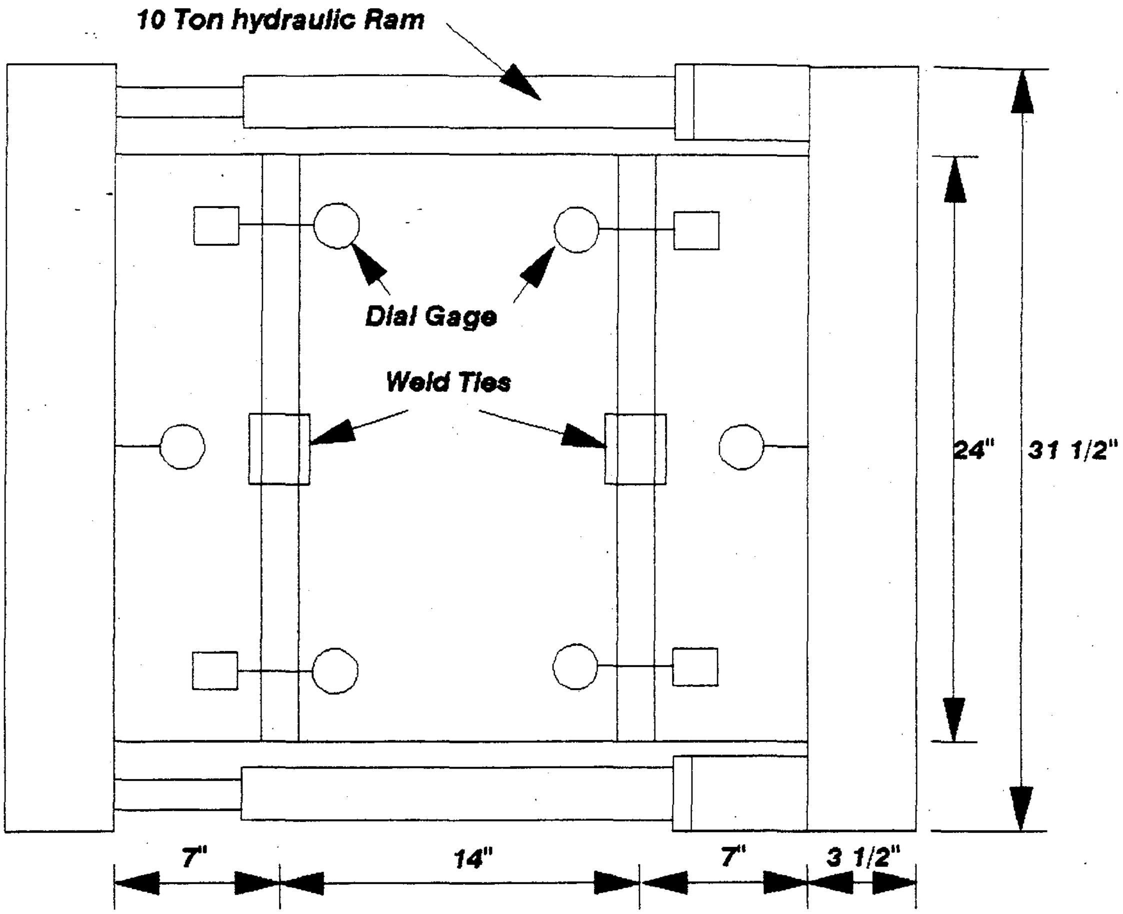

Plan View

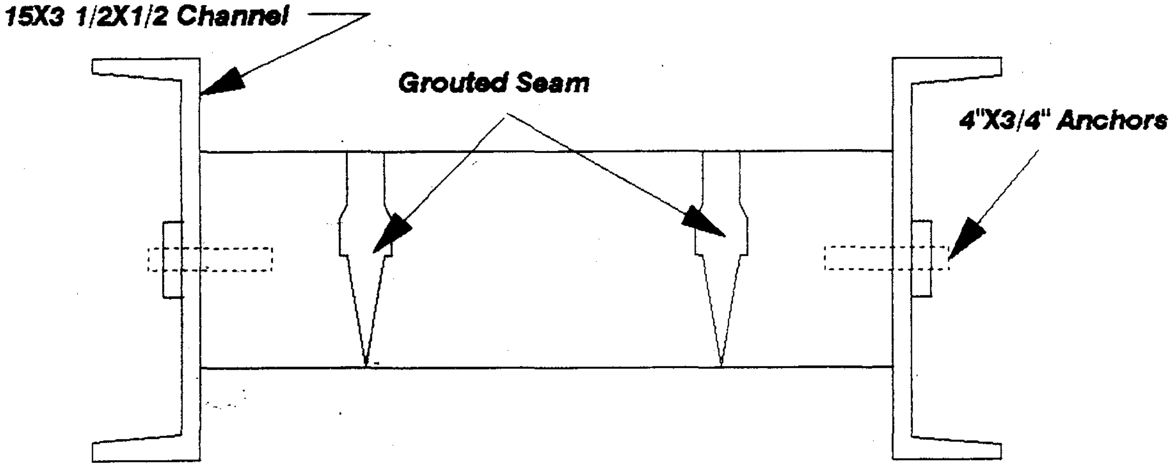

Cross-sectional View

Figure 28. Elemental tension testing frame

3.2.3 Data Acquisition System and Instrumentation

3.2.3.1 Shear Tests

Both seam slip and plank rotation were measured during the elemental shear tests. A DCDT or dial gauge was placed near each corner as is shown in Figure 29. A pair of DCDTs was also connected to the center plank in order to measure the relative movement of the outer components. The data from this information was recorded by the DAS and stored on a magnetic disk for future reference.

A minimal amount of instrumentation was used on the GORM and TOP test series due to the nature of these tests. Seam slip gauges were installed on the first few tests; however, they did not reveal any useful information because of the instantaneous nature of the failure. This type of instrumentation was not applied to the final tests in these series.

3.2.3.2 Tension Tests

The most significant measurements taken during the tension elemental tests involved seam split. Two dial gauges were placed transverse to each of the two seams as is shown in Figure 30. Additional instrumentation was not deemed necessary because of the nature of the failure of these specimens.

3.2.4 Load Program

3.2.4.1 Shear Tests

The elemental shear tests were conducted with two load programs depending on the type of test. Those specimens with only grout in the seams were tested monotonically. Thus, the loading procedure simply included a gradual increase in the total load until failure. The brittle behavior of these specimens under high load precluded the application of reverse loading.

The remaining shear elemental tests were tested with a reversed cyclic loading program very similar to the one used for the diaphragms. Although increments of displacement varied, most tests employed cycles at 0.025, 0.05, 0.1, 0.2, 0.3 and 0.4-inches of displacement.

3.2.4.2 Tension Tests

The elemental tension tests were tested monotonically to failure. For those specimens without weld ties, the load was simply increased until one of the seams failed. At this time, an inspection of the specimen was made. If the one of the seams was completely intact, the remaining portion of the specimen was reloaded to failure. Those specimens which utilized weld ties were tested in almost the same manner, with the exception that after the grout in the seam failed, the loading was continued until the weld tie failed.

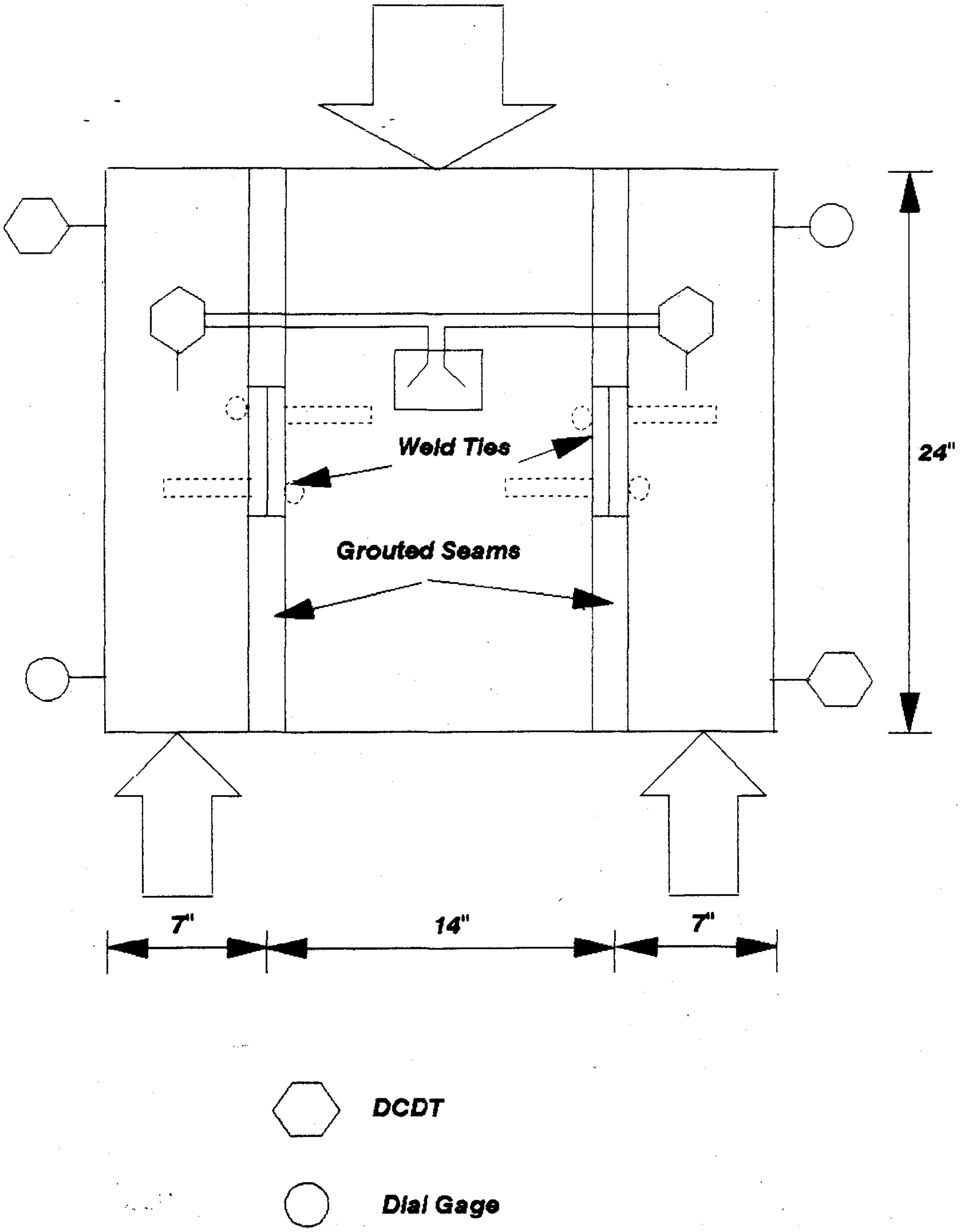

Figure 29. Instrumentation on elemental shear tests

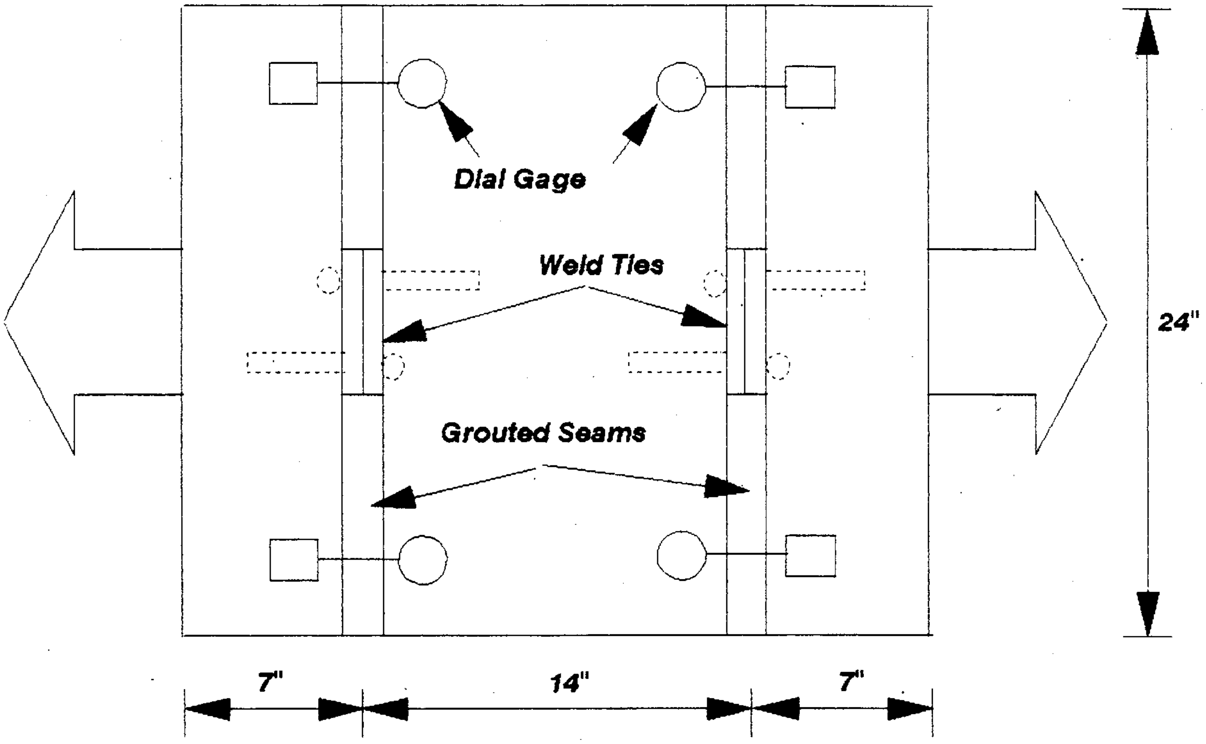

Figure 30. Instrumentation on elemental tension tests

4. EXPERIMENTAL RESULTS OF FULL-SCALE TESTS

4.1 Diaphragm Test Description and Behavior

This section includes a brief description of the diaphragm tests completed as part of this study. Throughout this section, the displacement increments will be referenced along with the direction of movement during which that event took place. Figure 31 is a schematic of the testing frame showing the orientation.

4.1.1 Diaphragm Test #1

The first pilot test was conducted on August 27, 1986. As shown in Figure 18, this test consisted of four hollow-core planks oriented transverse to the loading beam and connected along the loading beam and restrained edge. A preliminary version of the SPD loading program [31] was followed.

Stabilization cycles were completed at 0.025 inch and 0.05 inch displacements without any significant events. The west seam cracked at 0.1" west (load point 39) and a corresponding load of 70.2 kips and was therefore designated the first major event, FME. This interstice, as well as all others which occurred during this test, are sketched in Figure 32. The east and center seams subsequently cracked during the first increment of the 0.2" cycle at displacements of 0.15" east and 0.2" east, respectively. These events are distinctly shown in Figure 33. Note the significant loss of strength associated with these two seam cracks.

At the conclusion of the degradation cycles of the 0.2" increment, the testing system experienced a hydraulic surge which increased the displacement to approximately 3" east. The exact ultimate displacement and load were not recorded for this event. During this surge, longitudinal cracks formed along the outer thirds of the diaphragm. In addition, many of the weld ties were broken or damaged as reported in Figure 34.

In order to verify that the ultimate load had been reached and to obtain degradation behavior, the test was continued. Cycles were completed at displacements of 0.25", 1.0" and 3.0". As expected, the loads during these increments were quite low. The test was therefore terminated and the failure mechanism was attributed to seam failure.

4.1.2 Diaphragm Test #2

Pilot Test #2 was similar to the first pilot test; however, the planks were oriented parallel to the loading beam and were connected to the side beams. Only two studs were located on the loading beam and two on the reaction blocks. A schematic showing the stud placement is presented in Figure 35. Unfortunately, the two studs on the loading beam sheared off early in the test, and consequently no force was transferred from the loading beam to the diaphragm thereafter. This force was instead taken by the flexible tees (which connected the side beams to the loading beam), ultimately destroying them in the late stages of the test.

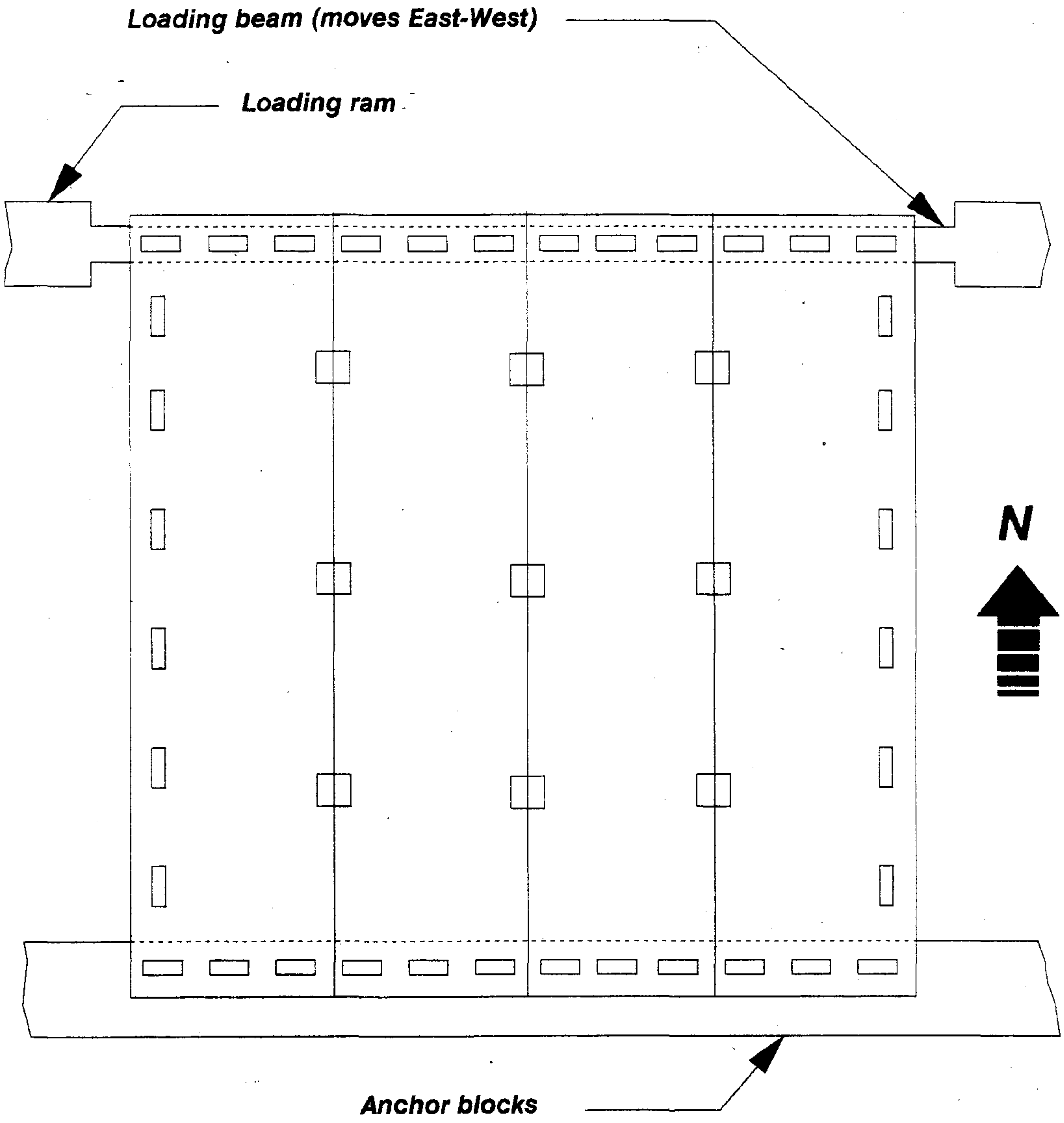

Figure 31. Orientation of the testing frame

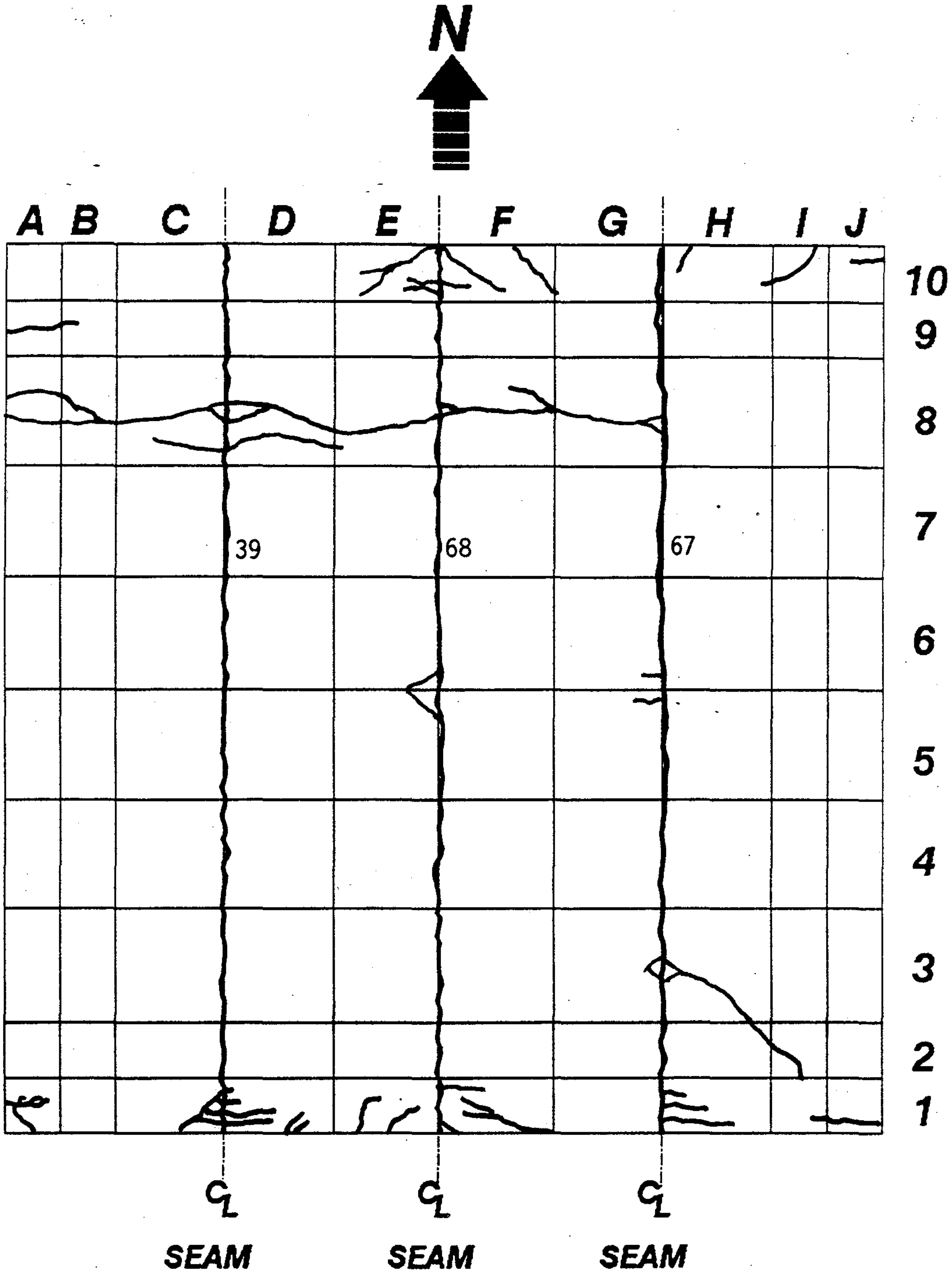

Notes:

Numbers by the cracks indicate the load point at which the crack was observed

All unmarked cracks occured during hydraulic surge

Figure 32. Crack pattern for Test #1

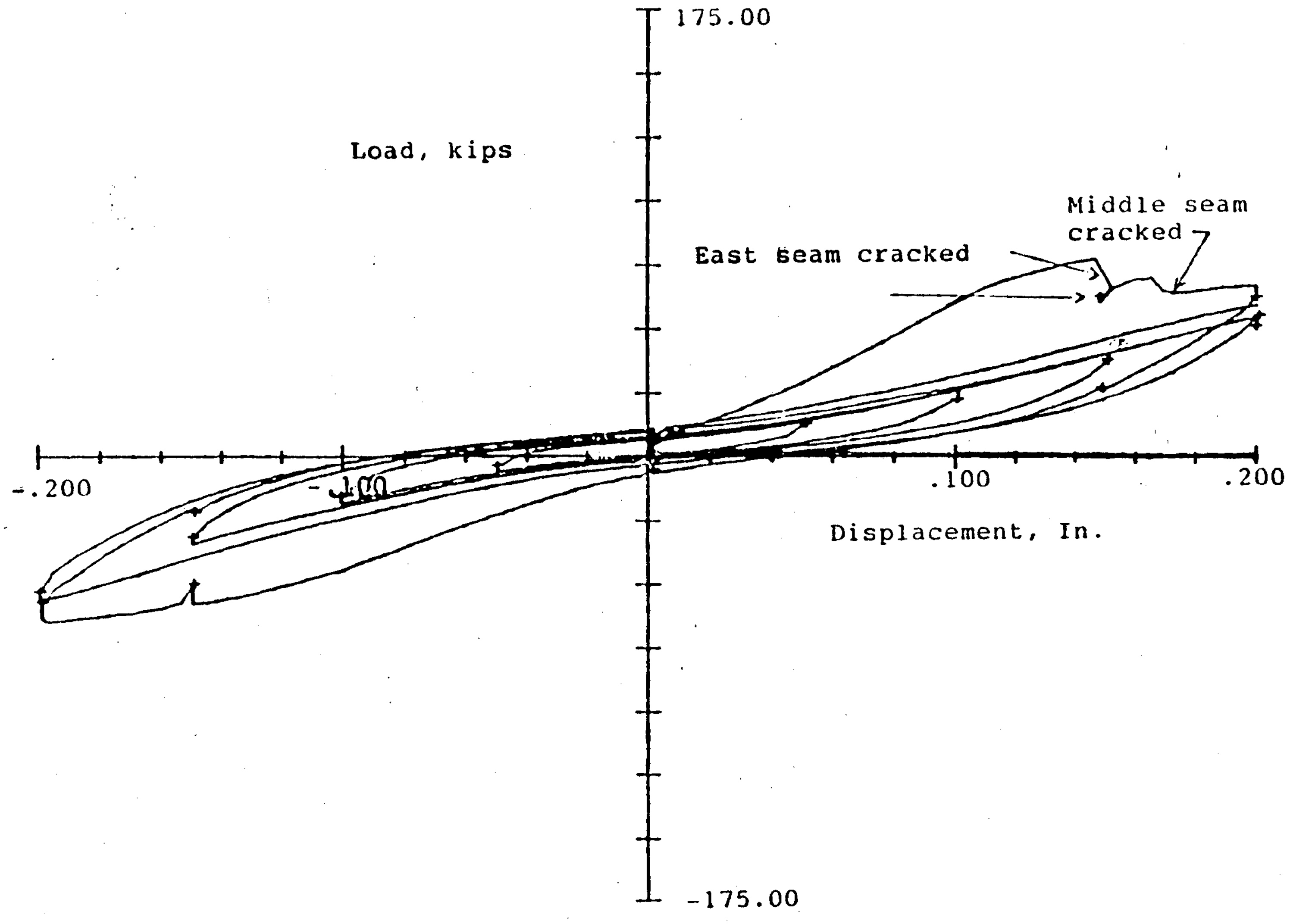

Figure 33. Hysteretic curve for pilot Test #1

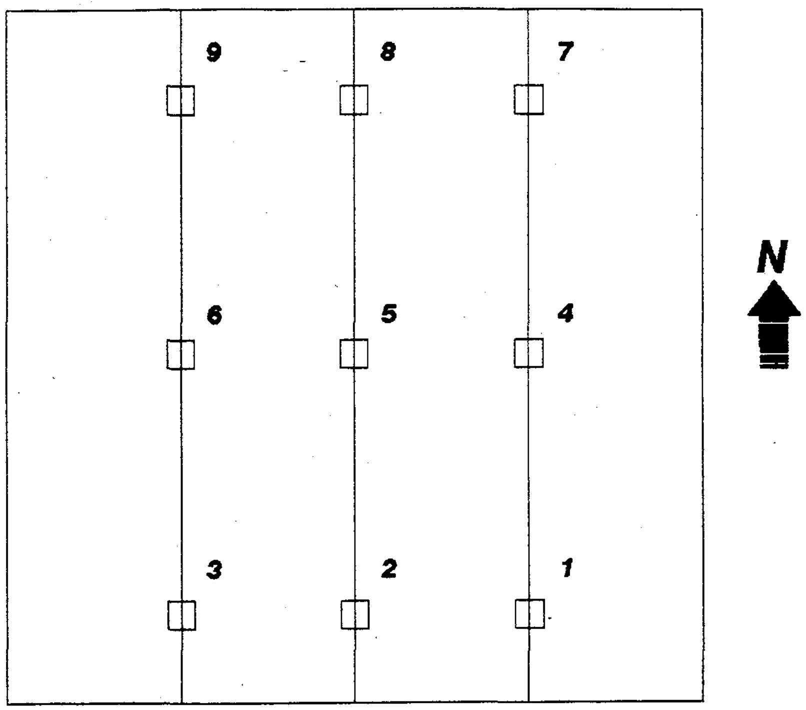

WELD TIE	CONDITION AFTER TEST
1	Weld Broken
2	Weld tie severely damaged
3	weld broken
4	Concrete spalling/weld broken
5	Some spalling
6	Weld broken/severe spalling
7	Weld tie in place but severely damaged
8	Concrete broken/weld cracked
9	Concrete spalled

Figure 34. Weld ties condition for Test #1

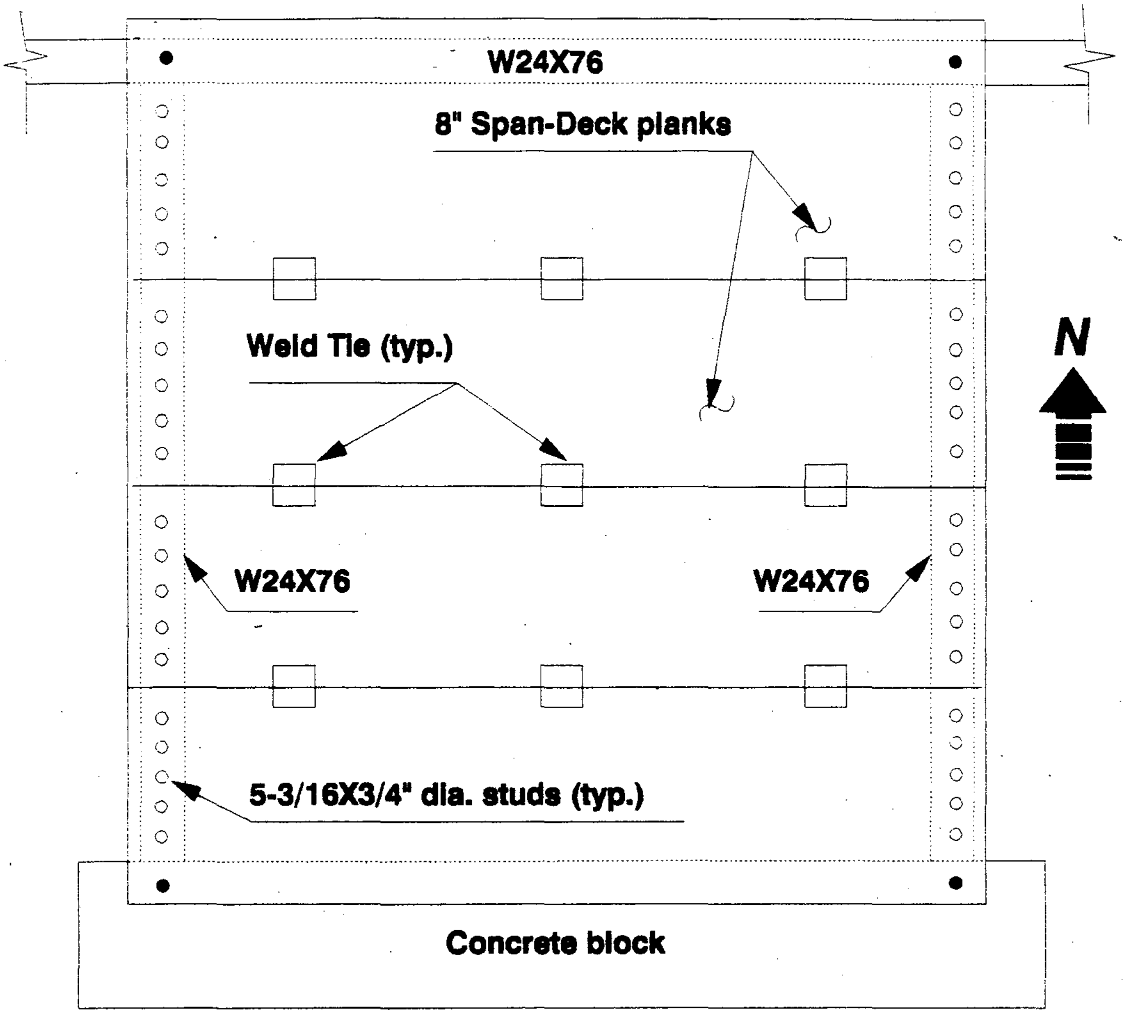

Note: Studs not located on edge beams are darkened

Figure 35. Test #2 stud placement schematic

Before the flexible tees were damaged too severely, a considerable amount of data was obtained. Since the SPD loading program does not require degradation cycles until the FME has been reached, only stabilization cycles were incorporated until load point 238. The load program is shown in Figure 36. At this load point, the north seam cracked under a load of 58.4 kips and a displacement of 1.27" (loading beam movement of 2.4"). The difference between the actual diaphragm movement and the loading beam movement reflects the fact that the tees connecting the side beams to the loading beam were undergoing significant deformations. These deformations are directly attributed to the high loads being transferred through this joint. Localized diagonal cracking occurred in the northeast and northwest corners at displacements of 1.27" and 1.59", respectively. These cracks began at load point 235 and are shown in Figure 37. At a displacement of 1.59" and a load of 50.1 kips, the south seam also cracked. A substantial decrease in strength (33%) was associated with this failure as is shown in Figure 38.

One final attempt was made to minimize the slippage at the flexible tees and further develop the failure mechanism for the diaphragm. Braces were attached along the loading beam. However, only concrete bearing failure resulted at these locations. This testing arrangement was therefore considered unsuitable for developing the diaphragm action.

4.1.3 Diaphragm Test #3

Pilot Test #3 consisted of only two planks oriented transverse to the loading beam. Studs were welded to the north and south ends of the testing frame. Since no distinguishable FME occurred during the test, only stabilization cycles were used. The only cracks noted were those on the north and south edges due to the bending of the studs. On the south side (restrained end), the four outermost studs on each plank were sheared, and rigid body motion occurred throughout the entire test. The maximum load for this edge zone failure was 21.7 kips at 2.0" displacement. As shown in Figure 39, a hysteretic plot for Test #3, minimal energy was dissipated in this testing configuration. In short, this slab illustrated that when an insufficient number of plank segments are used, only simple rigid body motion dominates.

4.1.4 Diaphragm Test #4

The fourth diaphragm test was a duplicate of the first test which was rendered incomplete due to a hydraulic surge. This test was performed on December 3, 1986 and was completed under the guidelines of the SPD loading procedure. Displacement increments of 0.025" through 5.0" were used as shown in Figure 40. Similar loading patterns were used on all the remaining tests.

The FME for this test occurred at load point 65 when the west seam cracked at 0.2" east under a load of 88.0 kips. The east seam cracked during the next displacement increment (0.3", load point 93) at a load of 90.0 kips. Cracks began propagating from the weld ties during the 0.5" displacement loading cycles at load points 110 through 155 as shown in Figure 41. Several of these cracks originated at the horizontal bars of the weld ties. The center seam cracked at

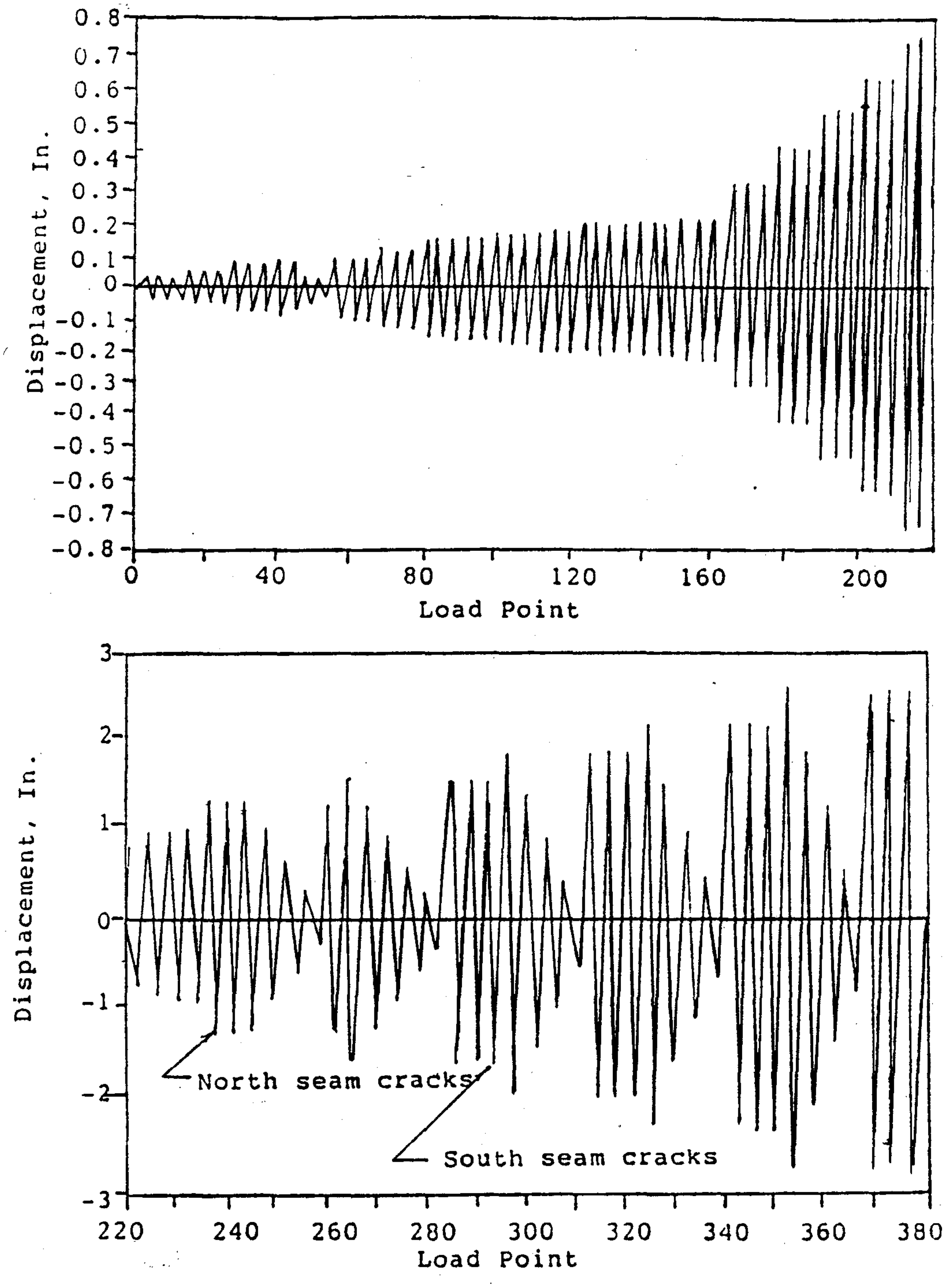

Figure 36. Load program for Test #2

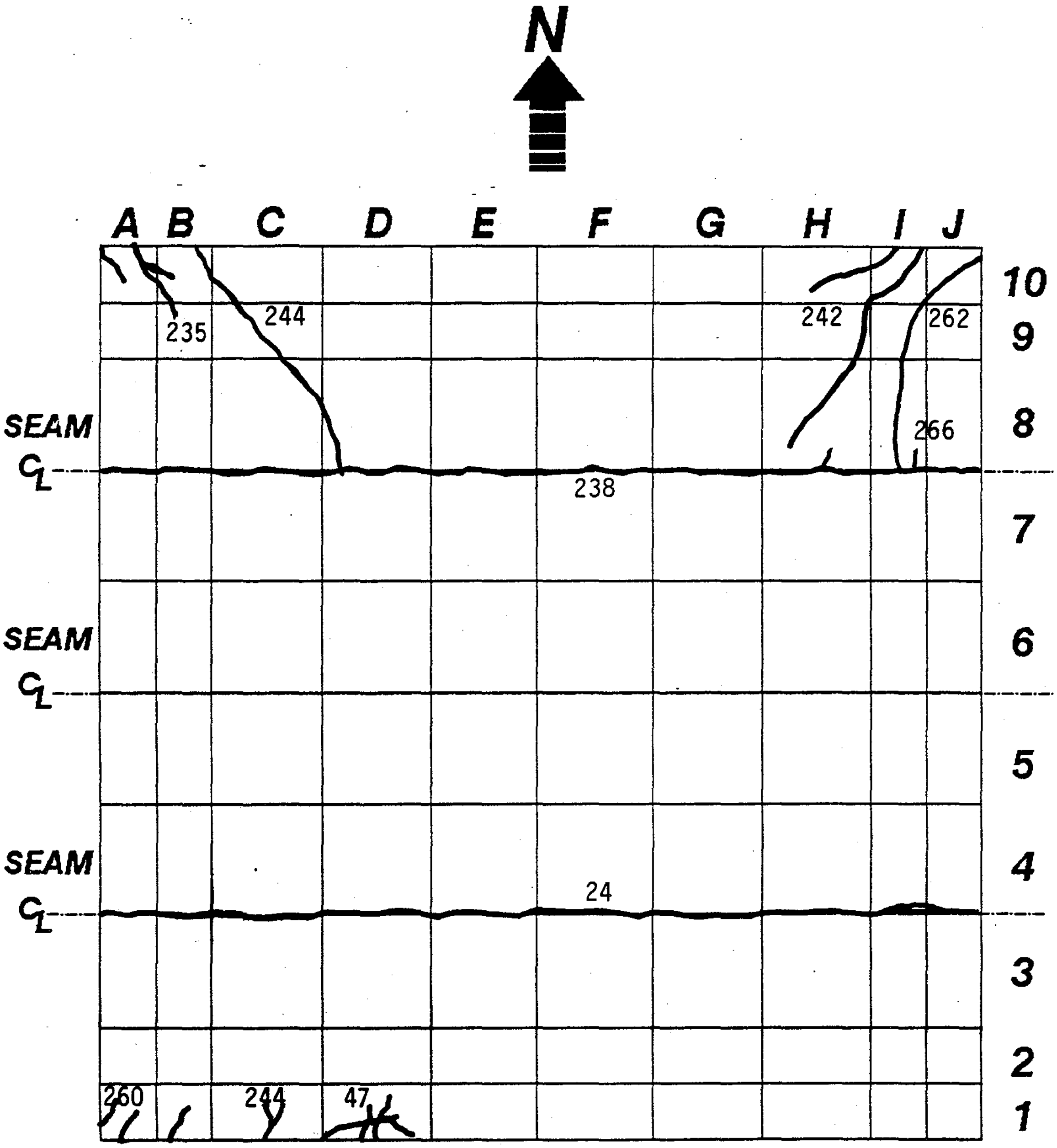

Notes:
Numbers by the cracks indicate the load point at which the crack was observed

Figure 37. Crack pattern for Test #2

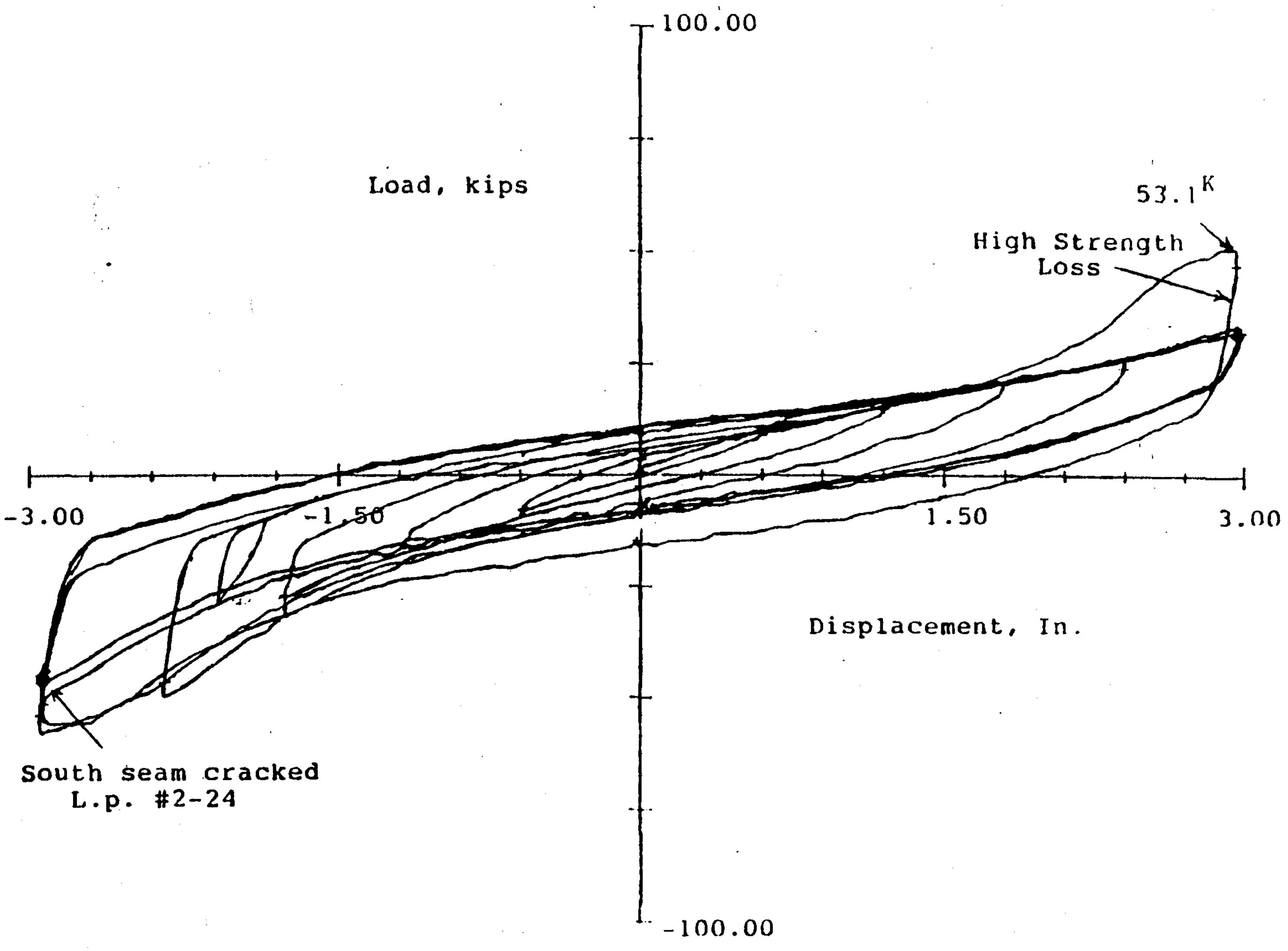

Figure 38. Hysteretic curve for pilot Test #2

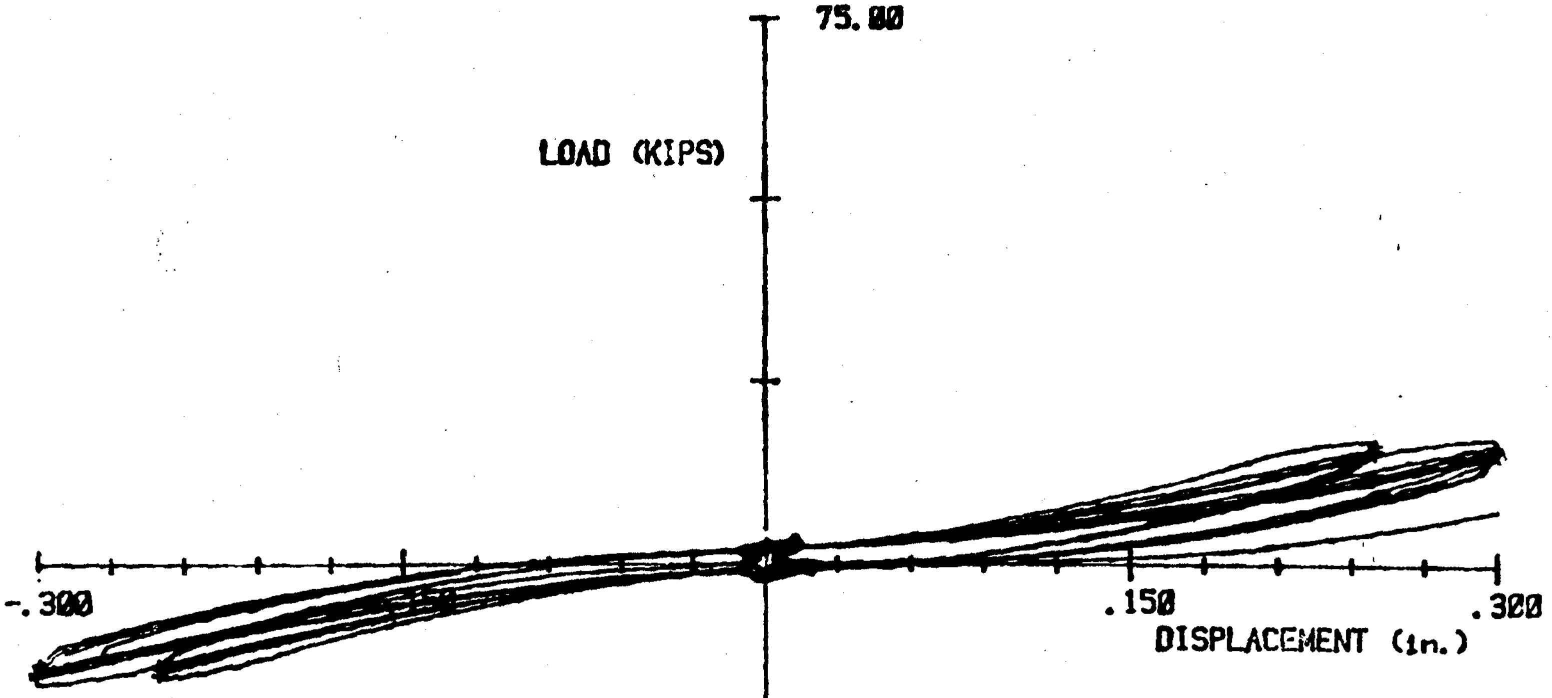

Figure 39. Hysteretic plot of Test #3

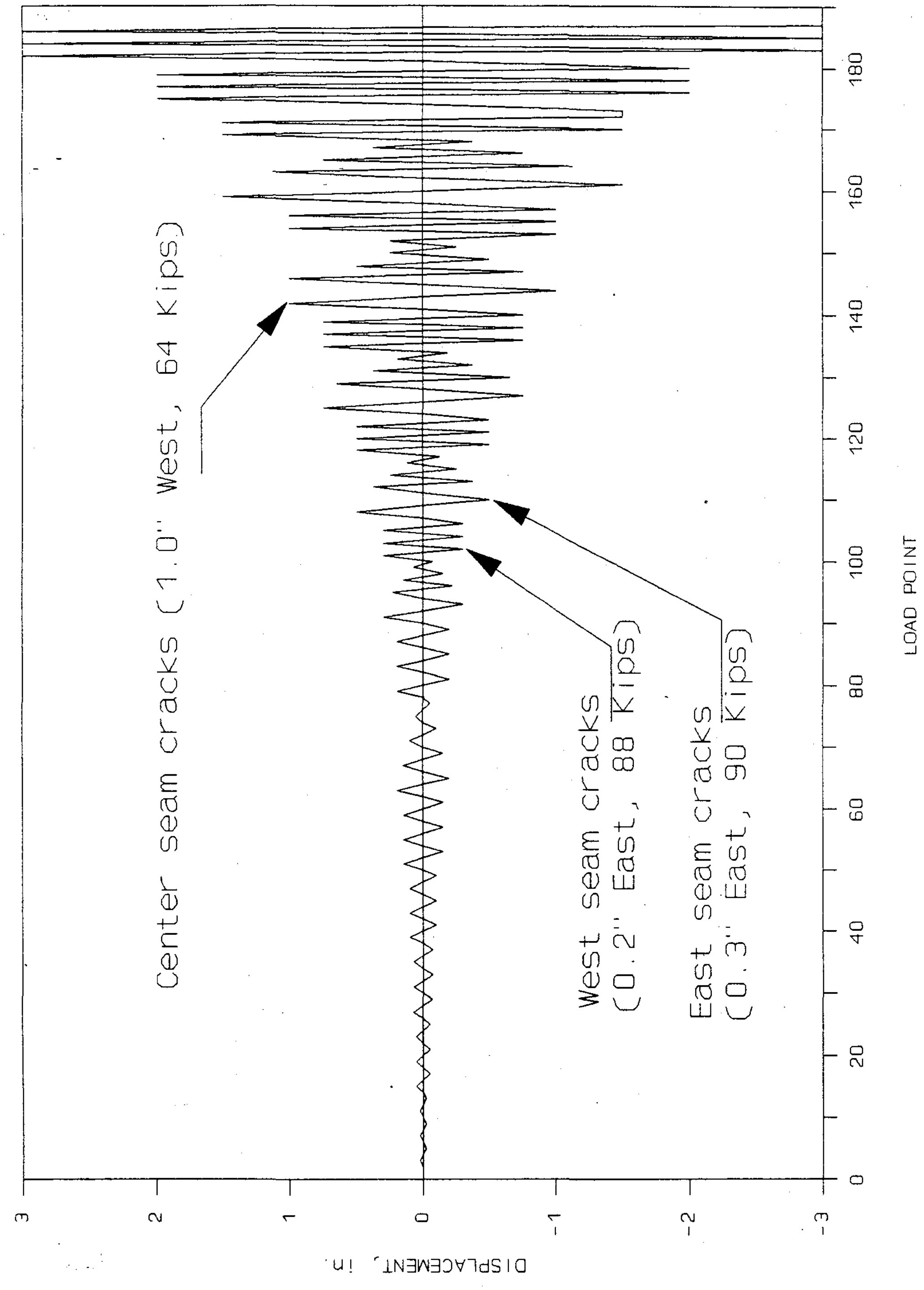

Figure 40. Load program for Test #4

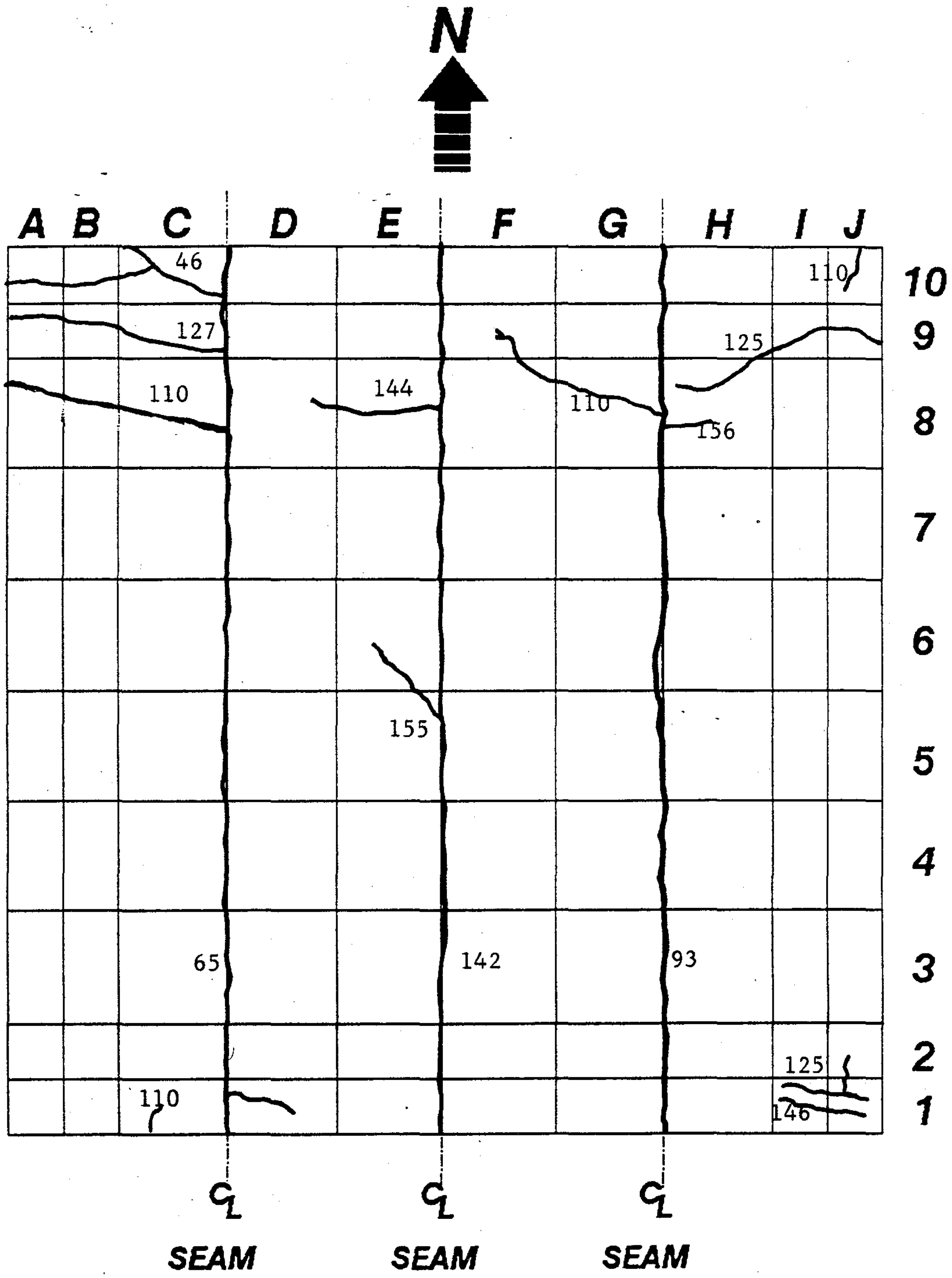

Notes:

Numbers by the cracks indicate the load point at which the crack was observed

Figure 41. **Crack pattern for Test #4**

1.0" west (load point 142) at a load of 64 kips. The peak load achieved during the test was 90.5 kips at a displacement of 0.5 inches east. Throughout the test, severe cracking was noted along the south edge of the diaphragm. Starting at 0.5 inches of displacement, a crack was documented between the interface of the core grout and the lower wythe of the Span-Deck extending across the exterior two planks. This crack widened to 1/4-inch at 1.0" east displacement and was followed by a similar crack at the top edge of the grout/upper wythe interface in the southeast corner. These localized edge zone failures partially contributed to the strength degradation after the peak strength was recorded. During the remainder of the test, several small interstices formed near the weld ties and the condition of these units continued to degrade. The final condition of the weld ties is recorded in Figure 42. The most common mode of failure for these inserts was shearing of the weld along the base plate and exposure of the horizontal bars. This test emphasized that the weld ties provided a means of maintaining close to 100% of the peak strength through 0.75" of displacement. Thus, the weld ties greatly enhanced the ductility of the specimen. Test #4 also revealed that the failure mechanism for this orientation was predominately shear-bond as is shown in Figure 43.

4.1.5 Diaphragm Test #5

Test #5, which also consisted of four planks oriented transverse to the loading beam, was conducted on January 12, 1987. Unlike the previous tests, this test was connected on all four sides of the diaphragm as shown in Figure 18.

During the first displacement to 0.025" (52.5 kips), cracks developed along the east and west vertical faces running parallel to the cores. The first major surface crack occurred at 0.05" west and a load of 84.0 kips (load point 12) at which time the entire west seam cracked. The southern two-thirds of the east seam also cracked as is shown in Figure 44. The remainder of this seam cracked on the reversed displacement (0.05" east) of this cycle.

Interstices began forming near the weld ties during the 0.1" cycle and continued forming until the failure of the weld ties later in the test. Figure 45 summarizes the condition of all of the weld ties near the completion of the test. The final seam cracked slowly during the 0.3" and 0.5" cycles (load points 97-105). The maximum load, 109.9 kips, was associated with this event and occurred during the first movement of the 0.5" cycle. Figure 46 summarizes the displacement history for the entire test. The failure mode of this test, as with the previous tests, was seam failure.

One of the initial requirements for the testing was that the diaphragm fail and not the connections between the testing frame and the diaphragm. Failure of the studs during the initial phases of testing was considered most undesirable due to changes in the force distribution. A more concerted effort was made during this test, therefore, to monitor the time of failure of the studs. Figure 47 reviews the history of five studs which were monitored on a trial basis during this test.

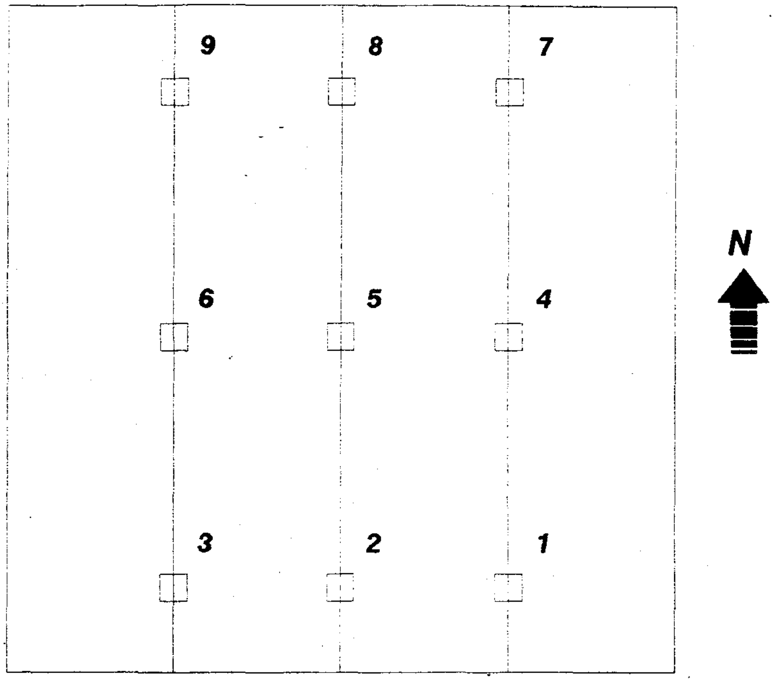

WELD TIE	CONDITION AFTER TEST
1	Intact at 5" displacement with only 1" of west leg uncovered
2	West leg popped out of the concrete
3	Horizontal leg sheared off
4	Horizontal leg sheared off
5	West leg popped out of the concrete
6	West leg popped out of the concrete
7	Horizontal leg sheared off
8	West leg popped out of the concrete
9	West leg popped out of the concrete

Figure 42. Weld ties condition Test #4

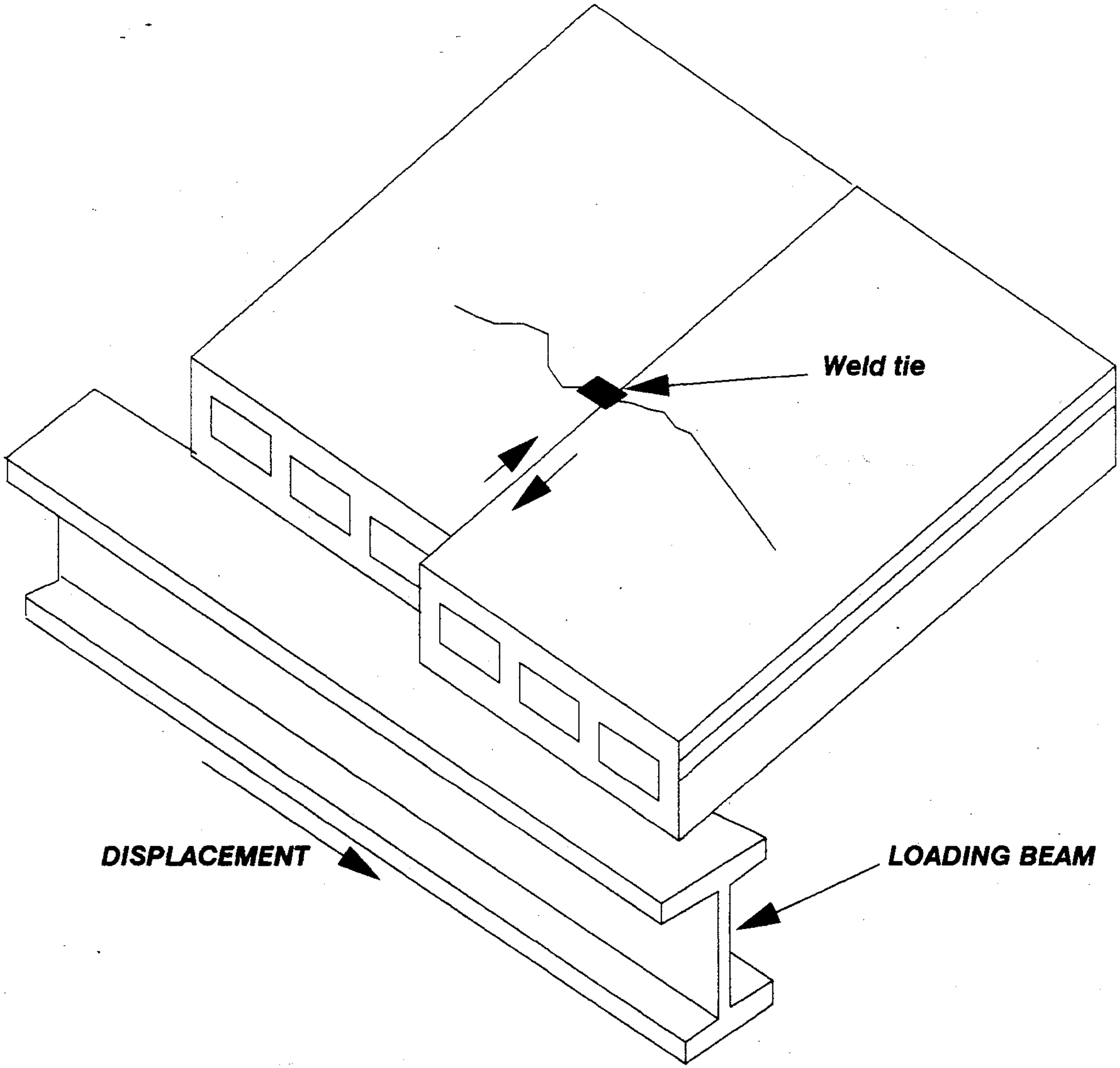

Figure 43. Seam shear-bond failure mode mechanism

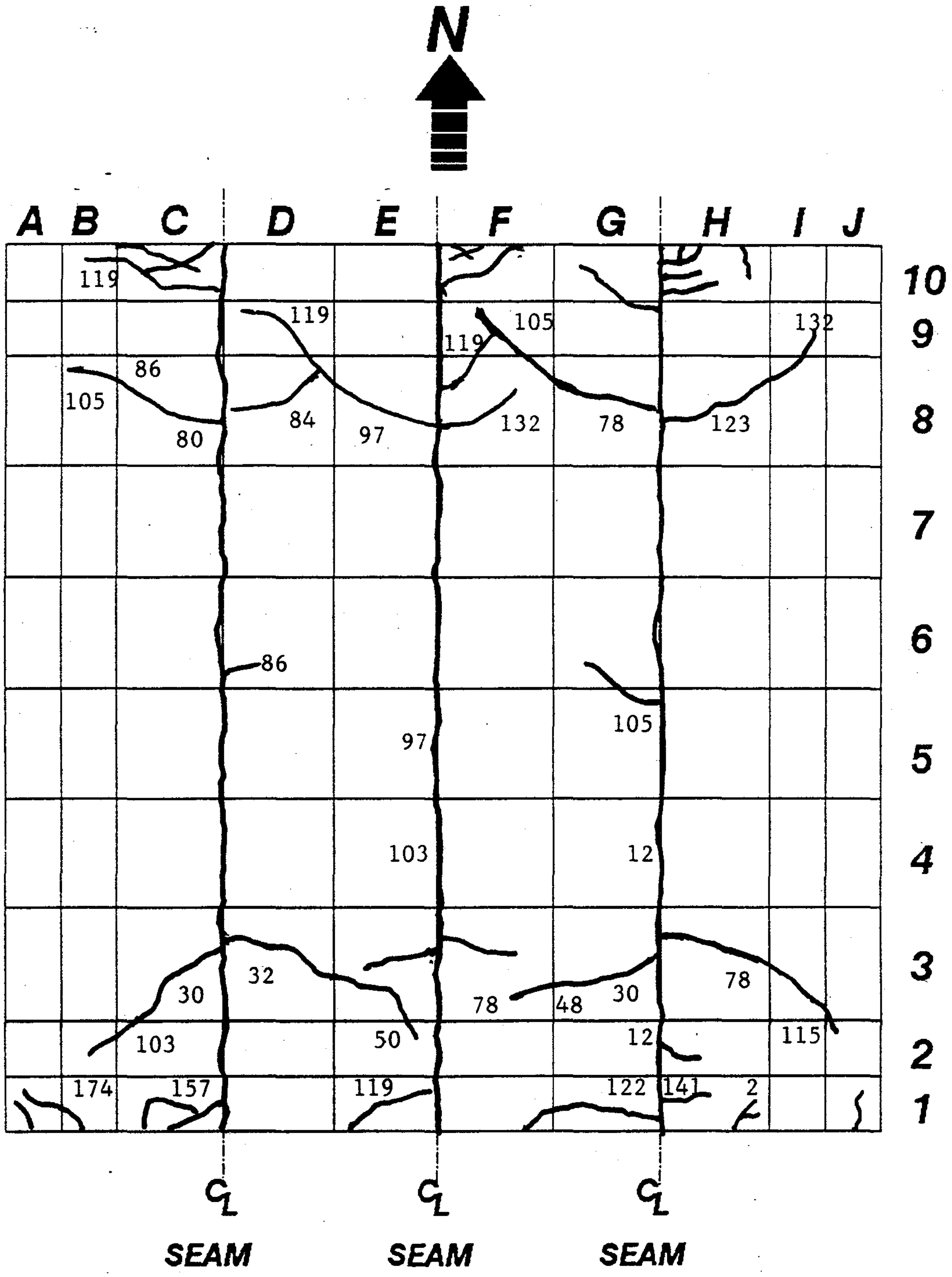

Notes:

Numbers by the cracks indicate the load point at which the crack was observed

Figure 44. Crack pattern for Test #5

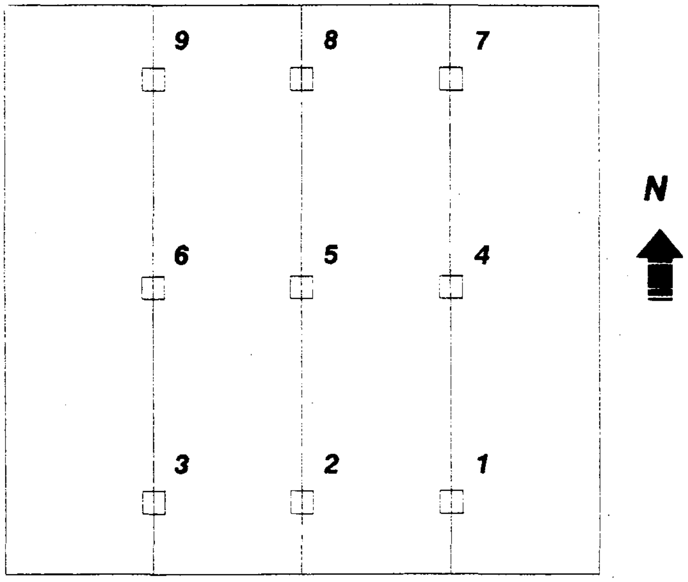

WELD TIE	CONDITION AFTER TEST
1	Horizontal bar exposed, weld on horizontal bar sheared
2	Weld on bar sheared, then horizontal bar exposed
3	Horizontal bar exposed, then weld on horizontal bar sheared
4	Weld between seams cracked
5	Weld on horizontal bar sheared
6	Weld on horizontal bar sheared
7	Weld between seams cracked
8	Horizontal bar exposed, weld on vertical bar sheared
9	Horizontal bar exposed, weld on vertical bar sheared

Figure 45. Weld ties condition for Test #5

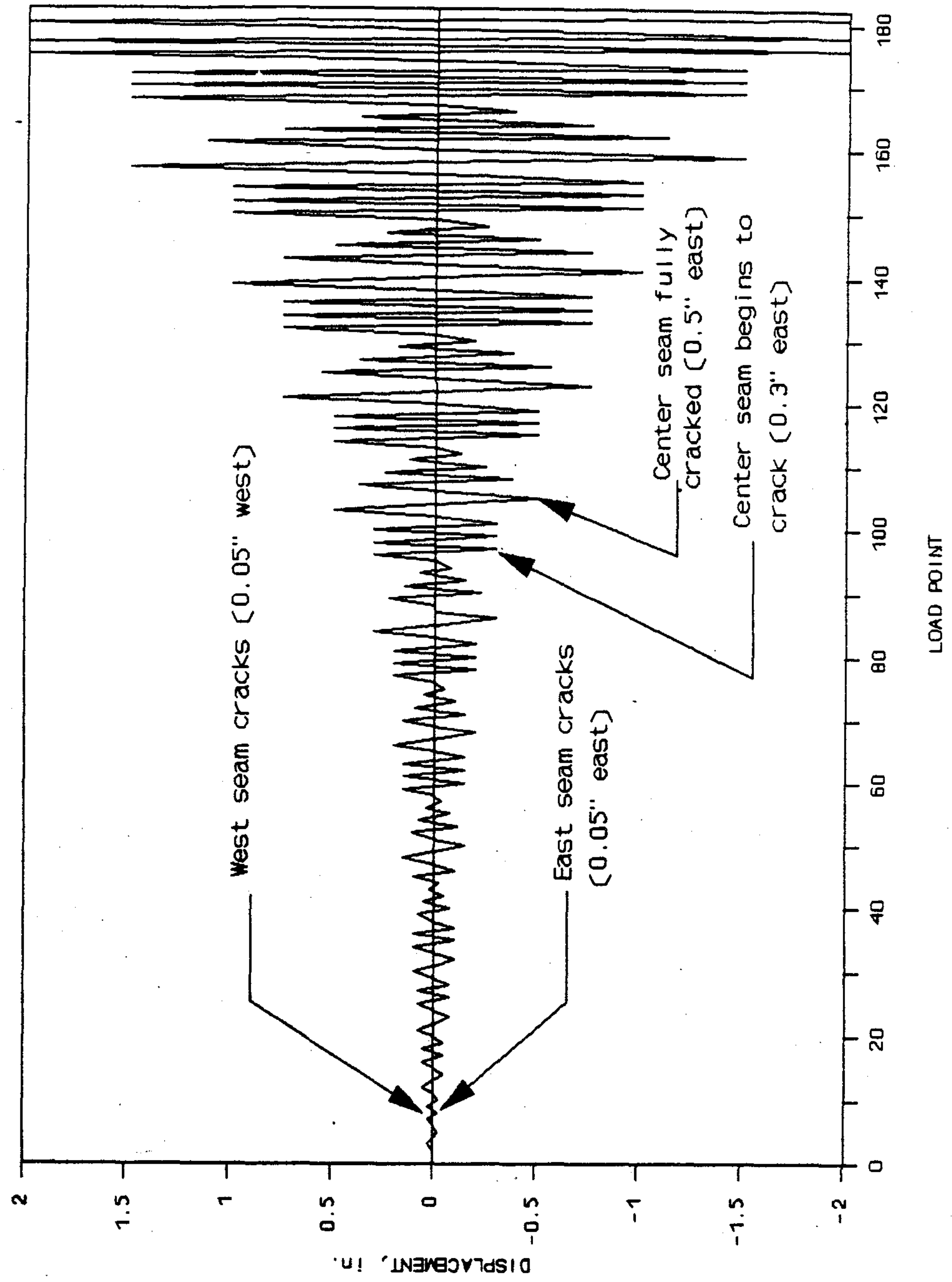

Figure 46. Load program for Test #5

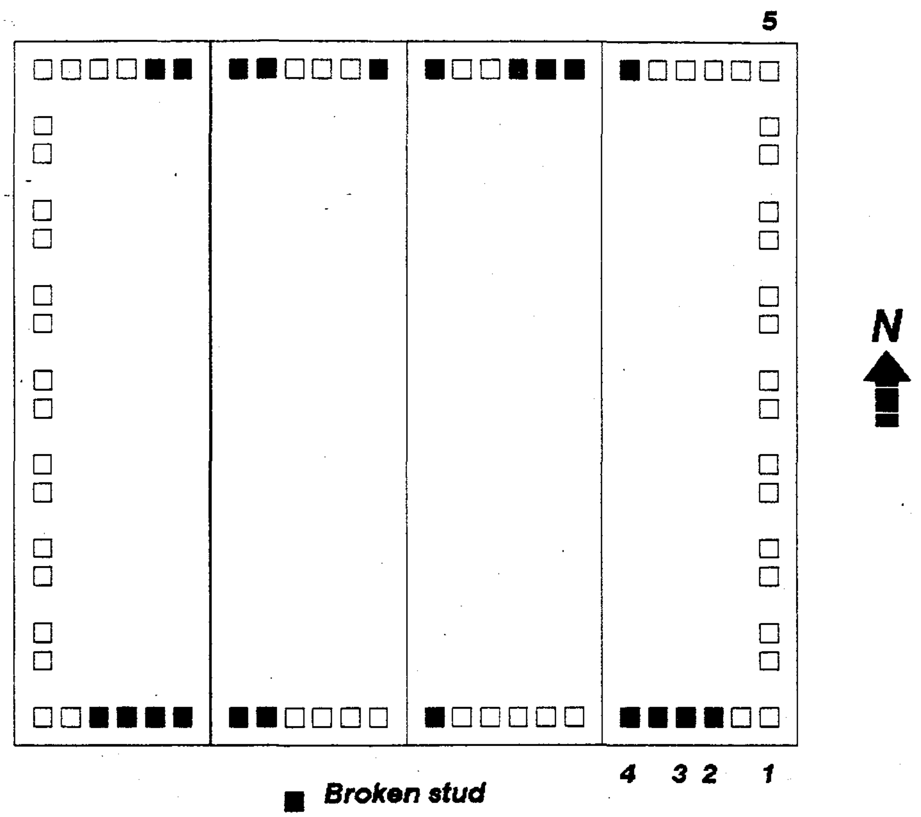

Load Point	Stud 1	Stud 2	Stud 3	Stud 4	Stud 5
84	○	○	○	✳	○
86	○	○	○	○	○
103	○	○	○	○	○
105	○	○	○	○	○
120	○	○	○	○	○
122	○	○	○	○	○
141	○	○	○	✳	○
157	○	○	○	✳	✳
159	○	○	○	○	○
175	○	○	○	✳	○
191	○	✳	✳	✳	○

✳ **Broken current** ○ **Continuous current**

Figure 47. Review of Test #5 stud history at the conclusion of the test

4.1.6 Diaphragm Test #6

The sixth diaphragm test was very similar to the previous one with the exception of the orientation of the planks. The hollow-core planks for this experiment were oriented parallel to the loading beam. The test was officially begun on February 6, 1987, but due to a pump temperature problem, it was resumed on the following Monday, the 9th of February. The FME was obtained during the first cycle of the second increment, 0.025 inch at load point 12. At this time, the seam nearest the restrained edge cracked completely and the seam nearest the loading beam (southern) cracked intermittently. The load for this event was 31.9 kips. The FME was attributed to tensile-seam failure. A pictorial of this failure mechanism is shown in Figure 48. During the first movement of the 0.75 inch west displacement cycle, five feet of the center seam cracked as shown in Figure 49. The remainder of this seam, as well as that of the southern seam, cracked shortly thereafter.

A large number of cracks began developing around the weld ties during the 0.2 inch displacement cycle. The majority of these cracks were noted in the two outer fourths of the diaphragm. During this experiment, only six of the nine weld ties failed. The failed units were located in the two seams closest to the restrained end. Figure 50 reviews the final condition of each of the weld ties. The weld ties exhibited four types of failure: horizontal bar exposure, angle weld failure, vertical bar shear, and horizontal bar shear. The most common mode of failure was shearing of the vertical bar.

As with the previous test, the condition of the studs was monitored throughout the test. Out of the original 72 studs, only 14 failed and they did not begin to fail until the latter stages of the experiment.

4.1.7 Diaphragm Test #7

Test #7 consisted of four planks oriented parallel to the loading beam and connected on three sides (north, west and south) as is shown in Figure 18. Testing began on March 16, 1987, with the FME occurring on the first movement of the loading beam (0.0125 inch, load point 3). At this time, the seam nearest the restrained end cracked intermittently along the east half joint. A load of 19.7 kips was reported for this event. Seam slip readings were negligible at this time which indicated that this crack was primarily due to tension and not shear. The remainder of the south seam cracked progressively during the stabilization cycles of the 0.0375 inch cycle (load points 12-35). This interstice, as well as all of those which occurred during this experiment are shown in Figure 51.

Cracking was noted in the seam nearest to the loading beam (north seam) at 0.1 inch east (68.4 kips). During the first movements of the 0.15 inch cycle, a localized failure occurred on the east side of the north seam (section A7). A crack then formed through both the upper and lower wythes, cracking off approximately twelve inches of the northeast corner. This crack marked the achievement of the maximum load for this test, 73.9 kips. Bearing cracks formed on the west side of the restrained end during the 3.0 inch displacement cycle. Figure 52 summarizes the complete load point verses displacement history for this test.

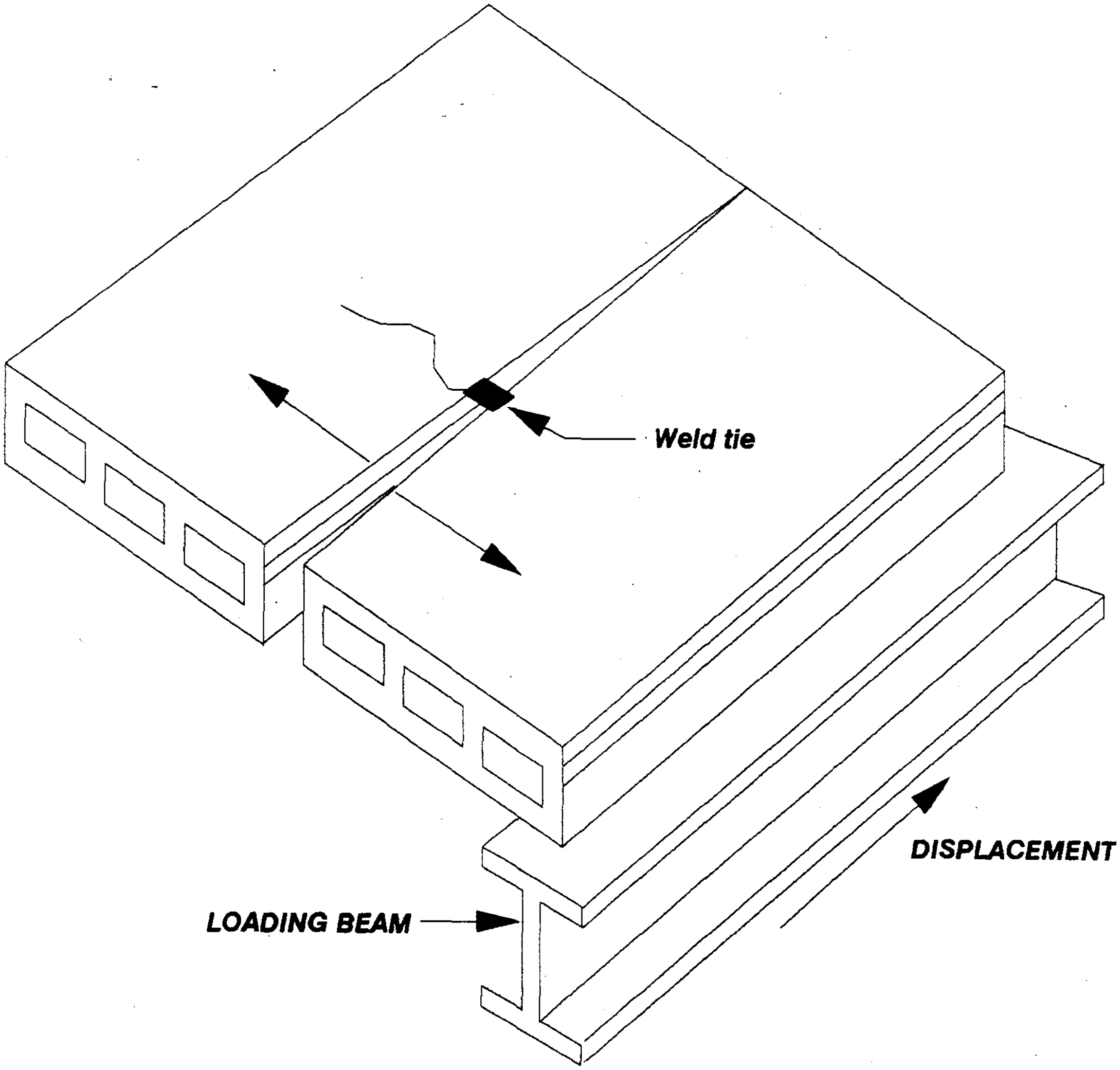

Figure 48. Seam tensile-bond failure mode mechanism

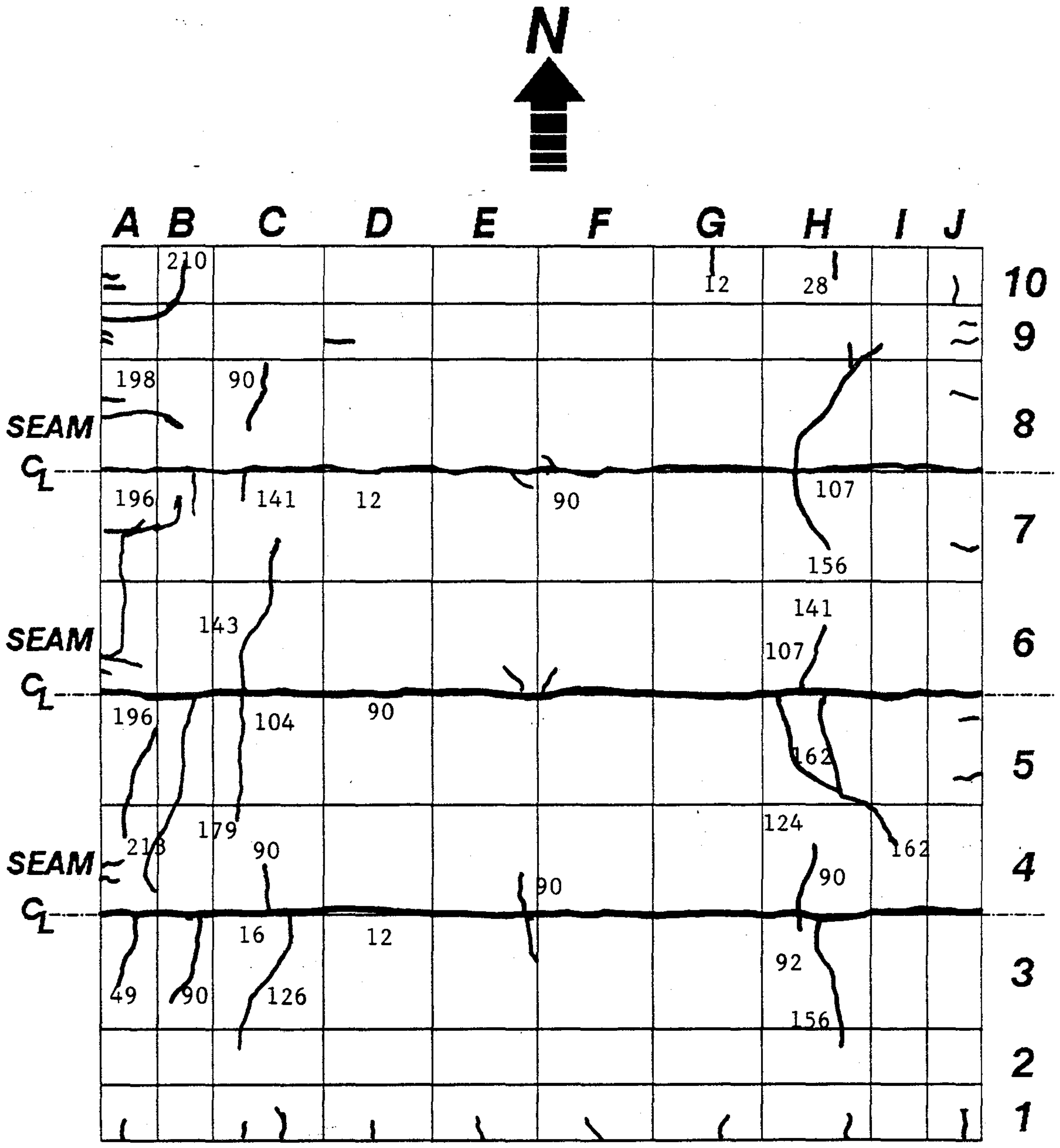

Notes:
Numbers by the cracks indicate the load point at which the crack was observed

Figure 49. Final crack pattern for Test #6

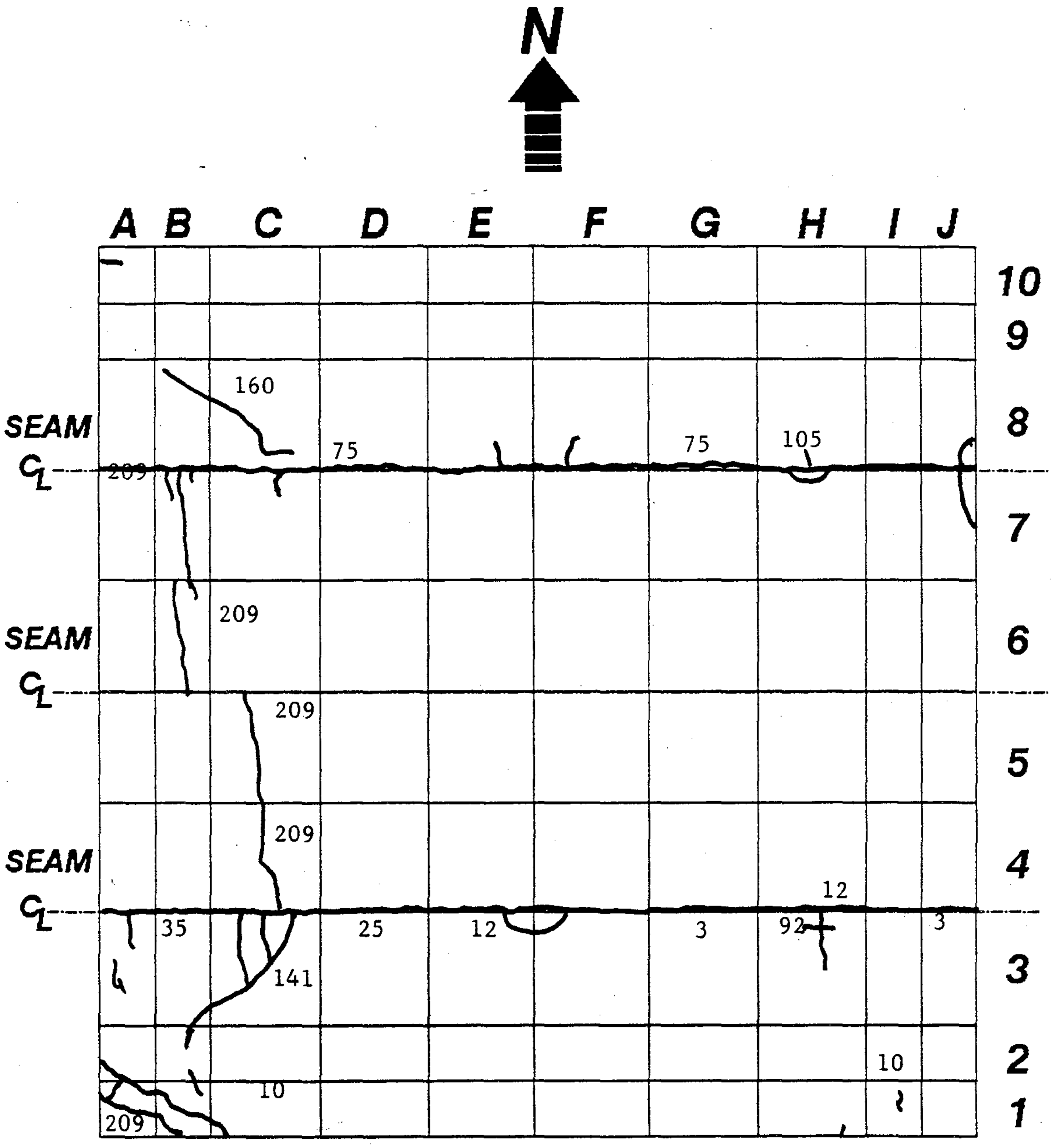

Notes:
Numbers by the cracks indicate the load point at which the crack was observed

Figure 51. Crack pattern for Test #7

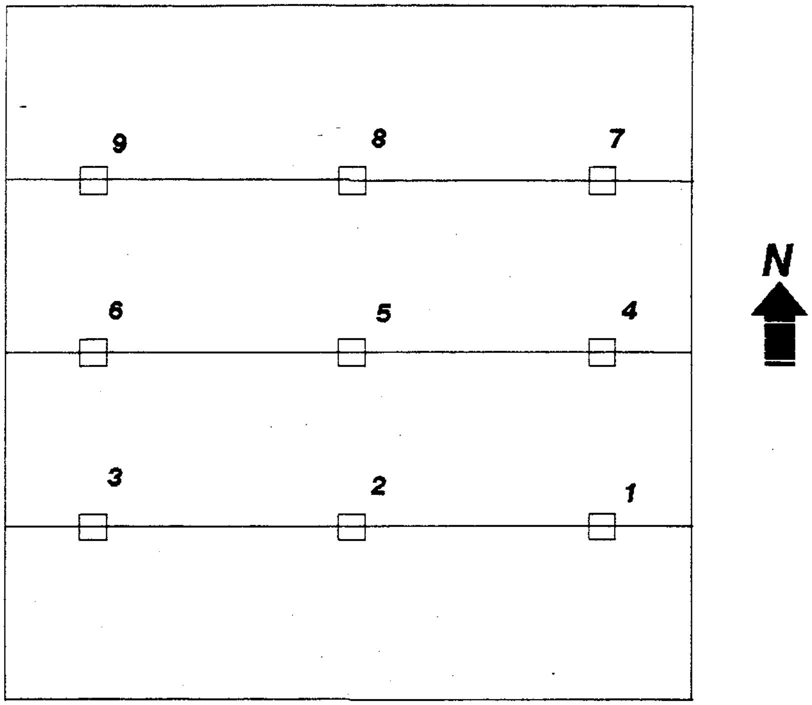

WELD TIE	CONDITION AFTER TEST
1	Horizontal and vertical bars sheared
2	Horizontal bar exposed and vertical bar sheared
3	Weld between seams cracked and vertical bar sheared
4	Vertical bar sheared
5	Horizontal and vertical bars sheared
6	Horizontal bar exposed and vertical bar sheared
7	Intact
8	Intact
9	Intact

Figure 50. Final weld ties condition for Test #6

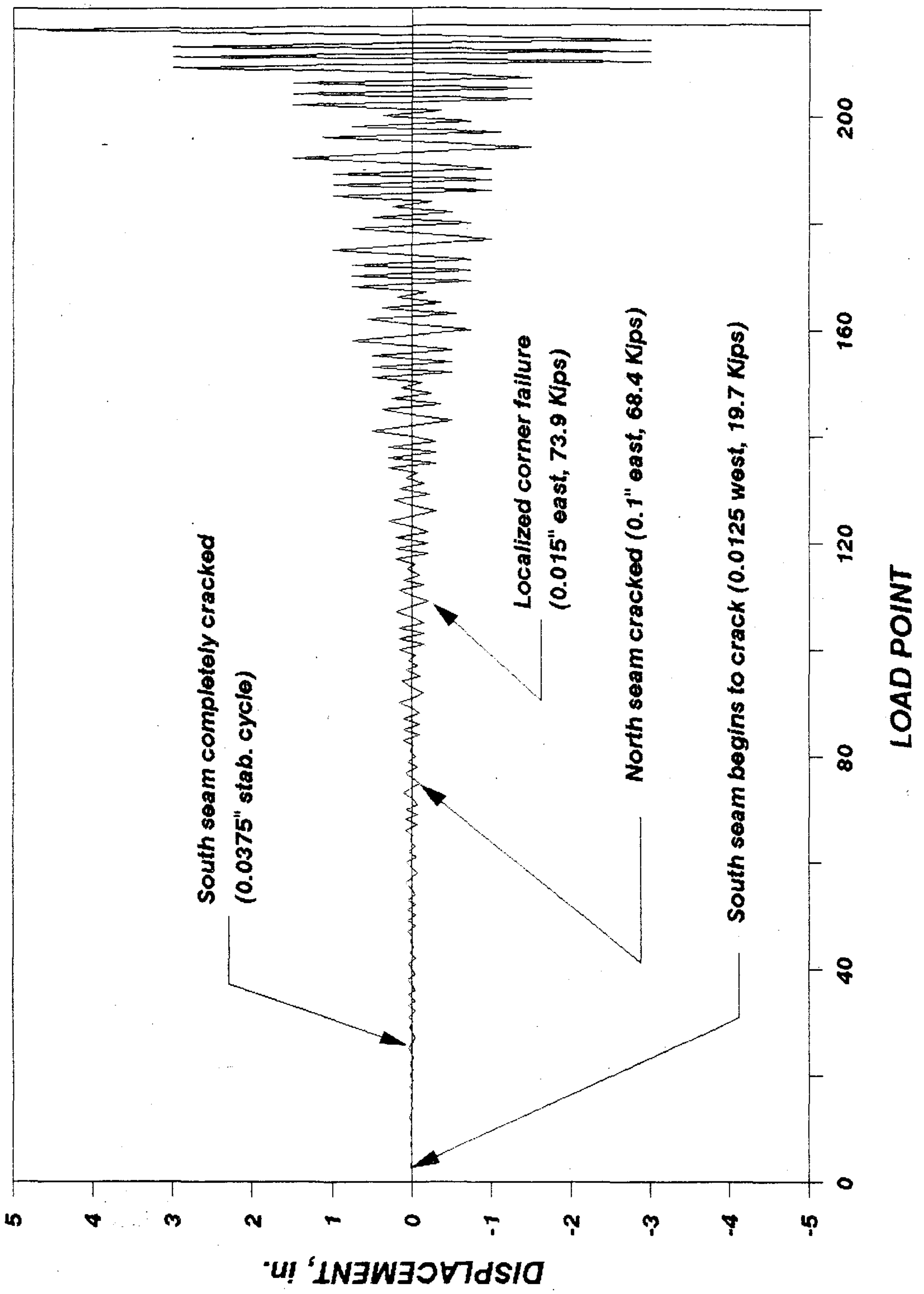

Figure 52. Load program for Test #7

During the 0.15 inch increment, cracks began propagating from the weld ties. Two of the six weld ties failed at the 0.5 inch displacement increments and the remaining four on the outer seams followed during the 0.75 inch cycles. The weld ties on the center seams remained intact throughout the test. Figure 53 reviews the condition of all the weld ties at the conclusion of the experiment.

The condition of the studs was monitored. One inch of displacement marked the first stud failure (l.p. 172). Most of the studs which did fail were on the west side beam near the northmost seams. The complete stud history is reviewed in Figure 54.

4.1.8 Diaphragm Test #8

The planks for this test were oriented in the east-west direction and were connected to the loading beam and the restrained end. A schematic of the test setup is shown in Figure 18. The experiment began on June 13, 1987, and the FME occurred on the first increment of movement to 0.0125 inch east (load point 4). At this time, the south seam partially cracked resulting in a maximum load of 18.5 kips. Since no measurable slip readings were recorded during this event, the cause of this crack was attributed to tension. During the first movement of the 0.025 inch cycle (load point 11), interstices propagated across the remainder of the south seam. A maximum load of 12.7 kips was recorded over this incremental movement. Testing was postponed until Monday, June 15, because of technical problems.

The next significant event did not occur until the stabilization cycles of the 0.15 inch displacement increment at load point 103. At this time, cracks began progressing from the weld ties in the south seam. Figure 55 reveals the extent of cracking during the test. During the degradation cycles of the 0.5 inch displacement increment, the first of the three weld ties in the seam closest to the restrained end failed. This failure was characterized by exposure of the horizontal leg followed by shearing of the vertical bar at the weld. Failure of the last two weld ties took place during the 0.75 inch displacement cycles (load point 157) and is readily apparent on the associated hysteretic curve shown in Figure 56. Figure 57 reviews the condition of the weld ties at the conclusion of the test.

A review of the overall force and displacement versus load point diagram found in Figure 58 reveals that the virgin curve exhibited a slight loss in load early in the test. This strength loss was associated with the cracking of the seam closest to the south side (restrained end). The maximum load for this test, 35.5 kips, occurred at 0.5 inch west displacement (load point 140). After this point, a dramatic loss in load occurred which was a result of the failure of the weld ties.

4.1.9 Diaphragm Test #8B

Since only the seam grout was damaged in Test 8, the same planks were utilized for a second test (referred to as part B). The center plank was lifted

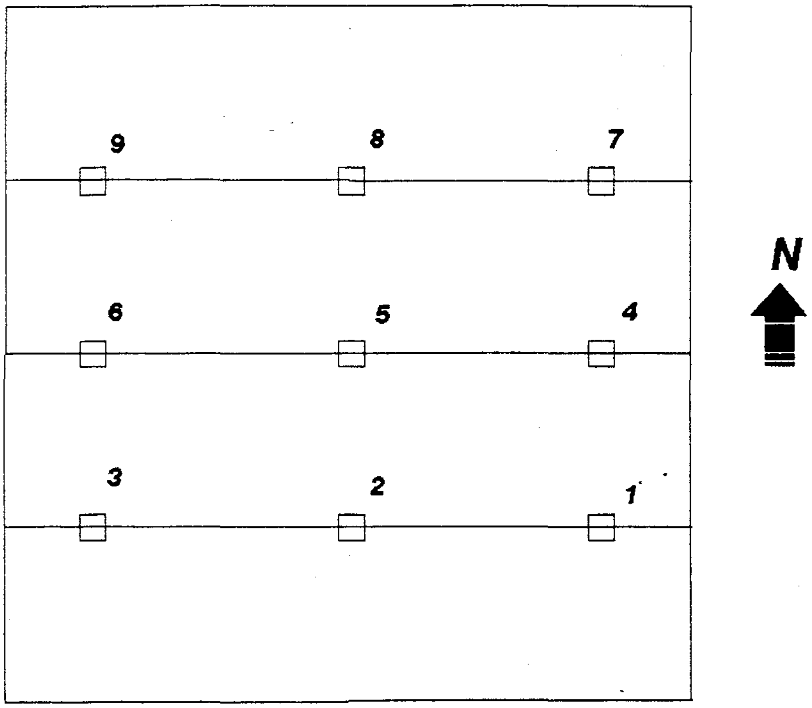

WELD TIE	CONDITION AFTER TEST
1	Weld on horizontal bar sheared
2	Weld on horizontal bar sheared
3	Weld on horizontal bar sheared
4	Intact
5	Intact
6	Intact
7	Horizontal bar exposed
8	Horizontal bar exposed
9	Horizontal bar exposed

Figure 53. Final weld ties condition for Test #7

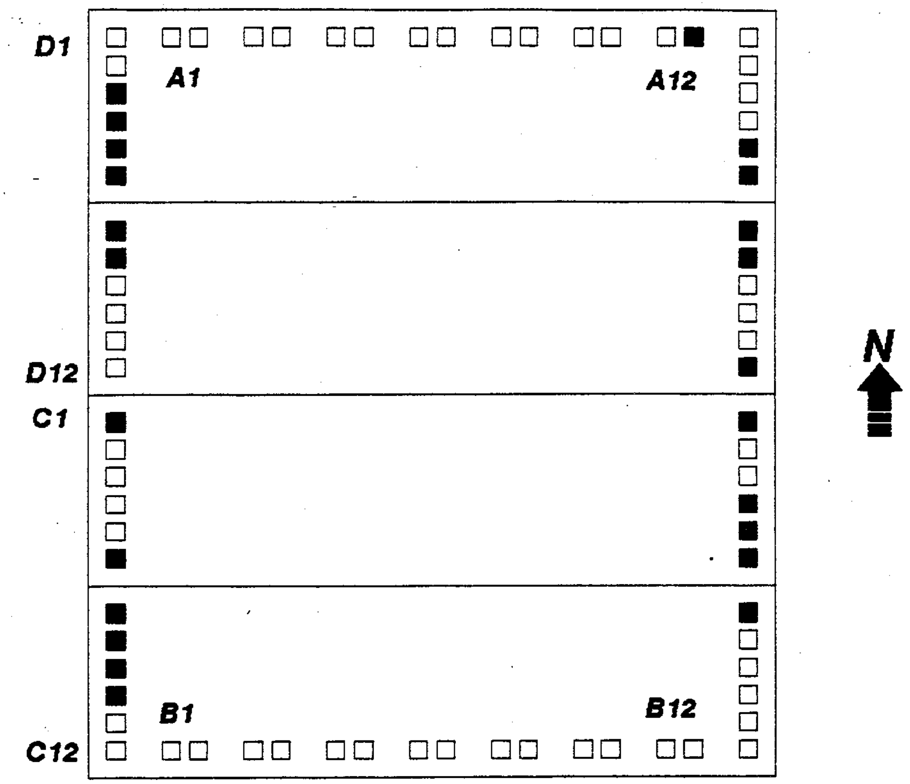

■ Broken stud

Load Point	A12	C6	C7	C8	C9	C10	D3	D4	D5	D6	D7	D8
172	*				*			*				
173	☐				☐			☐				
175	*				☐			*				
177	☐				☐			☐				
187	☐				☐			*	*	*		
189	*				☐			*	☐	*		
190	☐				*			☐	*	*		
192	*				☐			*	☐	*		
194	☐				☐			*	☐	*		
206	*		*	*	☐			*	☐	*		
207	☐		*	☐	☐			*	*	*		
209	*		*	*	*	*	*	*	☐	*		
210	☐		*	*	*	*	*	*	*	*	*	
213	*		*	*	*	*	*	*	*	*	*	
214	*		*	*	*	*	*	*	*	*	*	
216	*	*	*	*	*	*	*	*	*	*	*	
217	☐	☐	*	*	*	*	*	*	*	*	*	*

* **Broken current** ○ **Continuous current**

Figure 54. Review of Test #7 stud history at the conclusion of the test

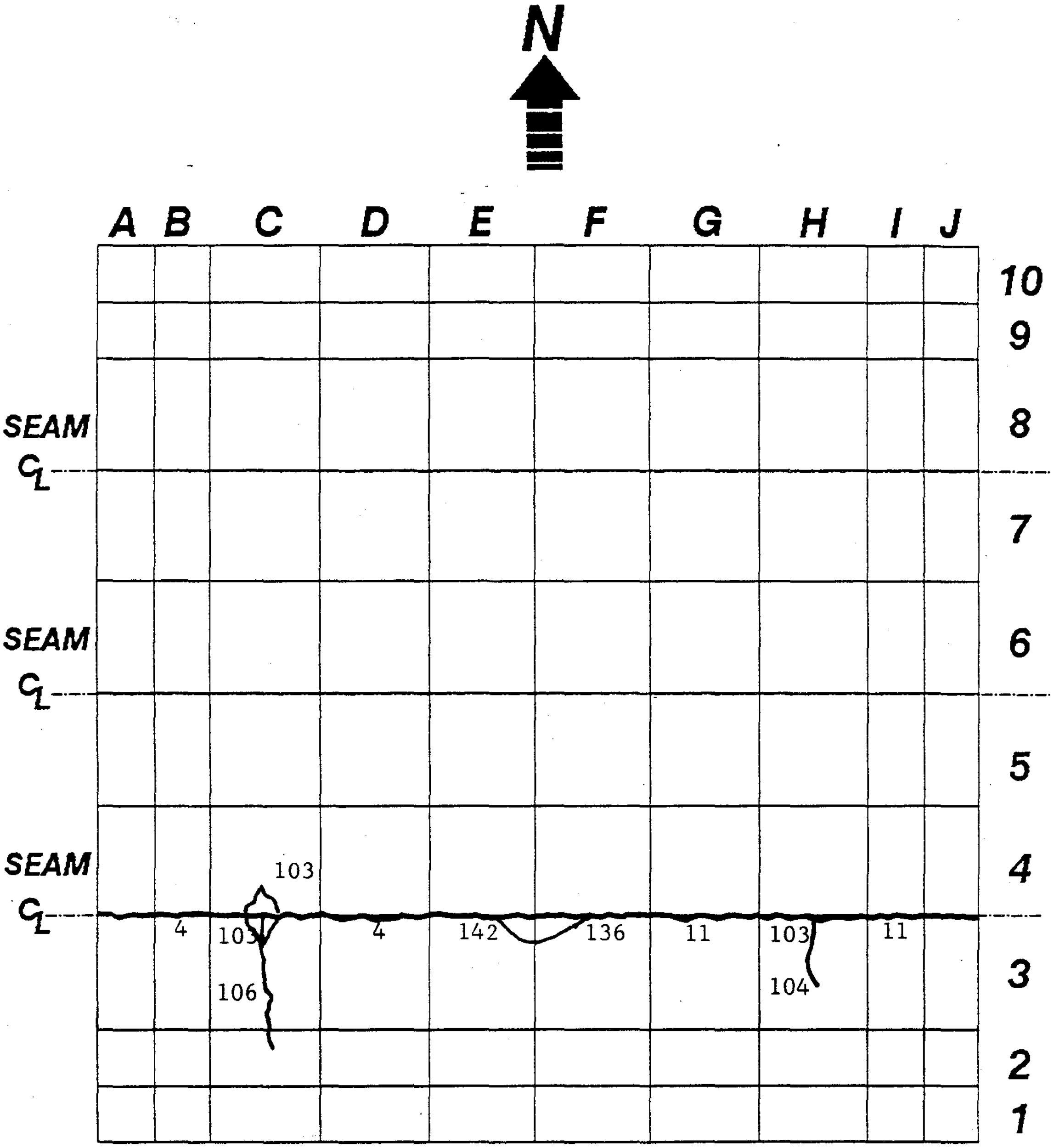

Notes:
Numbers by the cracks indicate the load point at which the crack was observed.

Figure 55. Crack pattern for Test #8

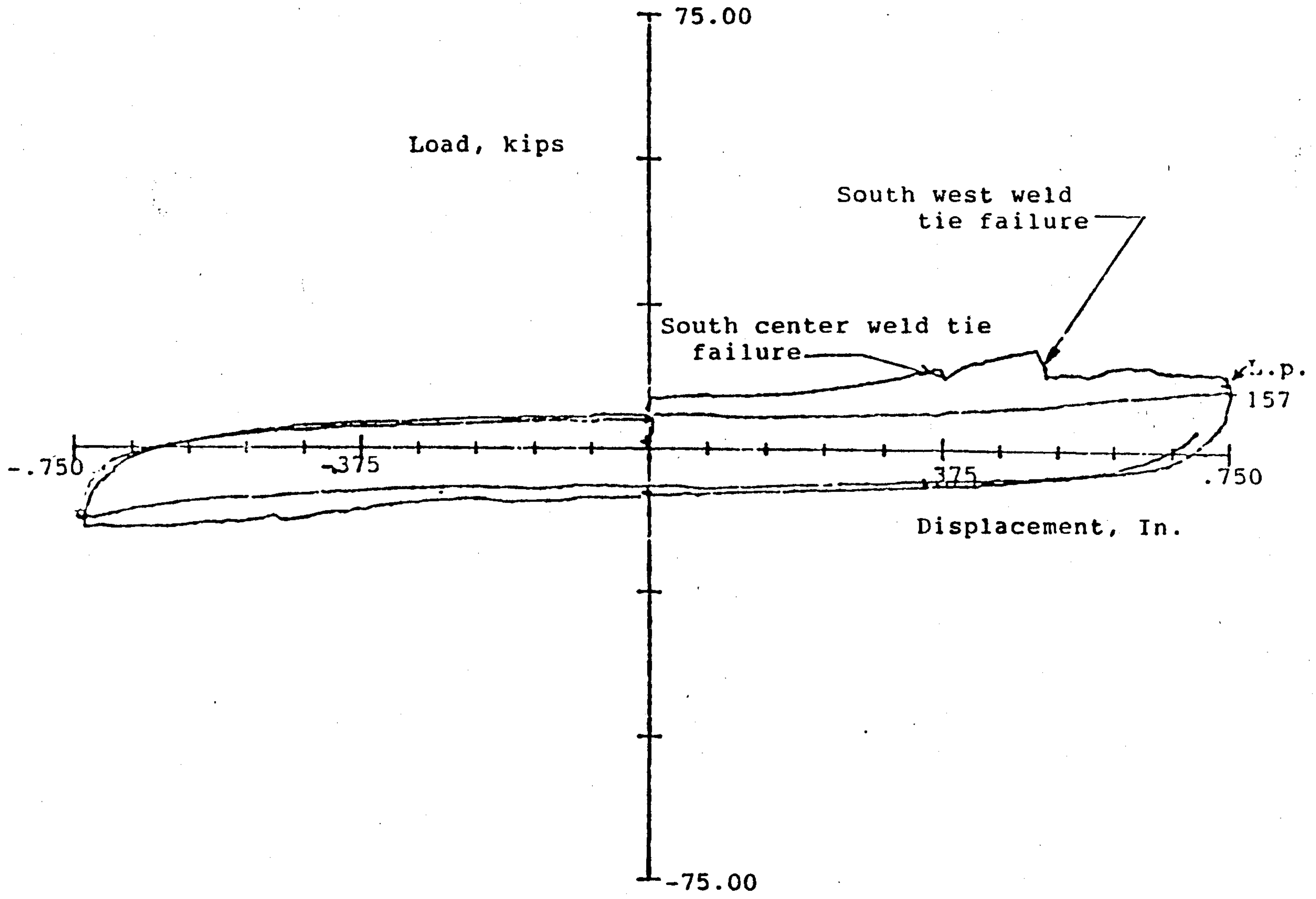

Figure 56. Hysteretic curve for Test #8

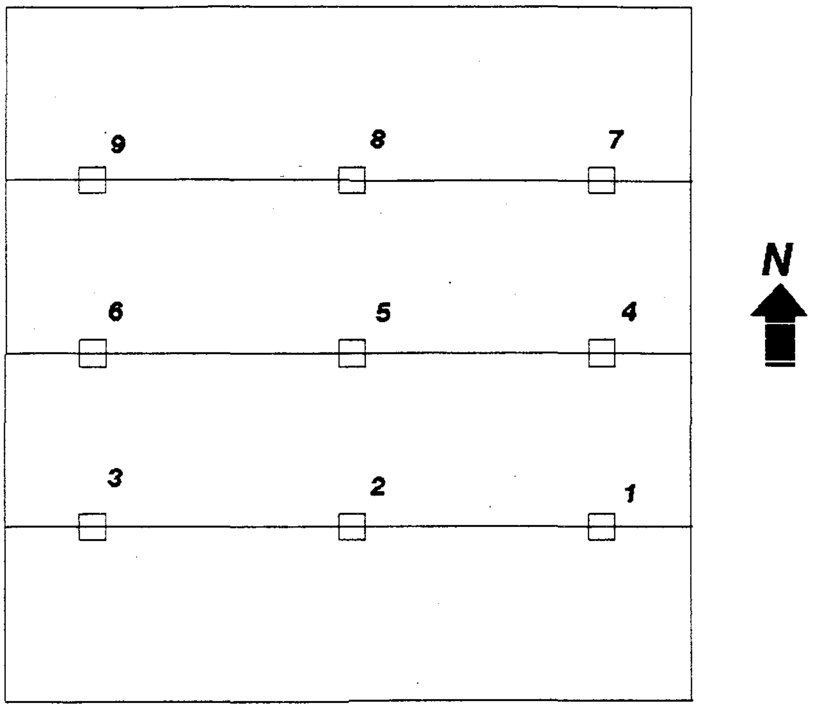

WELD TIE	CONDITION AFTER TEST
1	Horizontal bar popped out, vertical bar sheared
2	Horizontal bar popped out, vertical bar sheared
3	Horizontal bar popped out, vertical bar sheared
4	Intact
5	Intact
6	Intact
7	Intact
8	Intact
9	Intact

Figure 57. Final weld ties condition for Test #8

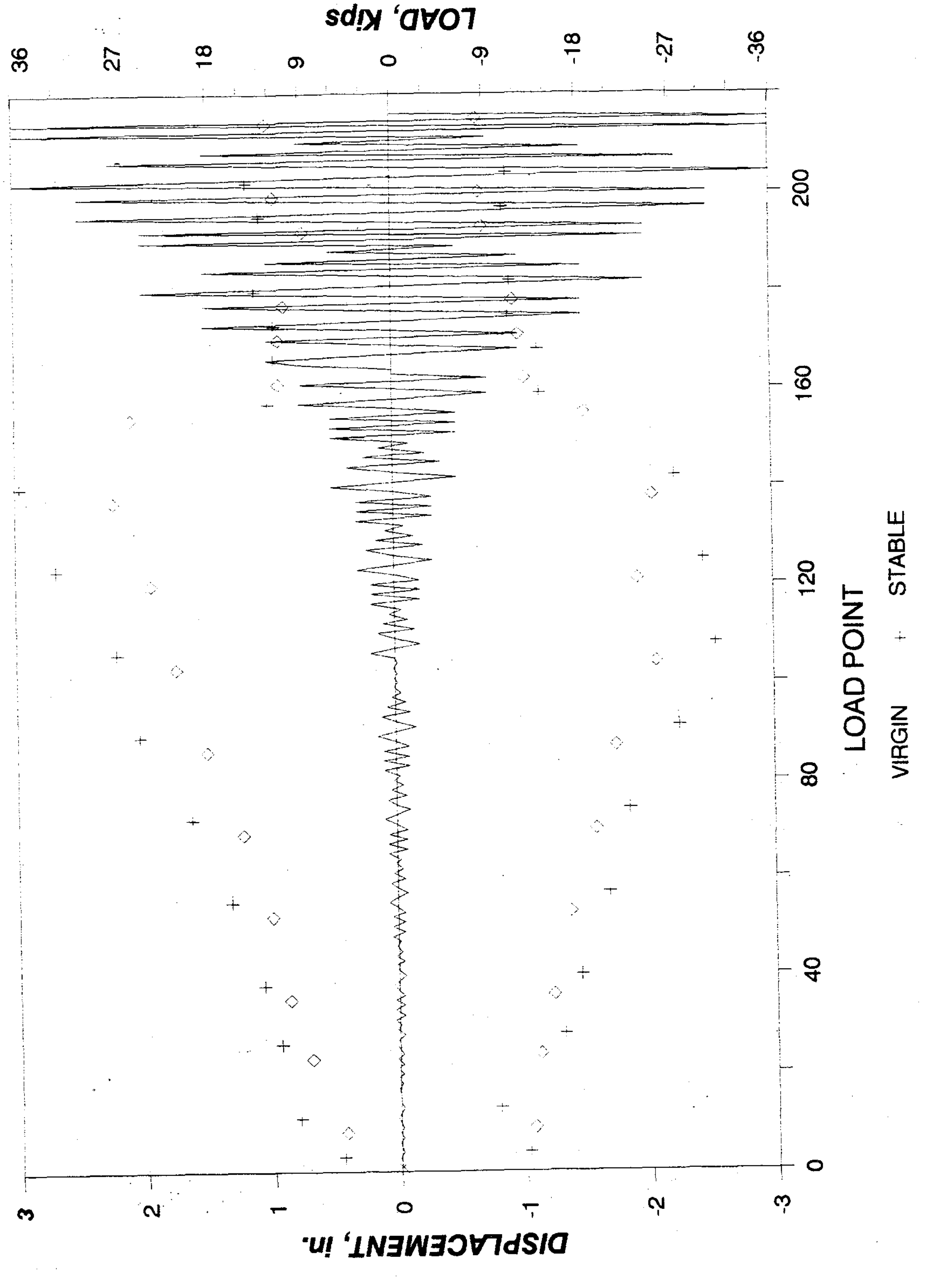

Figure 58. Force-displacement diagram for Test #8

out and the grout utilized in Test 8 was removed. Several methods were tried to roughen the planks' surface with little success. Welded wire fabric (6x6, 10/10) was used as temperature and shrinkage reinforcement for the 2 inch concrete topping. Weld ties were not incorporated into the seams, which was unique to the topped diaphragm tests. The lifting hooks were left in place and therefore contributed to the shear resistance between the topping and the planks.

A 4000 psi chip mix was cast on June 25, 1987 to form the topping. The seams were filled with this concrete as well. On the day of testing the compressive strength was 3636 psi. The planks fastened to the restrained end and loading beam edges were previously grouted into place prior to Test #8. Instrumentation used to monitor the deformed shape of the diaphragm system was attached. Also, dial gages were placed to register slip between the topping and planks. Finally, seam separation was checked in order to inform of a possible tension failure above the seams. (Test 8 had failed in this manner.)

Testing commenced on July 1, 1987. At l.p. 42, 0.074 inch east and 42.7 kips, the FME occurred with a four-foot tension crack along the west end of the seam. At the second loop to these particular increments, this crack extended to a total length of approximately ten feet. The maximum load was noted at 0.1 inch west, a load of 47.0 kips, and occurred prior to the failure of the south seam. The remaining portion of the south seam cracked during the first west stabilization cycle at the 0.1 inch increment.

Welded wire fabric across the south seam began failing in tension at the 0.15 inch increment loops. Bearing cracks were noted on the south plank at both the east and west ends at l.p. 127. This intersticial behavior continued propagating southward as testing progressed (see Figure 59). At l.p. 154 a localized failure materialized with the west end of the south plank cracking through the upper wythe to the mid-section. This failure was caused by bearing of the adjacent plank.

4.1.10 Diaphragm Test #9

The configuration of Test #9 was identical to that of Test #4 with the exception of plank depth. Test #4 consisted of 8-inch planks whereas Test #9 utilized 6-inch planks. Testing commenced on July 30, 1987. The FME occurred at a displacement of 0.15 inch west and a load of 78.0 kips with the west seam fracturing. The east seam cracked at a displacement of 0.3 inch east and a load of 75 kips (refer to Figure 60). Relative seam slip indicated that the failure mechanism was shear-bond as is shown in Figure 61.

During the stabilization cycles of the 0.5 inch increment, all three of weld ties in the east seam failed due to shearing of the weld on the connecting angle. Interstices in the vicinity of the south end on the east and west planks were documented during the 0.75 inch displacement increment. The cracks were located between the interface of the lower wythe and the cores.

During the 1-inch stabilization loops, the weld ties in the west seam failed due to shearing of the weld on the horizontal and vertical studs. Extensive cracking of the restrained end edge zone was noted (see documentation

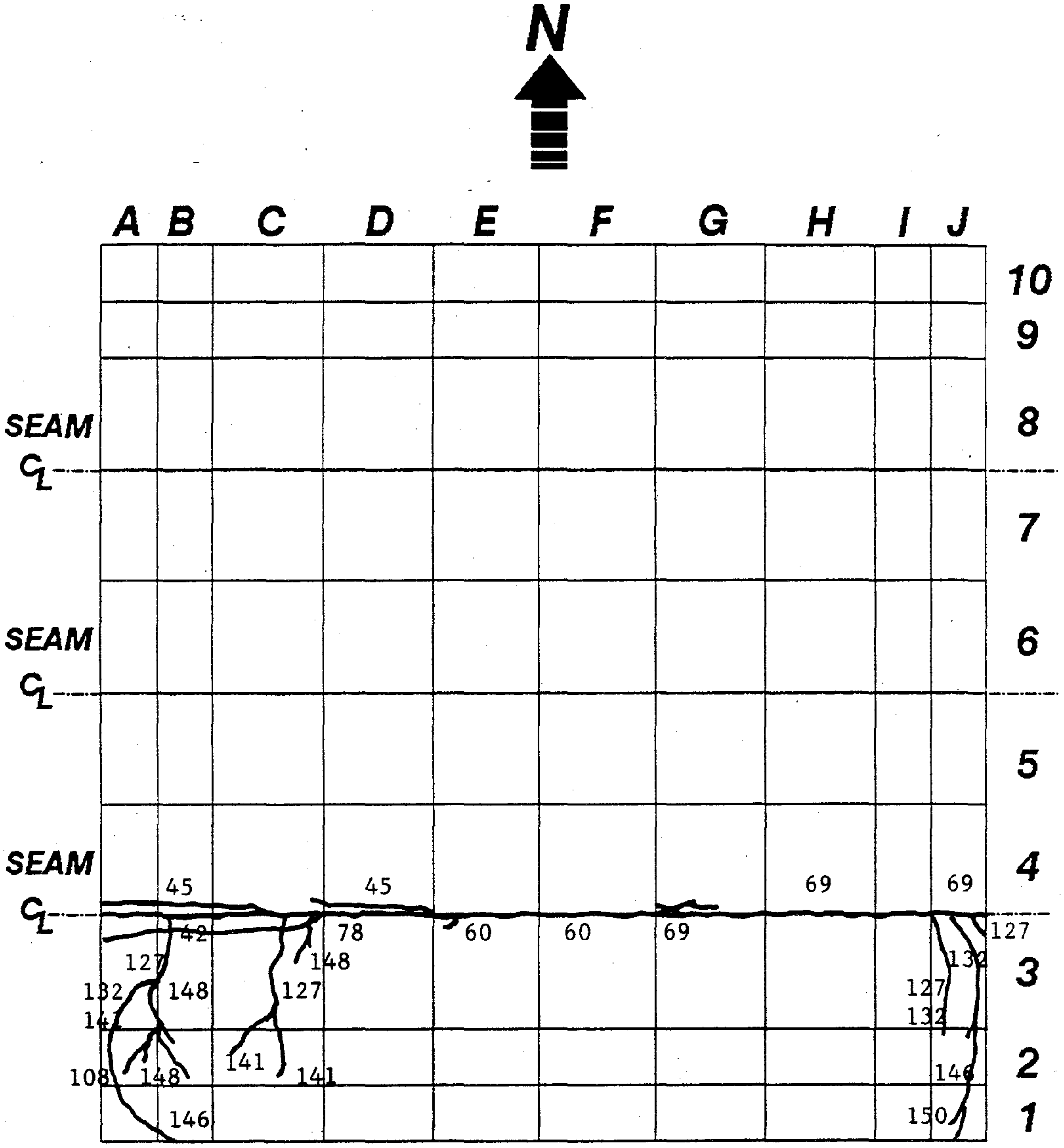

Notes:
Numbers by the cracks indicate the load point at which the crack was observed

Figure 59. Crack pattern for Test #8B

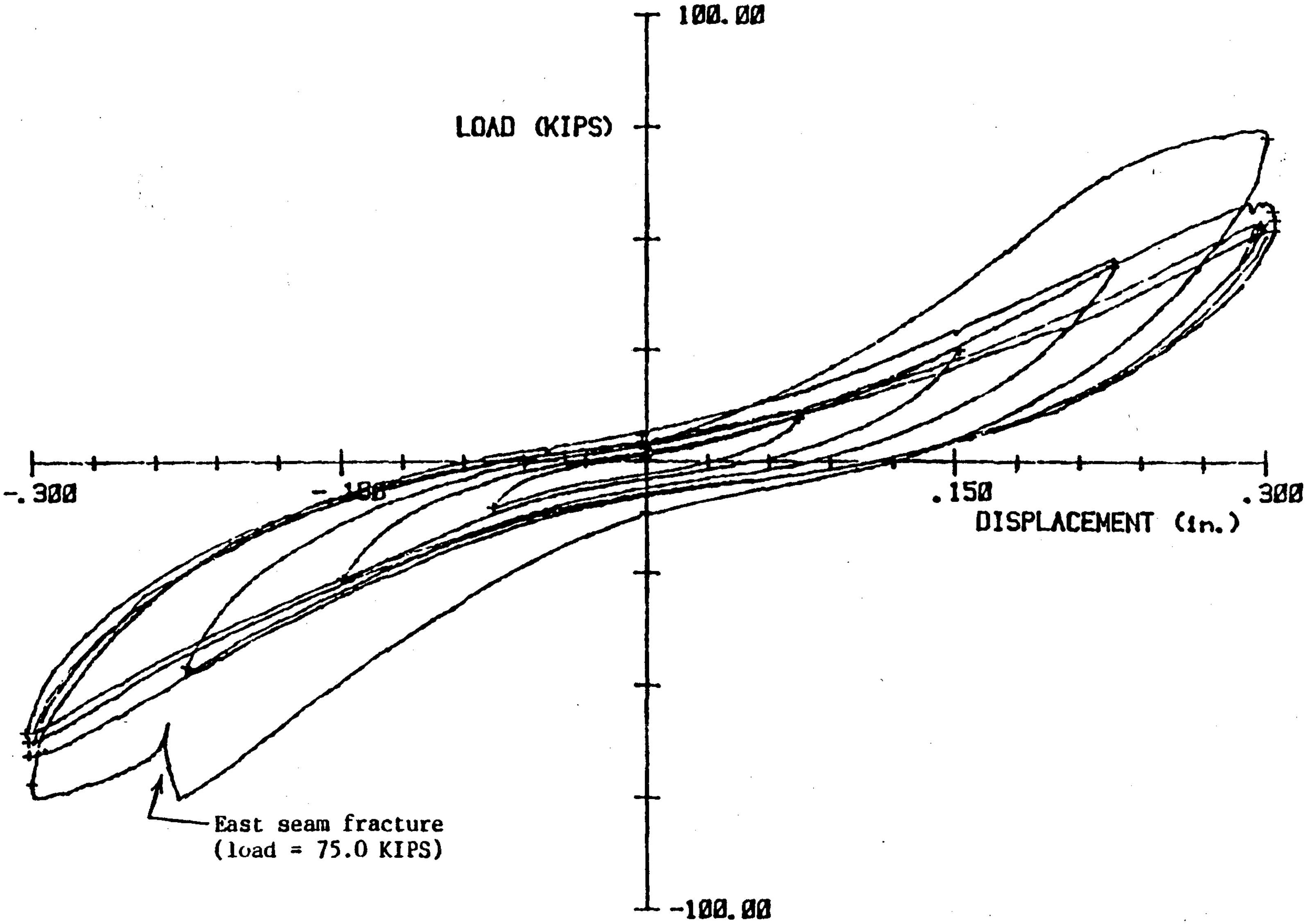

East seam fracture
(load = 75.0 KIPS)

Figure 60. Hysteresis loops from Test #9

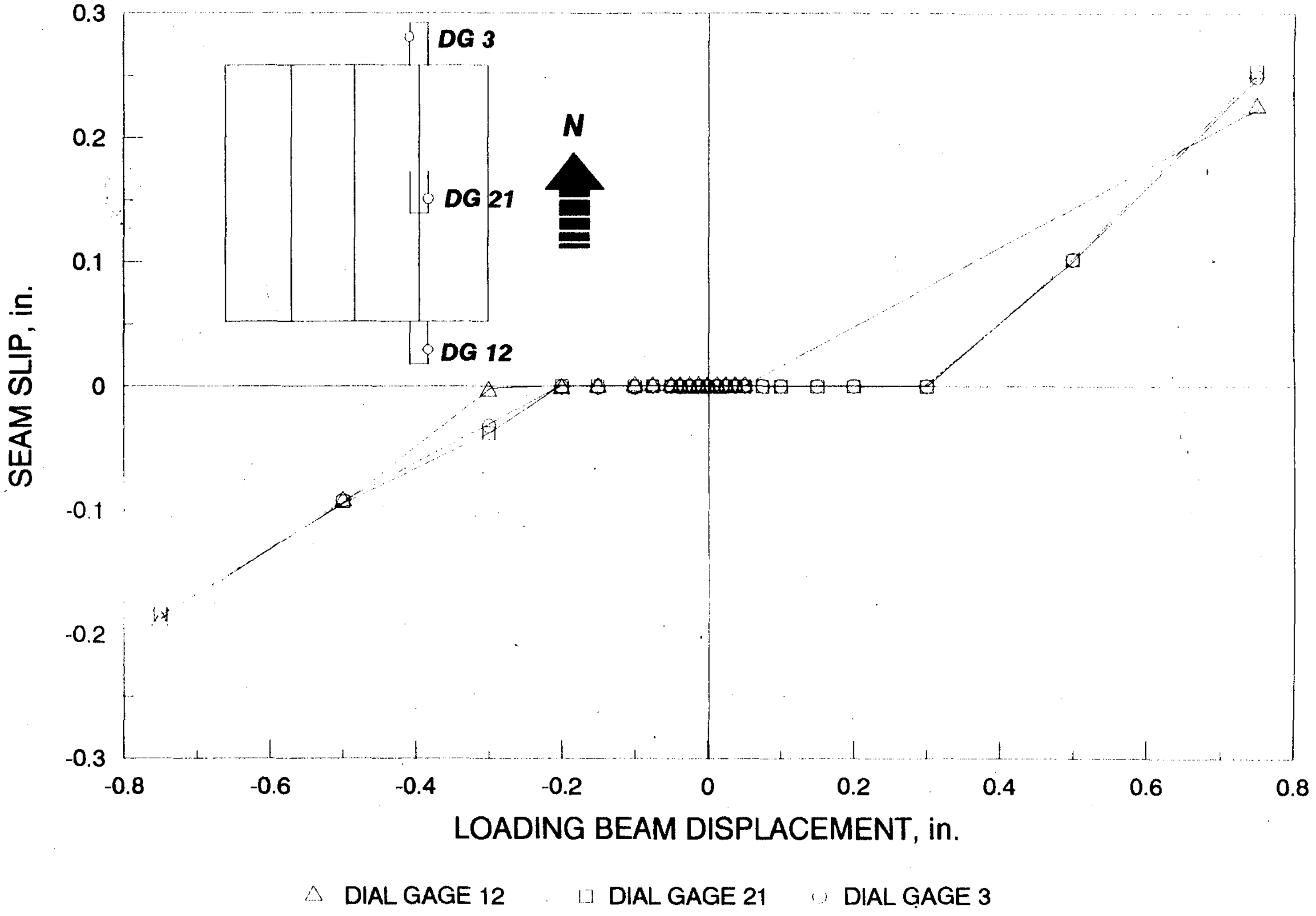

Figure 61. Relative east seam slip for Test #9

in Figure 62). During the 5-inch hysteresis loops the center seam fractured. Before the test completion, the remaining weld ties in this seam also sheared at the weld of the connecting angle. Figure 63 displays the displacement/load history for Test #9. A record of the final condition of the stud is shown in Figure 64.

4.1.11 Diaphragm Test #10

The floor slabs for Test #10 were oriented in a similar fashion to those of Test #6, with the four perimeter edges connected to the testing frame as well. Due to an error by the supplier, concrete with 3/4-inch diameter aggregate, was placed in the cores instead of the usual grout. This alteration was assumed not to affect the performance of the diaphragm significantly; however, increased difficulty was encountered when filling the perimeter cores. The key difference between Test #10 and #6 was the Span-Deck thicknesses, of six and eight inches, respectively.

A new technique for grouting the seams was developed for this particular test. In previous tests, the grout was wedged into the seams by hand and with the aid of 1/2-inch diameter rods. For this test, a narrow steel plate was attached to the end of a vibrator and was inserted into the seams during filling. Each seam was found to contain a larger percentage of grout than previous tests. This procedure was implemented in the remaining tests.

Testing was performed on September 10, 1987. The FME occurred with the first displacement to 0.0375 inch east (1.p. 30) with the south seam cracking about six feet. The load recorded for this event was 82.4 kips and is graphically depicted on the 0.05 inch set of hysteresis curves (refer to Figure 65). The remainder of the south seam cracked during the first stabilization loop of 0.0375 inch displacement west (1.p. 35) with a load of 80.8 kips. Instrumentation recorded both seam slip and split, although the readings indicated primarily slip. South seam slip and split for each of the stabilized points is documented in Figure 66. The magnitude of the load at the FME also suggested that the failure mode was shear-bond.

At 1.p. 66, the east side of the center seam cracked, extending to approximately three feet from the end to the weld tie (0.077 inch west, 103.9 kips). The north seam fractured at 1.p. 68 (0.08 inch east, 97.4 kips) with the crack extending from the west end to the weld tie at the east end. This seam crack continued across the rest of the seam at 1.p. 79. The remainder of the center seam cracked at 1.p. 88 (0.1 inch east, 70.0 kips). Similar data to that shown in Figure 66, from the center and north seams, indicated that both tension and shear contributed to the initial breakdown of the seams.

Cracks propagated from the weld ties, beginning at a displacement of 0.15 inch, and continued until failure of the weld ties. A sketch of the surface cracks and weld tie failures can be found in Figure 67. Once separated from the diaphragm unit, the planks pivoted individually, thereby creating bearing forces near the end of the planks. At 1.p. 188 major bearing cracks were noted in the exterior three feet at the west end of the planks. The load/displacement

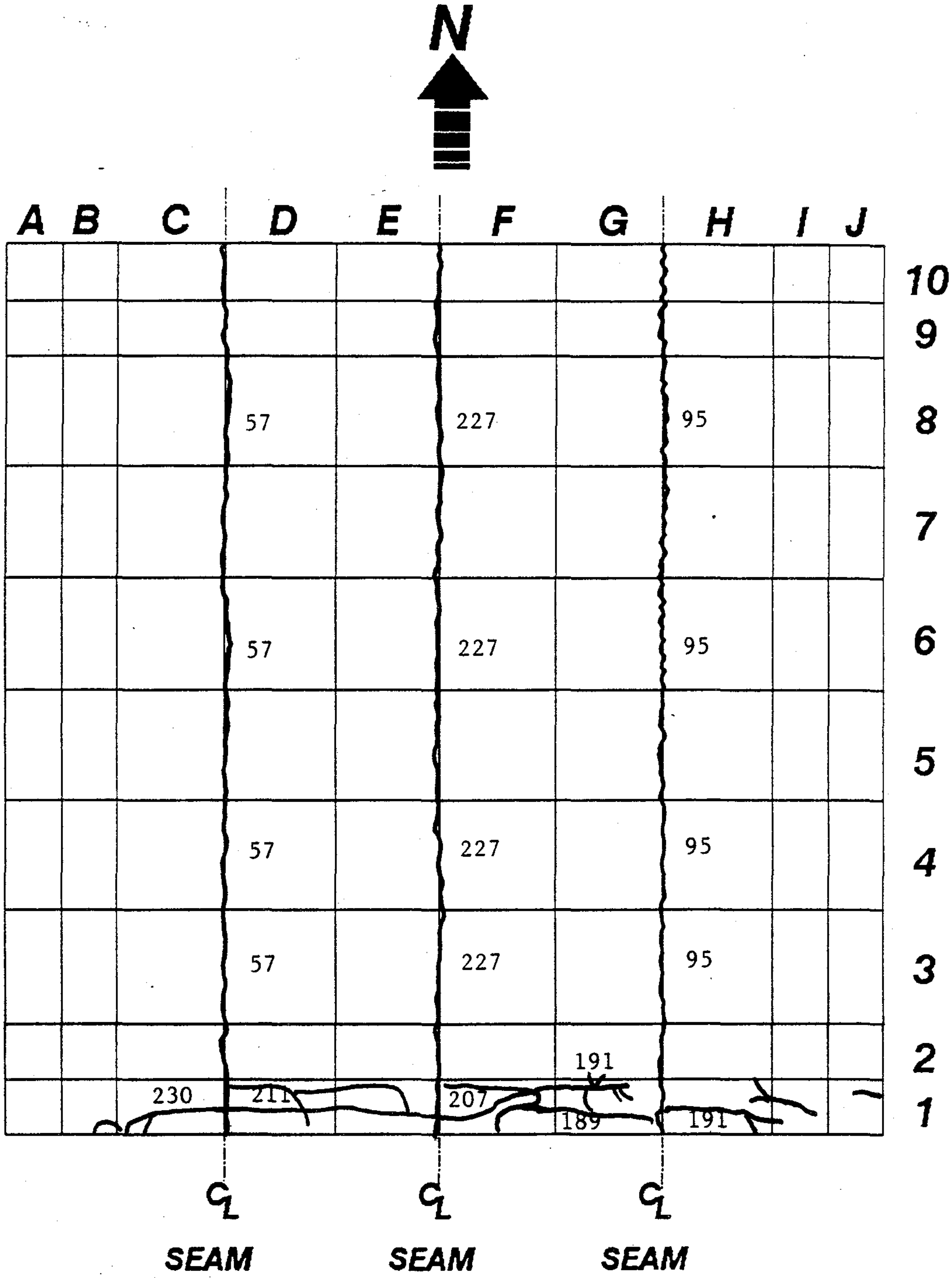

Notes:

Numbers by the cracks indicate the load point at which the crack was observed

Figure 62a. Surface crack pattern for Test #9

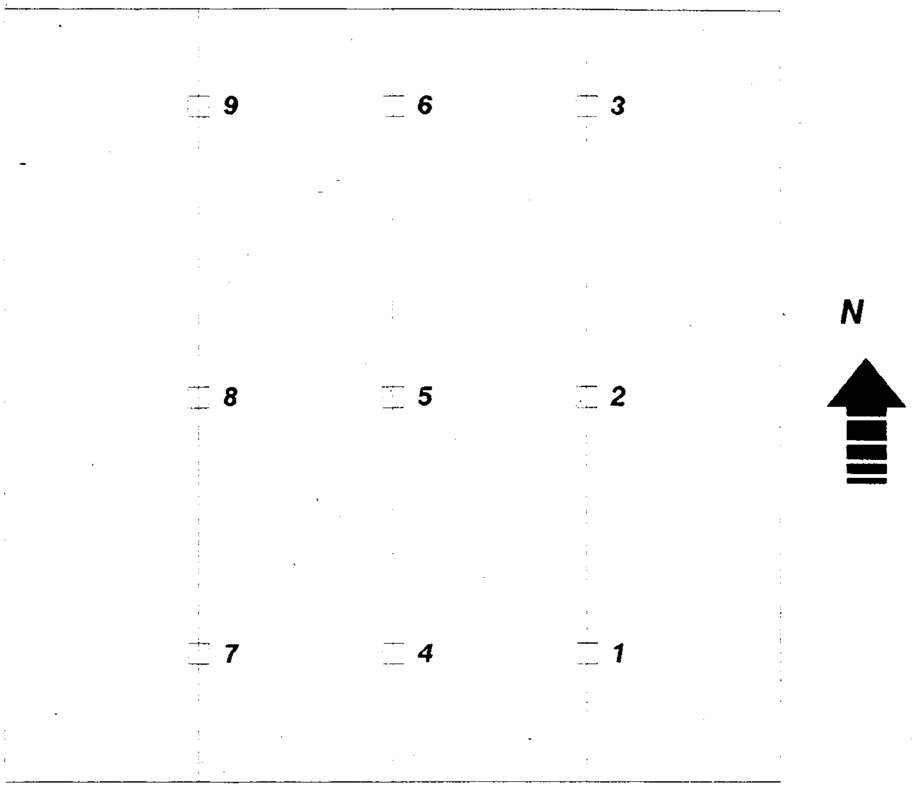

Weld Tie	Load Point	Failure Mode
1	134	Fracture of connecting angle weld
2	124	Fracture of connecting angle weld
3	126	Fracture of connecting angle weld
4	229	Fracture of connecting angle weld
5	231	Fracture of connecting angle weld
6	232	Fracture of connecting angle weld
7	169	Weld on vertical or horizontal stud exposed
8	180	Weld on vertical or horizontal stud exposed
9	180	Horizontal ~~stud~~ exposed

Figure 62b. Weld tie failure for Test #9

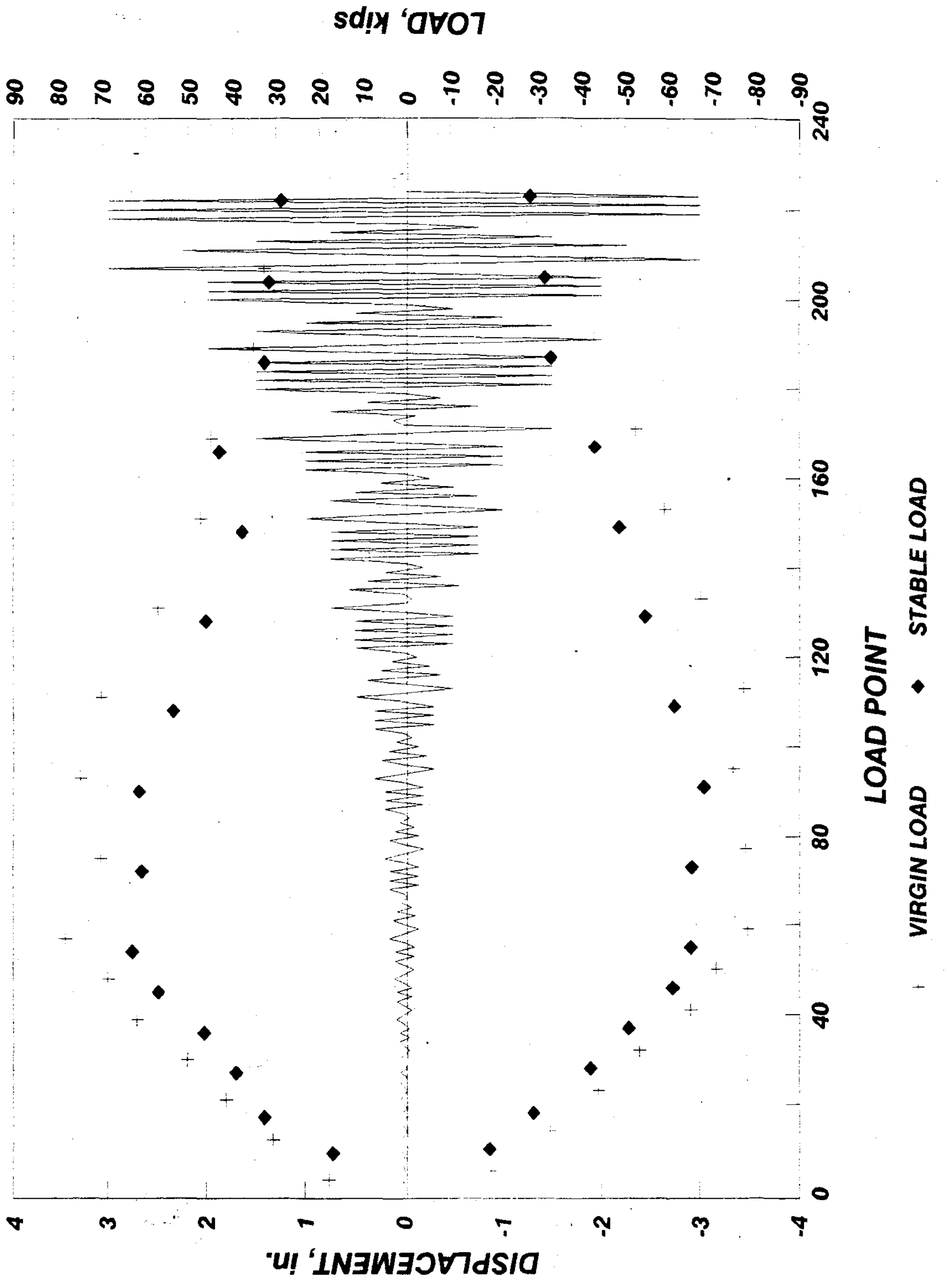

Figure 63. Displacement history and virgin/stabilized loads for Test #9

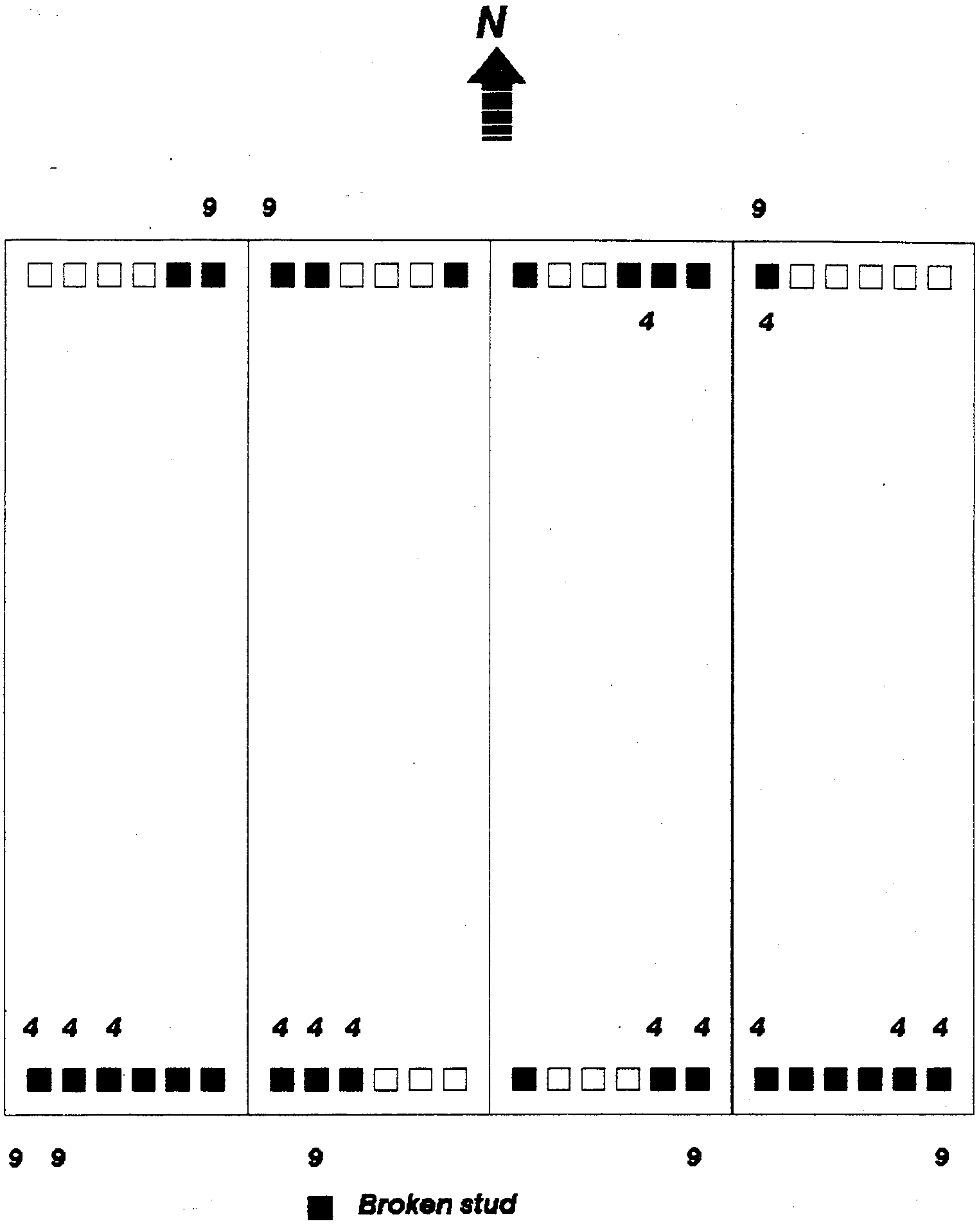

NOTE: The numbers "4" and "9" refer to test when these studs were known to be broken due to shear failure

Figure 64. Schematic of broken studs for Tests #4 and #9

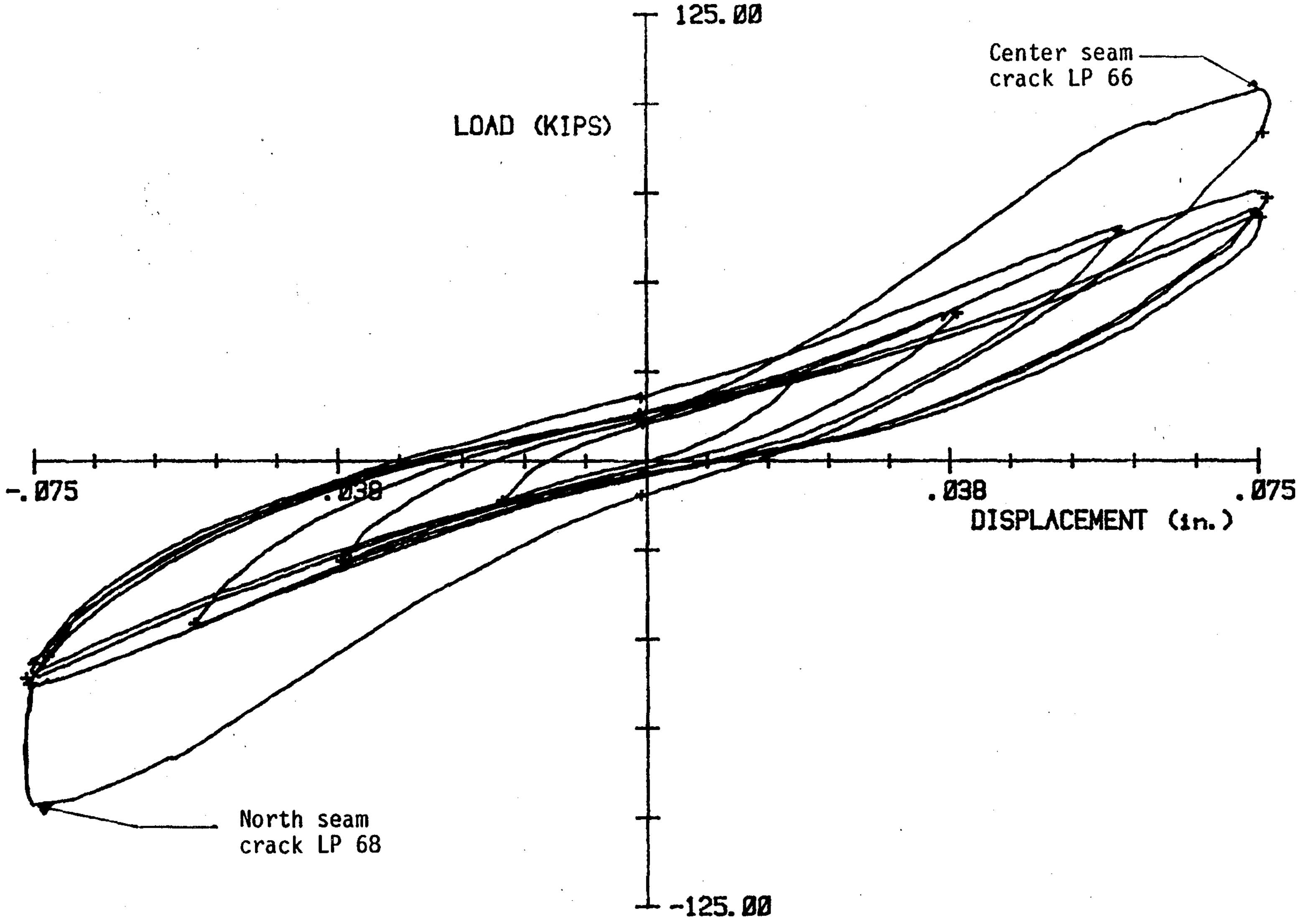

Figure 65. Hystersis loops from Test #10

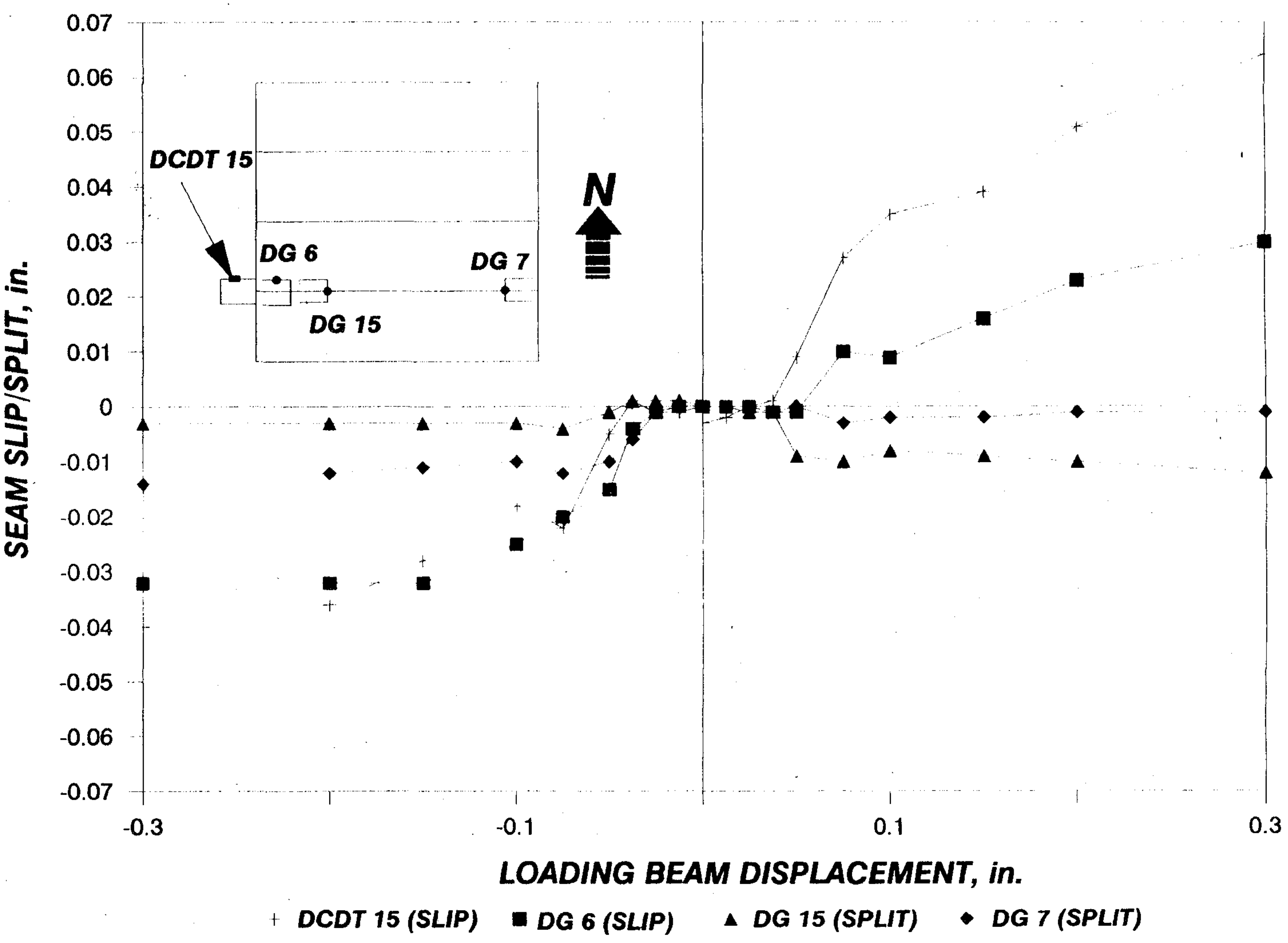

Figure 66. Relative seam slip and split of south seam for Test #10

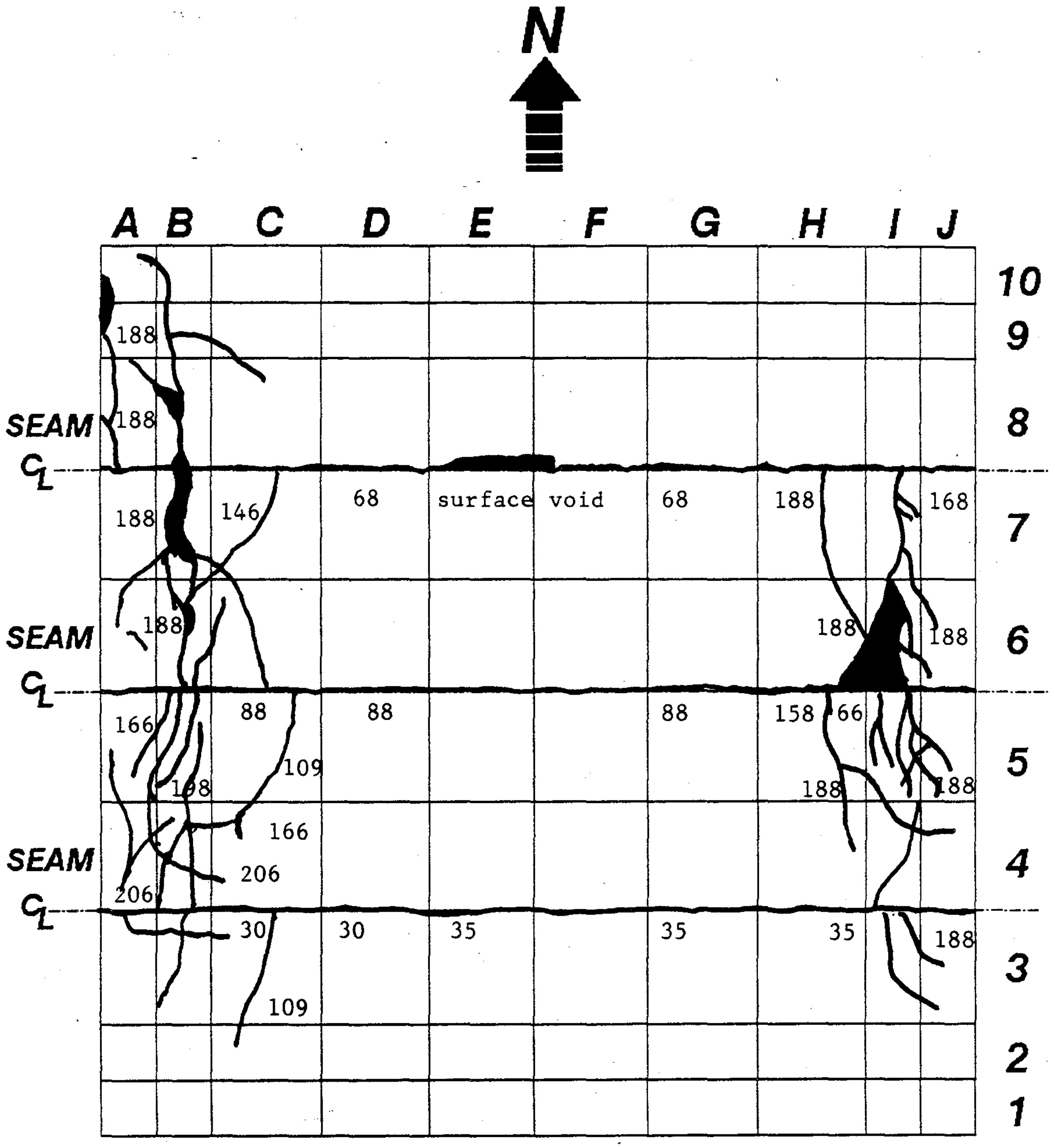

Notes:
Numbers by the cracks indicate the load point at which the crack was observed

Figure 67a. Surface crack pattern for Test #10

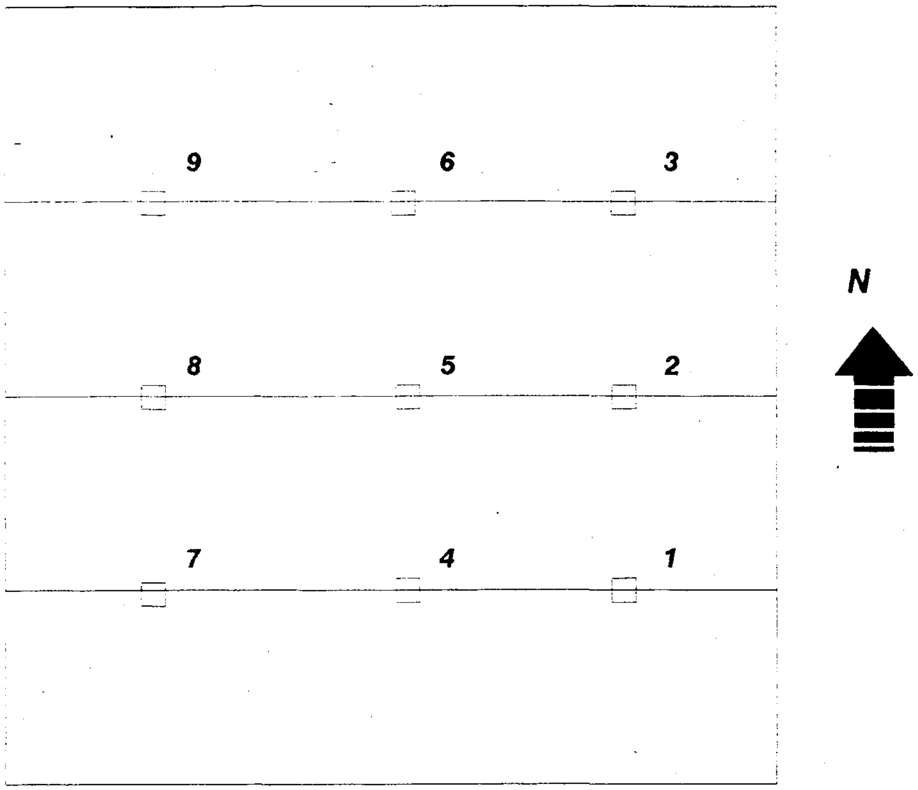

Weld Tie	Load Point	Failure Mode
1	O.K.	
2	224	Weld on vertical or horizontal stud exposed
3	188	Weld on vertical or horizontal stud exposed
4	O.K.	
5	167	Horizontal stud exposed
6	188	Fracture of connecting angle weld
7	O.K.	
8	224	Weld on vertical or horizontal stud exposed
9	166	Fracture of connecting angle weld

Figure 67b. Weld tie failure for Test #10

histories shown in Figure 68 and a schematic identifying broken studs for this test is shown in Figure 69.

4.1.12 Diaphragm Test #11

Test #11 was similar in arrangement to that of Test #4 and #9, with the exception of plank thickness (Test #11 utilized 12-inch thick planks). Testing was performed on November 21, 1987. At l.p. 83 the FME was identified as a diagonal tension crack across the diaphragm (see Figure 70 for crack pattern sketch). A load of 118 kips at 0.190 inch east was recorded. This crack was discontinuous in that the fracture projected on a new trajectory after crossing each seam. At l.p. 97 a similar diagonal crack was witnessed crossing the diaphragm from the northeast to the southwest corners.

The peak load coincided with the partial cracking of the west seam at l.p. 103. This occurred at 127 kips and a displacement of 0.3 inch east.. At l.p. 121 the entire west seam fractured, as did a three-foot section of the east seam. At the time of the fracture (0.405 inch west) the load dropped about 30 kips from 110 kips, but regained strength back to 99.1 kips at 0.506 inch displacement west (refer to Figure 71). During the stabilization loop of the 0.5-inch increment, the rest of the east seam cracked. Other diagonal cracks were noted on the surface as testing progressed. At l.p. 143 most of the center seam had cracked. Weld ties also began to fail at this time (see Figure 70).

Perhaps the most unique characteristic associated with this test was the rapid deterioration of the plank strength, due to the diagonal tension cracks propagating through the depth. Much of the concrete from the lower wythe had fallen to the floor at the later stages of testing. The loads at 2 inch displacement were roughly 10% of that of the peak load. For this reason Test #11 was terminated prematurely. Figure 72 shows the load/displacement program history.

4.1.13 Diaphragm Test #12

Test #12 was run on January 21, 1988. The FME occurred during the 0.3 inch west virgin displacement cycle of l.p. 93. This event was marked by several diagonal tension cracks extending across the northeast to southwest corners. A load of 127.5 kips was recorded for the FME (see Figure 73). Similar diagonal tension cracking oriented 90 degrees from the cracks associated with the FME were noted at l.p. 95. A load of 135.8 kips (ultimate strength) was achieved. Additional diagonal cracks were recorded during the subsequent increments as is depicted on the crack pattern sketch of Figure 74.

A localized failure due to the compression of the prestressing strands occurred during the displacement to 1.0 inch east (l.p. 172). This compression caused one strand to buckle and distort approximately 2 inch at the intersection of A2 and A3, which in turn caused minor concrete spalling at this location. Buckling may also have occurred in the other prestressing strands in the east plank causing a portion of the bottom wythe of the Span-Deck to fall to the floor during larger displacement increments. The load program is shown in Figure 75.

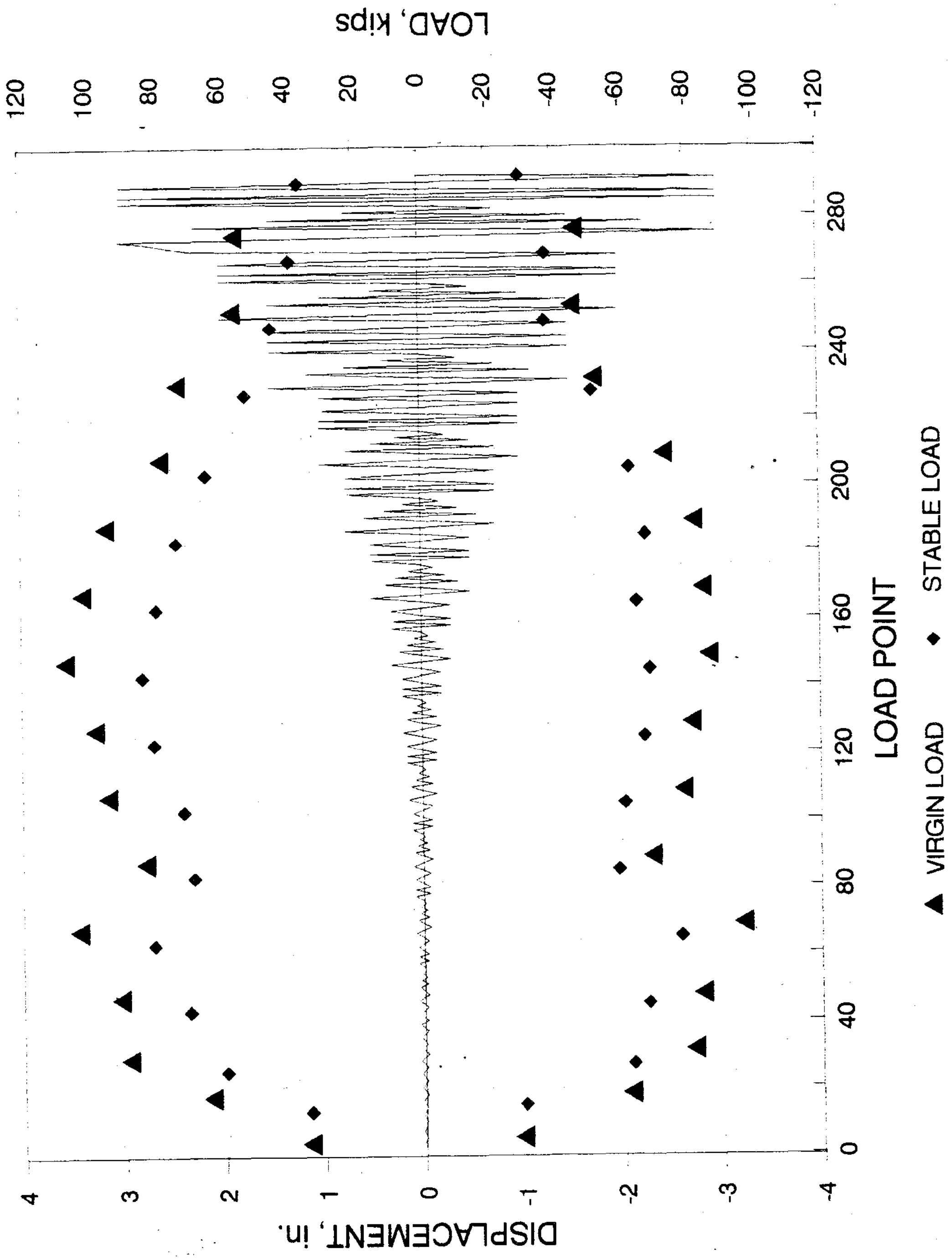

Figure 68. Displacement history and virgin/stabilized loads for Test #10

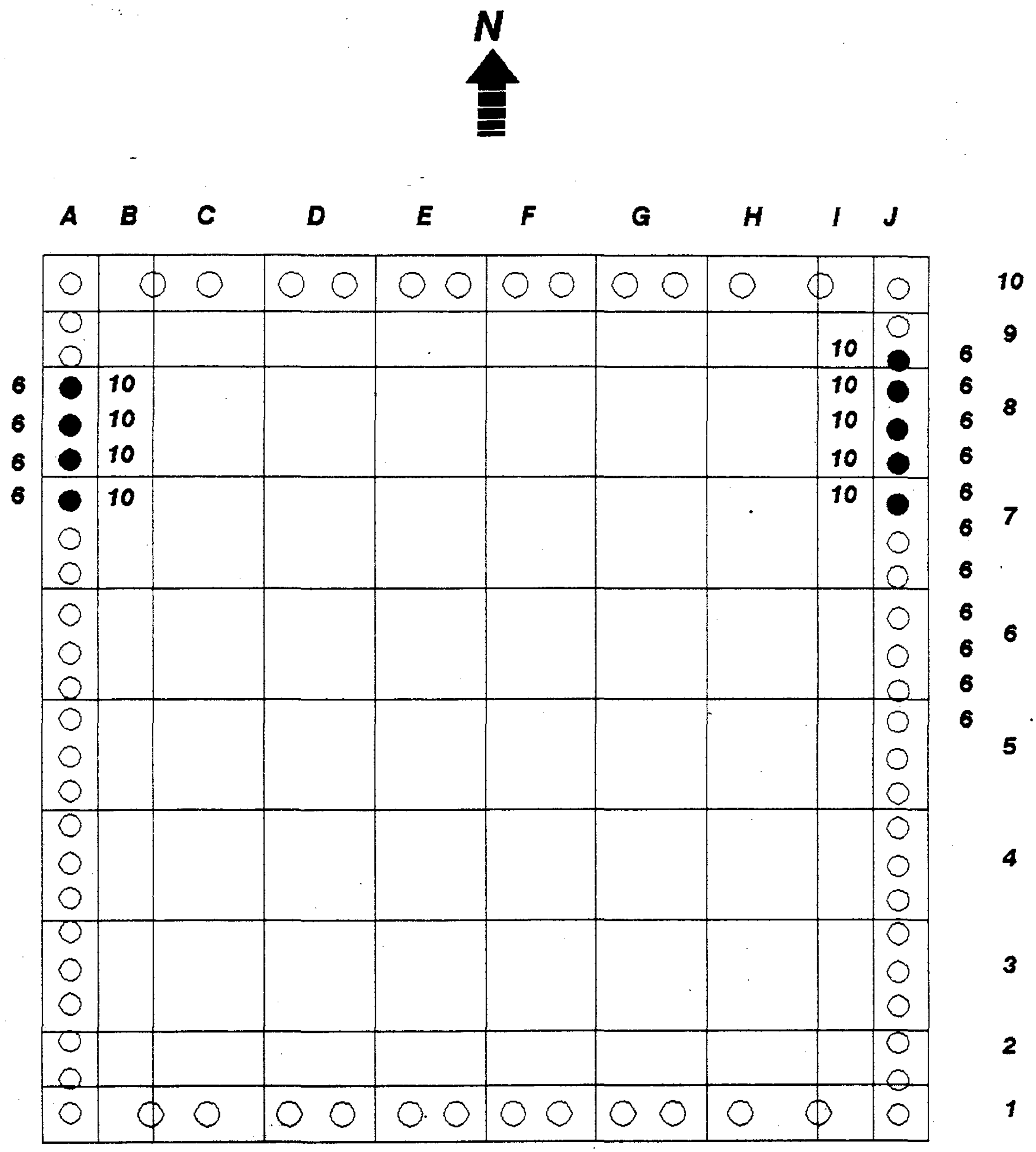

Note: The numbers "6" and "10" refer to the test when these studs were known to be broken due to shear failure

Figure 69. Schematic of broken studs for Tests #6 and #10

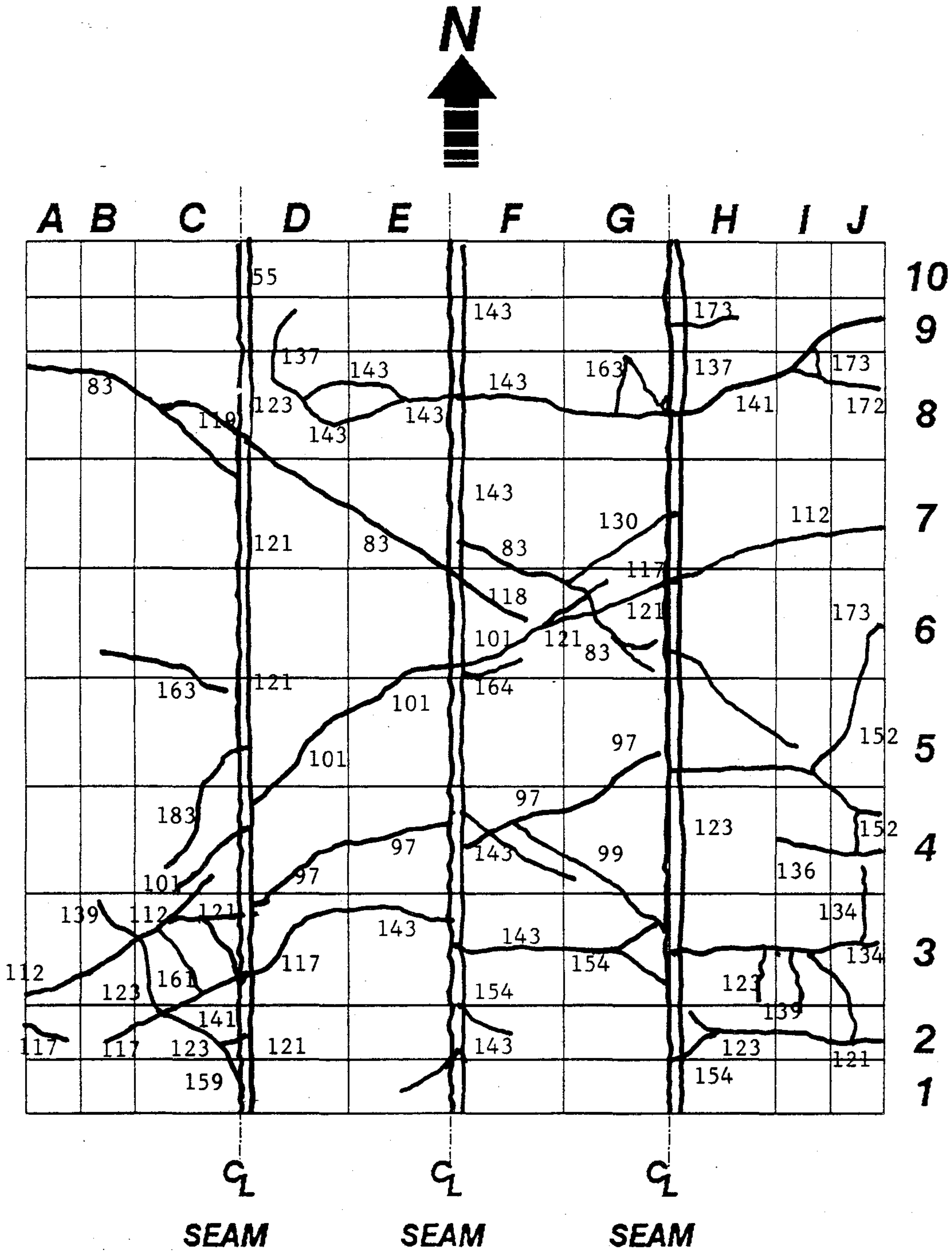

Notes:

Numbers by the cracks indicate the load point at which the crack was observed

Figure 70a. Surface crack pattern for Test #11

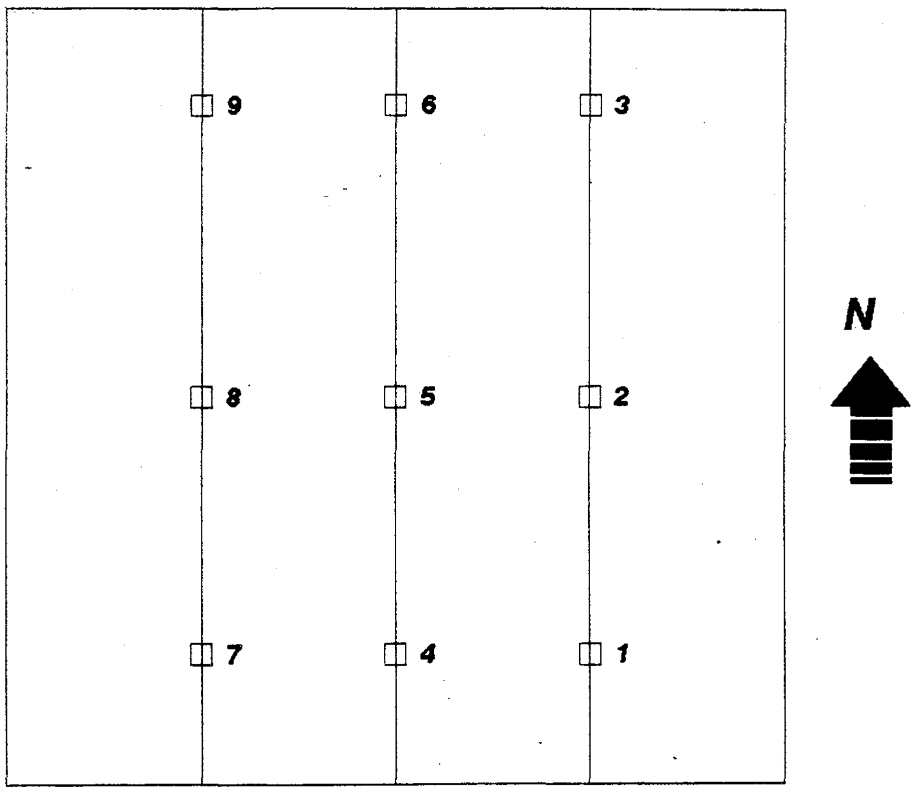

Weld Tie	Load Point	Failure Mode
1	154	Horizontal stud exposed
2	183	Horizontal stud exposed
3	183	Horizontal stud exposed
4	183	Horizontal stud exposed
5	185	Horizontal stud exposed
6	185	Horizontal stud exposed
7	183	Horizontal stud exposed
8	143	Horizontal stud exposed
9	163	Horizontal stud exposed

Figure 70b. Weld tie failure for Test #11

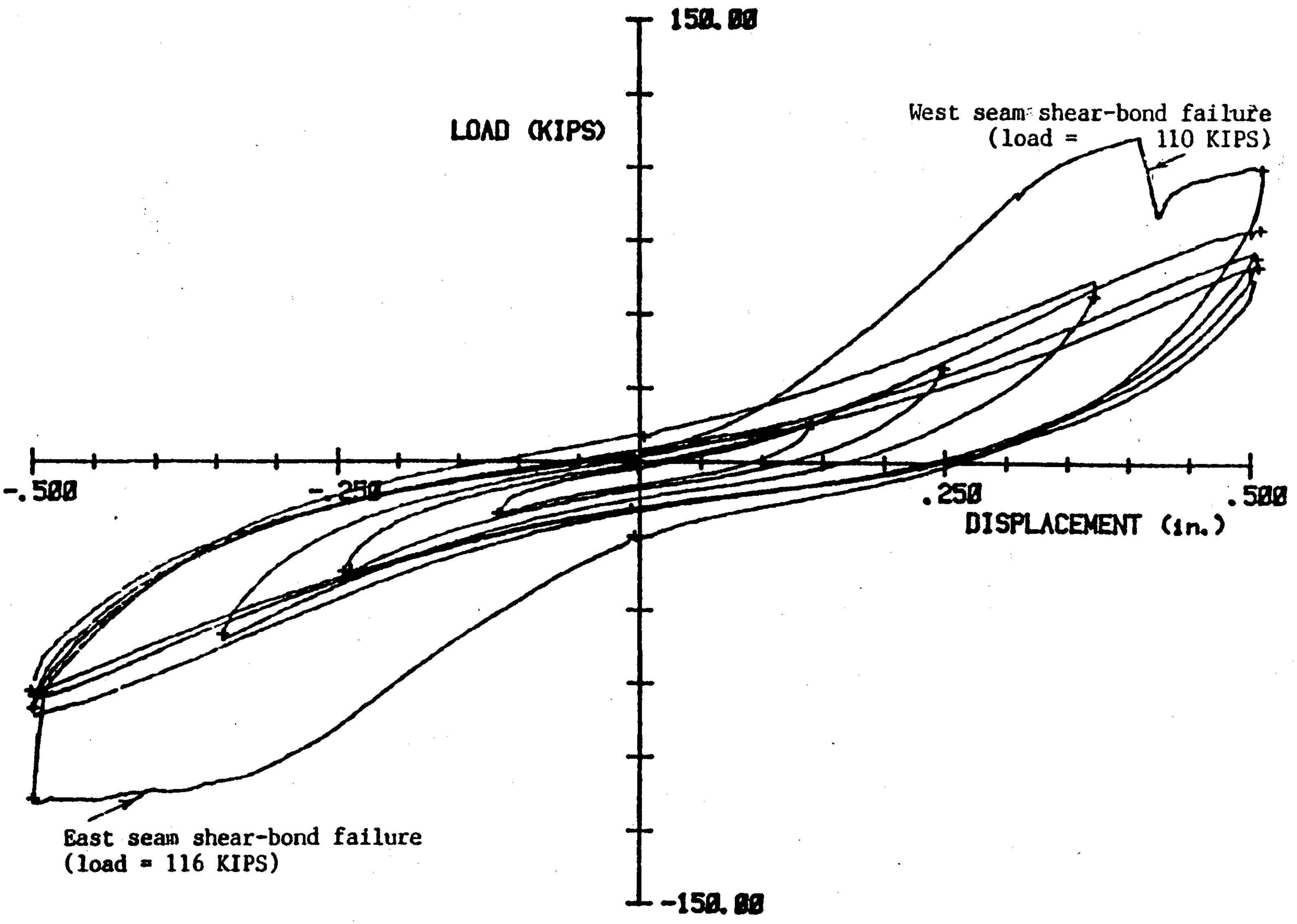

Figure 71. Hysteresis loops from Test #11

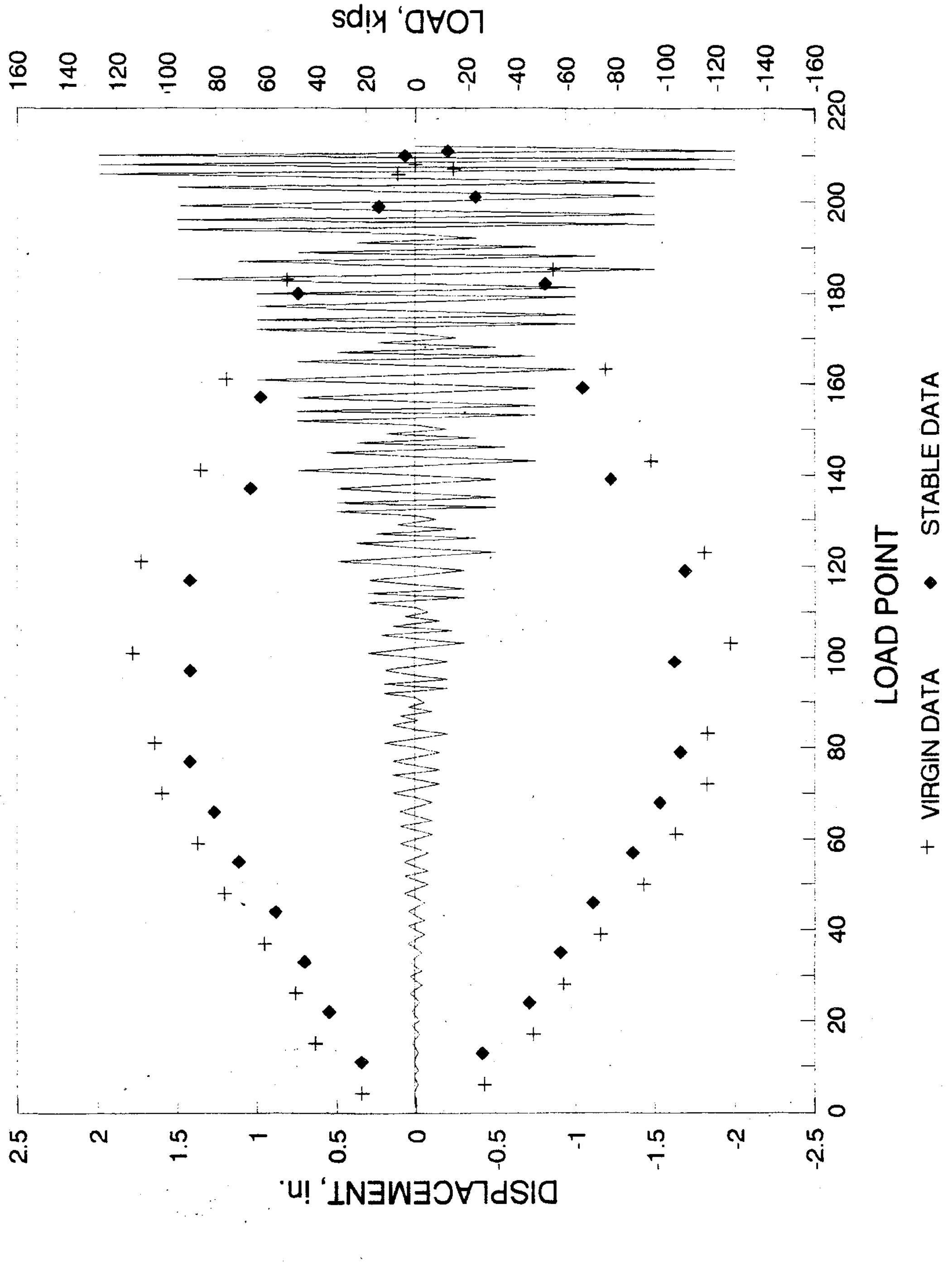

Figure 72. Displacement history and virgin/stabilized loads for Test #11

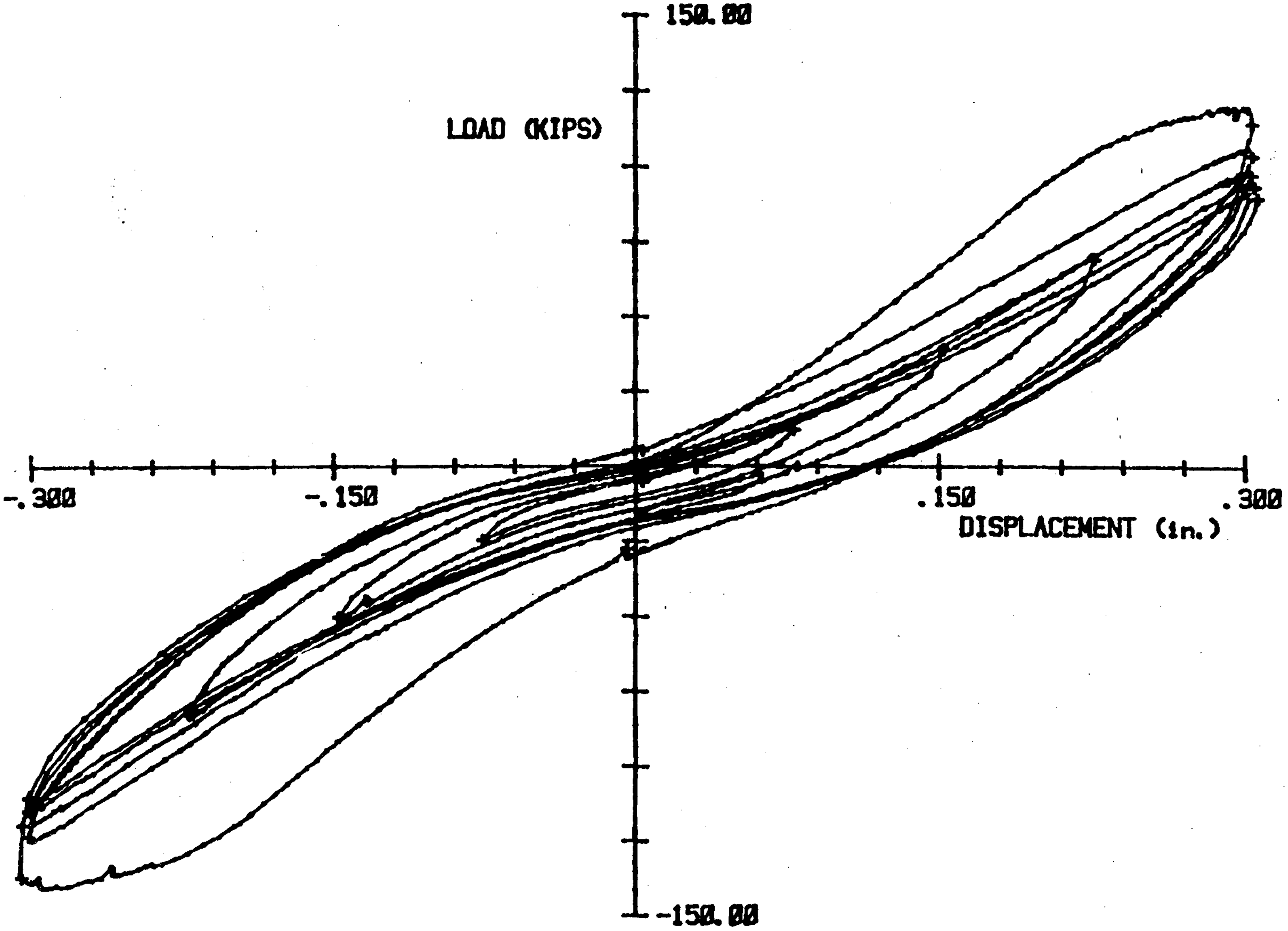

Figure 73. Hysteresis loops from Test #12

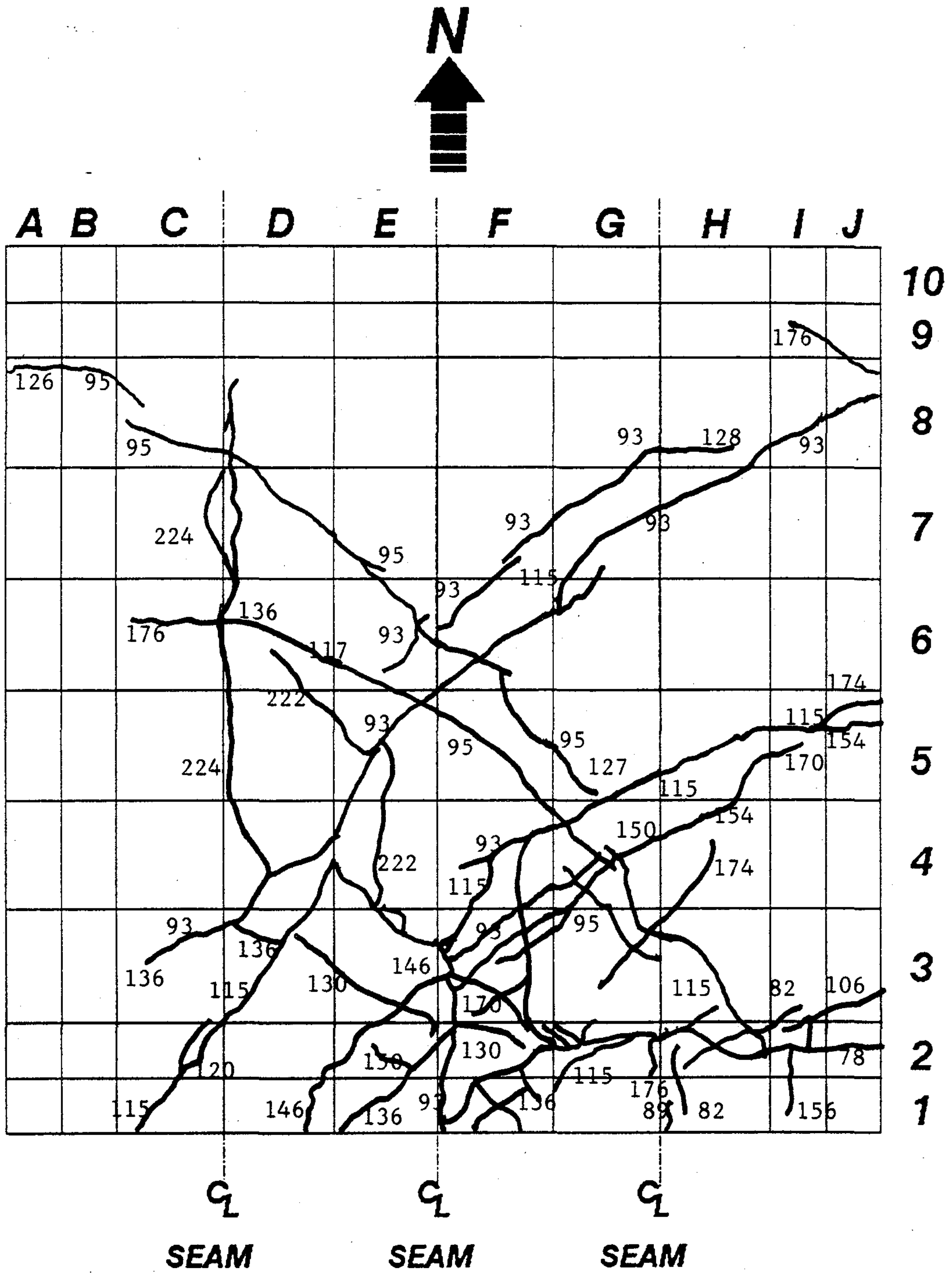

Notes:

Numbers by the cracks indicate the load point at which the crack was observed

Figure 74. Crack pattern for Test #12

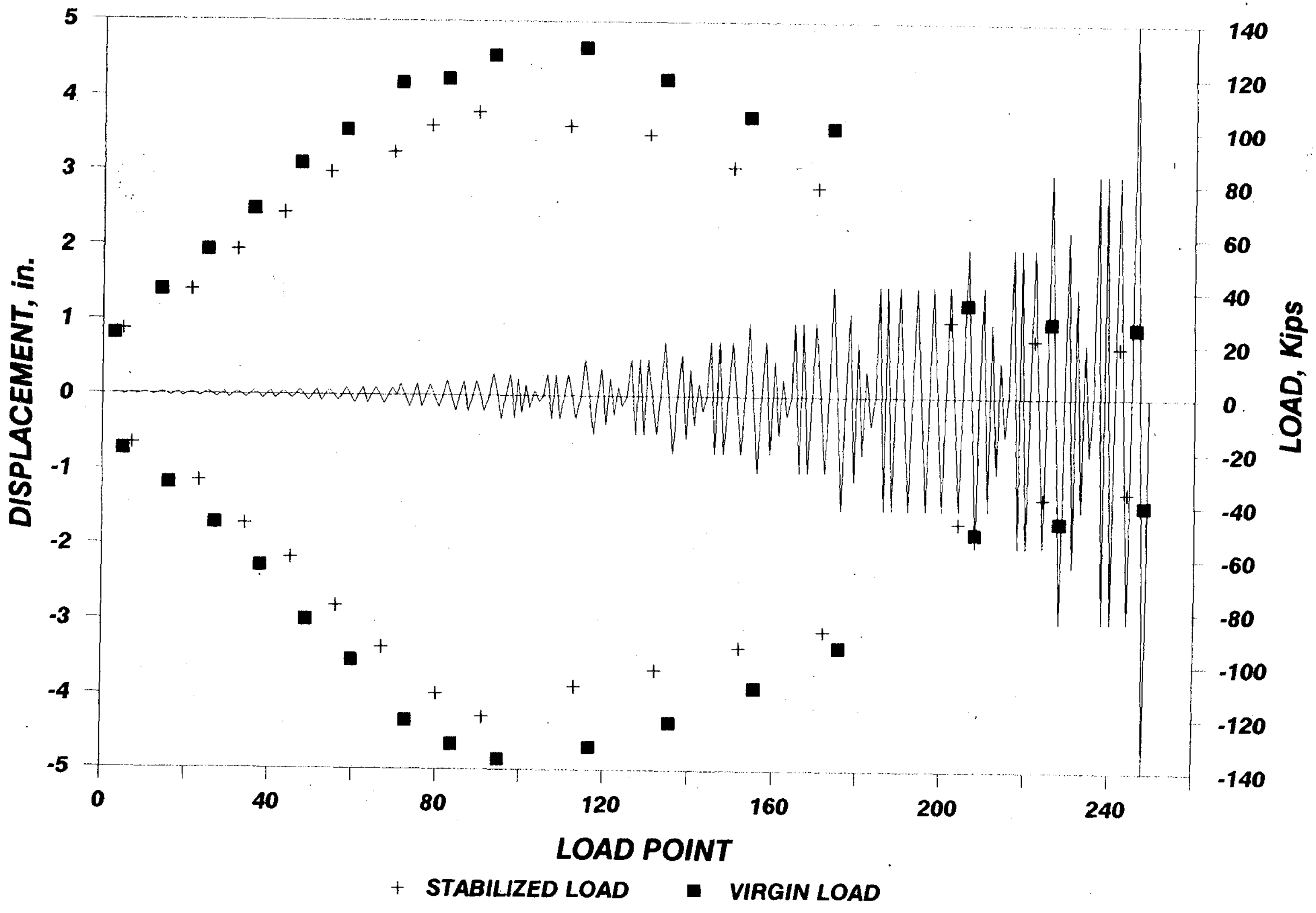

Figure 75. Load program for Test #12

Other localized cracking near the edge zone of the restrained end had occurred by l.p. 172. During the displacement to 1.5 inch east (l.p. 192, 61.2 kips) the edge zone of the southeast corner was noted to have been essentially separated from the rest of the diaphragm. Horizontal cracks were noted on the vertical profile of the longitudinally connected edges above the east and west edge beams. Cracks had completely traversed the east face of the diaphragm during l.p. 187 (1.5 inch west, 75.3 kips). Severe cracking continued along the intersection of the top and bottom wythes at the core region on the restrained end, especially during the 2 inch displacement cycles. At l.p. 224 (2 inch east, 37.2 kips) interstices were recorded above the west seam throughout sections G4 through G8. Testing continued through displacements of 5.0 inch, at which time the diaphragm had been thoroughly deteriorated. The maximum load for the final displacement of 5.0 inch east was 35.2 kips, which represented a considerable reduction in load capacity with respect to the ultimate strength.

4.1.14 Diaphragm Test #13

The 8-inch floor slabs for Test #13 were oriented with the seams perpendicular to the loading beam and were connected to the testing frame on all four perimeter edges (see Figure 18). The ends of the planks had three studs per void (i.e. nine per plank end), whereas the longitudinal edges incorporated only two studs per void. Grout was placed in the cores and a nominal 2 inch topping was cast on February 4, 1988. The compressive strengths of the grout and topping were 5109 and 4246 psi, respectively. The strength of the Span-Deck planks was assumed to be 8300, since actual data was not available.

Test #13 was executed on February 11, 1988. The FME occurred with a diagonal tension crack extending across the diaphragm from the northeast to the southwest corners (see crack pattern sketch in Figure 76). This event took place during the initial displacement to 0.15 inch west at a load of 230.4 kips (l.p. 69). During the virgin displacement to 0.15 inch east (l.p. 71, 217.2 kips as is shown in Figure 77), a second major diagonal crack occurred traversing the diaphragm from the southeast corner to the northwest corner. Diagonal cracking throughout the diaphragm continued with major cracks developing at l.p. 89, 111, and 129. Ultimate strength was recorded at l.p. 129 with 295.6 kips (0.5 inch west). At this time the crack which formed at l.p. 69 widened to about 0.25 inch.

Diagonal cracking and widening of existing interstices continued throughout testing. During the displacement to 0.75 inch west (l.p. 179, 221.5 kips), the concrete separated by the crack which occurred at l.p. 69, exhibited a 1 inch out- of-plane movement. The northwest corner displaced upward, while the southeast corner remained level relative to the floor. During the initial displacement to 0.75 inch east (l.p. 151, 193.0 kips) the crack which formed at l.p. 71 widened to approximately 0.75 inch, with the greatest separation occurring in the northwest corner. This crack widening accounts for the drop in strength during the 0.75 inch cyclic displacement, as is depicted on the virgin/stabilized load displacement diagram of Figure 78. Additional cracks were noted at this time in the northwest and southeast corners. At l.p. 169 (1.0 inch west, 116.2 kips) the diaphragm demonstrated considerable out-of-plane displacement, similar to that at l.p. 149. This buckling behavior was caused by

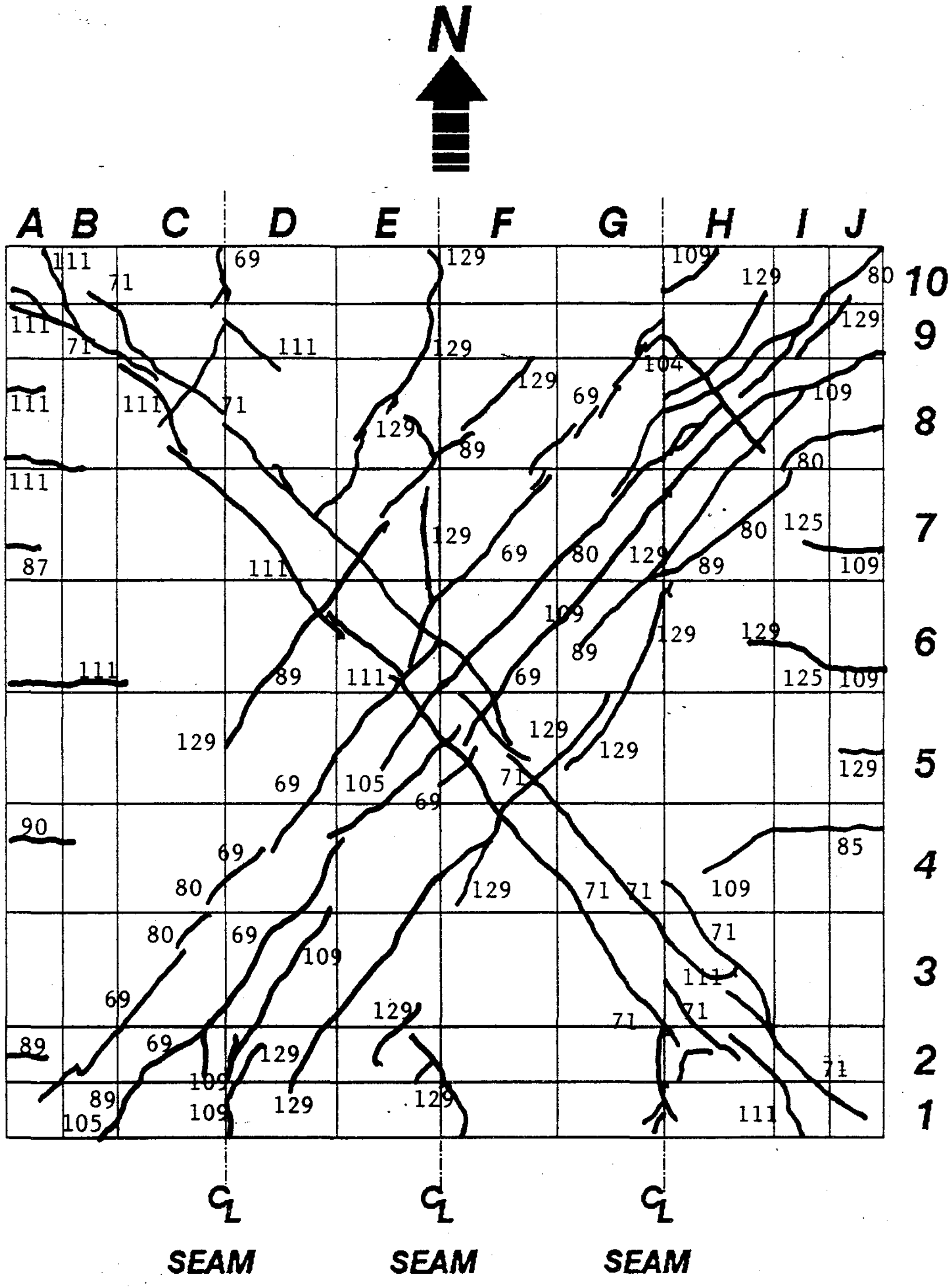

Notes:

Numbers by the cracks indicate the load point at which the crack was observed

Figure 76. Crack pattern for Teat #13

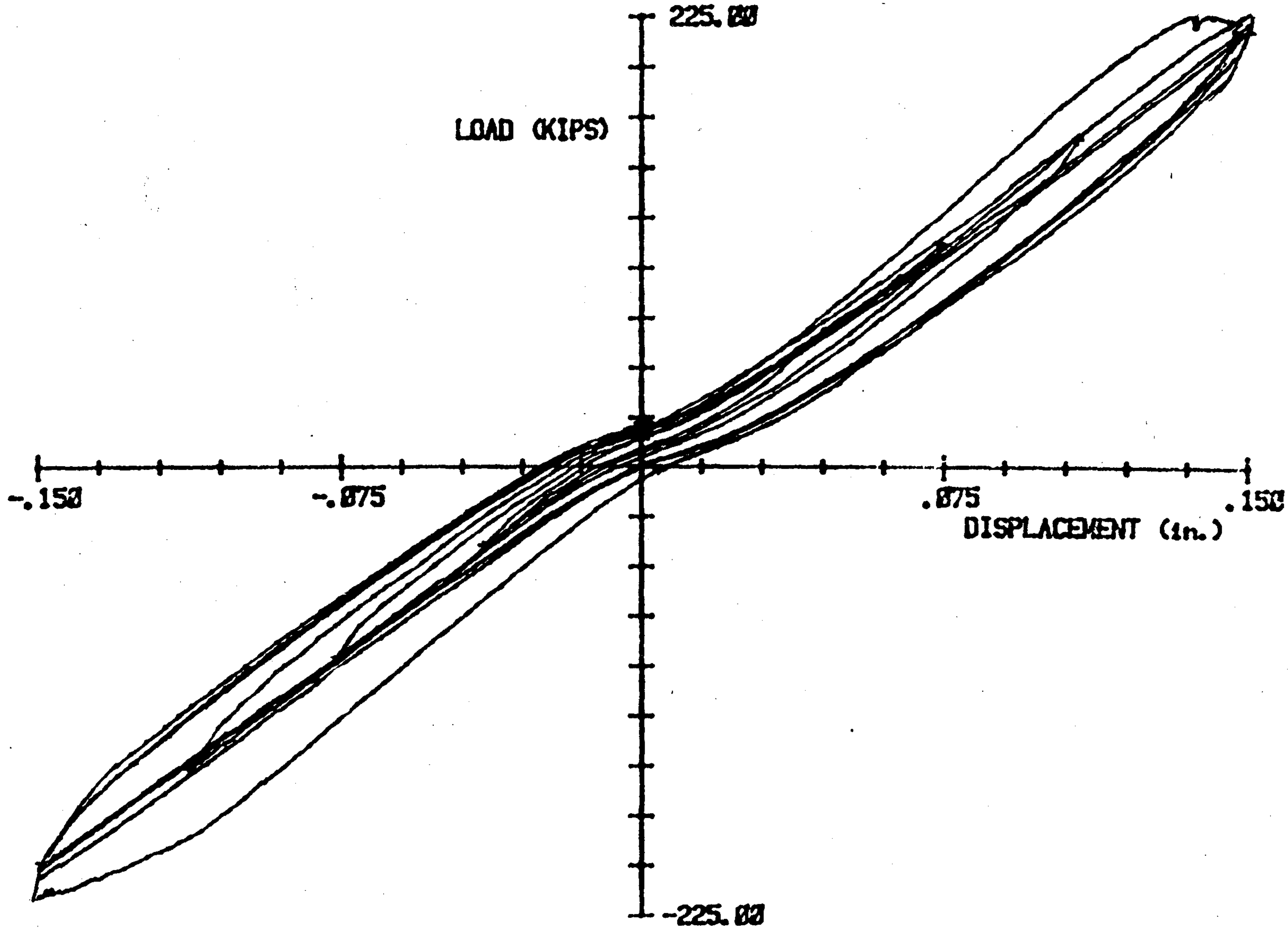

Figure 77. Hysteresis loops from Test #13

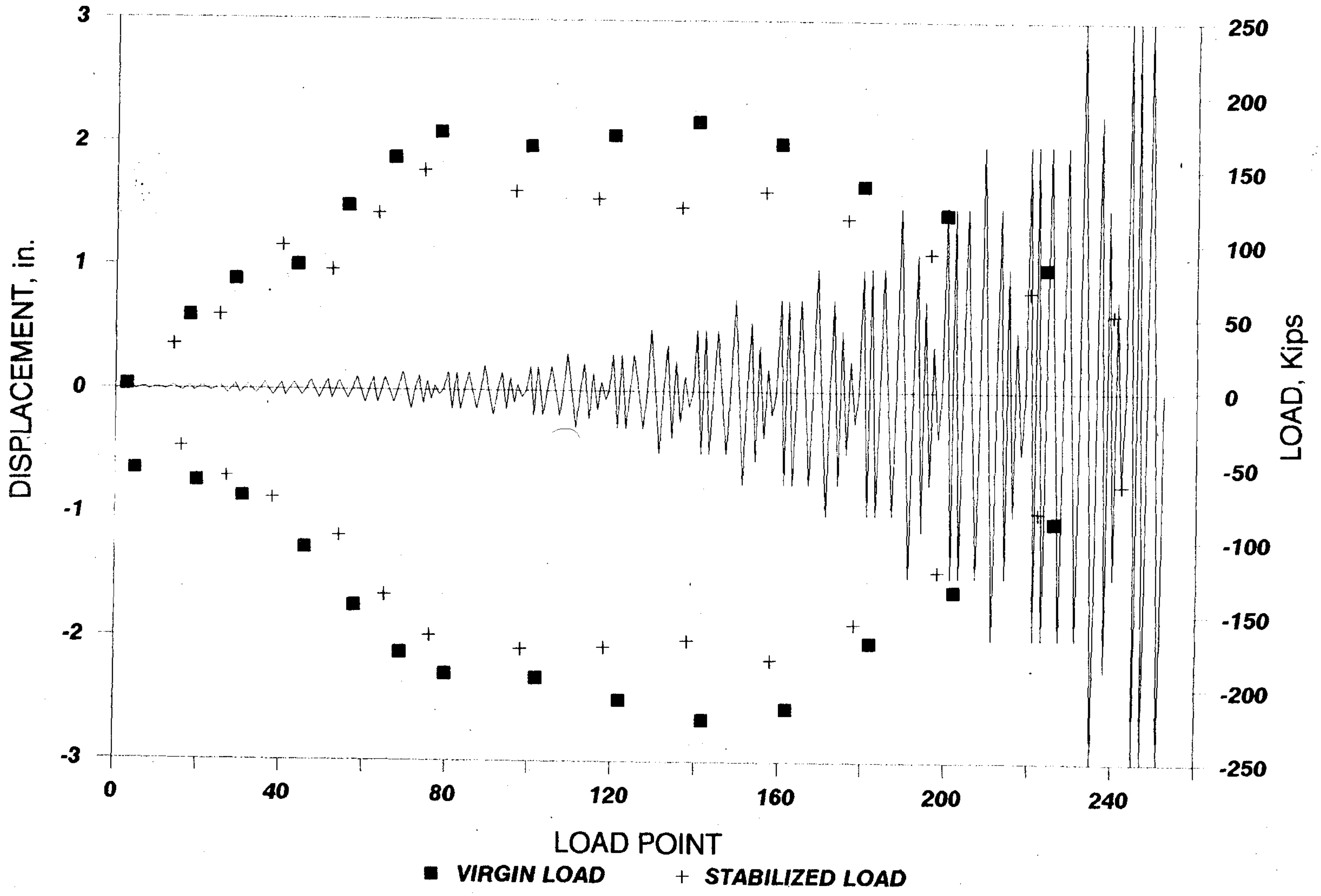

Figure 78. Load program for Test #13

the compressive forces in the diaphragm. During the displacements to the 1.0 inch increment, severe cracking had formed a crevasse in the center of the diaphragm. The bottom wythe of the planks was recorded to have fallen to the floor in some areas. Testing was continued through 3.0 inch cyclic displacements. Testing was terminated at this point because the diaphragm was only absorbing 8.6 kips during the final 3.0 inch displacement.

4.1.15 Diaphragm Test #14

The 8-inch Span-Deck floor slabs for Test #14 were oriented with the seams parallel to the loading beam. The four planks were connected to the testing frame on all four perimeter edges. The end of the planks had nine studs per plank end (i.e. three studs per void). Grout was placed in the cores on February 25, 1988, having a compressive strength of 6547 psi. A nominal 2 inch topping was cast on the planks having a compressive strength of 4895 psi. The strength of the Span-Deck planks was assumed to be 8300 psi since actual data was not available.

Test #14 was performed on March 4, 1988. During l.p. 48 and 50 several horizontal cracks propagated along the north and south seams at the edges. These cracks continued at l.p. 58, however, they did not result in a change in the stiffness properties. The FME was recorded at the initial displacement to 0.15 inch west (l.p. 70, 260.8 kips) with a diagonal tension crack extending across the northeast to southwest corners (see Figure 79). During the virgin displacement to 0.15 inch east (l.p. 72, 222.4 kips) a similar diagonal crack propagated in the opposite direction beginning in G2 and ending C6.

During the displacement to 0.2 inch west (l.p. 90, 192.0 kips) additional diagonal cracks formed from the exterior portions of the planks. Diaphragm cracking continued primarily in a diagonal fashion through displacements of 0.5 inch. Maximum load was achieved at 0.44 inch with 302 kips (l.p. 133, see Figure 80 for load displacement diagram). During this movement, the diagonal crack which formed during l.p. 112 widened to approximately 3/8 inch at one location. Cracks across the profile of the north plank were noted through the cores near sections J8 and J9. At l.p. 135 (0.5 inch east, 266.0 kips) additional diagonal cracking formed from the northwest corner to the southeast corner. During the first stabilization loops at 0.5 inch (see Figure 81), the cracks from l.p. 112 and 135 began widening as the loading beam moved to the west and east, respectively. Out-of-plane displacements were becoming noticeable at this time.

After the virgin 1 inch displacements, two one-foot square areas of the planks were removed to verify the failure mode mechanism. The shearing of the web at the lower wythe-web interface was common. During the 1 inch displacement cycle localized failures of the lower wythe (i.e. concrete pieces falling to the floor) were noted. Testing of the diaphragm continued through the 3 inch displacement cycle and terminated after the initial displacements to 5 inch.

During the post-test phase, no studs were found to have been broken during the testing. As with Tests #11, #12, and #13, Test #14 utilized three studs per void in the plank ends. This fact accounted for why so few if any studs broke during topped tests and why several usually broke during untopped tests.

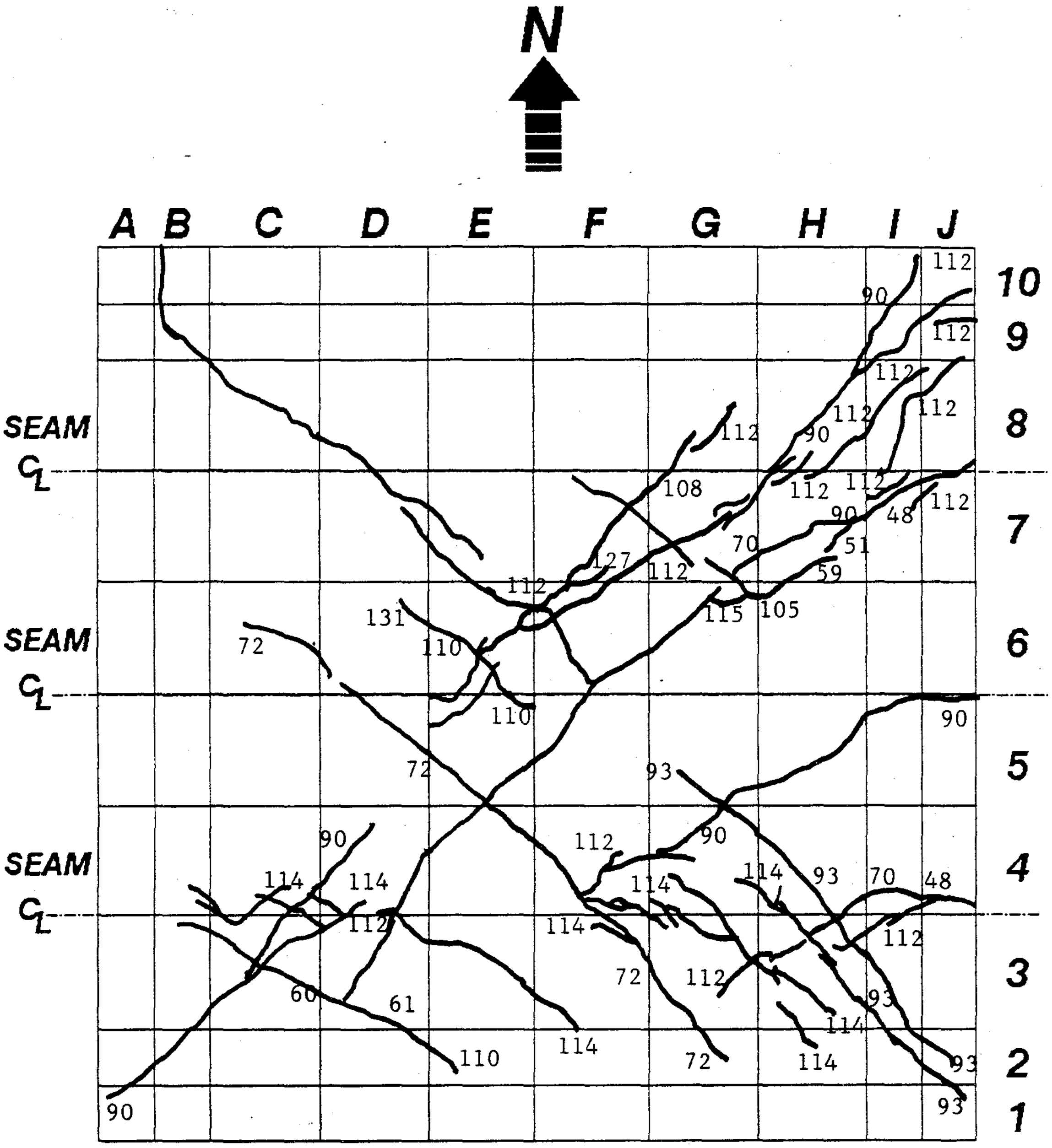

Notes:

Numbers by the cracks indicate the load point at which the crack was observed

Figure 79. Crack pattern for Test #14

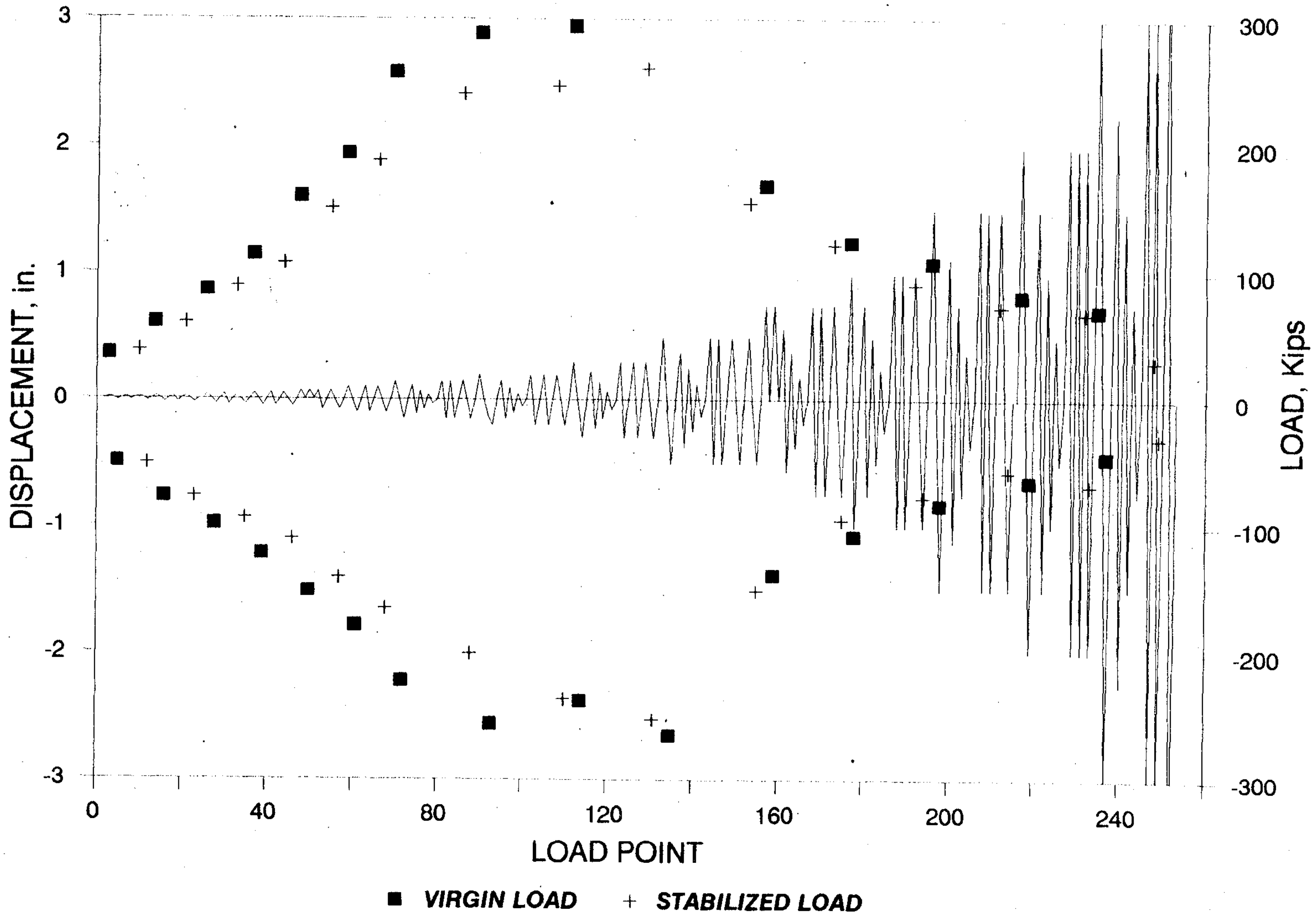

Figure 80. Load displacement diagram for Test #14

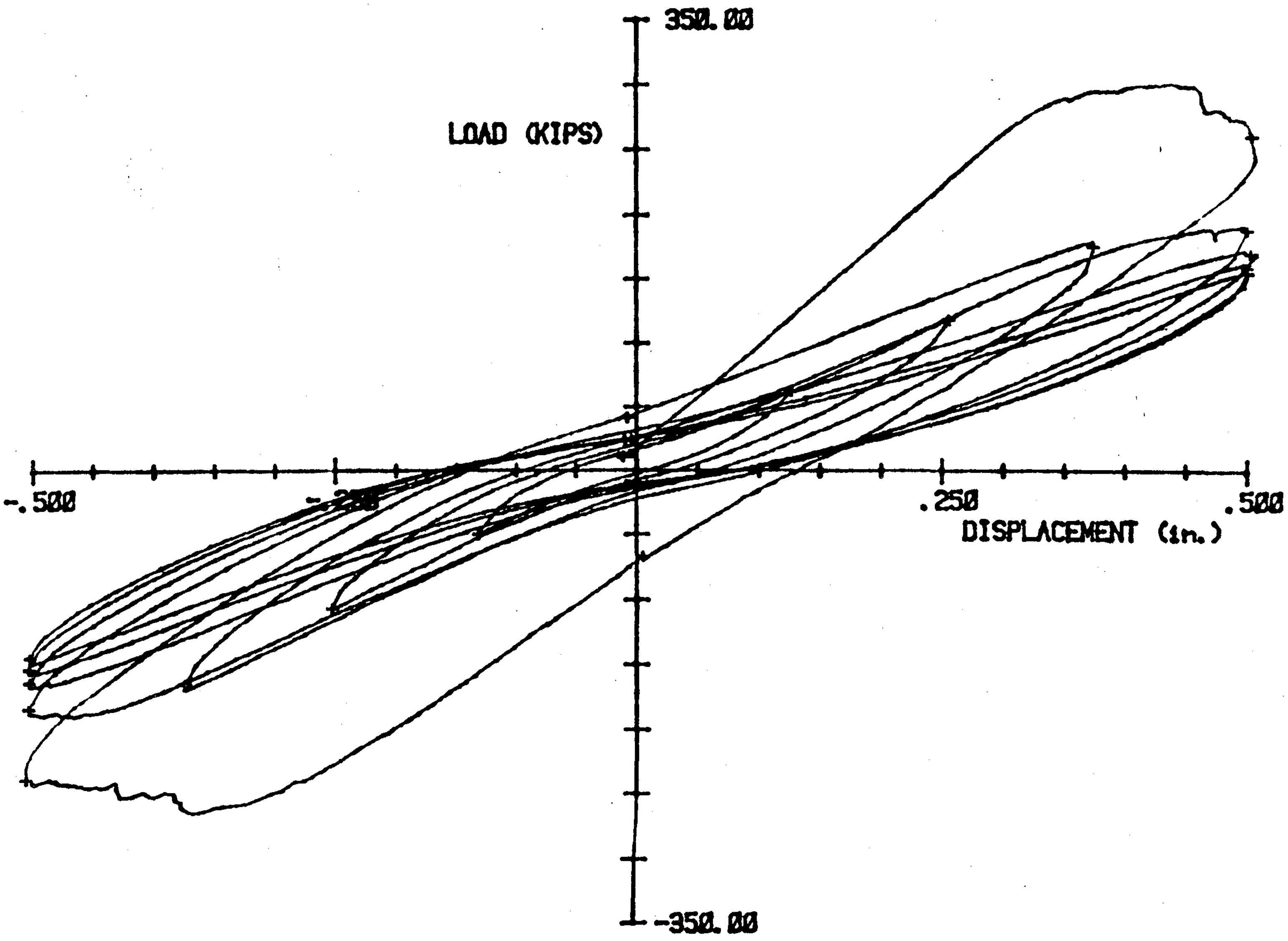

Figure 81. Hysteresis loops from Test #14

4.1.16 Diaphragm Test #15

The planks for Test #15 were oriented with the seams perpendicular to the loading beam. The slab was connected on all four sides to the loading frame using three studs per void. Weld ties were placed at 12 inches apart, which resulted in placing fifteen weld ties per seam. The grout strength in the core and seams were 3346 and 4399 psi., respectively.

Testing commenced on April 9, 1988. At load point 33 the center seam totally separated and the east plank developed a crack that extended from section F7 to H10 (refer to Figure 82). Diagonal cracks were noticed in the farthest west plank extending from the seam to section H2 and in the center west plank from the seam into section F2. This cracking at l.p. 33 (174.6 kips. and .153 inch) was recorded as the FME for this test. The failure mode was established as diagonal tension failure.

The east seam cracked all the way across except for two feet at the south end at l.p. 55. The stabilized envelope curve shown in Figure 83 reflects this seam cracking by a drop in load at that point. Diagonal cracking continued through the test, and by l.p. 97 most of the weld ties were partially exposed. The peak load for this test was recorded as 220.7 kips (l.p. 142 and .514 inch east). Weld ties exposure continued until l.p. 155, where the horizontal bars on the west seam were completely uncovered.

4.2 Orientation Comparisons

Orientation of the untopped precast planks has proven to be a significant factor in achieving diaphragm action. The planks can either be oriented parallel or transverse to the shear wall (loading beam). A comparison of several of the diaphragm tests allows for an assessment of the effects of this parameter on the overall behavioral characteristics of a hollow-core floor system.

4.2.1 Comparison of Tests #4 and #8

Test #4 consisted of four planks oriented transverse to the loading beam. The system was connected to the loading beam and the restrained end. Test #8 was connected in a similar fashion, however, the planks were oriented parallel to the loading beam. Test #4 produced dramatically higher FME and ultimate strength values than Specimen #8, 376% and 154% respectively. A comparison of the stiffness of each system throughout the test is a good indicator of the behavioral characteristics. The average cyclic stiffness is defined as the slope of the line between the maximum positive and negative load values of the third hysteresis loop of each displacement increment as is shown in Figure 84 [30]. An evaluation of the stiffness plots (Figure 85) confirms this statement. Test #4 had a much higher initial stiffness (1281 kips/in. verses 706 kips/in.) and maintained a higher stiffness through two inches of displacement.

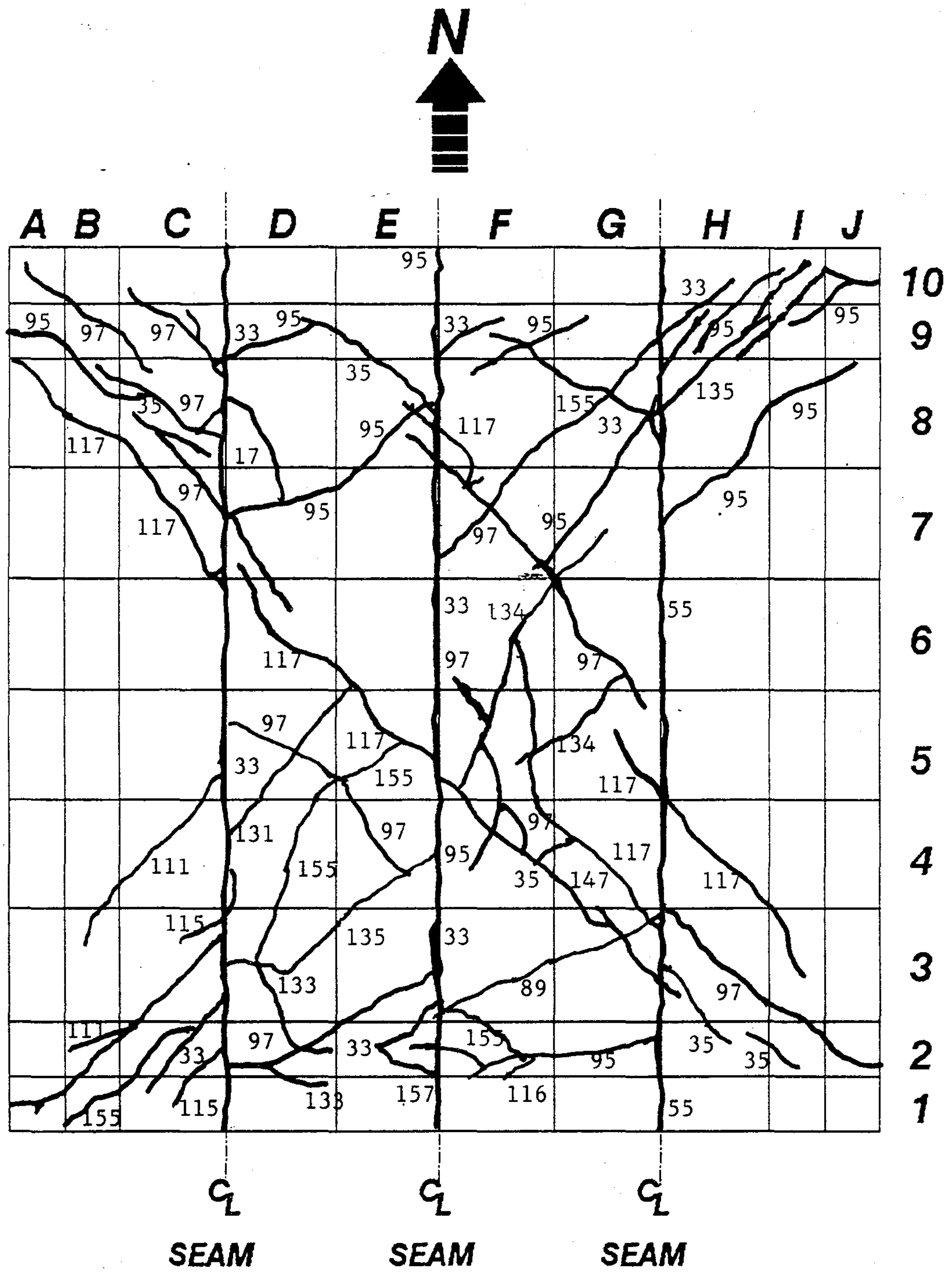

Notes:
Numbers by the cracks indicate the load point at which the crack was observed

Figure 82. Final crack pattern for Test #15

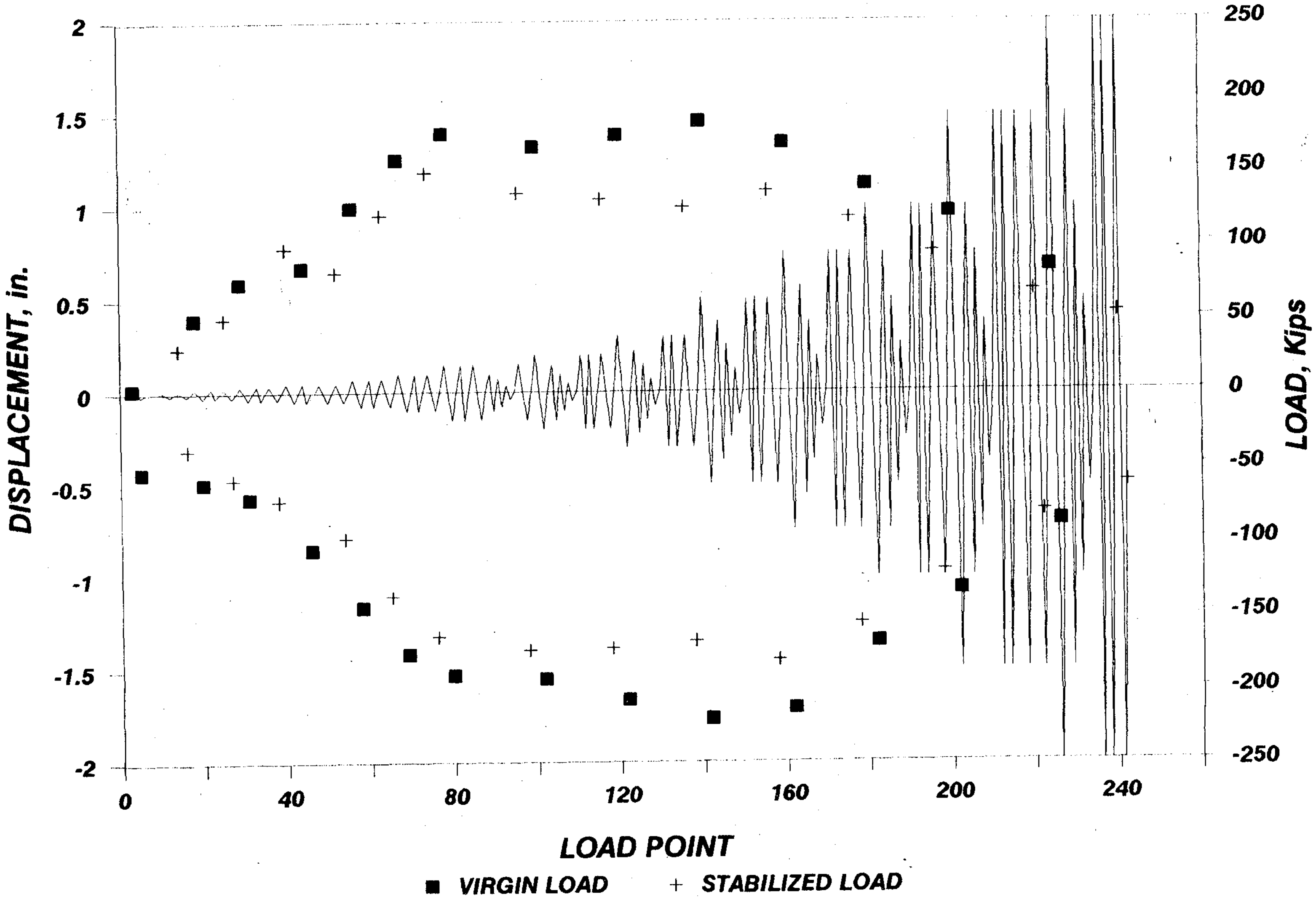

Figure 83. Load program for Test #15

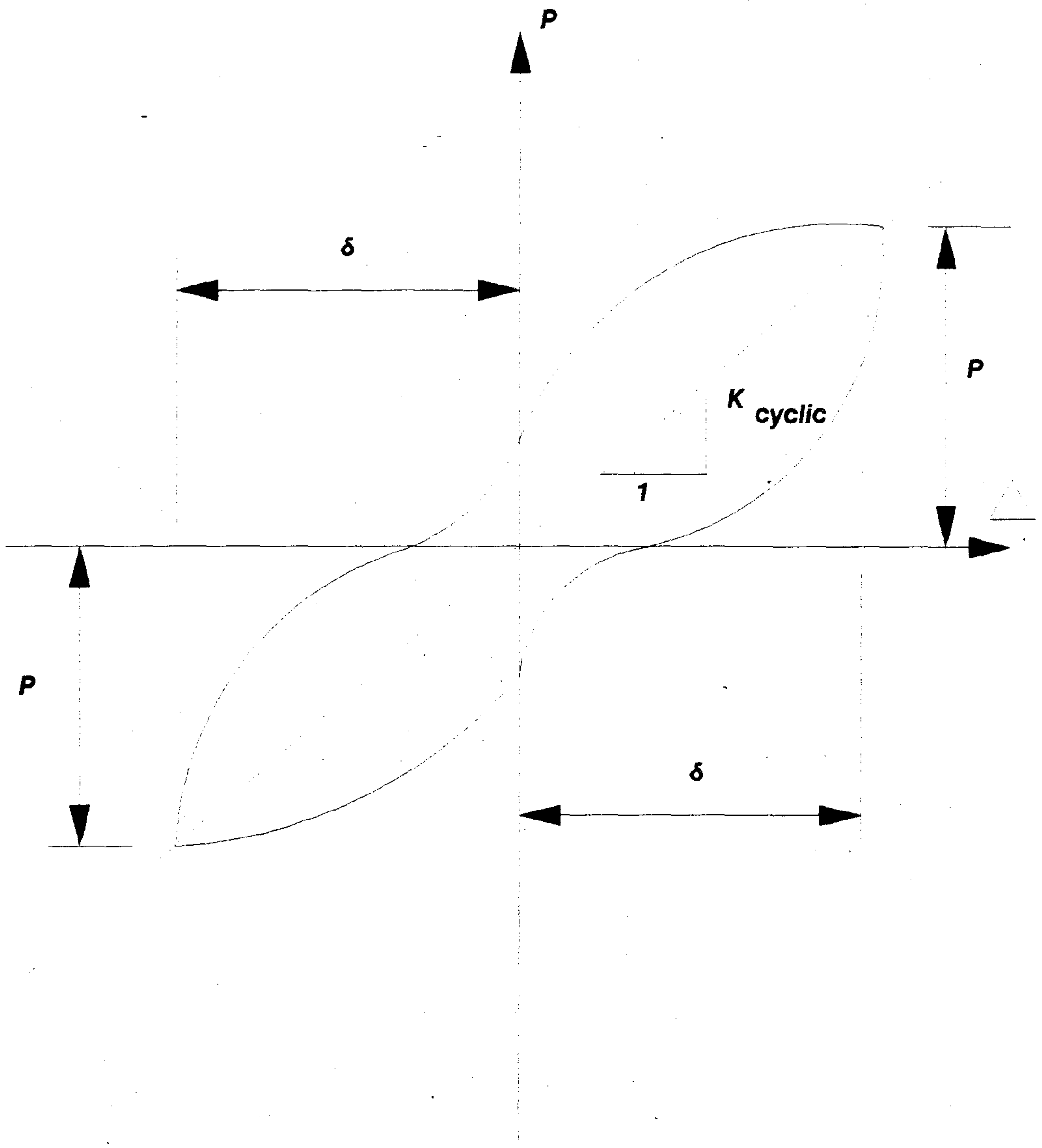

Figure 84. Calculation of average cyclic stiffness, K_{cyclic}

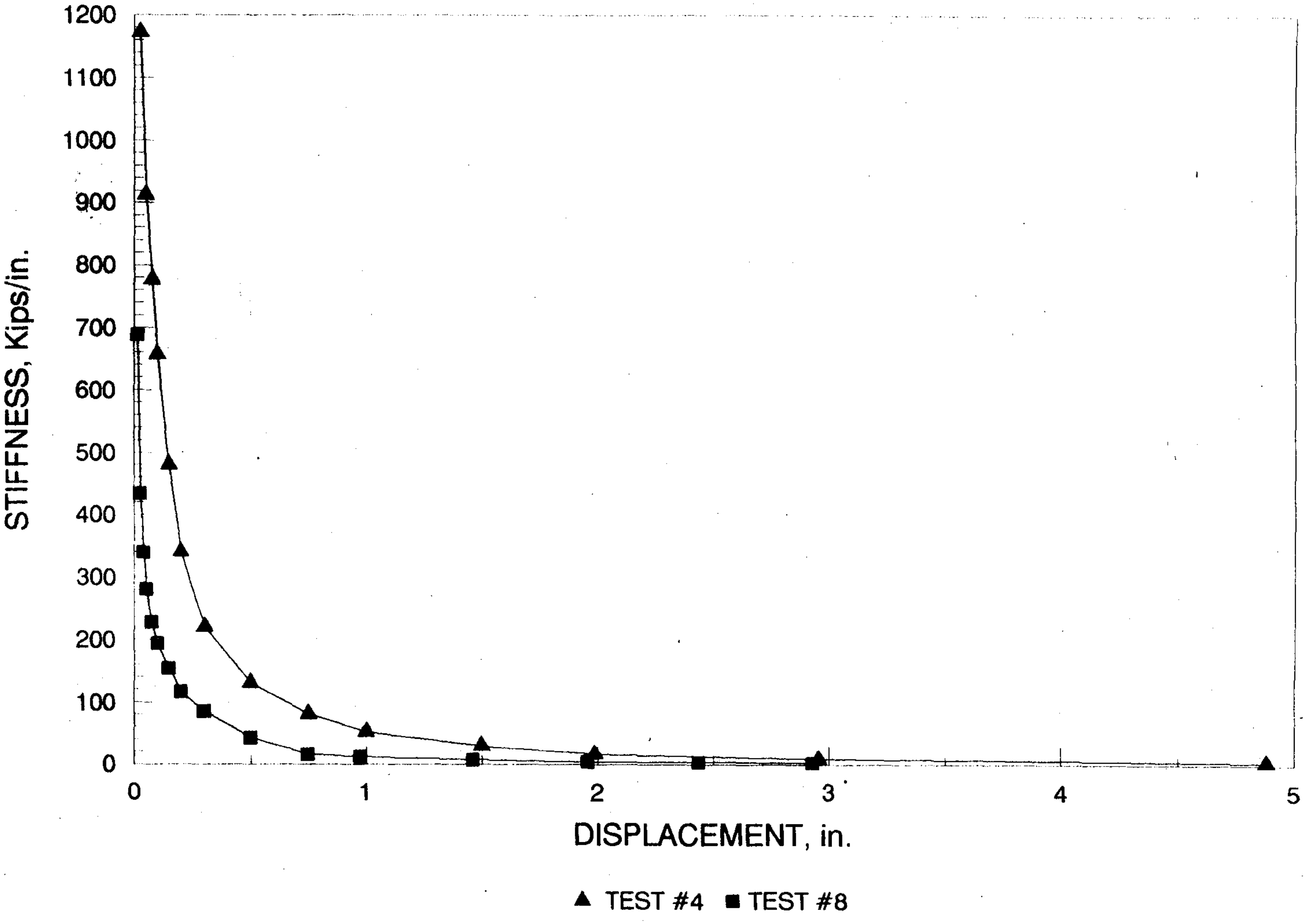

Figure 85. Cyclic stiffness comparison for Tests #4 and #8

A review of the total dissipated energy (Figure 86) also permits a good comparison. The dissipated energy for Test #4 was 151.5% greater than that for Test #8. Finally, the virgin and stabilized envelope curves, shown in Figure 87, further emphasize that Test #4 has a much stronger and stiffer diaphragm.

4.2.2 Comparison of Tests #5 and #6

A comparison of Tests #5 and #6 also serves to isolate the orientation parameter. These tests were identical with the exception of the orientation of the planks. Both were eight inches thick and were connected on all four sides. The planks in Test #5 were oriented transverse to the loading beam, and those in Test #6 were oriented parallel to the application of load. A study of the stiffness plots, shown in Figure 88, reveals that Test #5 maintained a higher stiffness throughout the test, although after 0.75 inch of displacements, the values were quite close.

Figures 89a and 89b, a plot of the virgin and stabilized curves, confirms that the transverse orientation produced a somewhat stronger system. This drawing, however, exposed another observation. After the ultimate load, or approximately one inch of displacement, the strength of both the virgin and stabilized load verses displacement envelopes for Test #6 exceed those for Test #5 in the east direction. A 50% to 70% loss in load occurred between the limit state and 3.0 inch of displacement for the virgin curve of Test #5. Only a 25% to 30% decline in virgin load occurred over a similar interval for Test #6. This phenomenon is probably due to the fact that Test #5 secured a greater amount of diaphragm action early in the test. Consequently, more studs failed at this time (24 broken in Test #5 and 14 in Test #6) which, in turn, caused a decrease in the later test loads.

4.2.3 Comparisons of Tests #13 and #14

Tests #13 and #14 contained both 8 inch floor slabs plus a 2 inch topping on the diaphragm. The floor slabs for Test #13 were oriented with the seams perpendicular to the loading beam and were connected to the testing frame on all perimeter edges. Thus, this comparison reflects a change in the orientation parameter. Figure 90 is a comparison plot of the stiffness versus cyclic displacement curves for Tests #13 and #14. The values of stiffness are nearly the same for similar displacements. The only minor alteration between the tests is the initial stiffness values. The initial stiffness for Test 14 was 3289 kips/in., which represents an increase of 21.9% with respect to the initial stiffness value of 2698 kips/in. for Test #13. The higher compressive strength of the topping may have influenced this behavior.

A comparison plot of the virgin displacement curves for Tests #13 and #14 is shown on Figure 91. The curves have a similar shape with the loads recorded for Test #14 being only slightly higher. The maximum load for Test #14 was 302 kips, which represents an increase of 2.2% with respect to the ultimate strength of 295.6 kips recorded during Test #13. Failure modes attained at the FME for both were the diagonal tension mode. Comparable FME strengths were also

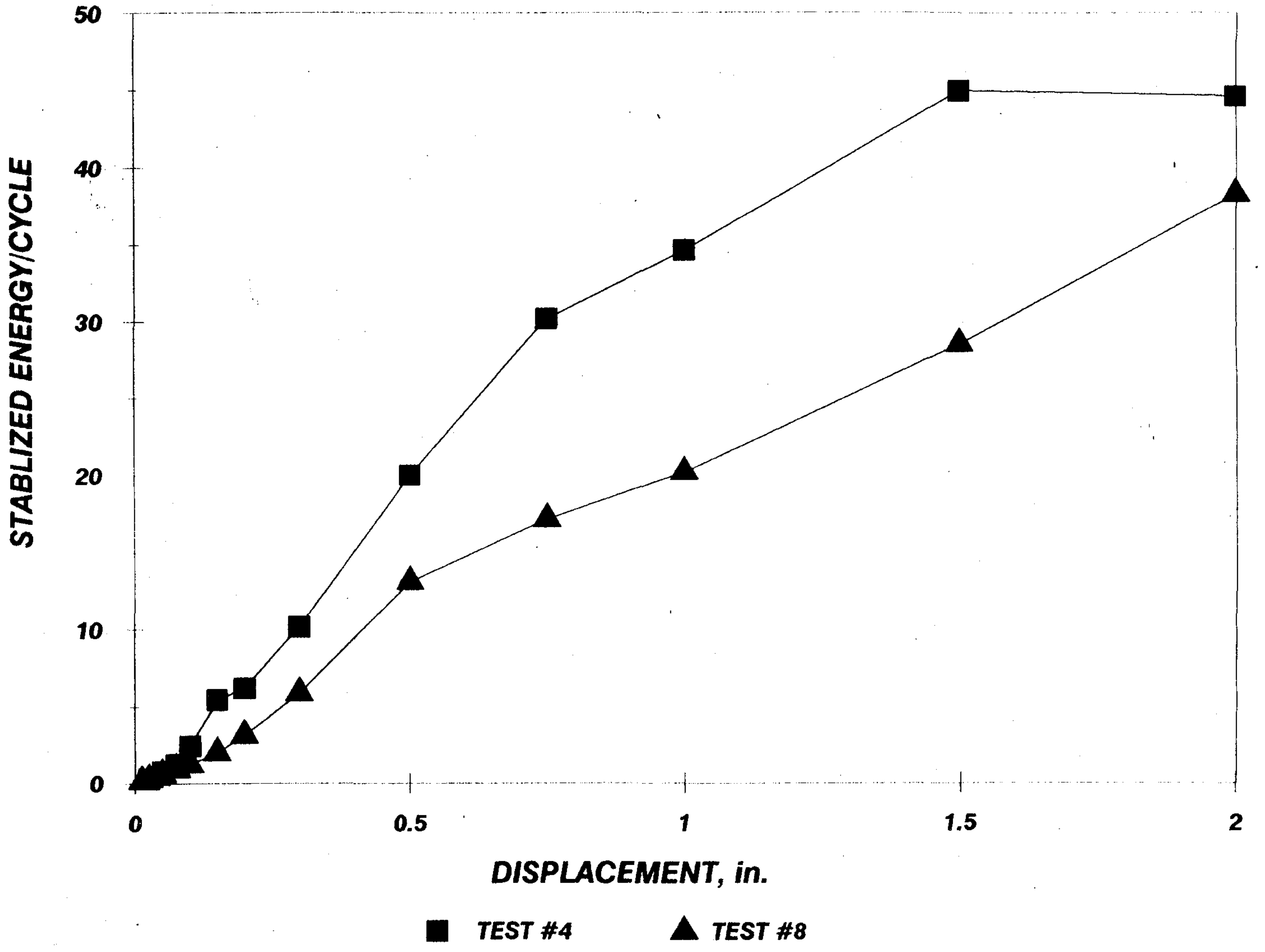

Figure 86. Dissipated energy plot for Tests #4 and #8

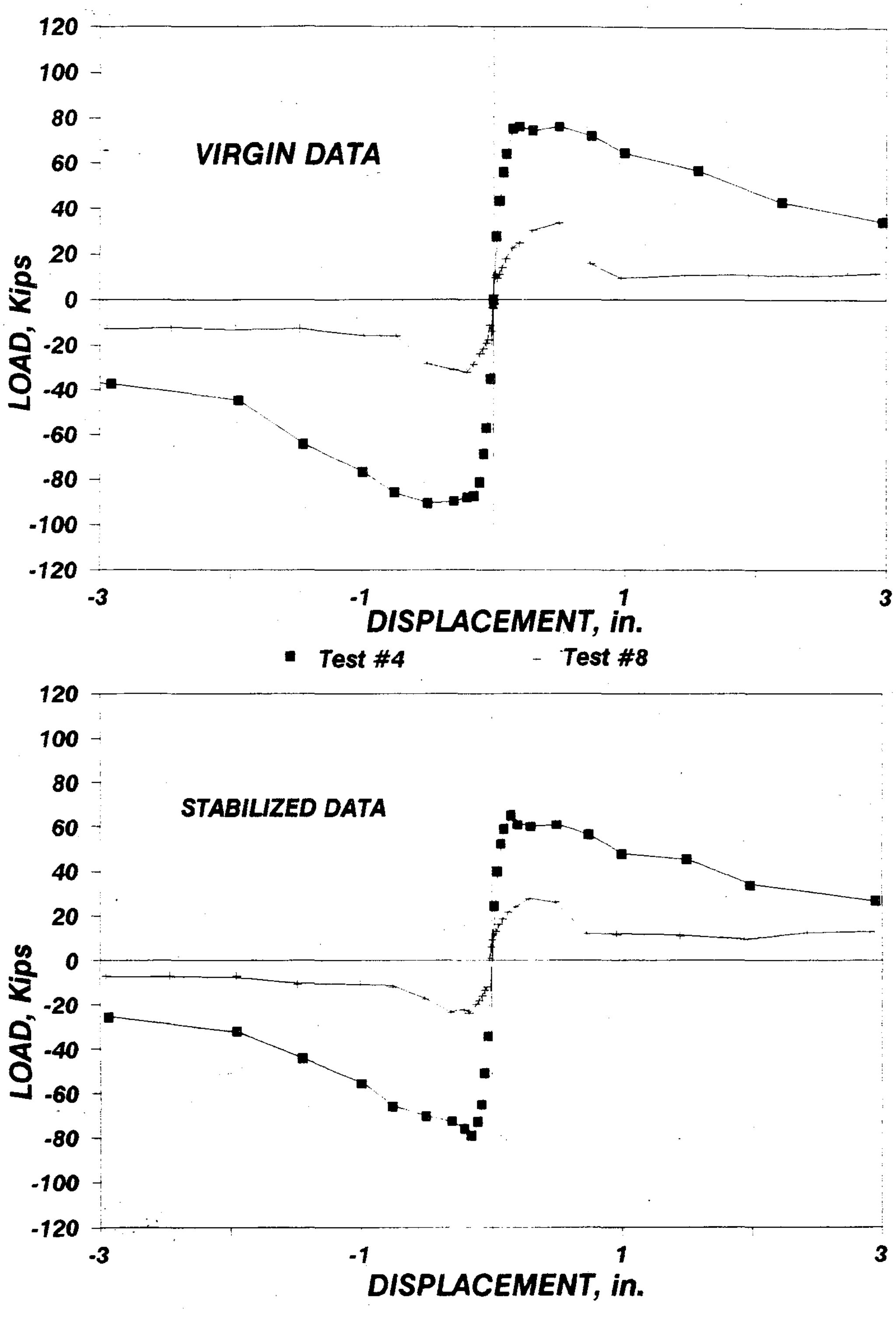

Figure 87. Envelope curves for Tests #4 and #8

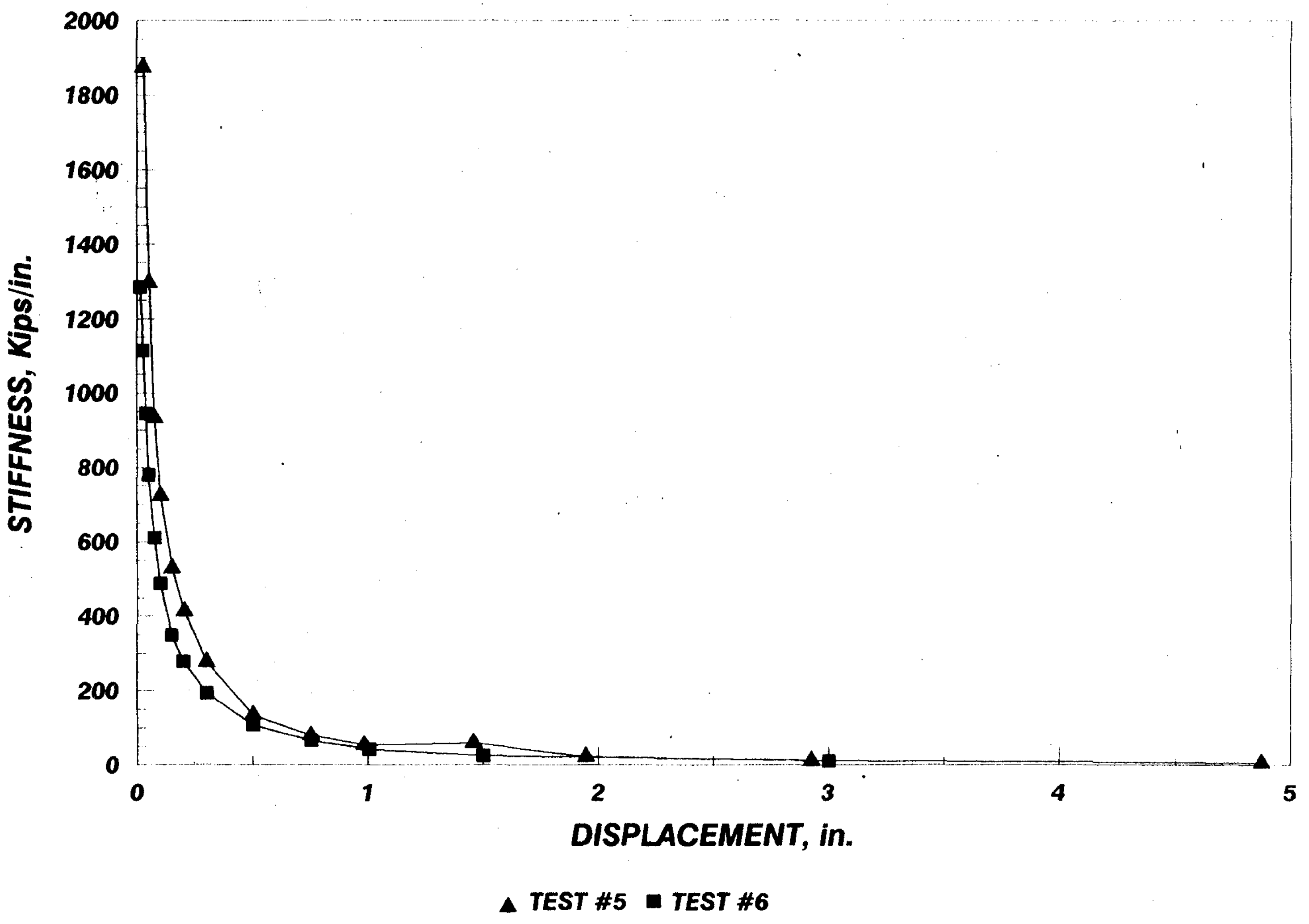

Figure 88. Cyclic stiffness comparison for Tests #5 and #6

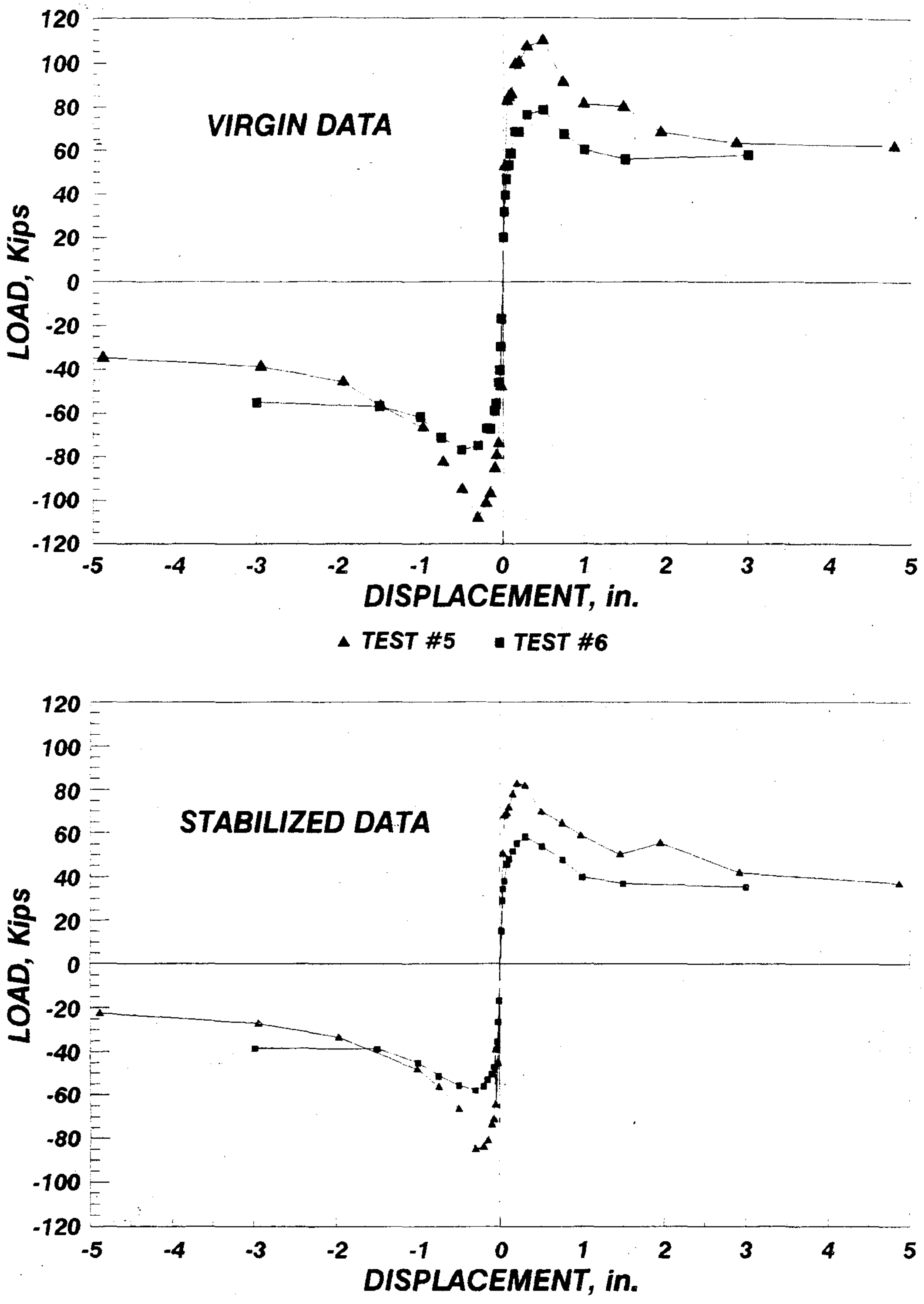

Figure 89. Envelope curves for Tests #5 and #6

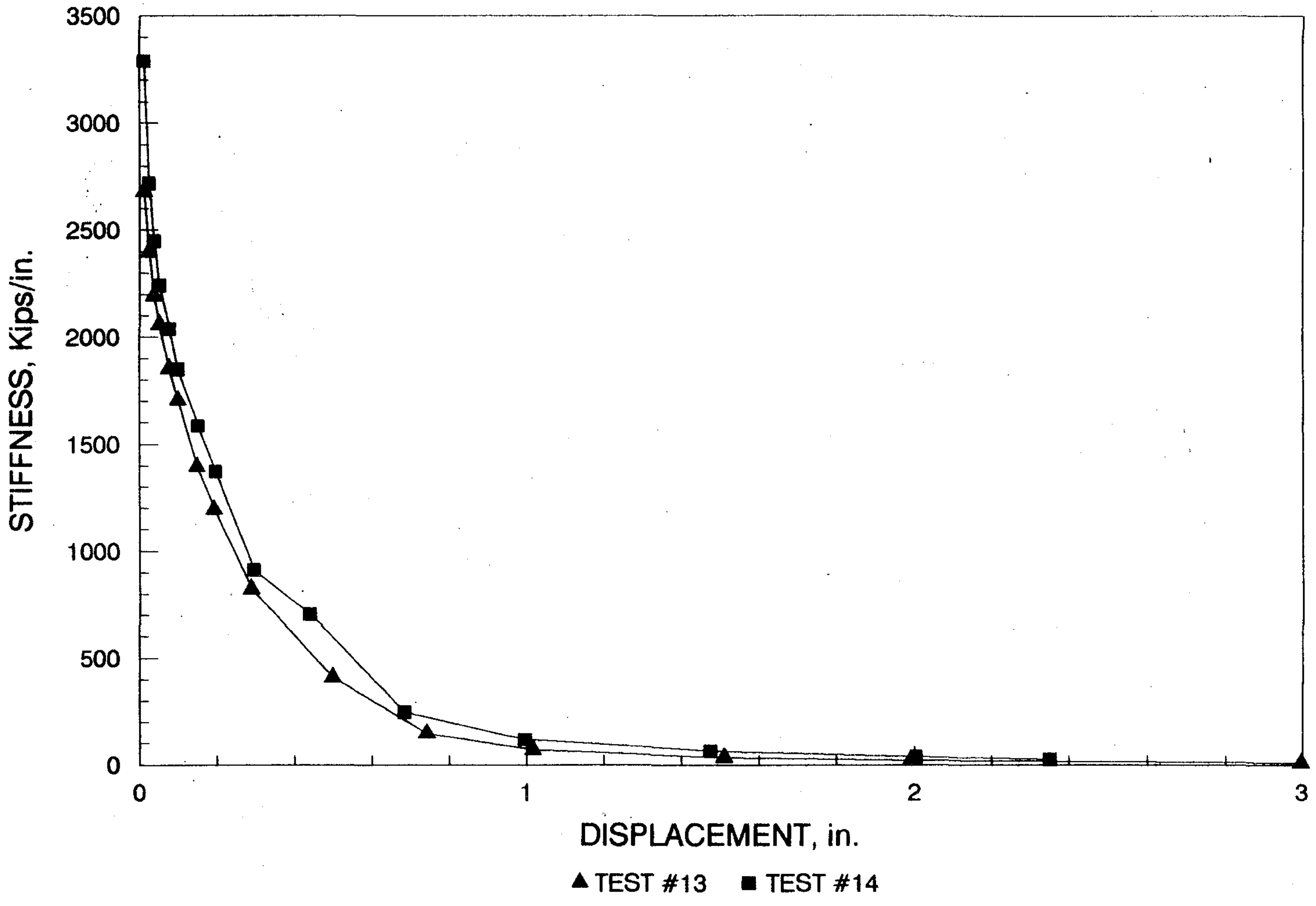

Figure 90. Stiffness comparison of Tests #13 and #14

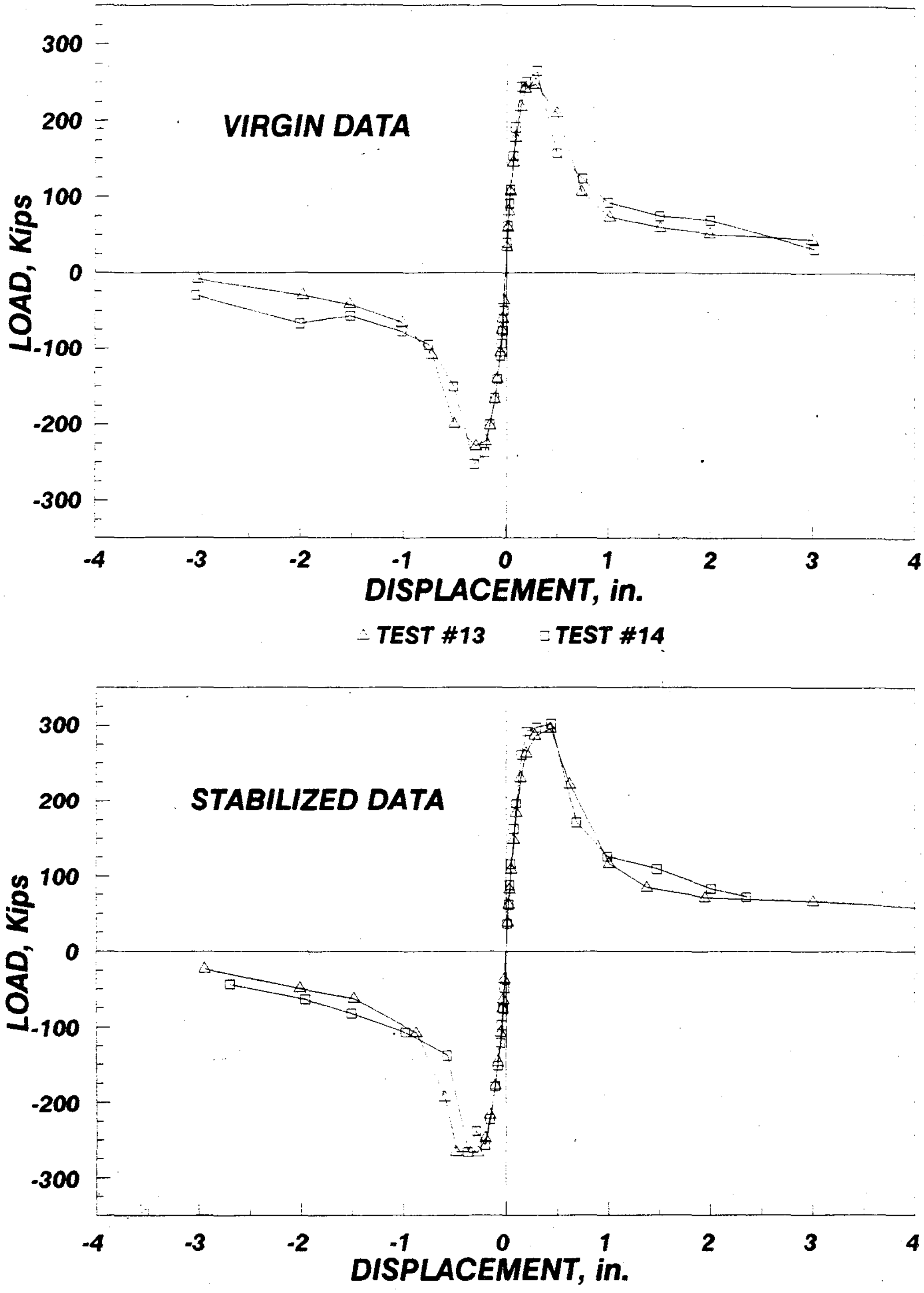

Figure 91. Envelope curve comparison of Tests #13 and #14

achieved, with 230.4 kips and 260.8 kips for Tests #13 and #14, respectively. This represents a difference of only 13.2% with respect to Test #13.

In general, these numbers reflect that experimentally, orientation of the planks under the topping has little influence on strength and other behavioral characteristics of the topped diaphragm.

4.2.4 Comparisons of Tests #2 and #4

Tests #2 and #4 both contained 8 inch floor slabs connected to the testing frame on two sides (the loading beam and restrained end). The floor slabs for Test #2 were oriented with the seams parallel, whereas, Test #4 planks were oriented with the seams perpendicular to the loading beam. Thus, this comparison reflects a change in the orientation parameter. A comparison plot of the envelope displacement curves for Tests #2 and #4 is shown on Figure 92. The curves have a similar shape with the loads recorded for Test #4 being higher up to 2 inch displacements. The maximum load for Test #4 was 90.5 kips, which represents an increase of 55% with respect to the ultimate strength of 58.4 kips recorded during Test #2. Failure modes attained at the FME for Test #2 was tensile-bond while Test #4 failed in shear-bond mode. FME strengths were different, with 58.4 and 88.0 kips for Tests #2 and #4, respectively. This represents a difference of 50.7% with respect to Test #2.

Figure 93 is a comparison plot of the stiffness versus cyclic displacement curves for Tests #2 and #4. The values of stiffness are higher for Test #4 than these recorded for Test #2. The initial stiffness for Test 4 was 1172 kips/in., which represents an increase of 81.6% with respect to the initial stiffness value of 645 kips/in. for Test #2.

These comparisons reflect that for the untopped slabs, diaphragms with the planks oriented perpendicular to the load directions attained a significantly higher strength than those with the planks oriented parallel to the load direction. This behavior is not evident in the topped slabs, thus, the addition of the topping nullifies the orientation parameter for topped diaphragms.

4.3 Boundary Condition Comparisons

By varying the number of sides of a diaphragm connected to the testing frame, the effects of the boundary condition parameter may be studied. As with any study of this nature, only the variable under consideration may be altered. Thus, Tests #4 and #5, which were identical with the exception of the number of sides which were connected, may be studied. Tests #6 verses #7, #6 verses #8, or #2 verses #6 may likewise be reviewed to determine the effects of this particular parameter.

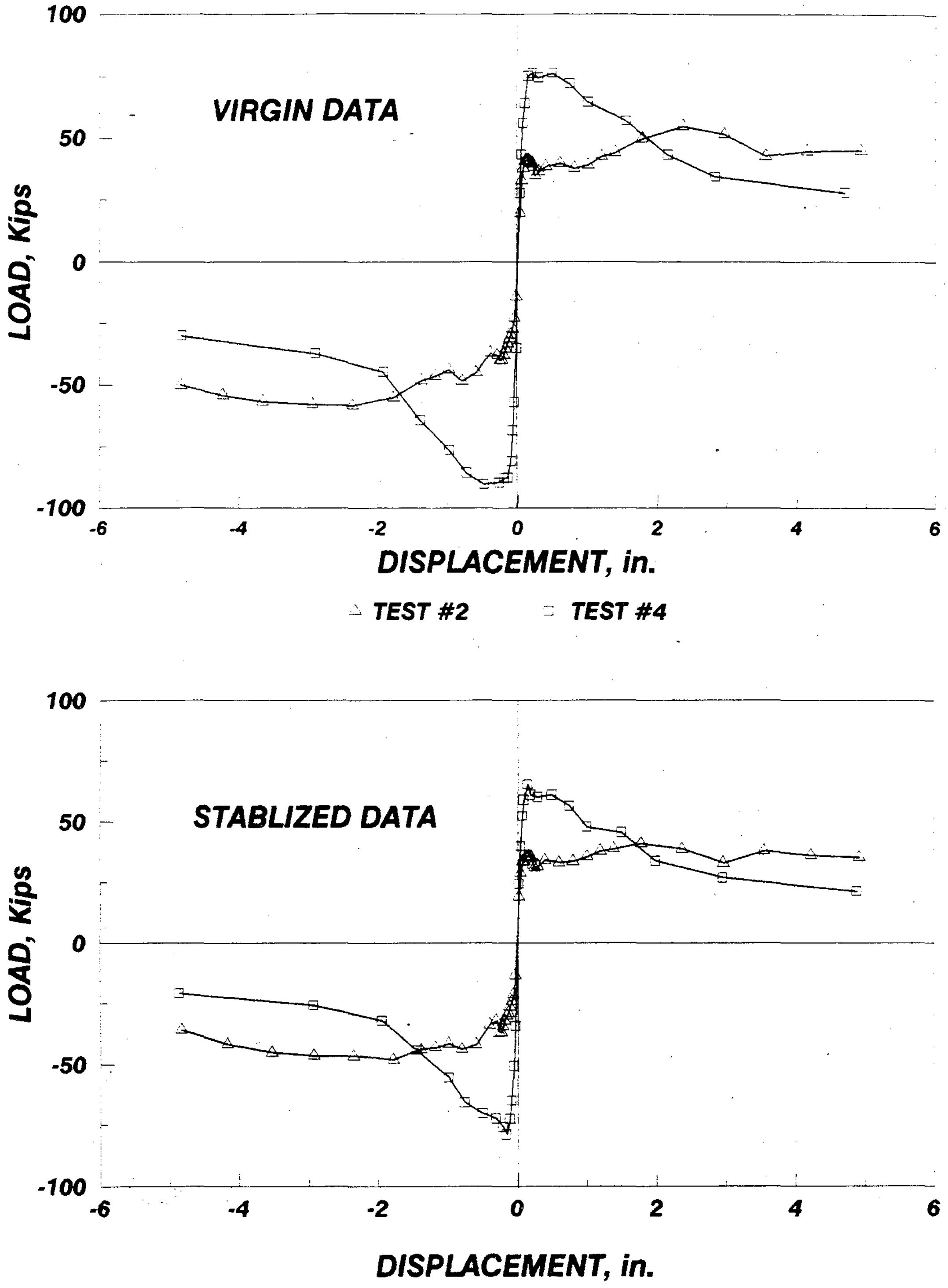

Figure 92. Comparison of virgin/stabilized plots for Tests #2 and #4

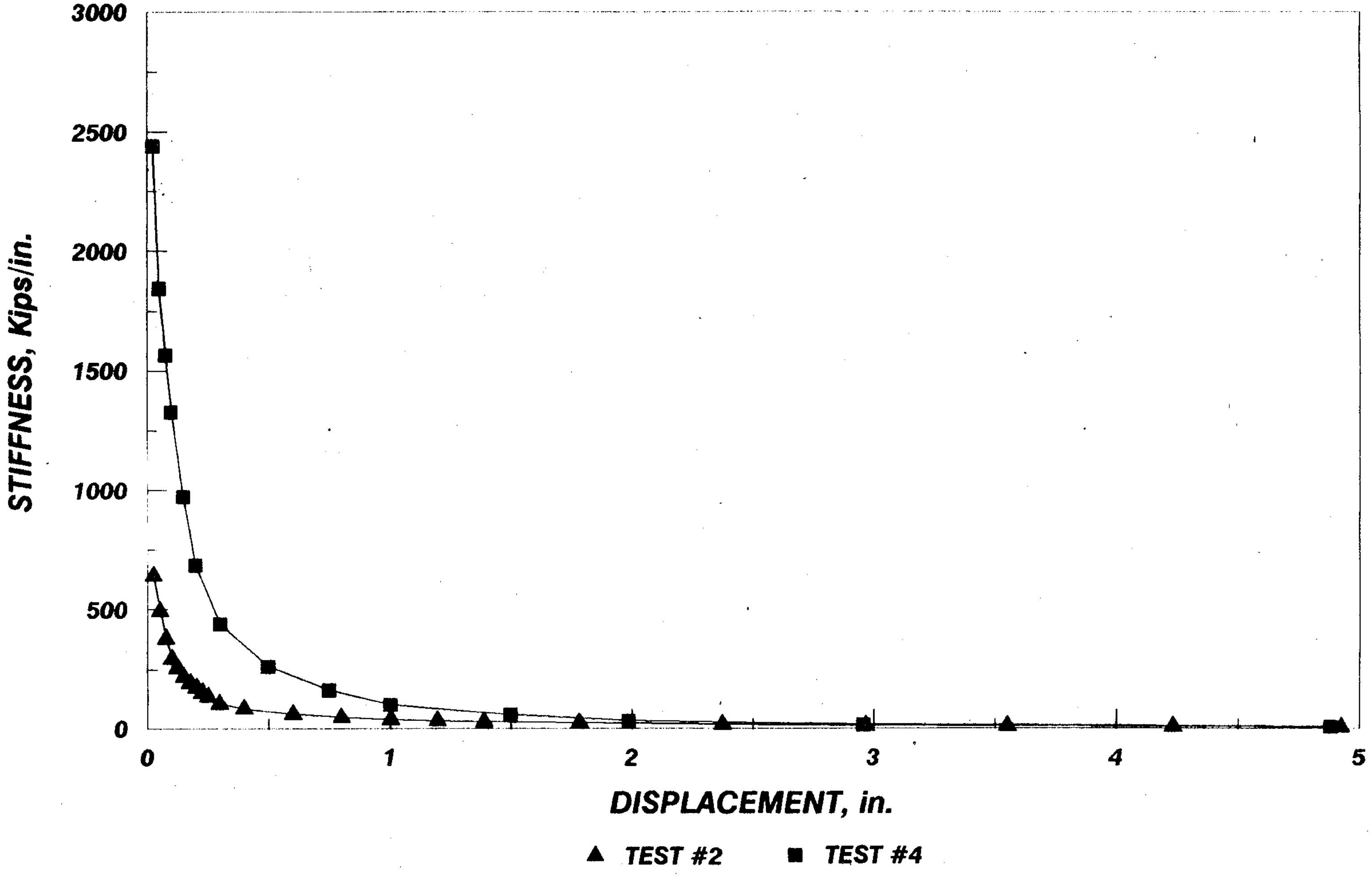

Figure 93. Cyclic stiffness comparison of Tests #2 and #4

4.3.1 Comparison of Tests #6, #7 and #8

A comparison of the results of Tests #6, #7 and #8 demonstrates the effects of connecting two, three and four sides of a diaphragm with similar orientation and thickness. Test #6 was connected on four sides, #7 on three sides (loading beam, restrained end and cantilever end), and Test #8 was connected on two sides (restrained end and loading beam). The FME strengths of Tests #6 and #7 were 72% and 65%, respectively, greater than Test #6. Similarly, the limit state strength of Test #6 and #7 was 122% and 108% greater than that for Test #8, respectively. The virgin and stabilized strength curves followed a similar pattern; that is, the four-sided connection resulted in significantly greater diaphragm action and consequently the highest strength.

The stiffness diagrams for each of these tests are given in Figure 94. The initial stiffness of Tests #6 and #7 was 1474 kips/in. and 1584 kips/in., respectively; while Test #8 yielded an initial stiffness of only 1101 kips/in. In addition, a careful inspection of this sketch reveals that the systems connected on three and four sides retained a higher stiffness throughout the test. This information serves to verify the conclusion that the greater the number of sides connected, the more diaphragm action achieved.

Surface cracking is another behavioral characteristic which can be used to study the effects of boundary conditions. The relative magnitude of diaphragm action achieved during a test can be determined by an inspection of the crack patterns. Test #6 exhibited the greatest amount of surface cracking which indicated higher concrete strains for this boundary condition. During Test #8, only one major crack formed. As expected, the limit state strength and stiffness were somewhat smaller for the latter test.

The hysteretic behavior of these tests can also be studied for general trends. A comparison of the dissipated energy, however, does not provide an exact comparison because it is dependent upon the load path. The SPD loading program allows for some variance between tests depending upon the behavior of the specimen. Fortunately, the load programs for each of these tests were very similar. Test #6 dissipated 49.5% more energy than Test #7 through 1.0 inch of displacement and 160.3% more than Test #6 over a similar interval. In brief, the amount of dissipated energy further substantiates the correlation between the number of sides connected and the amount of diaphragm action.

4.3.2 Comparison of Tests #4 and #5

Tests #4 and #5 were similar in every respect except that Test #4 was connected at the restrained end and along the loading beam, and Test #5 was connected on all four sides. Although the FME loads were very similar, the limit state load for Test #5 was 21.4% greater than that for Test #4. In addition, the stiffness comparison, shown in Figure 95, revealed that Test #5 had a higher initial stiffness (2005 kips/in compared with 1281 kips/in for Test #4). The stiffness remained higher until the 0.5 inch displacement cycle.

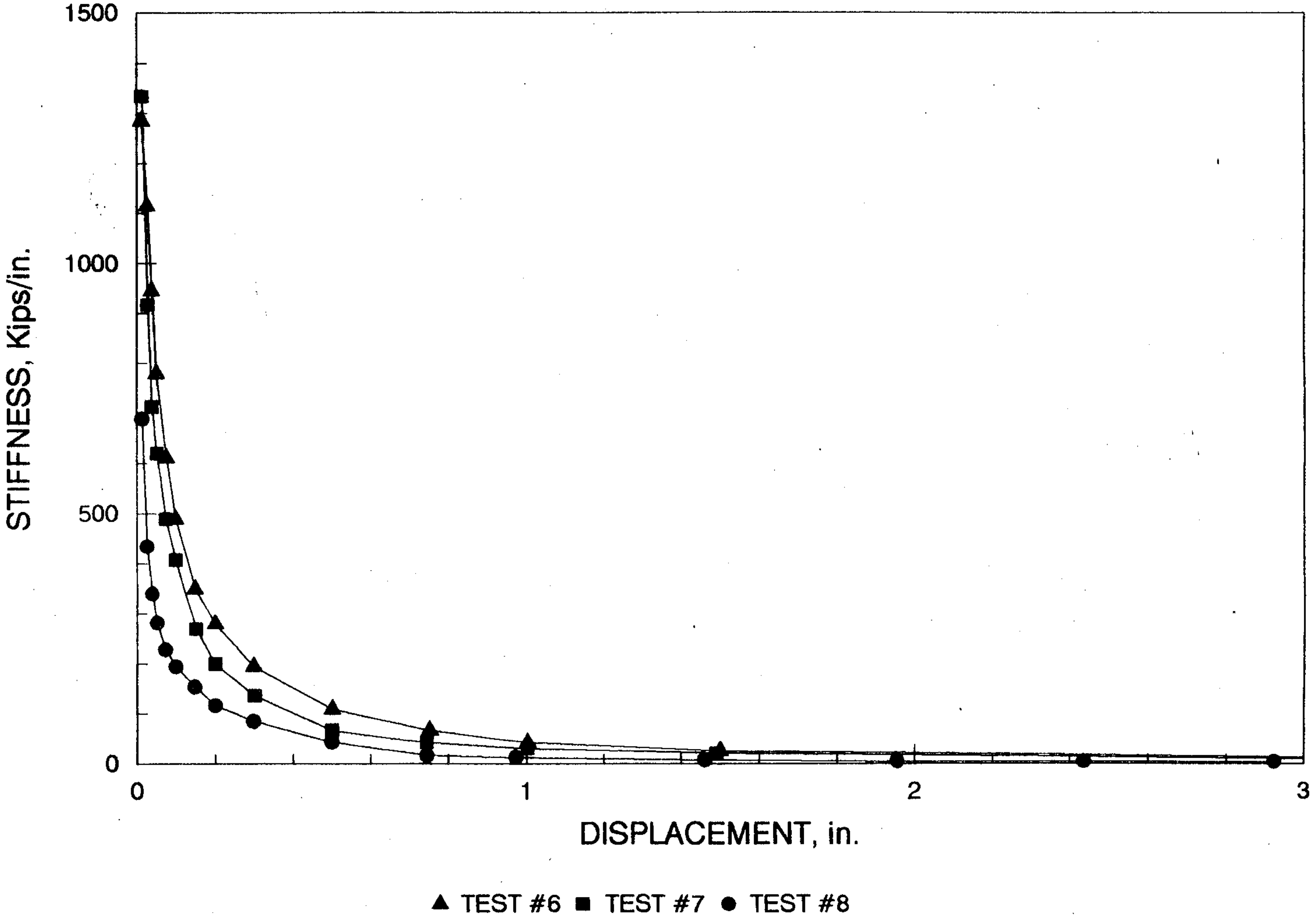

Figure 94. Comparison of stiffness for Tests #6, #7, and #8

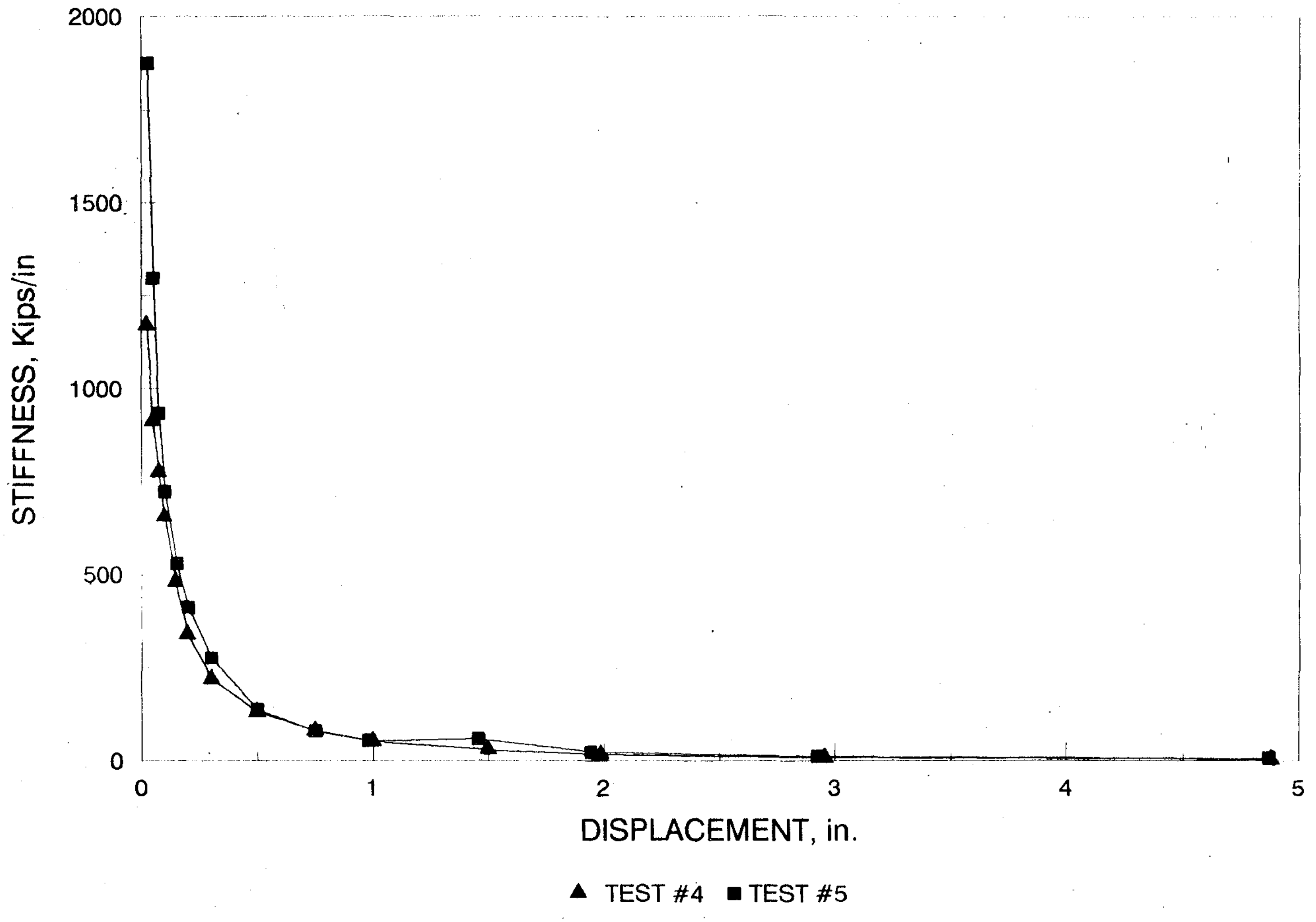

Figure 95. Cyclic stiffness comparison for Tests #4 and #5

The virgin and stabilized strength curves (Figure 96) further show that the four-sided test exhibited greater diaphragm action. Although both test configurations were symmetric and should have resulted in a symmetric envelope curve, clearly, on the average, Test #5 yielded a greater capacity.

Comparing the dissipated energy through one inch of displacement yields a similar conclusion. Test #4 dissipated only 596 kips-in., compared to 833 kips-in. for Test #5.

4.3.3 Comparison of Tests #12 and #13

The distinguishing parameter between Tests #12 and #13 was the boundary conditions difference. Test #13 was fastened to all perimeter edges of the testing frame while Test #12 was connected to only the loading beam and restrained edges. The other difference was the orientation which was proven not to affect the topped diaphragm strength (see Section 4.2).

Figure 97 is a comparison of the stiffness of the diaphragm in Tests #12 and #13. The stiffness of Test #12 was considerably less than the stiffness of Test #13 throughout most of test. The initial stiffnesses were 1596 kips/in. and 2698 kips/in. for Tests #12 and #13, respectively. This represents a 69.0% increase in stiffness with respect to Test #12. Indeed, the entirely fastened diaphragm system of Test #13 should have yielded a somewhat larger initial stiffness, however, a 69.0% is very significant.

Figure 98 is a comparison plot of the stabilized envelope curves for Tests #12 and #13. The general shape of the curves shows that a larger load was recorded for Test #13 than for Test #12, especially during the 0.10 inch to 0.5 inch range. The larger strength capacity for Test #13 was attributed to the boundary condition parameter.

The maximum load for Test #13 was 195.6 kips compared to an ultimate strength of 135.8 kips for Test #12. This represents a 118% increase in ultimate load for Test #13 with respect to Test #12. Some of this increase may have been caused by the cores, seams, and topping of Test #13 having slightly higher strength than those used in Test #12. Again, this difference must be primarily attributed to the boundary condition difference.

Tests #12 and #13 both failed in the diagonal tension failure modes, yet while attaining considerably different capacities. The FME loads for Tests #12 and #13 were 127.5 kips and 230.4 kips, respectively. No seams cracked in either test, indicating the nonexistence of the seam shear-bond failure mode. The major difference in the behavior of Tests #12 and #13 was the higher strength capacity associated with Test #13.

The comparison of Tests #12 and #13 corresponds with the results of Tests #4 and #5. In both comparisons, the connection to all four sides of the testing frame increased the strength of the diaphragm, although the extent to which the boundary condition parameter influenced the behavior was dependent upon whether or not the systems were topped.

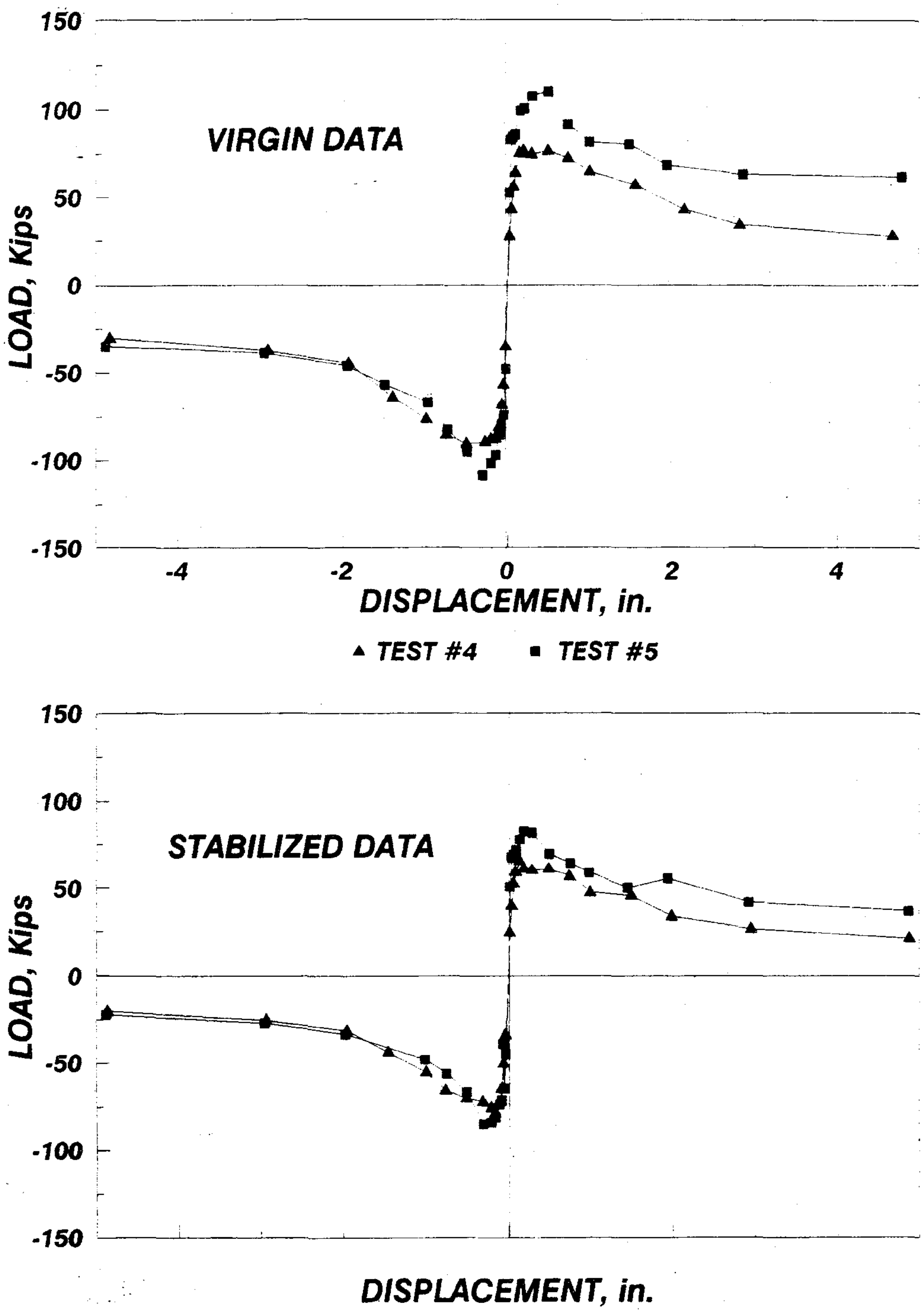

Figure 96. Envelope curve comparison for Tests #4 and #5

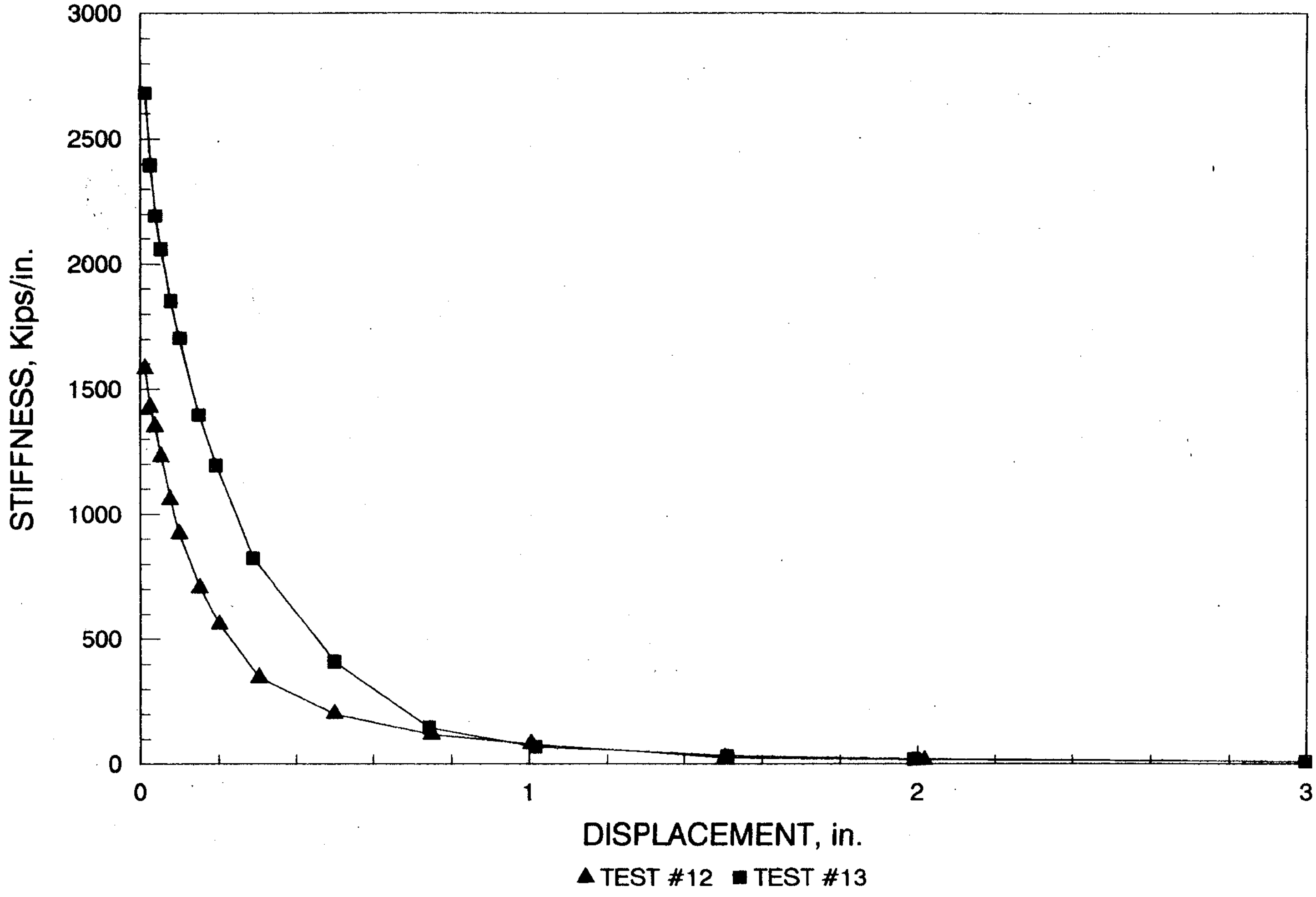

Figure 97. Stiffness comparison of Tests #12 and #13

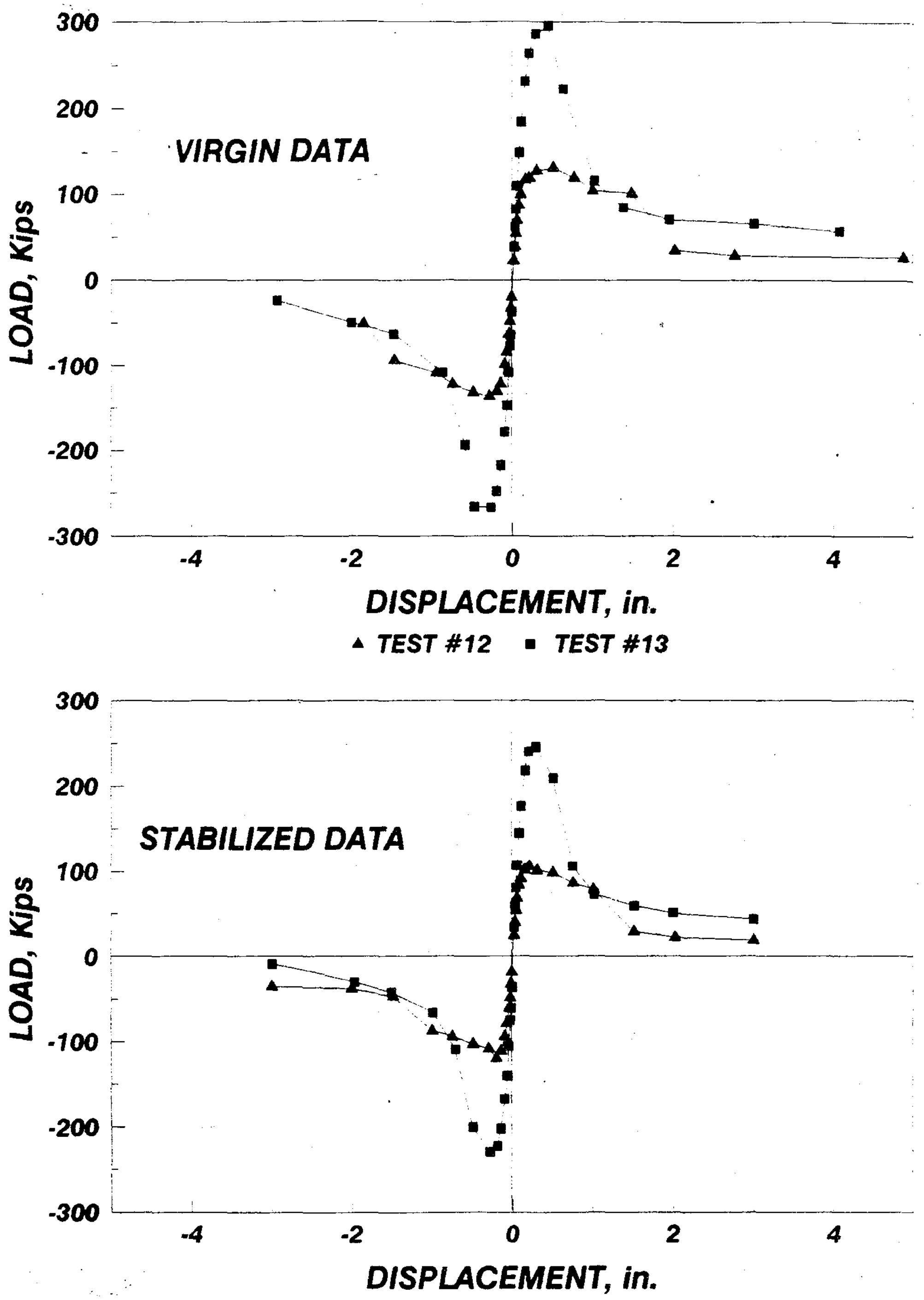

Figure 98. Envelope curves for Tests #12 and #13

4.3.4 Comparison of Tests #2 and #6

A final boundary condition comparison can be found in Tests #2 and #6. Note that any comparison utilizing Test #2 must be analyzed in the context in which it was tested. The results of Test #2 may not be utilized directly in the latter stages of the test because of the failure of the connections.

These tests exemplify another aspect of the boundary condition parameter; that is, the diaphragm must be adequately attached to the shear wall. Pilot Test #2 and Test #6 both consisted of four planks oriented parallel to the loading beam. Test #6 was connected to the loading beam (shear wall) and to the restrained end. Test #2, on the other hand, was mainly connected to the side beams (bearing walls). Only a minimal attachment was made to the loading beam. Diaphragm Test #6 exhibited a higher maximum load (35% higher). In addition, the initial stiffness of Test #6 was 54% higher than that for the second pilot test. In short, pilot Test #2 showed that when a plank floor system is primarily connected on the sides perpendicular to the applied shear load (masonry walls) and inadequately connected to the loading beam (shear walls), a significant deficiency in diaphragm action occurs.

4.4 Plank Thickness Comparisons

Another parameter of particular interest was the thickness of the diaphragm. Tests #4, #9, and #11 were all connected in a similar fashion, but they were all different thicknesses. In addition, Tests #6 and #10 were identical with the exception of the thickness of the planks. A review of these tests allows for the study of the effects of plank thickness on the behavioral characteristics of the system.

4.4.1 Comparison of Tests #4, #9 and #11

Data from the stiffness plot comparison for Tests #4, and #9 (shown in Figure 99) indicates that from 0.0125 inch to 0.05 inch of displacement, stiffness were greater for Test #9, contrary to expectations. A higher compressive strength of the edge zone grout may have triggered this occurrence. However, from 0.05 inch to 0.75 inch displacement, the diaphragms yielded slightly greater stiffness for Test #4. Differences were negligible after 0.75 inch values. Also shown in this figure is a comparison between these tests and Test #11. Test #11 yielded a considerable increase in initial stiffness over both Test #4 and #9 and continued this trend through displacements up to 0.3 inch. Greater stiffness were expected for Test #11, since the average plank depth was greater.

In comparing envelope curves for the virgin loads versus displacements for Tests #4 and #9 (Figure 100), similarities in contour are found. While a maximum value of 78.4 kips was attained in Test #9, 90.5 kips was the peak for Test #4. Given the fact that both tests utilized the same configuration, and that maximum strength was associated with impending failure of the first set of seam weld ties, peak strengths should have been comparable. Actually, this increase could be attributable to the depth parameter. With the greater 8-inch depth, greater frictional resistance in the seams developed as the displacements were induced.

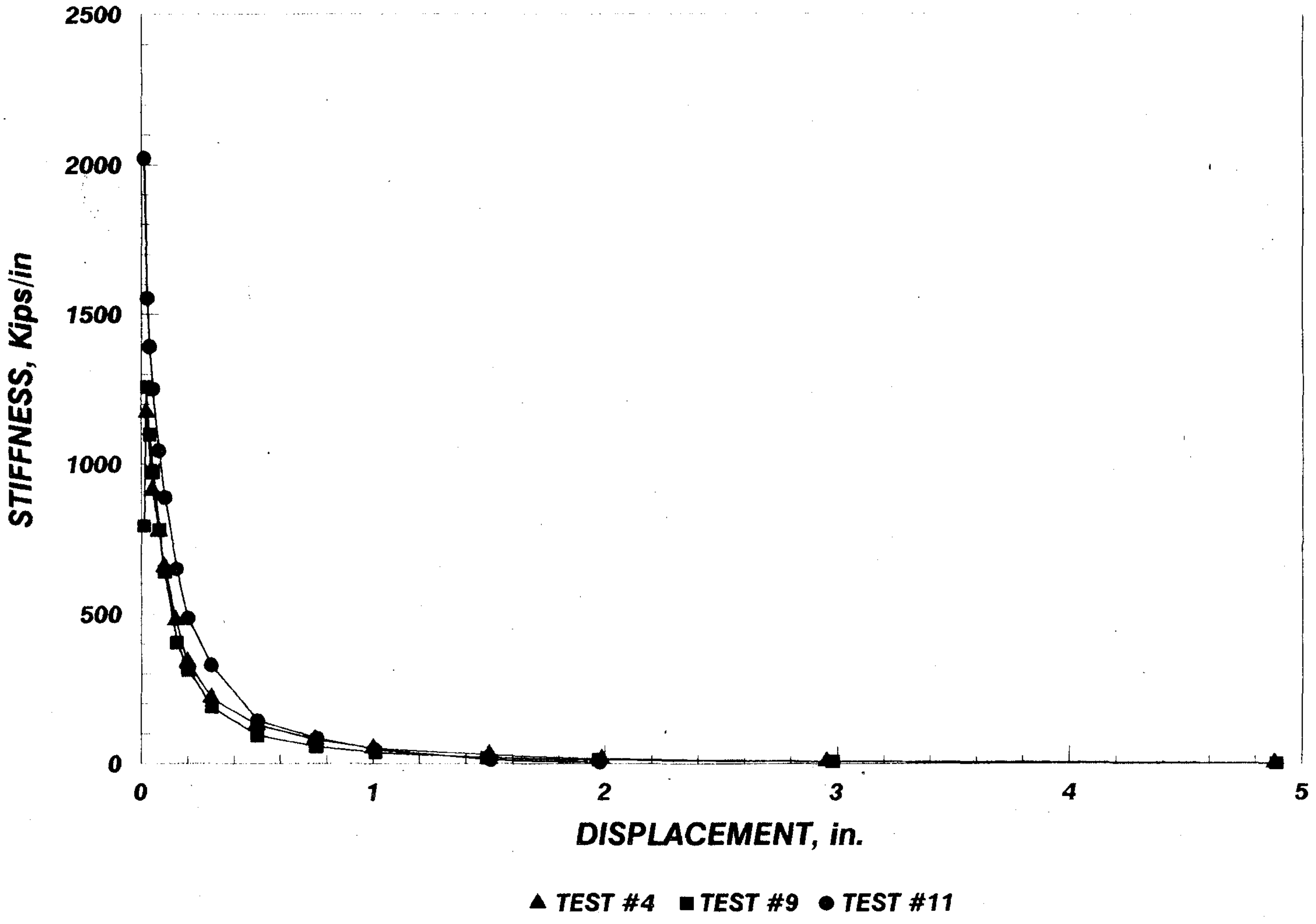

Figure 99. Cyclic stiffness for Tests #4, #9, and #11

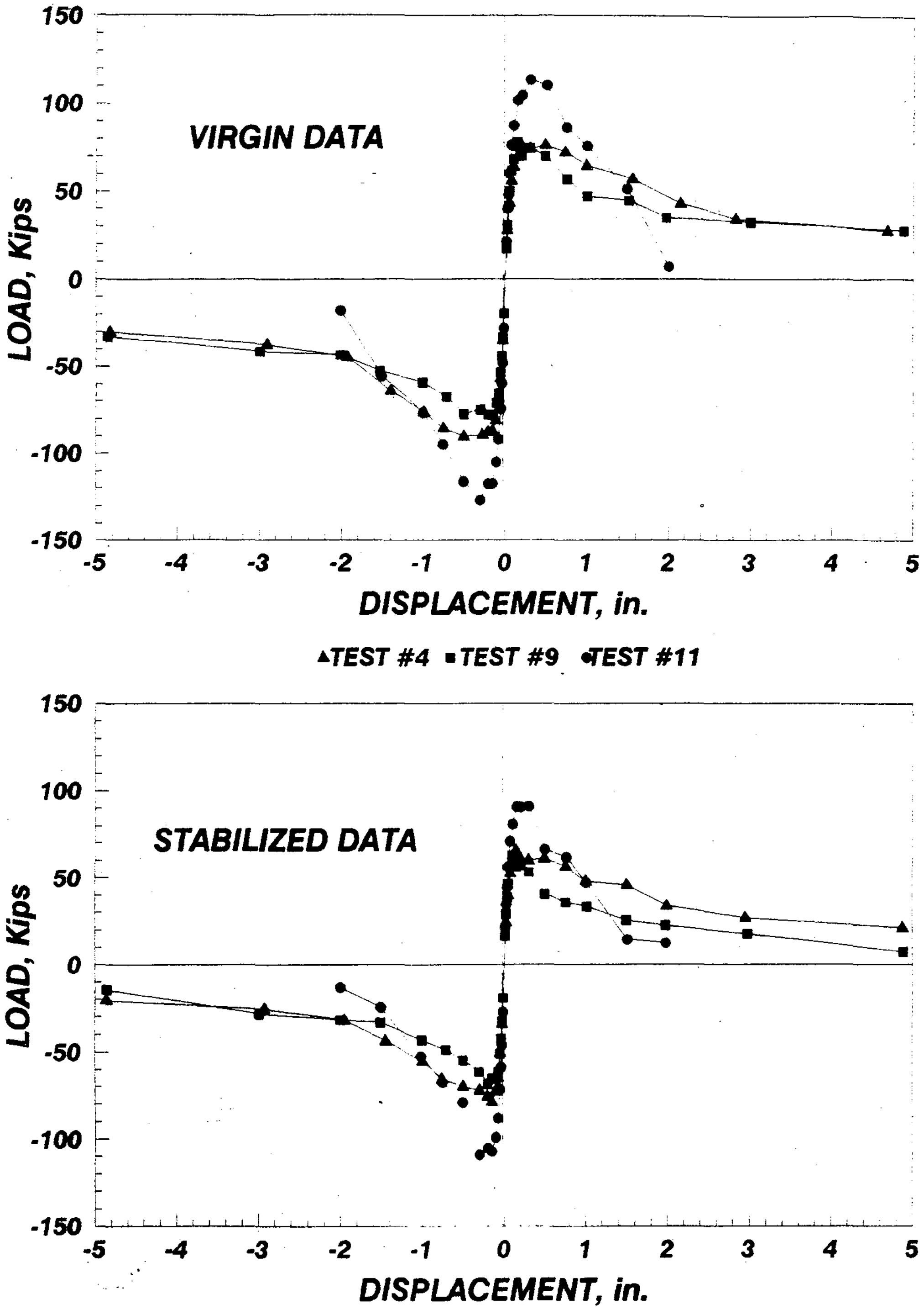

Figure 100. Envelope curves for Tests #4, #9, and #11

Also, the FME loads for Test #4 and #9 differed by a similar margin of 11.4% with respect to Test #4. The FME loads were 88.0 kips and 78.0 kips for Test #4 and #9 respectively. Since the seam shear-bond failure mode controlled for both tests, a proportional increase in the FME strengths should have reflected the grout penetration depths. Typical depths were approximately 6.5 and 5 inches for the 8- and 6-inch plank depths, respectively. (This would account for the 23.1% difference.) As expected, the thicker 8-inch diaphragm in Test #4 revealed a larger load capacity than the 6-inch diaphragm Test #9.

Test #11 can also be compared with Test #4 and #9. Since the FME strength of Test #11 resulted from the diagonal tension failure mode, a direct comparison of these numbers cannot realistically be of value. The 12-inch diaphragm system in Test #11 did yield a higher peak strength by 40.2% and 53.7% than Test #4 and #9, respectively, with respect to Test #4. The diagonal tension failure mode combined with the shear-bond failure of the seams severely damaged the diaphragm system, such that at 1.5 inch displacement less than 50% of the peak capacity was achieved during the virgin cycle. At the 2-inch displacement cycle this value fell to just 10% of the peak capacity.

4.4.2 Comparison of Tests #6 and #10

The stiffness for Test #10 was generally higher than the stiffness recorded in Test #6 as is shown in Figure 101. Stiffness values of Test #10 were approximately twice the values of Test #6 between displacements of 0.025 inch and 0.05 inch. Between 0.05 inch and 0.5 inch of displacement, the stiffness of Test #10 was about 40% higher than that recorded from Test #6.

A comparison of the virgin curves, as shown in Figure 102, indicates that the diaphragm in Test #10 recorded a larger load for similar displacements than Test #6, contrary to expectations. The FME in Test #6 was at a displacement of 0.025 inches and load of 31.9 kips; however, the FME in Test #10 occurred at a displacement of 0.035 inches and a load of 82.4 kips. These FME strengths indeed reflect the different failure modes attained. The peak strengths for Tests #6 and #10 were 78.6 and 106.2 kips, respectively. This represents a 35.0% increase of load in Test #10 with respect to Test #6, again contrary to expectations. Certainly, the fact that both the north and south seams broke very early in the testing program limited the capacity of Test #6. Note that only the south seam fractured at the FME for Test #10.

4.5 Topping Comparisons

4.5.2 Comparison of Tests #4 and #12

After removal of the planks during the post-test phase of Test #12, no studs were found to have broken during testing. The increase from two to three studs per core end allowed for the force distribution through the edge zone, while maintaining a minimal edge zone deterioration. Note that during Test #4 several of the studs near the seams sheared during the latter stages of testing.

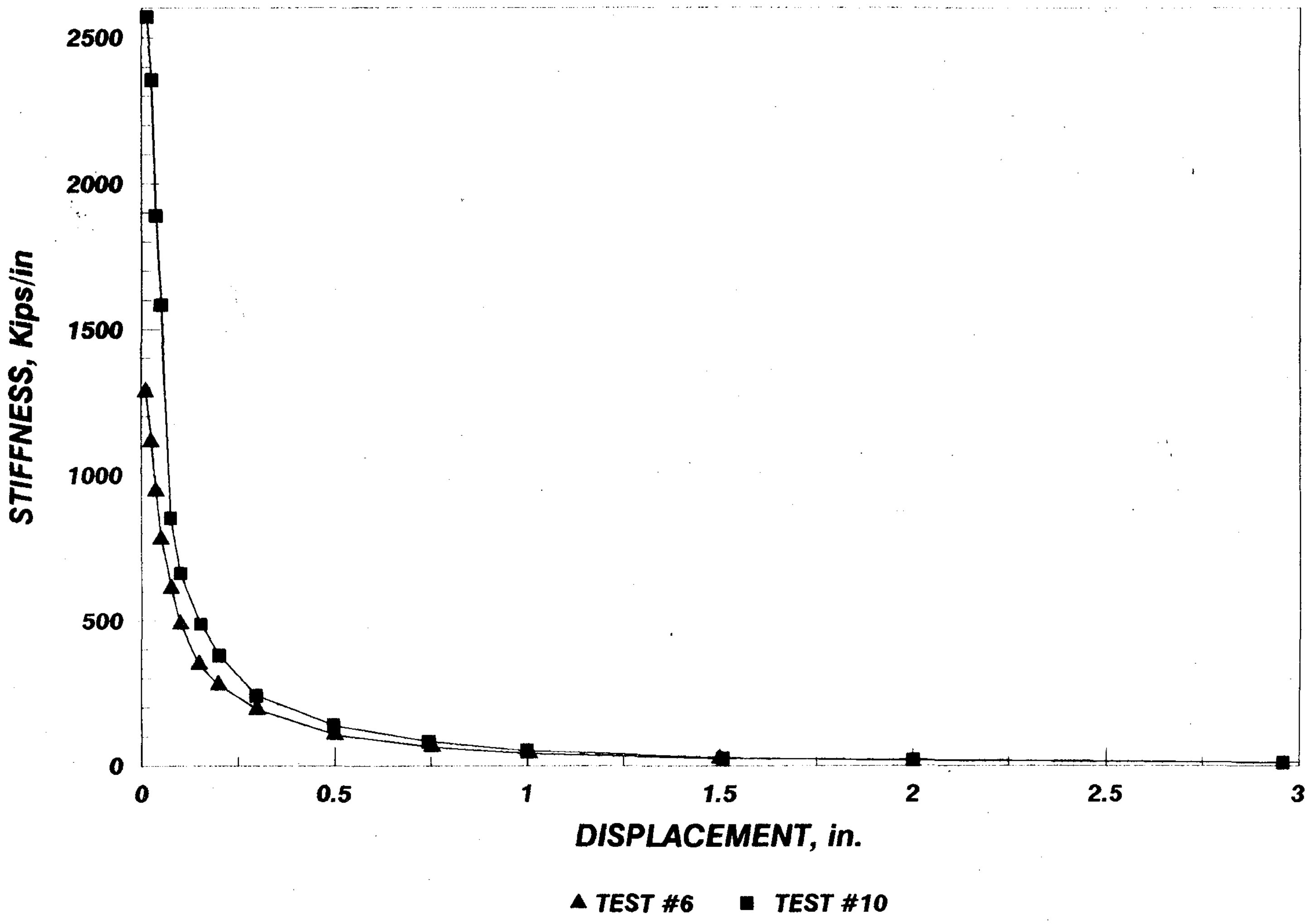

Figure 101. Cyclic stiffness for Tests #6 and #10

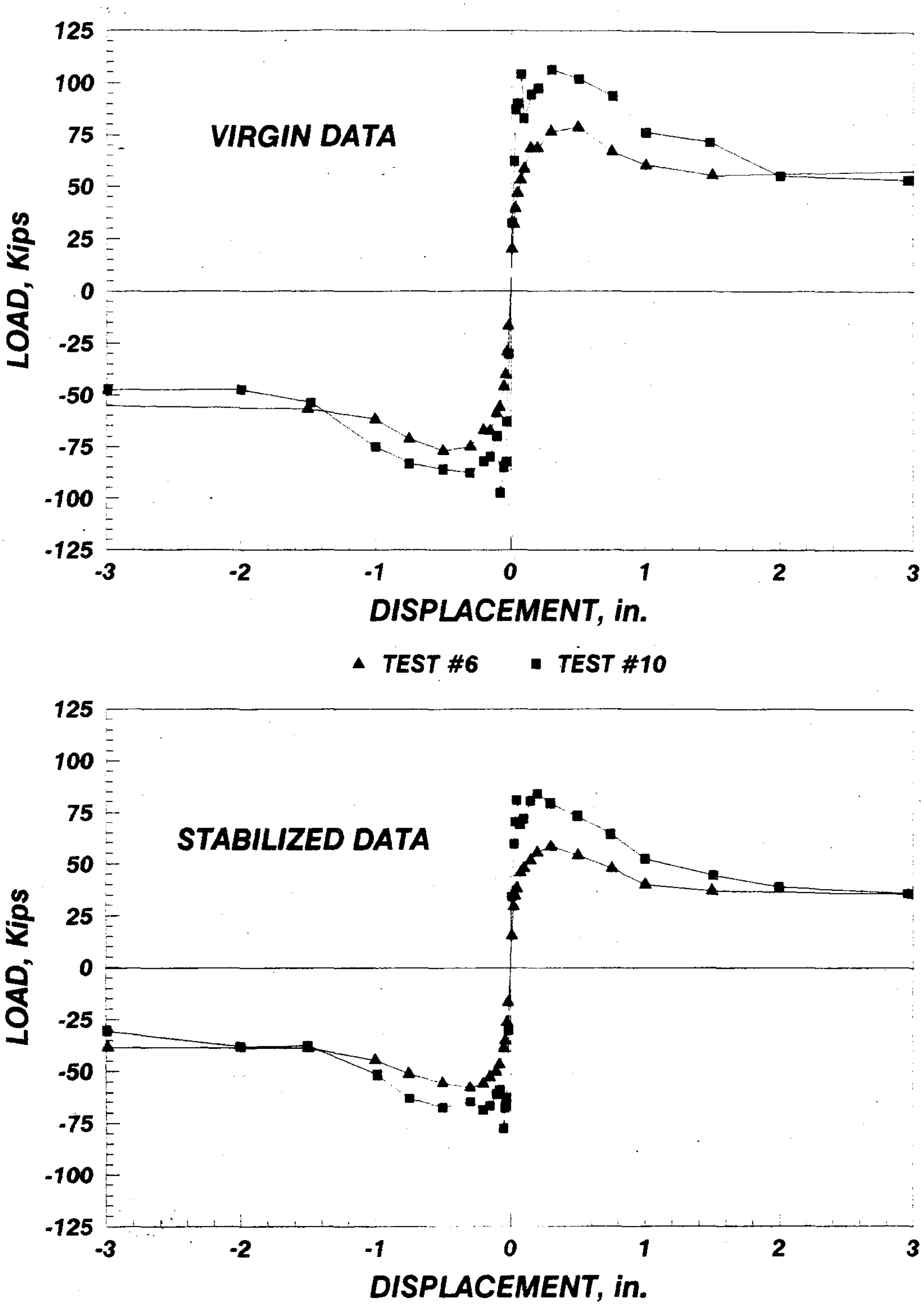

Figure 102. Envelope curves for Tests #6 and #10

Data from the stiffness versus cyclic displacement plots for Tests #4 and #12 (see Figure 103) indicate that stiffness was greater for Test #12 for all displacements. The initial stiffness for Test #12 was 1596 kips/in. which represents an increase of 24.6% with respect to the Test #4 initial stiffness of 1281 kips/in. An increase in Test #12 stiffness was expected due to the additional 2-inch topping on the Test #12 diaphragm.

Figure 104 is a comparison plot of the Test #4 and #12 virgin envelope curves. The general shape of the graph demonstrates that larger loads were recorded for Test #12 than for Test #4, through the 1.0 inch displacement increment. The ultimate strength for Test #12 of 135.8 kips represents a 50% increase with respect to the maximum load of 90.5 kips for Test #4. Limit state strengths were 119.7 kips and 70.0 kips for Tests #12 and #4, respectively. The increase in load capacity of Test #12 can be attributed to the 2 inch nominal thickness topping, which provided for a 62% increase in average slab depth. The FME for Test #12 was recorded at 0.3 inch displacement and load of 127.5 kips (diagonal tension failure). The seams did not crack during Test #12 (except during the late stages of testing) indicating the absence of a shear-bond or tensile-bond failure. The FME load for Test #4 was 88.0 kips and resulted from a shear-bond failure at the seam and grout interface.

4.5.3 Comparison of Tests #5 and #13

Tests #5 and #13 were oriented with the diaphragm seams transverse to the loading beam with all four sides of the planks fastened to the testing frame. Test #5 had a plank thickness of 8 inch, while Test #13 had a plank thickness of 8 inch plus 2 inch of topping.

The failure mode for Test #5 was seam shear-bond failure at an FME load of 84.0 kips. All seams failed during this test. The failure mode for Test #13 was diagonal tension with no seam failures recorded. The FME load of Test #13 was 230.4 kips, which represents a 174% increase with respect to Test #5. The addition of the topping with Test #13 causes a significant and beneficial behavior alteration.

Figure 105 is a comparison plot of the cyclic stiffness for Tests #5 and #13. Test #13 generally had higher stiffness values than Test #5 as expected due to the addition of the topping. The initial stiffness for Test #13 was 2698 kips/in., which represents an increase of 34.9% with respect to the Test #5 value of 2005 kips/in.

The stabilized displacement curves for Tests #5 and #13 are shown in Figure 106. The general shape of the curves shows that generally a larger load was recorded for Test #13 displacements, especially during the range from 0.1 inch to 0.75 inch. After displacements of 1 inch the recorded loads are similar for each test. The maximum load recorded for Test #13 was 295.6 kips compared to an ultimate load of 109.0 kips attained during Test #5, indicating the potential strength benefits of adding a topping to the diaphragm system.

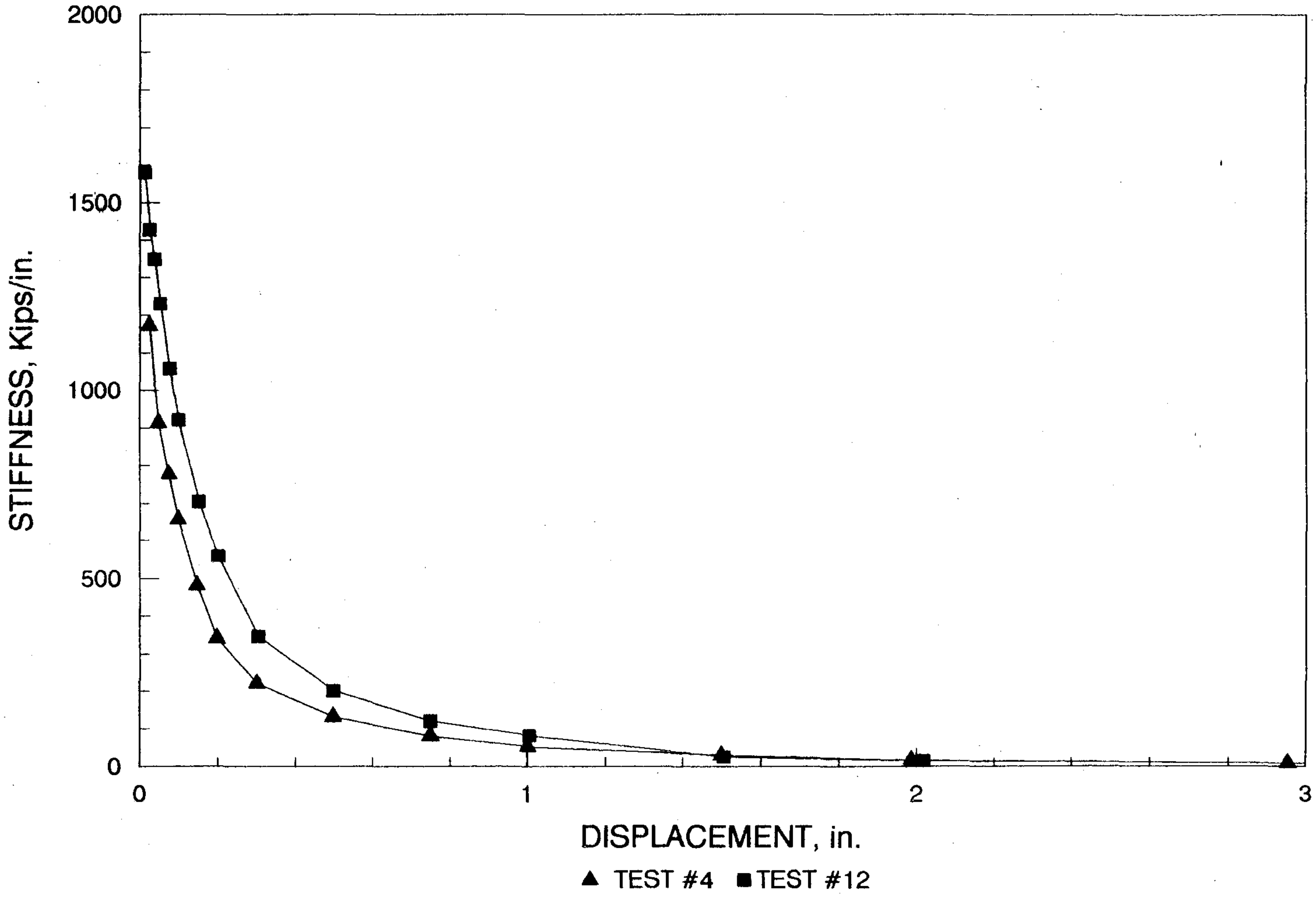

Figure 103. Cyclic stiffness of Tests #4 and #12

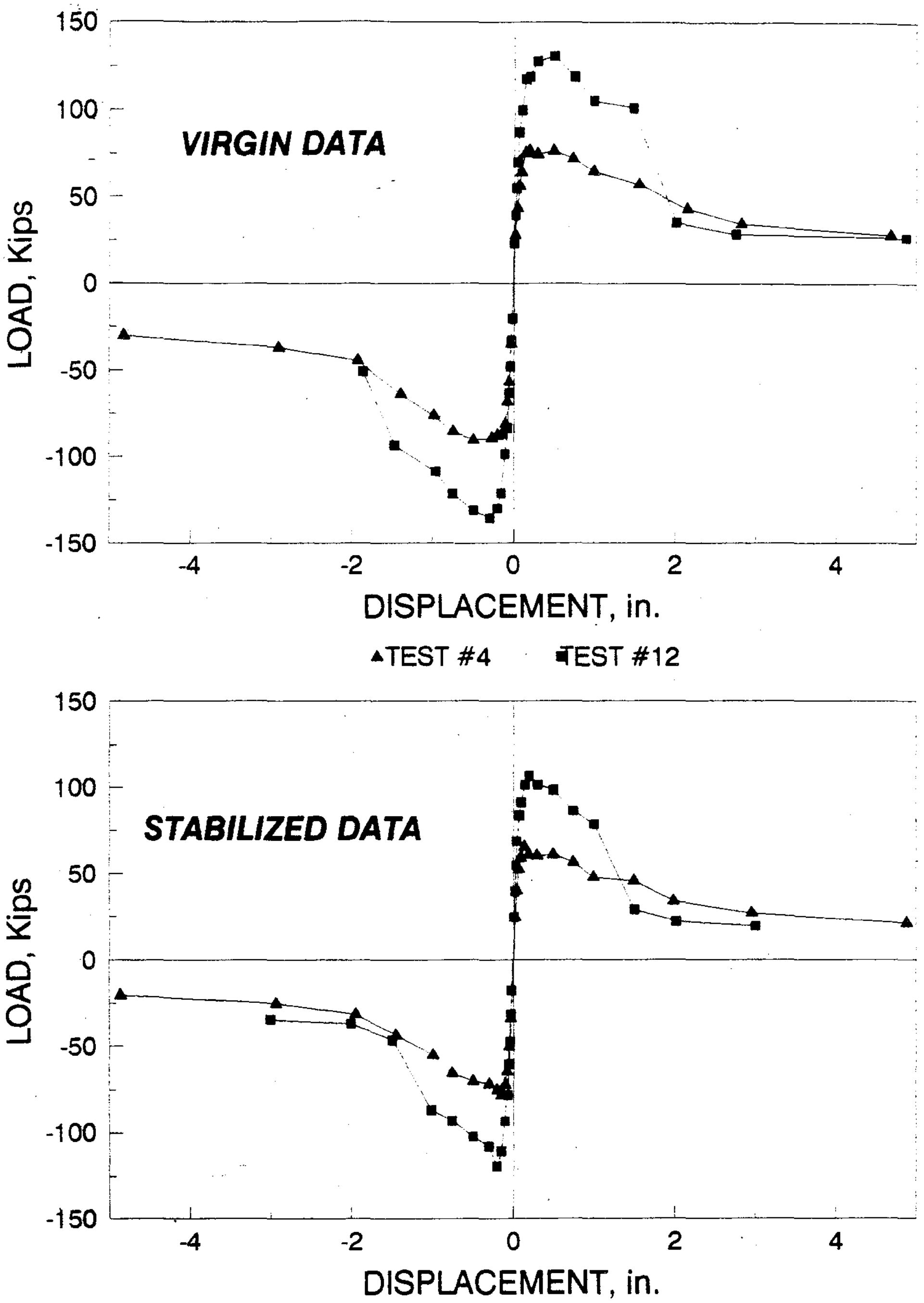

Figure 104. Envelope curves for Tests #4 and #12

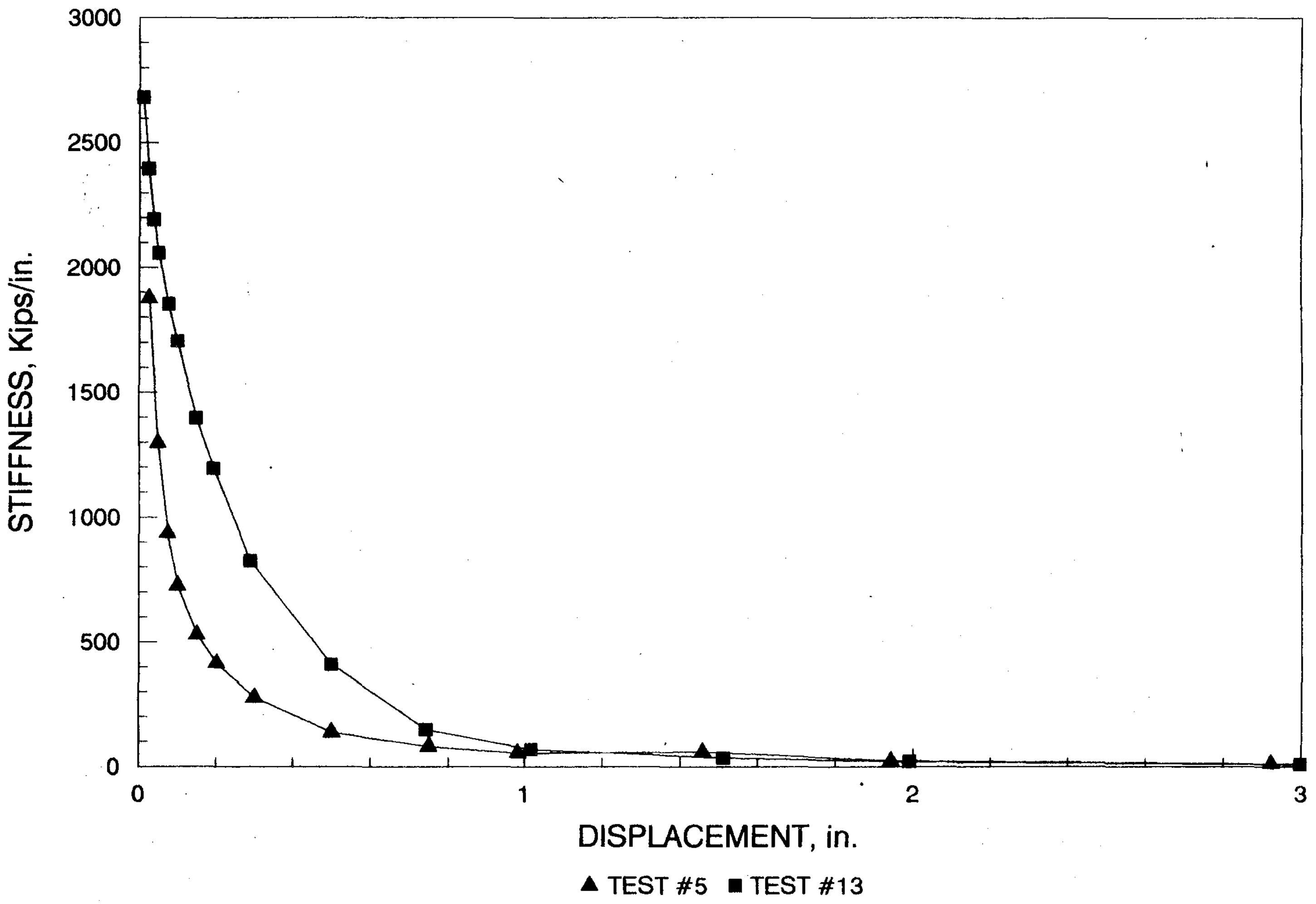

Figure 105. Stiffness comparison of Tests #5 and #13

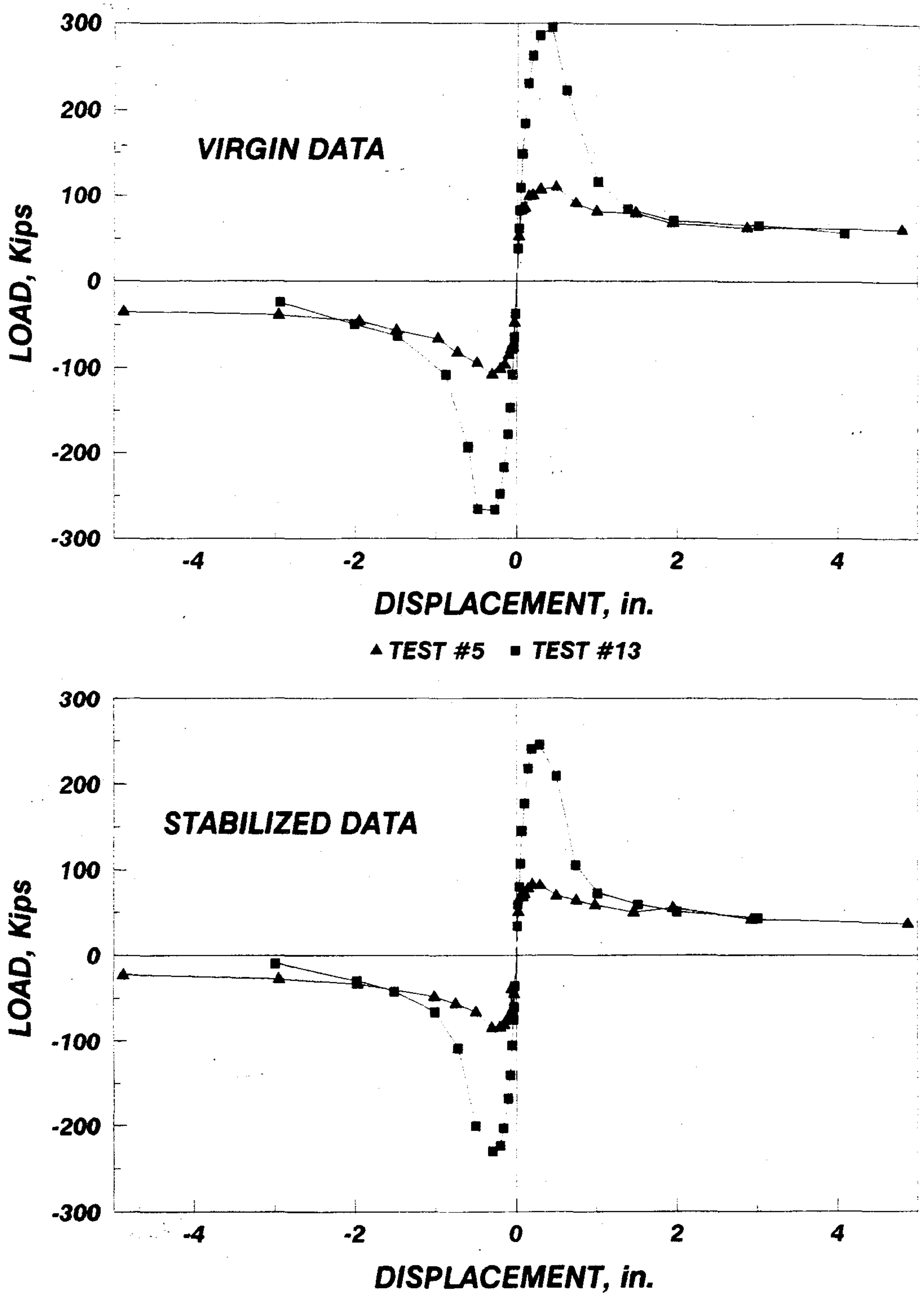

Figure 106. Envelope curve comparisons of Tests #5 and #13

4.5.3 Comparisons of Tests #6 and #14

Data from the stiffness versus cyclic displacement plots for Tests #6 and #14, see Figure 107, indicate that stiffness were greater for Test #14 for all displacements. The initial stiffness for Test #14 was 3289 kips/in., which represents an increase of 123% with respect to the Test #6 initial stiffness of 1474 kips/in. The increase in stiffness that the topping contributed was quite significant.

The FME load for Test #14 of 260.8 kips was reached as the diaphragm recorded a diagonal tension failure. In contrast, Test #6 was a seam tensile-bond failure and yielded a FME load of 31.9 kips. Figure 108 is a comparison plot of the virgin envelope curves for Tests #6 and #14. Test #14 generally required a much larger load for displacements than the loads for Test #6. The maximum load for Test #14 was 302.0 kips, which represents a 284% increase with respect to the maximum strength for Test #6 of 78.6 kips. This increase in capacity for Test #14 was expected due to the additional 2 inch topping.

4.6 Summary of Experimental Results

A summary of test results for the diaphragms which are included in this study is given in Table 4. Included in this table are the load and displacement at the limit state, the load at first major event and the initial stiffness for each test.

Several comparisons were made in order to study the boundary condition parameter. Boundary conditions are extremely important in achieving maximum diaphragm action. A definite correlation between the number of sides connected and the amount of diaphragm action achieved was determined. Connecting four sides results in the greatest strength and stiffness and is thus the most desirable.

Comparisons involving the orientation of the planks within the diaphragm revealed that the most diaphragm action was obtained by placing the planks transverse to the applied shear load. Higher strengths and stiffness were obtained in those systems which were oriented transverse to the loading beam. One possible theory associated with this phenomenon is that the diaphragms with planks oriented parallel to the applied shear load initially crack primarily tension across the seam joints. This event is most clearly demonstrated in Test #8. The FME and other seam cracks in this test were documented as being caused by a tensile splitting of the seam between the two southernmost planks. Diaphragms #6 and #7 also revealed a similar situation although not to the extent shown in Test #8. The boundary conditions of the two latter tests prohibited the dramatic tensile cracking which Test #8 demonstrated. With the seams of the planks oriented transverse to the applied shear load, the system cracked in shear-bond between the planks. Although tension was present at these locations, it was not the controlling mode of failure. Calculations will be presented in Chapter 6 which will validate this theory.

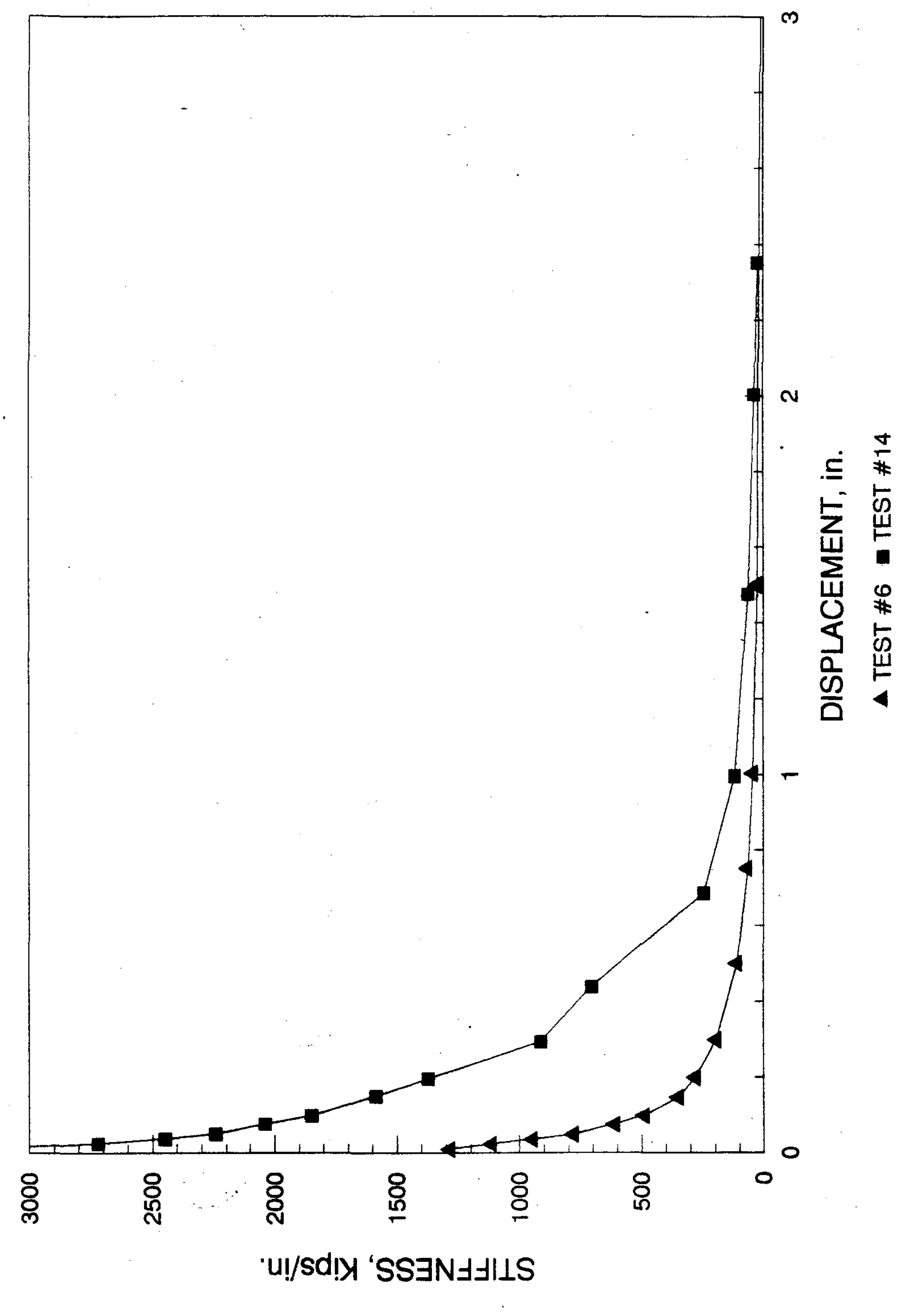

Figure 107. Cyclic stiffness of Tests #6 and #14

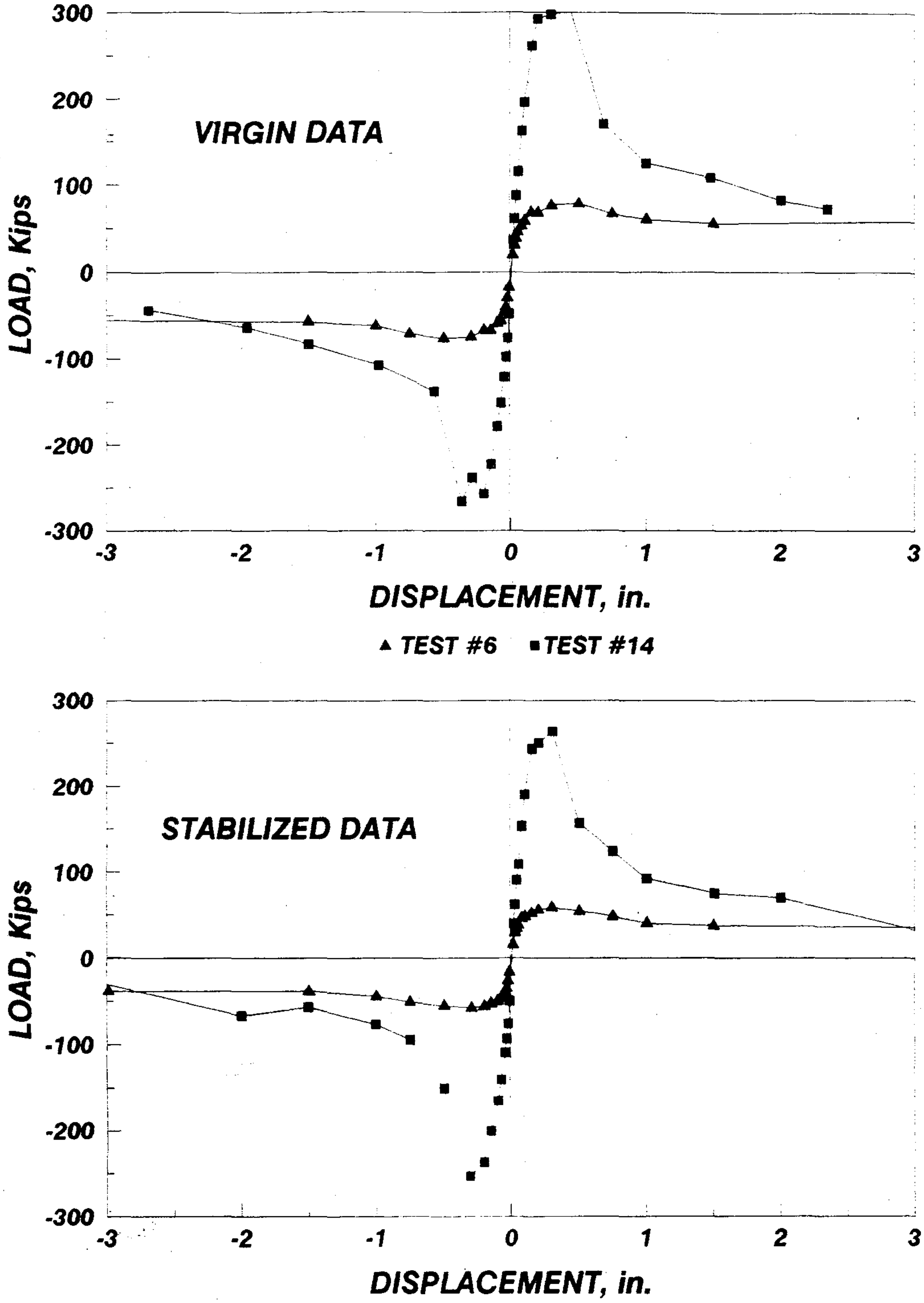

Figure 108. Envelope curve comparisons of Tests #6 and #14

Table 4. Diaphragm Test Results

Test No.	Initial Stiffness (Kips/in)	FME Load (Kips)	Limit State Displacement (in.)	Limit State Load (Kips)
1	1375	70	-----	83
2	675	68	-----	58
3	504	22	-----	22
4	1281	88	0.496	91
5	2005	84	0.490	110
6	1376	32	0.500	79
7	1647	20	0.133	74
8	716	19	0.498	36
8b	1003	43	0.099	78
9	1486	78	0.151	78
10	2734	82	0.303	106
11	2143	118	0.303	127
12	1569	127	0.292	136
13	2698	230	0.433	296
14	3298	261	0.440	302
15	2518	98	0.514	220

Notes:

Test #1 experienced hydraulic surge.

Test #3 had only two planks and experienced rigid body motion.

Test #4 is a duplicate of Test #1.

A study of the thickness parameter revealed several interesting conclusions. For planks oriented transverse to the applied shear load, the greater the diaphragm depth, the greater the diaphragm strength and stiffness. The 12-inch depth demonstrated the failure mode of diagonal tension prior to also failing in shear-bond. This diagonal tension mode hastened deterioration of the diaphragm energy absorption capacity. For planks oriented parallel to the applied shear load, the 8-inch diaphragm yielded lower FME and limit state strengths than the 6-inch system, contrary to expectation.

A review of the final parameter, the addition of the a two-inch topping, revealed that topping created a much stiffer and stronger system. The general effects of the other parameters, such as boundary condition, were still apparent and similar to those observed in the untopped tests. However, the effect of the orientation in topped diaphragms was not apparent. The failure mode for the topped diaphragms was diagonal tension regardless of orientation.

5. EXPERIMENTAL RESULTS OF ELEMENTAL TESTS

As discussed in Chapter 4, most of the untopped diaphragm tests conducted indicate that the limit state was reached when the seam connection between the adjacent panels failed. Many of the articles discussed in Chapter 2 reached a similar conclusion. A series of elemental tests was therefore undertaken to study the behavior of the various types of seam connections under both direct shear and tensile loading conditions.

5.1 Preliminary Shear Test Results

The first elemental shear test was performed on full-scale hollow-core plank specimens. The specimens utilized weld ties and grouted connections. Reversed cyclic loading (without degradation cycles) was followed throughout the test. A maximum load of 25.2 kips was recorded before slip was noted, at which time the load began to stabilize. Failure was attributable to exposure of one of the horizontal studs of the weld tie. In order to evaluate the strength of the unbroken seam, the ram was positioned closer to the unfailed seam. A significantly greater peak strength of 33.7 kips was recorded for the latter seam.

The average seam depth of the weaker seam was recorded as 5.5 inches. This value yielded a modified shear stress of 62 psi. The stronger seam had a grout depth of 6.5 inches and a modified shear stress of 161 psi. (The term modified shear stress accounts for the non-uniformity in the shear stress distribution of a small elemental specimen, as stated in Chapter 2.) Due to the amount of scatter in the results of the preliminary test, the need for others was evident. A revised design, however, was opted for, since cost needed to be minimized.

5.2 Shear Test Results

This section contains a description of the elemental shear tests completed as part of this project. Table 5, summarizes the significant data for each of the elemental shear tests. The key for the specimen name and for the failure mode is listed on the last page of this table. The most significant columns of the table are the FME load, the failure mode type, and the average grout penetration depth. The ultimate strength reflects the effect of the weld tie, since it allows for the development of normal forces. Although the ultimate strength is significant, this value is only applicable to these particular elemental tests and may not be extended directly for use in the diaphragm tests. Figure 109 presents the results of each series.

5.2.1 GOSM Series

The GOSM series was performed in order to study the behavior of a seam which had a grouted connection only. The nomenclature denoted the parameters which were under consideration. As stated in Table 5, these tests involved a seam which contained grout only. This grout was bonded to an eight-inch plank with smooth edges and tested monotonically. The term smooth edges indicated that

Table 5. Elemental Shear Test Summary

Elem. Test No.	Specimen Name	FME Load (kips)	FME Displ. (in.)	Ultimate Strength (lbs.)	Displ. at Ultimate (in.)	Failure Mode	Strength (psi)	Avg. Grout Penetr. (in.)
1	GWSM 1	12503	.013	13072	.017	I	2961	7.0
2	GWSM 2	16025	.005	17021	.021	I	2852	7.5
3	GWSM 3	14029	.017	14817	.269	II	2852	6.5
4	GWSM 4	16031	.003	16031	.003	II	3630	7.5
5	GWSM 5	17258	.006	17760	.225	III	3630	7.5
6	GWSM 6	9772	.004	13259	.054	I	3630	7.5
7	GOSM 1	-	-	21610	Instant.	IV	5178	7.5
8	GOSM 2	-	-	21308	Instant.	IV	5178	7.5
9	GOSM 3	-	-	14265	Instant.	IV	5178	5.0
10	GOSM 4	-	-	10065	Instant.	IV	5178	6.5
11	GOSM 5	-	-	27778	Instant.	IV	5633	7.5
12	GOSM 6	-	-	20000	Instant.	IV	5633	6.0
13	GWSC 1	7707	.005	22147	.107	V	2933	7.0
14	GWSC 2	11804	.002	16428	.056	V	2933	5.0
15	GWSC 3	8172	.005	17978	.021	V	2933	5.5
16	GWSC 4	12973	.004	16858	.109	VI	4086	5.0
17	GWSC 5	14708	.005	17032	.056	V	4086	5.5
18	GWSC 6	9905	.003	12935	.106	I	4086	6.0
19	GWUM 1	-	-	10222	.036	II	3630	---
20	GWUM 2	-	-	9530	.205	III	3630	---
21	GWUM 3	-	-	10865	.540	I	3630	---
22	GWUC 1	-	-	12302	.016	I	4190	6.0
23	GWUC 2	-	-	11725	.033	I,II	4190	6.5
24	GWUC 3	-	-	11985	.198	II,III	5190	6.5

Table 5. Continued

Elem. Test No.	Specimen Name	FME Load (kips)	FME Displ. (in.)	Ultimate Strength (lbs.)	Displ. at Ultimate (in.)	Failure Mode	Strength (psi)	Avg. Grout Penetr. (in.)
25	TOPW 1	-	-	43190	Instant.	IV	4419	6.0
26	TOPW 2	-	-	46830	Instant.	IV	4419	7.875
27	TOP 1	-	-	34120	Instant.	IV	4419	5.25
28	TOP 2	-	-	53240	Instant.	IV	4419	4.875
29	TOP 3	-	-	40060	Instant.	IV	4419	5.625
30	TOP 4	-	-	39840	Instant.	IV	4419	6.50
31	GORM 1	-	-	25130	Instant.	IV	3867	5.75
32	GORM 2	-	-	15520	Instant.	IV	3867	4.25
33	GORM 3	-	-	29850	Instant.	IV	3867	6.125
34	GORM 4	-	-	36940	Instant.	IV	3867	6.375
35	GORM 5	-	-	22350	Instant.	IV	3867	5.375
36	GORM 6	-	-	21340	Instant.	IV	3867	5.375
37	GOSM 7	-	-	7191	Instant.	IV	4176	5.25
38	GOSM 8	-	-	8911	Instant.	IV	4176	7.25
39	GOSM 9	-	-	8963	Instant.	IV	4176	6.50
40	TOPNM 1	-	-	30970	Instant.	IV	4176	6.00
41	TOPNM 2	-	-	32190	Instant.	IV	4176	6.75
42	TOPNM 3	-	-	29130	Instant.	IV	4176	6.50
43	GO6SM 1	-	-	6800	Instant.	IV	3015	5.75
44	GO6SM 2	-	-	6201	Instant.	IV	3120	5.75
45	GO6SM 3	-	-	6305	Instant.	IV	3437	5.75
46	GW6SC 1	12986	.003	14878	.011	VII	3543	5.75

Table 5. Continued

Elem. Test No.	Specimen Name	FME Load (kips)	FME Displ. (in.)	Ultimate Strength (lbs.)	Displ. at Ultimate (in.)	Failure Mode	Strength (psi)	Avg. Grout Penetr. (in.)
47	GW6SC 2	8846	.003	17051	.324	VII	3754	5.75
48	GW6SC 3	9004	.003	14439	.001	VII	3859	5.75
49	GWSM 7*	-	-	18760	Instant.	IV	3203	8.00
50	GWSM 8*	-	-	20479	Instant.	IV	3365	8.00
51	GWSM 9*	-	-	19333	Instant.	IV	3203	8.00
52	GWSC 7*	18622	.002	22526	.023	VII	3203	8.00
53	GWSC 8*	28200	.002	29154	.005	VII	3203	8.00
54	GWSC 9*	24000	-	31300	---	VII	3203	8.00

Failure Mode Key:

I	Vertical bar uncovered
II	Horizontal bar pop-out
III	Vertical bar weld sheared
IV	Brittle seam crack
V	Weld at connecting angle broke
VI	Horizontal bar weld sheared
VII	Diagonal fracture of outer slab through weld tie location

Name Key:

G	Grout
M	Monotonic
W	Weld tie
S	Smooth bond
C	Cyclic testing
O	Only
R	Roughened edges
U	Unbonded
TOP	Monolithically cast topping
TOPW	Same as TOP but with wire mesh
6	6-inch specimen (opposed to 8-inch)
TOPNM	Non-monolithically cast topping
*	Different style of weld tie

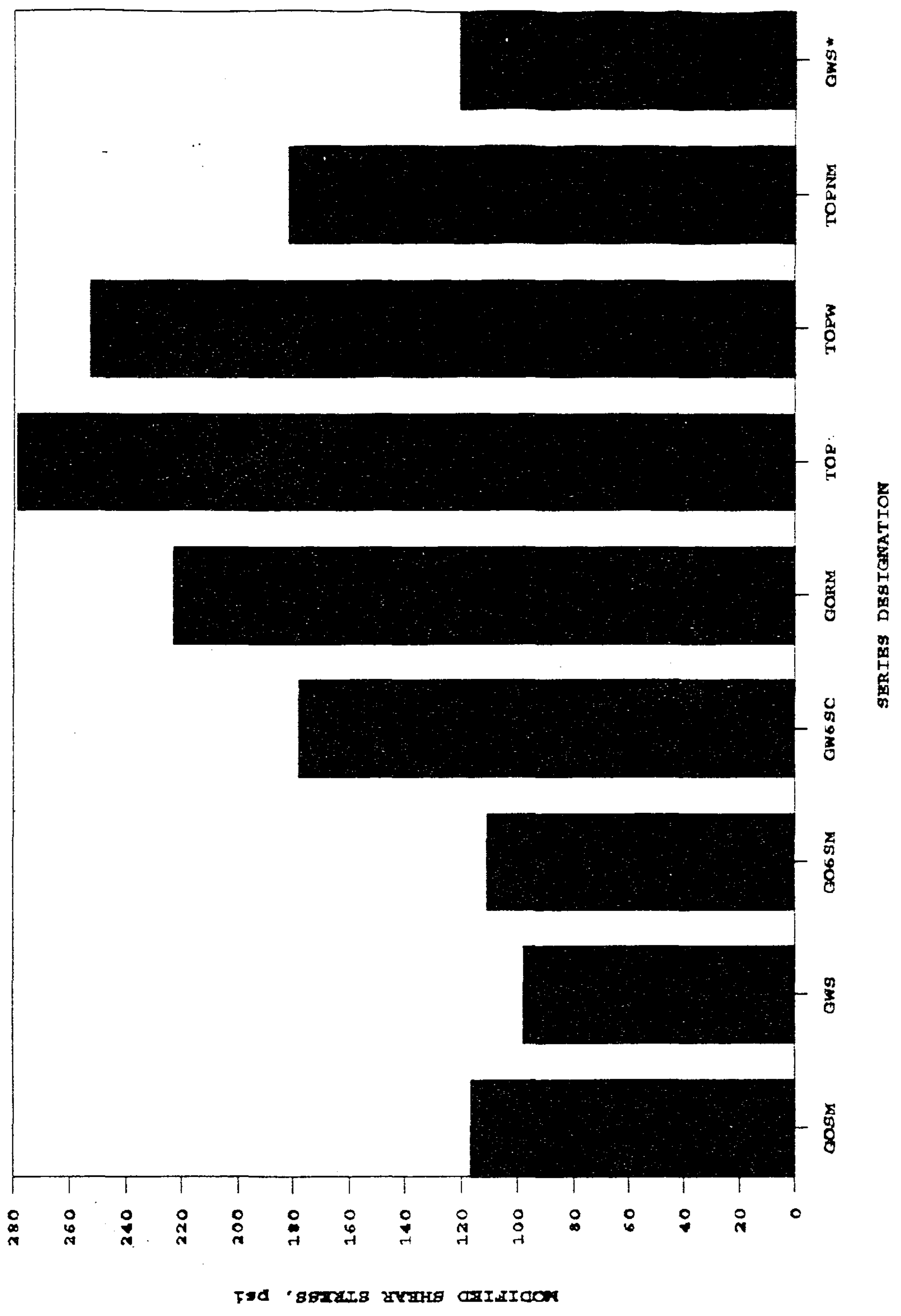

Figure 109. Elemental shear test results

the bonded edges were not intentionally roughened. Nine tests were performed in this series.

As expected, failure of the GOSM series was quite sudden. No slip occurred until one seam had fully cracked. At this point, the specimen rotated noticeably and one of the exterior planks became completely separated from the remaining two units. The average ultimate strength was 20,992 lbs. The average maximum shear stress was 117 psi which exceeded the conservative value of 80 psi recommended by the Prestressed Concrete Institute (9,10).

At the conclusion of these tests, the components were put back together on the testing frame. A normal force was applied to the sides of the specimen. Shear force was again applied and the value of load at which slip occurred was recorded. This load was divided by the normal force in order to obtain the coefficient of friction. The results of these tests varied due to the sensitivity of the procedure; however, an average conservative value of 0.95 was obtained.

5.2.2 GORM Series

The purpose of the GORM series was to determine the effect of roughened edges on the behavioral characteristics of the grouted seam. As the name designated, this series of tests utilized a seam which was grouted to eight-inch thick roughened edges. These specimens also exhibited a sudden, brittle failure thereby eliminating cyclic tests of this nature.

The tests in this series performed very much like the tests of the GOSM series. The limit state strength, however, was considerably higher. The average ultimate strength was 25,188 lbs which represented a 20% increase over the GOSM series. The average ultimate shear stress for this series was 223 psi which corresponded to a 90% increase over the previous series. Therefore, intentional roughening of the adjacent plank edges dramatically increased the strength of the seam.

5.2.3 GWS Series

This series of tests was conducted in order to study the behavior of a seam with both grout and weld tie connections. Unlike the previous tests, this series revealed a more ductile behavior. This type of behavior allowed for testing of these specimens both cyclically and monotonically. Six specimens were tested under each loading condition.

For those specimens which were tested monotonically, the load was applied slowly from one direction until the seam cracked. After the grout had cracked, the weld ties served to clamp the specimen together. As the load, and consequently the slip, increased, concrete surrounding the horizontal and vertical deformed studs began to spall and crack. Eventually, the shear capacity of the weld tie or the surrounding concrete was reached. The average ultimate shear stress (at cracking of the grout) was 98 psi and the average ultimate load (at weld tie failure) was 15,327 lbs.

Those specimens tested cyclically behaved somewhat differently. Loading commenced with ram #1 and continued until the groat in one of the seams cracked and the displacement reached 0.025". An average ultimate shear stress of 98 psi was recorded for these specimens. The load was then reversed until a displacement of 0.025" in the other direction was reached. Testing continued as discussed in section 3.2.4.1. Cracking and spalling developed around the weld tie early in the test. The average limit state load was 17,230 lbs.

5.2.4 GWO Series

The GWO Series was performed to study the behavior of the weld tie alone. The name designated that the specimens employed unbonded grout and weld ties in eight-inch thick specimens. Six tests were performed in this series.

During construction of the planks, a layer of plastic was inserted on both sides of the seam. Although this procedure greatly reduced frictional forces, it did not completely eliminate them. The tests were conducted both monotonically and cyclically and resulted in an average limit state strength of the two seams of 10,205 lbs and 12,004 lbs, respectively.

5.2.5 GO6SM Series

With the inclusion of the six-inch thick diaphragms into the testing array, this series type, with its new profile, naturally followed. The nomenclature of this series implies that the tests contained only grout bonded to smooth seams and utilized monotonic testing procedure. Three specimens of this nature were completed.

The GO6SM series posted an average modified shear stress of 56 psi, which was considerably lower than the GOSM series. Two explanations exist for this significant decrease. The first option is that the slight increase in grout strength (of the GOSM series) created a better bond, thus providing for larger strengths. The second option is that unrepresentative results were obtained due to the small sample size.

5.2.6 GW6SC Series

As with the previous series of elemental tests, this set of tests was designed to determine the characteristics of the six-inch specimen thickness. The nomenclature of this series reflects a seam with weld tie and grout bonded to smooth edges and cyclic testing. Three specimens of this type were tested. The average modified shear stress value for this series was 89 psi which is comparable to the GOSM series. One interesting feature in comparing the six- and eight-inch depth tests was that the effective grout areas were only slightly higher for the eight-inch series. This phenomenon was due to the difficulties associated with grouting the eight-inch seam profile.

5.2.7 TOP Series

Several of the planned diaphragm tests utilized a nominal two-inch topping; therefore, a series of topped elemental tests was deemed necessary. Four specimens of this type were tested. Failures for this series were similar to those of the untopped specimens, with cracks propagating through the grout/slab interface in the seam and directly above through the topping. The average modified shear stress for this series was 253 psi, which represents a 139% increase over the GOSM series. This comparison is not direct, since the topping failure strength was dependent upon the topping compressive strength, as opposed to the interface strength.

5.2.8 TOPW Series

This series of elemental tests was similar to the preceding series (TOP) with the exception of the reinforcement of the topping. The TOPW series utilized a weld wire fabric in the topping to prevent temperature and shrinkage cracks. Two tests of this nature were completed. Comparisons of strength data at the FME reflect a 7% increase in average strength over those topped tests which did not possess the weld wire fabric. The average modified shear stress suggests a value of 253 psi for this series, which is the same as for the previous series.

5.2.9 TOPNM Series

The purpose of this series was to investigate the effects of casting the grout in the seams and the topping at different times. The nomenclature of this series represents topped tests non-monolithically cast. Three tests of this type were performed. The average modified shear stress was 182 psi which represents a 56% increase in maximum stress over the GOSM series. As expected, the stress for this series was significantly lower than for the TOP and TOPW series.

5.2.10 GWSM* and GWSC* Series

Although the standard weld tie was used in the diaphragm tests, another type of weld tie with a continuous bar was also being manufactured. (See Figure 6 for a comparison of the two types of weld ties.) This series of six tests was therefore designed to determine the characteristics of this alternate type of tie. Results of the FME average modified shear stress for the monotonic tests were comparable (121 psi). The average ultimate strength of this series was 14,317 lbs which represents a 12% reduction over the strength of the original type of weld tie.

5.3 Tension Test Results

Those diaphragms with planks oriented parallel to the loading beam exhibited a combined shear and tension failure. The strength and behavioral characteristics of a seam in tension, therefore, were essential to the analytical investigation of the full-scale diaphragm tests. The significant data from each of the elemental tension tests is included in Table 6. This table lists the

Table 6. Elemental Tension Test Summary

Elem Test No.	Specimen Name	FME Strength (lbs)	Ultimate Strength (lbs)	Seam Strength (lbs)	Avg. Grout Penetr. (in.)
1	TGO6S1A	--	7295	3821	5.00
	B	--	8494	3821	5.25
2	TGO6S2A	--	4325	3821	5.50
	B	--	5159	3821	5.75
3	TGO6S3A	--	6879	3821	5.00
	B	--	--	3821	5.75
4	TGOS1A	--	11673	3821	6.50
	B	--	--	3821	6.00
5	TGOS2A	--	8494	3821	6.00
	B	--	--	3821	6.25
6	TGOS3A	--	10005	3821	7.00
	B	--	11464	3821	7.00
7	TGW6S1A	3231	4742	3821	5.00
	B	--	5055	3821	5.50
8	TGW6S2A	3908	5107	3821	5.25
	B	4325	6670	3821	5.375
9	TGW6S3A	3752	5570	3821	5.50
	B	3908	5263	3821	5.00
10	TGWS1A	6201	6201	3821	6.00
	B	--	5680	3821	6.00
11	TGWS2A	9953	--	3821	7.00
	B	11829	11829	3821	7.75
12	TGWS3A	5211	5211	3821	5.50
	B	--	--	3821	6.50

Note:

Failure mode of weld ties was spalling of the concrete surrounding the vertical leg.

ultimate strengths and corresponding displacements. For those specimens without weld-ties, normally only one seam fractured. The remaining portion of the specimen was then reloaded to fracture of the second seam. For those cases where the strength of the second seam was at least as great as the first, it was assumed that the first fracture did not alter the results of the second. The final results of all the tension tests are presented in Figure 110. The tension tests with weld ties usually fractured at both seams simultaneously. Ultimate load was the peak strength recorded for either of the seams. This load was normally associated with the failure of the concrete slab cover near the vertical and horizontal bars of the weld tie and not of the weld tie itself.

5.3.1 TGOS Series

The TGOS series was conducted in order to determine the tensile strength of an eight-inch grouted seam. As the name designated, this series utilized specimens where the seams were grouted to the smooth edges of two eight-inch thick planks. A total of three such tests were conducted.

Tensile load was applied to the specimens in a gradual, continuous manner. No significant events occurred prior to reaching the limit state. At this point, one of the seams instantaneously split. The same procedure was repeated on the remainder of the specimen. The average ultimate tensile stress achieved was 67 psi.

5.3.2 TGWS Series

This series is similar to the preceding one with the exception of the addition of weld ties. Because of the presence of the weld ties; however, the specimens showed a more ductile behavior.

The test procedure was the same as for the TGWS series. After the initial tension crack, the weld ties served to tie the system together. After further loading, the concrete on the slab edge surrounding the vertical leg spalled. The horizontal bar of the weld tie then simply slipped out, resulting in the failure of the specimen.

The average FME strength was only 5,975 lbs. The value is considerably less than the FME strength for the specimen without weld ties. The reason behind this loss in capacity was associated with the area of bonded grout. Those specimens with weld ties have a reduced effective grout area due to the presence of the tie. Thus, taking into account this reduction in area, the average FME stress was 73 psi. This value is quite close to that obtained without the weld ties. The limit state strength (weld tie failure) was 5,680 lbs. During these tests, only the concrete surrounding the weld ties cracked. The results, therefore, were not conclusive due to the eccentricity in the applied tensile force.

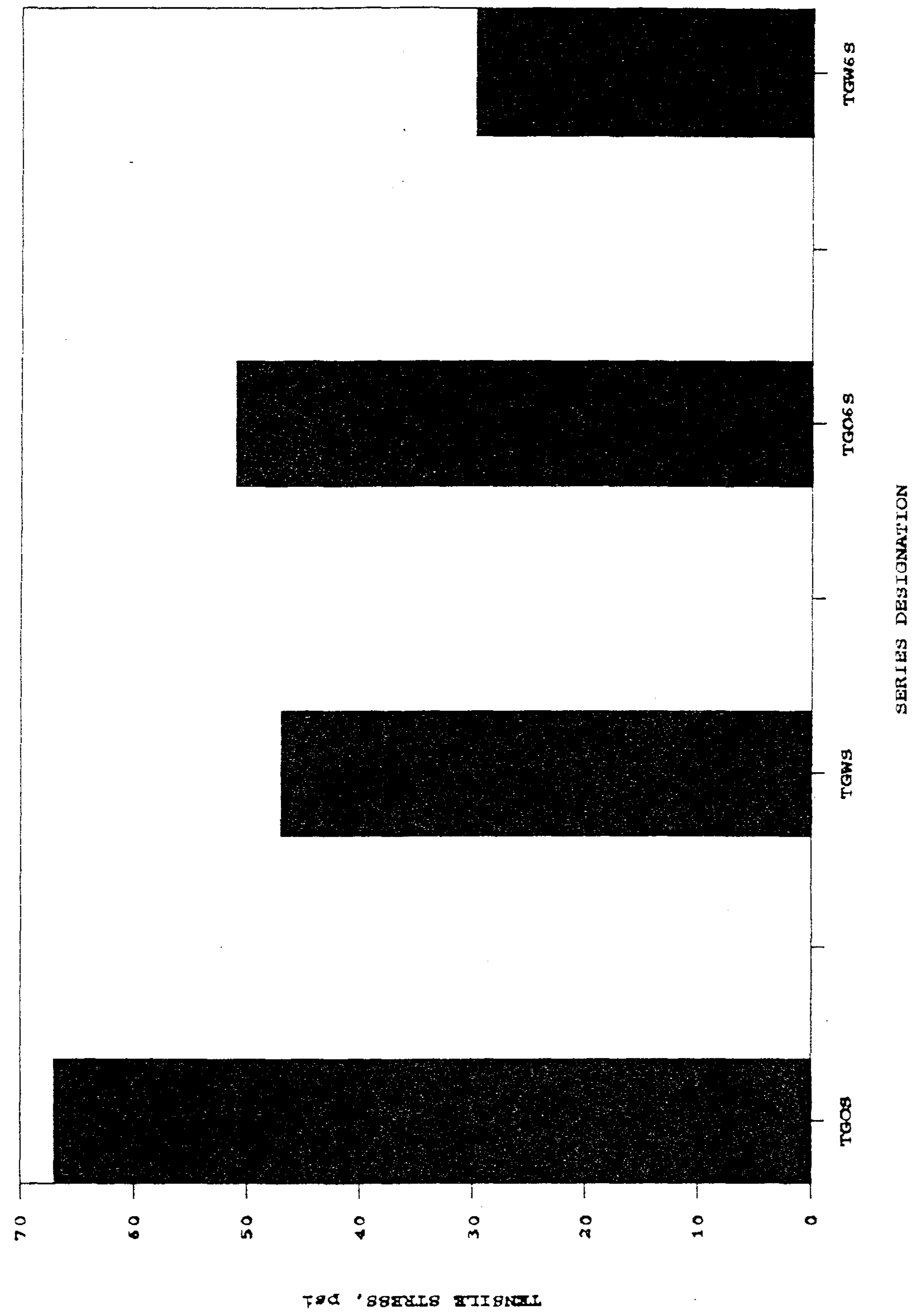

Figure 110. Elemental tension test results

5.3.3 TGO6S Series

Six-inch tension plank tests were also conducted. The seams of the specimens in this series utilized only grout bonded to smooth edges. Three tests were contained in this series. As was the case with the shear tests, grout depths were only slightly smaller due to the difference in seam profiles. An average tensile stress value of only 51 psi and a standard deviation of 14 psi were obtained for this series. The difference between the average stress for this series and that of the previous series (TGOS) could be attributed to experimental scatter.

5.3.4 TGW6S Series

This series of three tension tests was also similar to the eight-inch counterparts. As with the grout only specimens, the six-inch plank tensile specimens with weld ties had a considerably lower tensile strength at grout failure (30 psi). This difference can only be explained by bond intensity related to the condition of the material and bonding surface.

5.4 Summary of Elemental Tests

From the elemental test data, the average ultimate shear strength of the grouted seams approximately 98 psi. This value has been confirmed for tests both with and without weld ties. By roughening the edges of the planks, a much higher shear stress was obtained. In direct tension, the average stress was found to be around 59 psi for both the tests with and without weld ties. The static coefficient of friction for the smooth edged planks was determined to be 0.95. Those tests with bonded grout had a 46% higher limit state strength due to the friction and confining forces introduced by the grout. In shear, the average limit state capacity of the seam with weld ties was approximately 5,500 lbs.

In general, the specimens with grout only exhibited a sudden brittle failure; whereas, the slabs with the weld tie inserts showed a more ductile behavior. The information presented above indicates that most of the initial strength is obtained from the grout; however, the weld ties are required to resist much of the force later in the test. In conclusion, the grout appears to serve as the major strength developing agent, while the weld tie demands a ductile failure.

6. ANALYTICAL INQUIRY

In order to fulfill the final part of the stated objectives, an analytical investigation was undertaken. This study encompassed the development of a method for predicting initial stiffness, FME strength, and limit state strength. This chapter discusses the methods and procedures used in the determination of these items, as well as a comparison of the predicted and experimental results.

6.1 Background

6.1.1 Analysis Techniques

The strength and stiffness predictions for the hollow-core plank systems were based the assumption that the connections between the planks and the testing frame would not fail before the diaphragm reached its limit state. Thus, by determination of the distribution of forces in the edge zone, the forces throughout the diaphragm were studied. The edge zone force concept was used to achieve this first step. This procedure was developed at Iowa State University. A discussion of it may be found in Reference 30 which was later modified in References 9 and 34. As stated in the edge zone concept, the majority of the force transfer occurs in a relatively narrow band around the perimeter, known as the edge zone. For diaphragms connected with studs, the edge zone is the distance from the edge to the point where 95 percent of the horizontal force is transferred from the edge beams to the concrete plank units.

An idealized force transfer distribution was developed by Porter and Greimann [30]. The initial distributions were determined using a general purpose finite element program (SAP 6). In the computer model, the framing beams and the concrete reaction block were connected to the slab using one dimensional spring elements with an assumed stiffness of 30 kips/in./in. The concrete slab was idealized as a thick plate using three-dimensional, 20-node, isoparametric, solids. Figure 111 shows the idealized force distribution if the edge springs were in the elastic range. If the edge springs were strained to the perfectly plastic state, the edge distribution appeared as shown in Figure 112. This analysis, failed to account for the axial deformations which occur in the edge beams when the diaphragm is very stiff. Modifications were therefore made by Prins and Dodd (Reference 34 and 9) to account for these deformations. Figure 113 reveals the modified edge zone force distribution of the framing beams.

An additional finite element analysis was accomplished as part of this study and the results obtained in the earlier studies were confirmed. The finite element model consisted of three dimensional elastic beam elements representing the framing beams and three dimensional quadrilateral shell elements modeling the diaphragm. These shell elements possessed both bending and membrane capabilities. Constraint equations were used to form a rigid region connection. Refinement of this model, and consequently improvement of the results, is possible in defining the connections between the planks diaphragm and test frame.

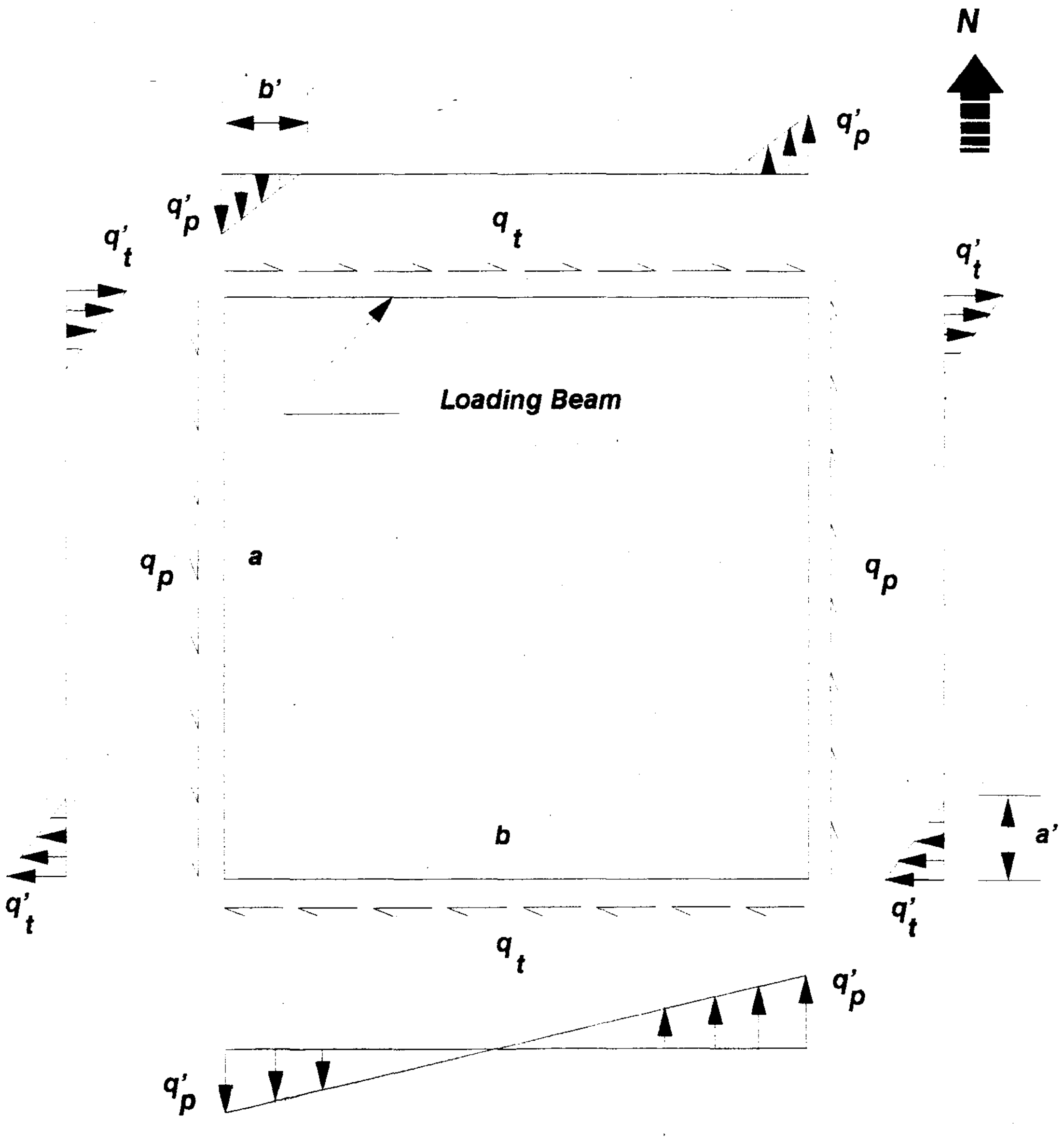

Figure 111. Idealized force distribution in elastic range [30]

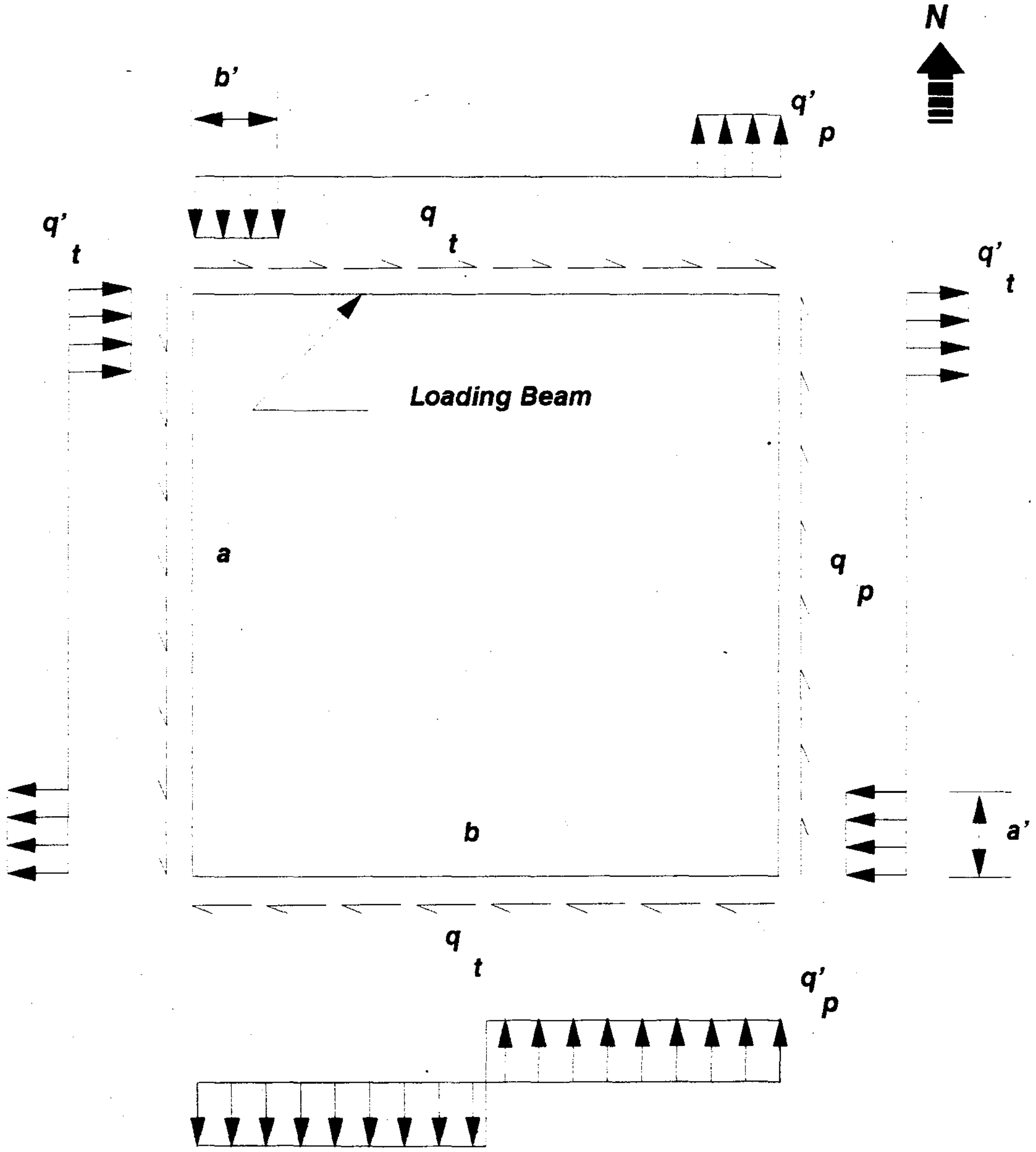

Figure 112. Idealized force distribution in plastic range [30]

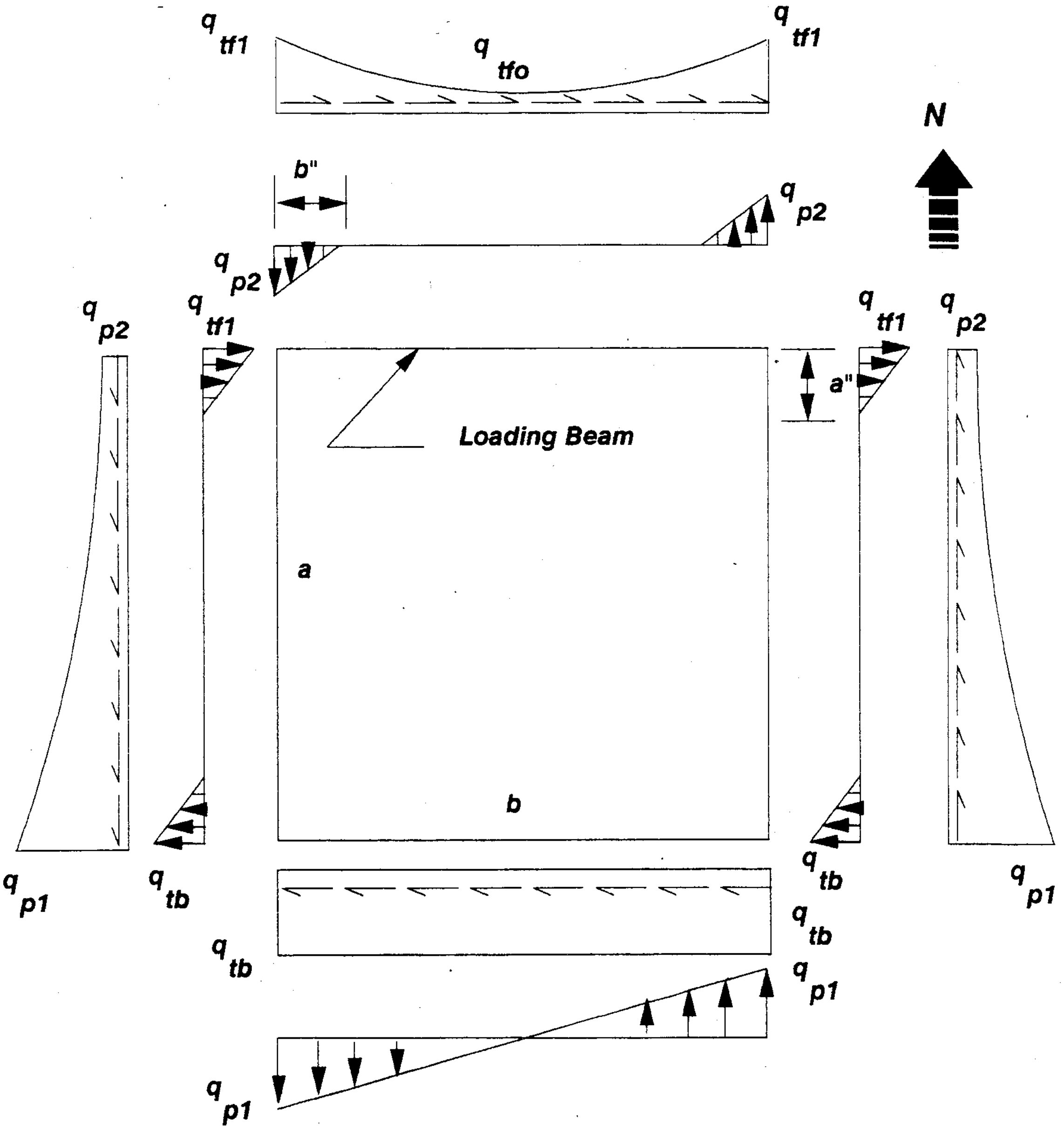

Figure 113. Modified edge zone force distribution [9]

6.1.2 Hysteresis Model Selection

Many different hysteretic models were discussed in Chapter 2. The two models which most accurately represented the hollow-core concrete plank systems were the modified Takeda models and the LPM model. Both of these models employed characteristics necessary to accurately portray the experimental curves such as stiffness degradation and pinching action. The LPM model was ultimately decided upon because the experimental curves fit this model more closely than the other model which was based on a trilinear skeleton curve. Figure 114 compares the LPM and linear curves as well as the experimental data for Iowa State University diaphragm Test #6, as an example.

6.2 Application of Elemental Tests

The elemental tests yielded unit values for limit state stress under both direct shear and tension modes of loading. However, in the actual diaphragm tests, some combination of these modes occurred. The actual proportion of tension and shear forces on the critical seam were some fraction of the maximum possible quantities. Under conditions of cyclic loading, the ratio of tension to shear components was observed to be changing. Conservative values were therefore adopted for use at any time throughout any particular event.

The reduction in tensile and shear values at the bond interface was accomplished by reducing the net stress resultant. The procedure assumed an elliptical curve to represent the interaction between the tensile and shear components as is shown in Figure 115. The resultant stress was established through the method described in Reference 29:

$$R_s^2 = \sigma_c^2 T^2 / (T^2 \sin^2 \Theta + \sigma_c^2 \cos^2 \Theta) \qquad (6\text{-}1)$$

where:

R_s = resultant stress, psi
σ_c = normal tensile stress, psi
T = shear bond stress, psi
$\Theta = \tan^{-1} \sigma/T$

The modified values of shear and tension for the bond were determined as follows:

$$\begin{aligned} \sigma_c' &= R_s (\sin \Theta) \\ T' &= R_s (\cos \Theta) \end{aligned} \qquad (6\text{-}2)$$

The procedure resulted in a reduced tensile stress value of 41 psi and a reduced shear stress value of 68 psi.

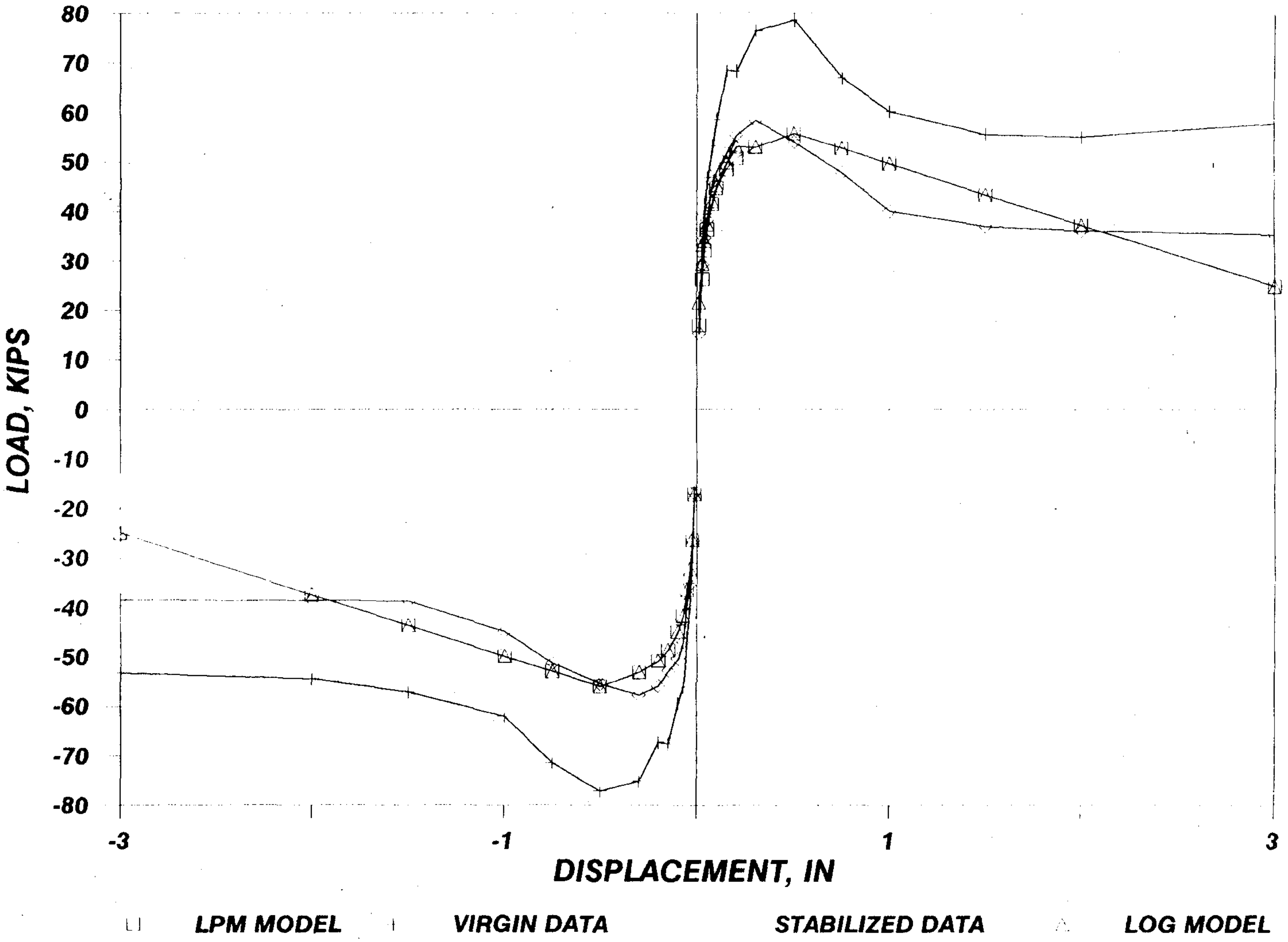

Figure 114. Sample comparison of hysteresis curves for Test #6 including experimental data

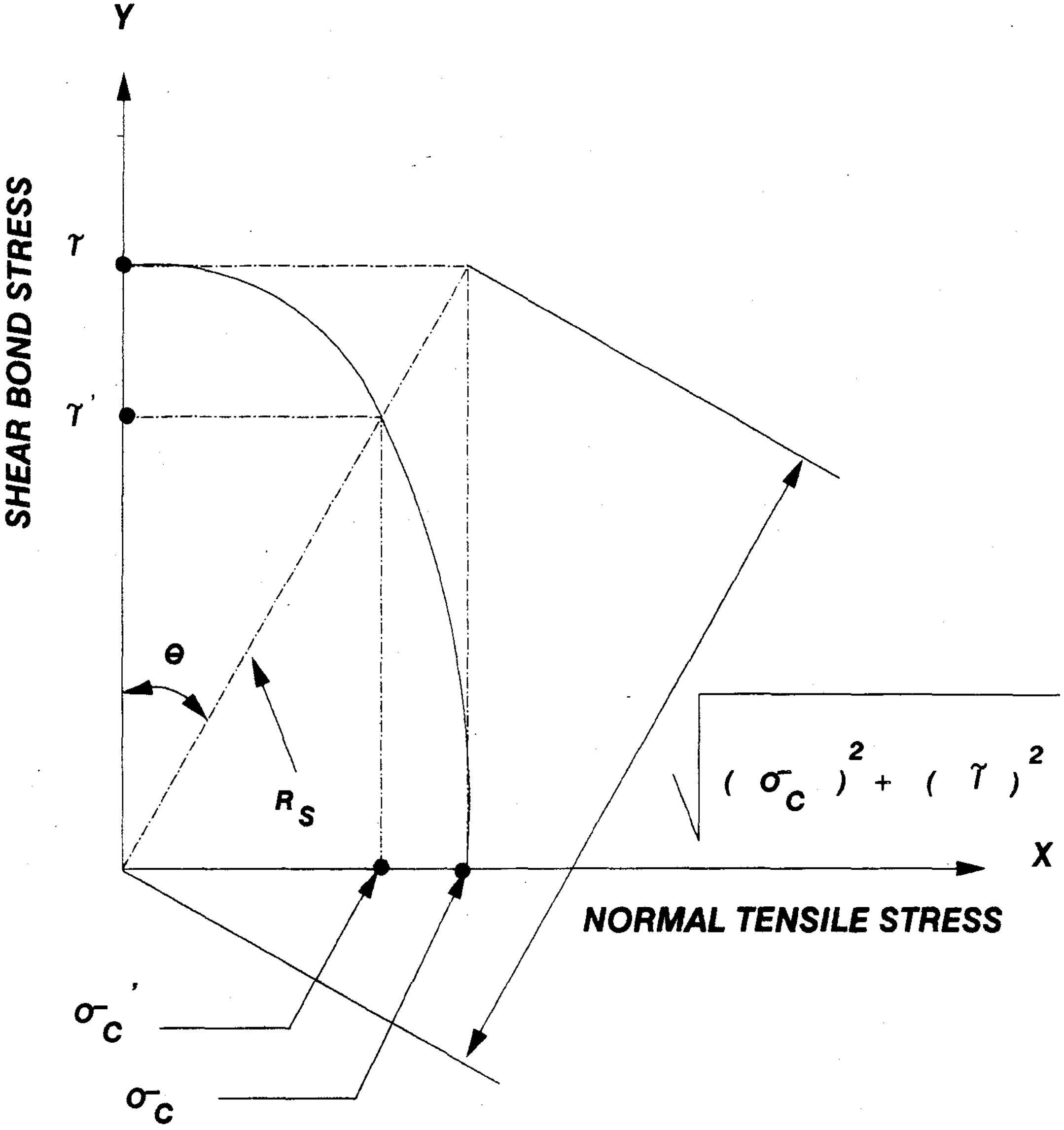

Figure 115. Elliptical interaction curve [29]

6.3 Proposed Predictive Methods

The proposed predictive methods that follow were based upon the edge zone concept. A discussion of this concept's relation to the current study follows.

6.3.1 Edge Zone Distance

The edge zone distance was defined as the distance in from the edge of the slab where 95% of the horizontal force was transferred from the loading beams to the diaphragm. Previously, the edge zone distances were assumed to be a/12 for edge zones parallel to the applied load and b/12 for edge zones transverse to the applied load [30], where a and b are slab dimensions parallel and transverse to the applied load, respectively. Additional studies have indicated that the edge zone distance decreases as the spacing of studs along the edge beam decreases. Nelson Stud Welding Company has experimentally determined that the shear cone of a 3/4 inch nominal diameter stud will be contained within a radius of only one and a half inches [24]. Observations from the diaphragm tests have indicated that the edge zone distance is approximately six inches. A value of six inches was therefore incorporated into the calculations.

6.3.2 Initial Stiffness

In calculating the initial stiffness of a hollow-core diaphragm slab, the total deflection consisted of several components:

$$\Delta_{tot} = \Delta_b + \Delta_s + \Delta_z + \Delta_f \qquad (6\text{-}3)$$

where

Δ_{tot} = total deflection of system, in.
Δ_b = bending deflection of system, in.
Δ_s = shear deflection of system, in.
Δ_z = edge zone deflection, in.
Δ_f = deflection due to axial flexibility of edge beam framing connections, in.

The majority of this derivation was taken from References 9 and 34.

6.3.2.1 Bending Component

For bending, the diaphragm was considered to be a cantilever girder with the hollow-core planks acting as the web and the edge beam acting as the flanges. The bending deflection, Δ_b, at the end of the girder was taken as:

$$\Delta_b = V a^3 / 3(E_c I_c + E_b I_b) = V / K_b \qquad (6\text{-}4)$$

where

a = length of cantilever girder, in.
E_c = concrete modulus of elasticity, ksi.
I_c = moment of inertia of web, in^4.

E_b = modulus of elasticity of edge beam, ksi.
I_b = moment of inertia of edge beams about girder neutral axis, in^4.
K_b = bending stiffness of system, kips/in.

The thickness used in computing the moment of inertia for the web was the average thickness of the concrete plus n, $= E_s/E_c$, times the effective area of steel in the prestressing strands for those systems oriented transverse to the loading beam. For tests with the strands oriented parallel to the applied shear load, the prestressing steel was assumed not to contribute to the effective area of the system. In the calculating the moment of inertia of the edge beams, the depth of the edge beams effective in bending was reduced due to shear lag as stated in Reference 37. For a cantilever beam with span to depth ratio of 3.75, the percentage of flange width effective in resisting bending was 86 percent. Thus, under the assumption that the upper portion of the edge beams was effective in bending, the net effective cross-sectional area of each edge beam was 15.0 square inches.

6.3.2.2 Shear Component

The shear deflection, Δ_s, of the composite girder was given by:

$$\Delta_s = V a / b (G_c t_c) = V / K_s \qquad (6\text{-}5)$$

where

a = length of cantilever girder, in.
b = depth of cantilever girder, in.
G_c = shear modulus of concrete, ksi
t_c = average thickness of concrete, in.
K_s = shear stiffness of system, kips/in.

This equation assumed that only the web was effective against shear. A value of 0.175 was assumed for Poisson's ratio.

6.3.2.3 Edge Zone Component

Previously, the deflection of the system due to edge zone deformation was based on the idealized edge zone force distribution shown in Figure 111. This analysis did not take into account the deformations of the edge beams. For a rigid slab, the change in the edge zone displacement must equal the axial strain in the edge beams. Figure 113 shows the initial edge zone distribution including axial deformation of the edge beams.

A condensed version of the development of edge zone stiffness including axial deformations, as given in References 9 and 34, follows. The horizontal forces on a typical edge beam segment are shown in Figure 116. The symbol Δ represents the edge zone displacement and σ is the axial stress in the edge beam. Summation of the forces in the x-direction on this segment yields

$$K \Delta(x)\, dx = A_b ((\sigma + d\sigma) - \sigma) \qquad (6\text{-}6)$$

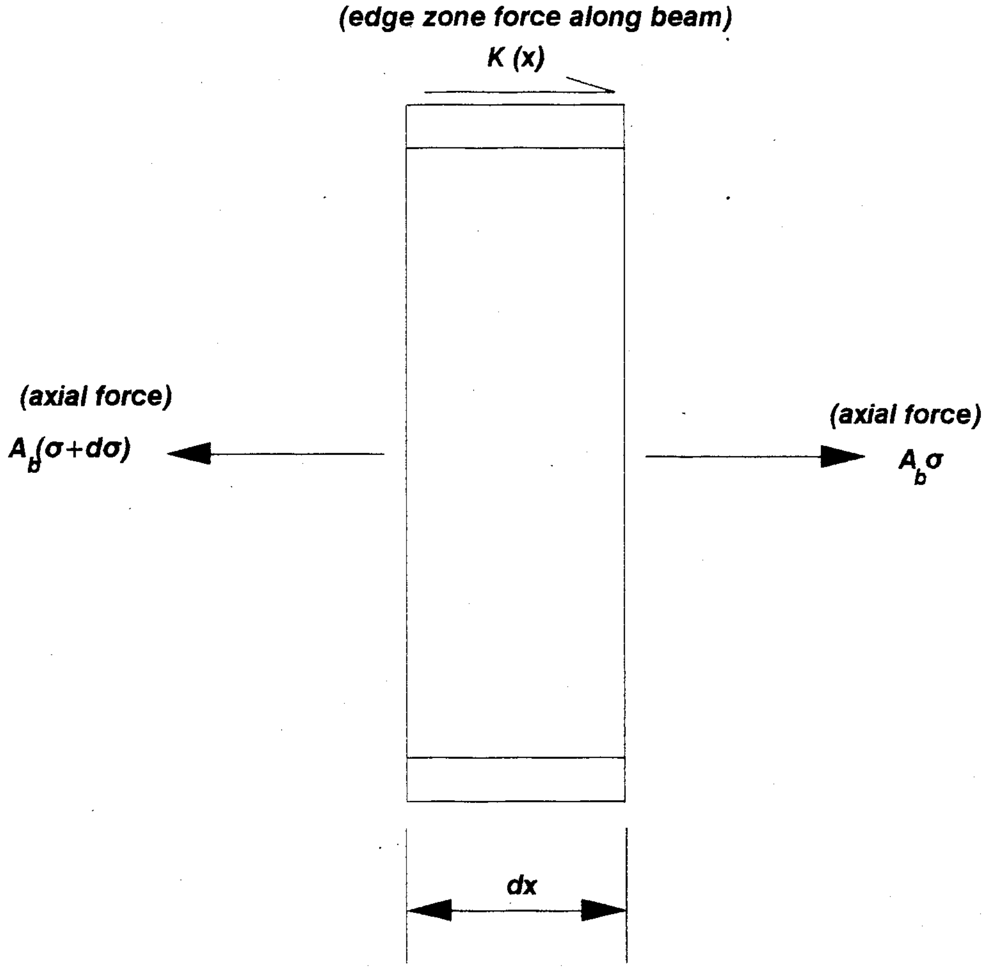

Figure 116. Horizontal forces on typical edge beam segment

where K is the edge zone stiffness, and the left hand side of the equation equals the total edge zone force over the length dx, while the right side equals the change in axial force on the edge beam over the length dx. Using derivative notation, this equation becomes

$$K \, \Delta(x) = A_b \, \sigma'(x) \tag{6-7}$$

Since the slab is assumed to act as a rigid body, the change in edge zone displacement, $\Delta'(x)$, must equal the axial strain in the edge beam. Therefore,

$$\Delta'(x) = \sigma(x) \, / \, E_b \tag{6-8}$$

and by differentiating again

$$\Delta''(x) = \sigma'(x) \, / \, E_b \tag{6-9}$$

substituting this into Eq. (6-6), the controlling differential equation is obtained,

$$\Delta''(x) - (K \, / \, A_b E_b) \, \Delta(x) = 0 \tag{6-10}$$

This equation is solved separately for the side beams and the loading beam because each requires a different set of boundary conditions. The edge zone displacements can be linearly related to the edge zone forces by the following relationships:

$$\begin{aligned} q_{tfo} &= K_t \, \Delta_{tfo} \\ q_{tb} &= K_t \, \Delta_{tb} \\ q_{tf1} &= K_t \, \Delta_{tf1} \\ q_{p1} &= K_p \, \Delta_{p1} \\ q_{p2} &= K_p \, \Delta_{p2} \end{aligned} \tag{6-11}$$

where

q_{tfo} = edge shear force at center of loading beam, kips.

Δ_{tfo} = slab to edge beam relative displacement at the center of the loading beam (parallel to the applied shear), in.

K_t = equivalent edge spring stiffness parallel to the applied shear, kips/in.

q_{tb} = edge shear force along the abutment (restrained end), kips.

Δ_{tb} = slab to abutment relative displacement, in.

q_{tf1} = edge shear force at end of loading beam, kips.

Δ_{tf1} = slab to edge beam relative displacement at end of loading beam (parallel to applied shear), in.

q_{p1} = edge shear force at restrained end of side beam, kips.

Δ_{p1} = slab to edge beam relative displacement at the restrained end of side beam (transverse to applied shear), in.

K_p = equivalent edge zone spring stiffness transverse to applied shear, kips/in.

q_{p2} = edge shear force at the free end of side beam, kips.

Δ_{p2} = slab to edge relative displacement at free end of the side beam transverse to applied shear load, in.

The origin was placed at the center of the loading beam. At this point the boundary conditions are

$$\sigma(0) = 0 \quad \text{and} \quad \Delta(0) = \Delta_{tfo} \tag{6-12}$$

Using the controlling differential equation (6-10), the transformation equations (6-11) and these boundary conditions, the edge force along the loading, moving, beam becomes

$$q_{tf}(x) = q_{tfo} \cosh(g_t x) \tag{6-13}$$

where

$$g_t = \mathrm{SQRT}(K_t/E_bA_b)$$

By substituting the distance to the end of the beams, x=b/2, into Eq. (6-13), the shear at the end of the front beam is obtained and is given by

$$q_{tf1} = q_{tfo} \cosh(g_t\, b/2) \tag{6-14}$$

The procedure for the side beams is very similar; however, the boundary conditions are different. For the side beams with the origin at the abutment, restrained end, the boundary conditions are as follows:

$$\sigma(a) = 0 \quad \text{and} \quad \Delta(0) = \Delta_{p1} \tag{6-15}$$

Again, using the controlling differential equation, Eq. (6-10), the transformation equations, Eqs. (6-11), and these boundary conditions, the edge force distribution along the side beams becomes

$$q_p(x) = q_{p1}\, \mathrm{sech}(g_p a) \cosh(g_p(x-a)) \tag{6-16}$$

where

$$g_p = \mathrm{SQRT}(K_p/E_bA_b)$$

At the free end of the beam the variable x equals the distance a. Thus, equation (6-16) yields

$$q_{p2} = q_{p1}\, \mathrm{sech}(g_p a) \tag{6-17}$$

The average edge forces (found by integrating and dividing by the length) for the front loading beam, q_{tav}, and the side beams, q_{pav}, are given by

$$q_{tfav} = (2q_{tfo}/bg_t) \sinh(g_t b/2) \tag{6-18}$$

$$q_{pav} = (q_{p1}/ag_p) \tanh(g_p a) \tag{6-19}$$

For simplification, the following variables are defined:

$$r_1 = \Delta_{p1}/\Delta_{pav} = q_{p1}/q_{pav} = g_p \ a \ \coth \ (g_p a) \tag{6-20}$$

$$r_2 = \Delta_{p2}/\Delta_{pav} = q_{p2}/q_{pav} = g_p \ a \ \operatorname{csch} \ (g_p a) \tag{6-21}$$

$$r_3 = \Delta_{tf1}/\Delta_{tfav} = q_{tf1}/q_{tfav} = g_t(b/2) \ \coth(g_t(b/2)) \tag{6-22}$$

The resulting forces in the edge beams and abutment are shown in Figure 117. As demonstrated in Reference 14, the total edge zone deflection can be determined from statics and geometry. Summing the forces on the front moving beam results in the following equation

$$V = q_{tfav}(b+(r_3a''/3a)) - q_{tb}(a''^2/3a) \tag{6-23}$$

Similarly, summing forces on the reaction blocks gives

$$V = q_{tb} \ b + (a''/3a)(q_{tb}(3a-a'')-q_{tfav}r_3a'') \tag{6-24}$$

Combining these equations yields

$$q_{tfav}(b+r_3a''(2-a''/3a)) = q_{tb}(b+a'') \tag{6-25}$$

and simplifying,

$$r_4 = \Delta_{tb}/\Delta_{tfav} = q_{tb}/q_{tfav} = (b+r_3a''(2-a''/3a))/(b+a'') \tag{6-26}$$

by solving for q_{tb} and letting

$$l_t'' = a'' \ (r_3 \ (3a - a'') - a'' \ r_4 \ ) \ / \ 3a,$$

Equation (6-23) becomes:

$$V = q_{tfav}(b+l_t'') \tag{6-27}$$

Summing moments on the south reaction block yields

$$V = q_{pav}((r_1b^2/6a)+b+(r_2b''/6a)(3b-2b'')) \tag{6-28}$$

or letting

$$l_p'' = (r_1 \ b^2 + 3r_2bb'' - 2r_2b''^2)/6a,$$

this equation becomes

$$V = q_{pav} \ (\ b + l_p'') \tag{6-29}$$

Figure 118 shows the geometrical relation between Δ_{tf1}, Δ_{tb}, Δ_{p1} and Δ_z. The total edge zone displacements are separated into transverse and parallel edge zone displacements. Addition of the two contributions results in

$$\Delta_z = \Delta_{tf1} + \Delta_{tb} + 2a\Delta_{p1}/b \tag{6-30}$$

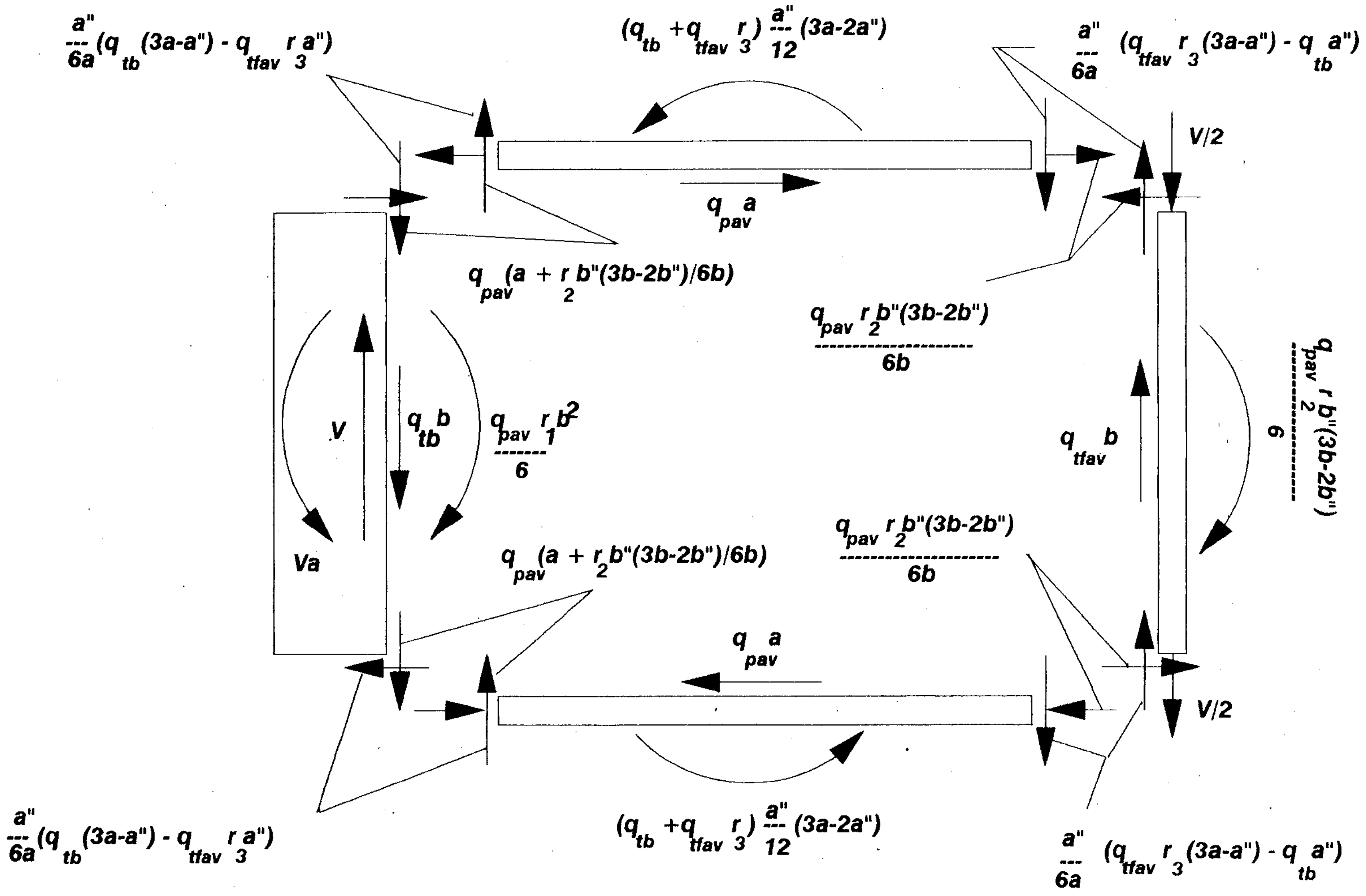

Figure 117. Initial framing member forces

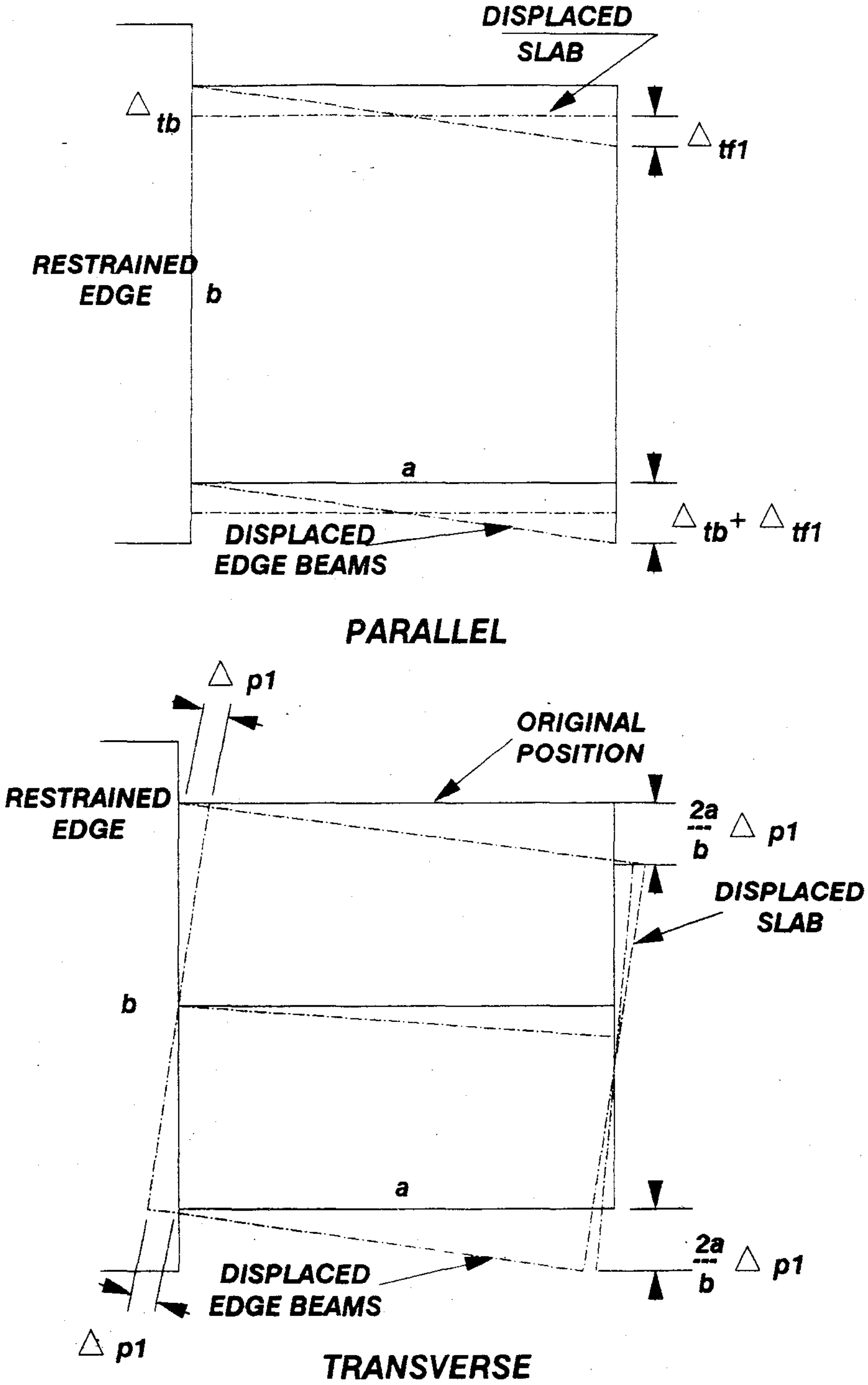

Figure 118. Edge zone displacements

By substituting Eq. (6-30) into Eqs. (6-20), (6-22), (6-24), (6-27) and (6-29), the following expression is obtained

$$\Delta_z/V = (r_3+r_4)/(K_t(b+l_t'')) + 2ar_1/(K_b b(b+l_p'')) \tag{6-31}$$

The total edge zone stiffness is the reciprocal of Eq. (6-31) or

$$K_z = 1/((r_3+r_4)/K_t(b+l_t'') + 2ar_1/K_p b(b+l_p'')) \tag{6-32}$$

The equivalent edge zone spring stiffness, K_t or K_p, is determined using the empirical stud load/displacement relation from Reference 34 as follows

$$K_{eq} = 145.3\ Q_{su} / S_s \tag{6-33}$$

where

K_{eq} = equivalent stiffness, K_t or K_p, kips/in.
Q_{su} = stud connector capacity in the load direction, kips
S_s = stud spacing, in.

The variable for stud spacing reflects the outer two studs and equal spacing between the remaining studs.

The stud load/displacement relation requires the stud connector capacity, Q_{su}. The following equation predicts this capacity [24]:

$$Q_{su} = 6.66\text{x}10^{-3} A_s f'_c{}^{0.3} E_c{}^{0.44} \tag{6-34}$$

$$Q_{su} \leq 0.9\ A_s\ f_s$$

where

Q_{su} = ultimate shear capacity, kips.
A_s = area of stud, in^2.
E_c = modulus of elasticity of the concrete, psi.
f_s = yield strength of the stud, ksi.
f_c' = compressive strength of the concrete, psi.

6.3.2.4 Framing Beam Component

The final component of the initial diaphragm deflection was the axial flexibility of the edge beam abutment connections. This frame connection stiffness component served as a correction due to framing and connection movements. No additional strain was introduced into the diaphragm because this component was caused by a small amount of rigid body notion. The displacement of the edge beam to abutment connection (Δ_c) was related geometrically to the diaphragm displacement by

$$\Delta_f = (2a/b)\ \Delta_c \tag{6-35}$$

This component has been experimentally determined to be approximately 10,000 kips/in [9,34,10].

The total stiffness was therefore calculated by substituting the values for the individual components into Eq. (6-3) as follows

$$V/K_{tot} = V/K_b + V/K_s + V/K_z + V/K_f \qquad (6\text{-}36)$$

where

K_{tot} = total diaphragm stiffness, kips/in.
K_b = bending stiffness component, kips/in.
K_s = shear stiffness component, kips/in.
K_z = edge zone stiffness component, kips/in.
K_f = frame connection component, kips/in.

Simplification of this equation yielded the total initial stiffness directly as follows

$$K_{tot} = 1/(1/K_b + 1/K_s + 1/K_z + 1/K_f) \qquad (6\text{-}37)$$

6.3.3 FME and Limit State Strength Prediction

The FME load capacity of the plank diaphragm systems was limited by one of three major categorical failure modes: shear-bond seam failure, tensile-bond seam failure, or diagonal tension failure. Limit states were identified as one of three potential events: initial weld tie shear failure, initial weld tie tension failure, or initial diagonal tension crack. The following subsections discuss the theory and assumptions involved with the prediction of the FME and limit state strengths.

6.3.3.1 FME Prediction for Shear-Bond Failure (N-S Orientation)

The edge zone theory was utilized for the prediction of the FME and limit state loads for the shear-bond failure mode. Figure 119 shows the force distribution for the east plank of a test oriented transverse to the loading beam. (The critical case involved either the west or east seam fracturing first.) The following initial step-by-step procedure allowed for the computation of each of the required forces in order to attain the predicted FME load. Each of these forces was a function of the predicted shear load at the loading beam, V^p_{FME}.

Step #	Eq.	Determine:
1	6-29	q_{pav}
2	6-19	q_{p1}
3	6-17	q_{p2}

Summing forces in the direction of the seam shear force, V_{seam}, gave

$$V_{seam} = (q_{p1}/b)\ (b^2/4 - z^2) + q_{pav}\ a + (b''/2)\ q_{p2} \qquad (6\text{-}38)$$

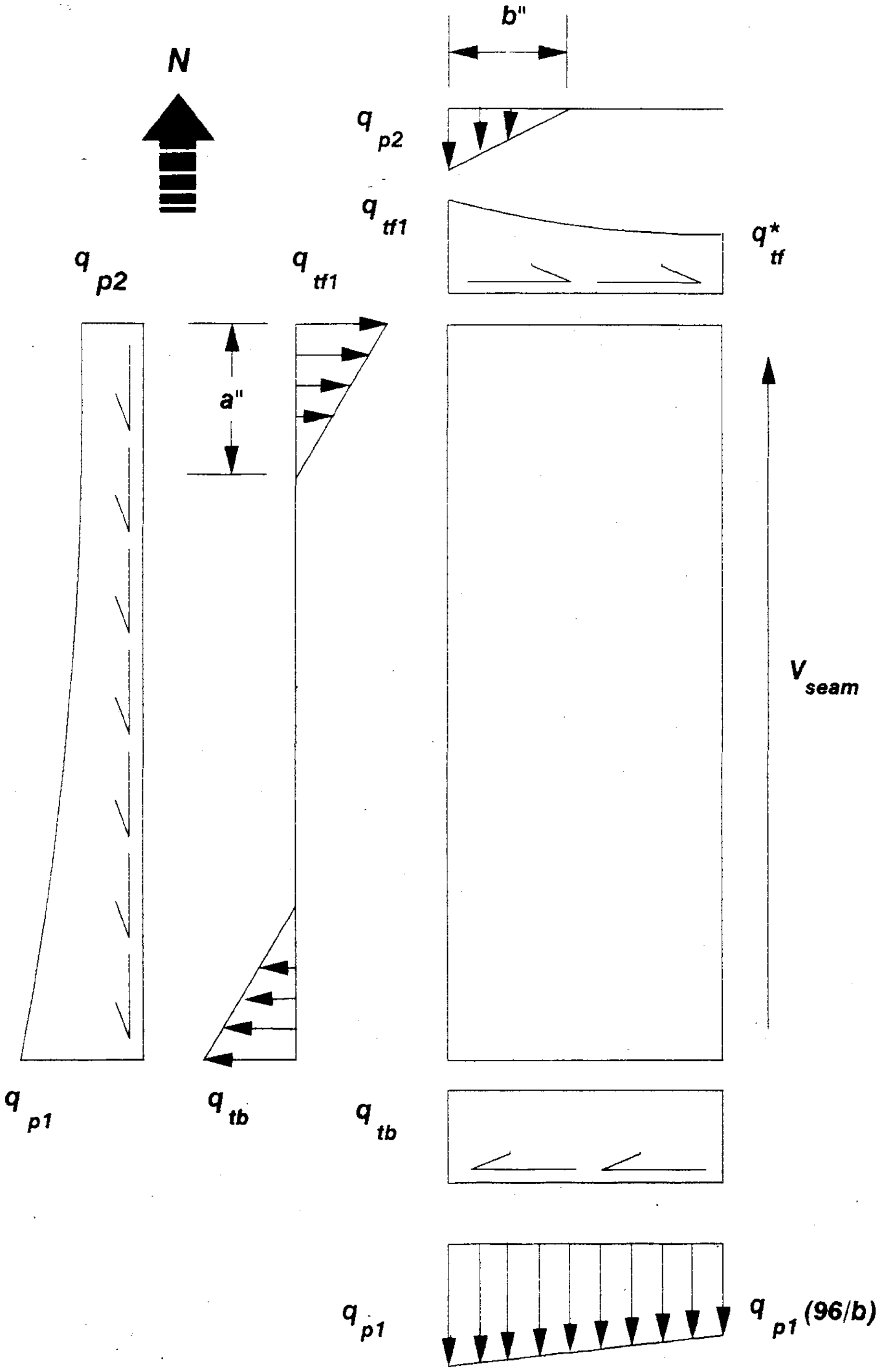

Figure 119. FME force distribution on exterior plank for shear-bond failure

Note that for this investigation z is equal to 48 inches. Other solutions involving a significant change in this parameter will need further investigation. Also the effective width of this exterior plank was dependent upon the length of b; however, for Tests #4, #9, and #11, this width was a constant value of 42 inches.

Based on information from the elemental shear and tension tests, the reduced shear stress, T_{av}', was determined to be 69 psi from the shear-stress/tensile-stress interaction curve. Grout depths of penetration, d_p, were measured from the broken diaphragm specimens. The bond length, l_s, was assumed to be the entire 16-foot length of seam in all cases. Thus, the seam shear force was written as

$$V_{seam} = T_{av}' \, d_p \, l_s \tag{6-39}$$

With these assumptions the predicted shear force at the loading beam, V^P_{FME}, was attained by substitution with the previous two equations.

6.3.3.2 Limit State Prediction for Shear-Bond Failure (N-S Orientation)

The force distribution of Figure 120 was assumed for the limit state condition. However, due to the symmetry of this system of forces, normal forces acting at the seam could not be determined directly. Therefore, the FME force distribution was assumed for normal force computations. This normal force was assumed to vary linearly across the seam with compression at the south end and tension at the north end as the loading beam moved to the west. The length of this seam compression zone, l_c, was assumed to be a/2 (90 inches) for tests of this orientation. The length of the tension zone, l_t, was assumed to be $a-l_c$ (90 inches).

An initial step-by-step procedure is listed for the purpose of calculating the limit state strength. These forces can be determined exactly since V^P_{FME} is now known.

Step #	Eq.	Determine:
1	6-29	q_{pav}
2	6-19	q_{p1}
3	6-17	q_{p2}
4	6-27	q_{tfav}
5	6-18	q_{tfo}
6	6-14	q_{tf1}
7	6-26	q_{tb}

The shear along the loading beam was determined based on the known q_{tfav}, q_{tf1}, and q_{tfo}. The value of q_{tf} was previously calculated as:

$$q_{tf}(x) = q_{tfo} \cosh(g_t x) \tag{6-13}$$

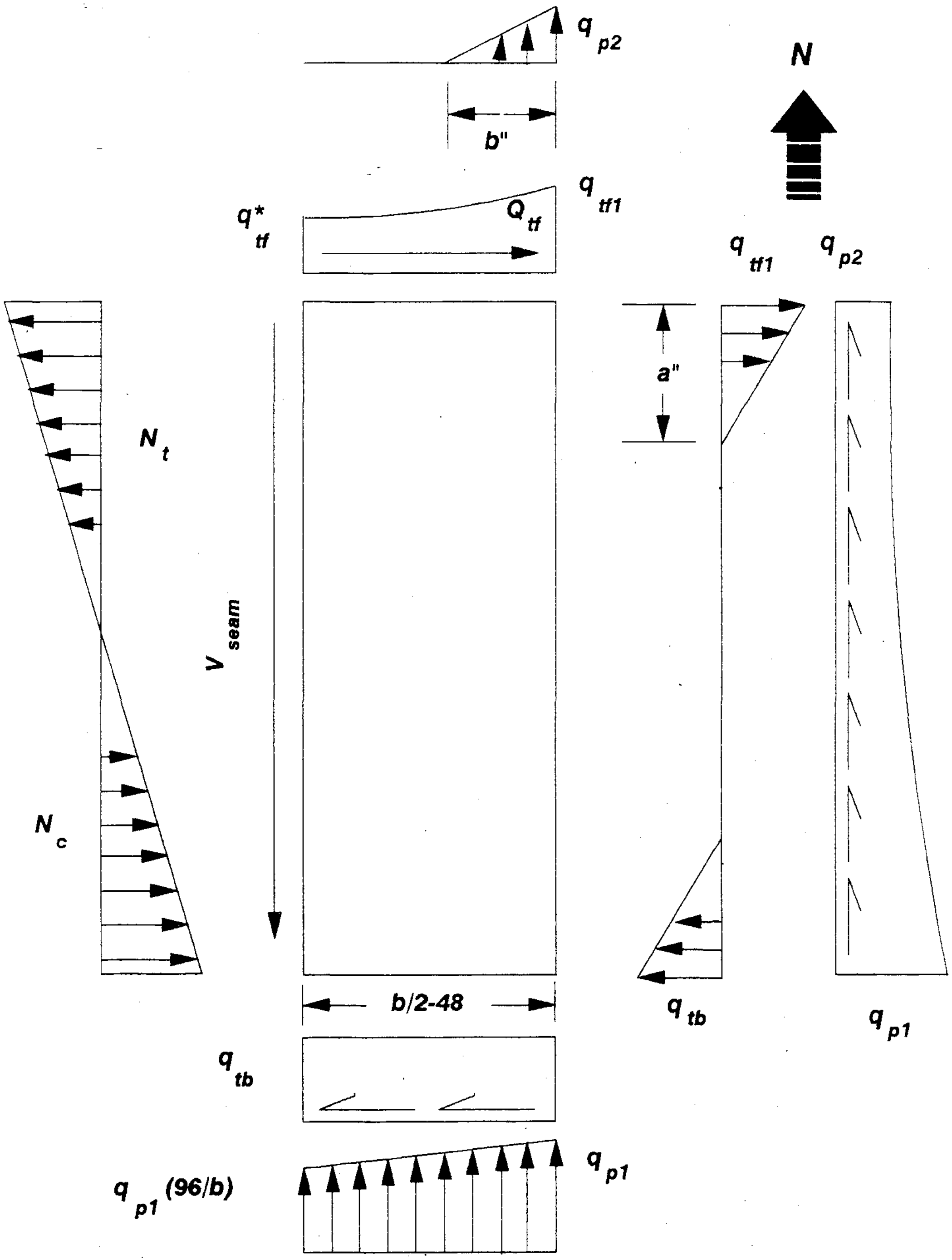

Figure 120. FME force distribution to be used to determine normal stress at ultimate load

The magnitude of the shear force at the seam along the front loading beam,

$$q^{*}_{tf} = q_{tfo} \cosh (g_t\ 48) \qquad (6\text{-}40)$$

Subsequently, the shear along the loading beam for the exterior plank, Q_{tf}, was given as

$$Q_{tf} = (q_{tfo}/g_t) \sinh (g_t\ x) \qquad (6\text{-}41)$$

Summing forces transverse to the seam shear force yielded

$$N_c = N_t - Q_{tf} + q_{tb}(b/2-48) + a''/2\ (q_{tb}-q_{tf1}) \qquad (6\text{-}42)$$

Finally, summing moments about the front loading beam at the seam gave

$$\begin{aligned} N_c = (&l_t\ N_t/3 + a\ (b/2 - 48)(q_{tb}-q_{pav}) - (a''^2/6)(q_{tb} + q_{tf1}) \\ &+ (a\ a''/2)\ q_{tb} - (q_{p2}\ b''/6)\ (3b/2 - b'' - 144) \\ &- q_{p1}\ (b/2 - 48)^2(16/b + 1/3))\ /\ (\ a - l_c/3) \end{aligned} \qquad (6\text{-}43)$$

The normal forces, N_c and N_t, were determined by solving Eqs. (6-42) and (6-43) by substitution. Note that the normal tensile force, N_t, should not exceed the combined capacity of the exterior and center weld ties along the seam.

The shear capacity of the seam at the limit state, V^{ls}_{seam}, had three components: the capacity of the three weld ties in shear ($F_{v(wt)}$), the shear friction contribution due to the normal compressive forces ($F_{f(c)}$), and the weld tie frictional contribution due to self-inducing normal forces, ($F_{f(t)}$). In equation form,

$$V^{ls}_{seam} = F_{v(wt)} + F_{f(c)} + F_{f(t)} \qquad (6\text{-}44)$$

Based on information from the elemental shear tests for the GWUC and GWUM series, the average weld tie shear capacity was 5.5 kips. A value for the coefficient of friction, u, acting in the seams was taken as 0.90 based on information from the elemental shear tests. A tensile strength for the weld tie of 16.3 kips was calculated based on the horizontal and vertical bar contribution in tension. Thus, the equation describing the, seam capacity at the limit state was simplified to the following

$$V^{ls}_{seam} = 5.5\ n + 0.9\ (N_c+N_t) \qquad (6\text{-}45)$$

where n is the number of weld ties.

From the limit state force distribution, V^{ls}_{seam}, was related to q_p and q_p'. For this distribution, q_p and q_p' were assumed to be equal. Summing moments at the abutment (restrained edge) gave

$$V^{P}_{ls} = q_p b + q_p' b^2/4a + b'' q_p'/a(b-b'') \qquad (6\text{-}46)$$

and letting $l_p' = (b^2 + 4bb'' - 4b''^2)/4a$, yielded

$$V^p_{ls} = q_p'(b + l_p') \quad (6\text{-}47)$$

From the limit state force distribution

$$V^{ls}_{seam} = q_p' \ (a + b/2 - 42) \quad (6\text{-}48)$$

By substituting Eqs. (6-49) and (6-46) into Eq. (6-48), V^p_{ls} was determined to be

$$V^p_{ls} = (5.5\ n + 0.9(N_c + N_t))/(a + b/2 - 42)\ (b + l_p') \quad (6\text{-}49)$$

6.3.3.2 FME Prediction for Tensile-Bond Failure (E-W Orientation)

Predictions for both the FME and limit state strengths for the tensile-bond failure mode again utilized the edge zone concept. Figure 121 shows the force distribution for the plank located nearest to the abutment (the critical case). The tensile-bond failure mode was shown to control for tests with seams oriented parallel to the loading beam (Tests #6 and #10).

An initial step-by-step procedure for force computations involved with the FME load prediction follows. Each of these forces was a function of V^p_{fme}

Step #	Eq.	Determine
1	6-29	q_{pav}
2	6-19	q_{p1}
3	6-17	q_{p2}
4	6-27	q_{tfav}
5	6-18	q_{tfo}
6	6-14	q_{tf1}
7	6-26	q_{tb}

From statics, the normal compressive and tensile forces, N_c and N_t, were shown to be equal. Therefore, two unknowns required solution for the FME prediction: the normal force and the seam shear force, V_{seam}. The shear along the edge beams was determined based on q_{p1}, q_{p2}, and q_{pav}. From Equation 6-16

$$q_p(x) = q_{p1} \ \ \text{sech}(g_p\ a)\ \cosh(g_p(x\text{-}a))$$

The magnitude of the q_p force acting along the edge beams at the seam, q^*_p was given as

$$q^*_p = q_{p2} \cosh(g_p(42\text{-}a)) \quad (6\text{-}50)$$

The shear force along the edge beams for the south plank, Q_p, was found by integration of Equation 6-50

$$Q_p = (q_{p2} / g_p)\ (\ \text{-sinh}(\text{-}g_p a) + \sinh(g_p(42\ \text{-}a))\ ) \quad (6\text{-}51)$$

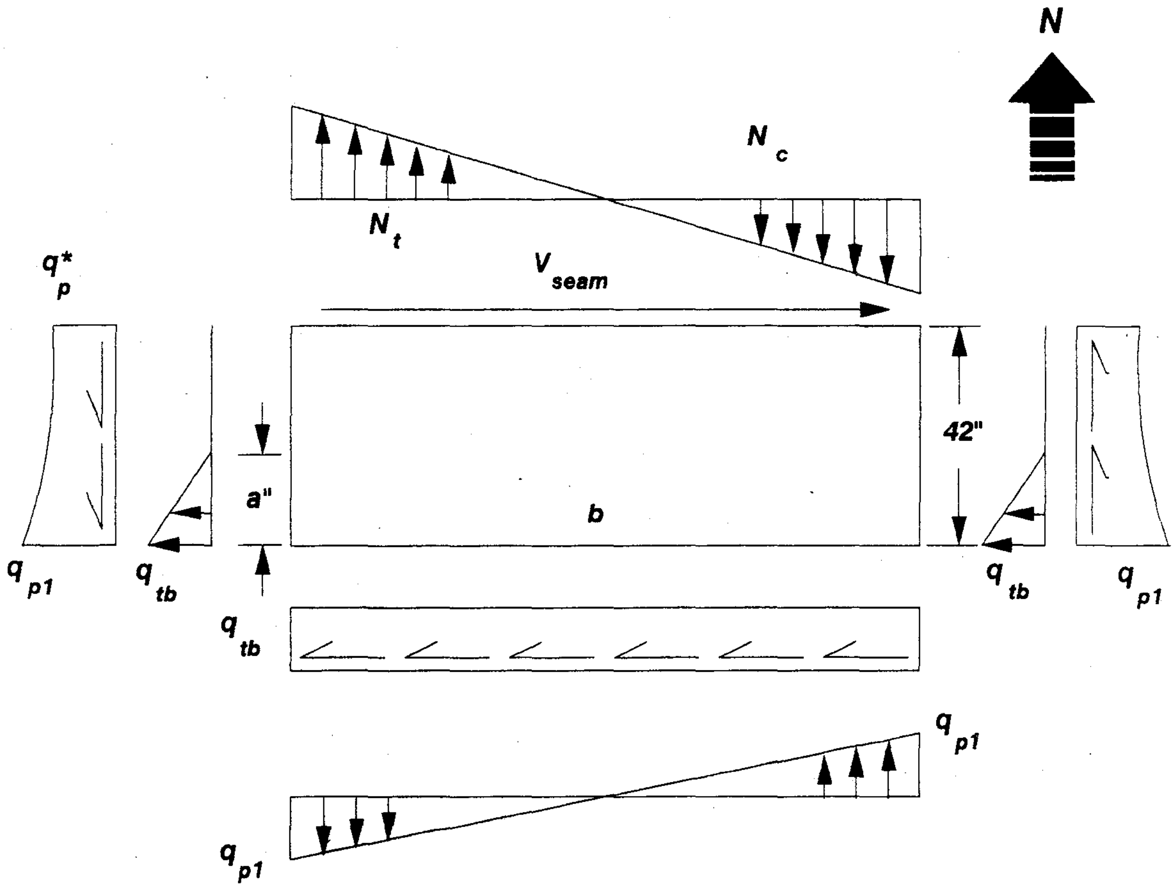

Figure 121. FME force distribution on south plank for Tensile-Bond failure

The normal compressive and tensile forces were assumed to vary linearly across the seam with tension at the west end as the planks were moving east. Summing moments about the west edge beam at the south seam gave

$$N_c = N_t = (-3/(3b - l_t - l_c))\ (q_{tb}\ (42a'' - a''^2/3 + 42b) + q_{pl}\ (b^2/6) - Q_p\ b) \tag{6-52}$$

Subsequently, the normal forces can be determined from Eq. (6-52). (Note: These normal forces are a function of V^p_{FME}.) Dividing the normal tensile force by the area of grout under tension yielded

$$\sigma_{av}' = N_t / (d_p l_t) \tag{6-53}$$

Summing forces parallel to the seam shear force and dividing by the area of the grout of the seam resulted in

$$T_{tav}' = (q_{tb}\ (b + a'')) / (d_p l_s) \tag{6-54}$$

Assuming both tension and shear were acting simultaneously on the seam, values from the shear-bond/tensile-bond interaction curve were utilized. A shear stress of 69 psi and tensile stress of 40 psi were taken from this curve as discussed in the elemental test chapter. The predicted FME strength at the loading beam was taken as the lower value of V^p_{FME} as determined by Eqs. (6-53) and (6-54) with the shear stress and tensile stress constraints incorporated.

6.3.3.4 Limit State Prediction for Tensile-Bond Failure

The normal forces determined from the initial distribution were utilized for the limit state condition, since the limit state distribution had not allowed for their computation. For the case when shear along the seam controlled (see Figure 122)

$$V^p_{ls} = q_t\ b + 2q_t'\ b'' \tag{6-55}$$

For this distribution, q_t and q_t' were assumed to be equal. Summing forces in the E-W direction, and letting $l_t' = 2a'' - (2a''^2/a)$ yielded

$$V^{ls}_{seam} = q_t'\ (b + l_t') \tag{6-56}$$

Solving for V^{ls}_{seam} in terms of V^p_{ls} gave

$$V^{ls}_{seam} = V^p_{ls}\ (b + 2a') / (b + l_t') \tag{6-57}$$

Utilizing Eq. (6-45) together with Eq. (6-57) allowed for the simultaneous solution of V^p_{ls} as

$$V^p_{ls} = (n * 5.5 + 0.9\ (N_c + N_t)\ (b + l_t'))\ /\ (b + 2a') \tag{6-58}$$

Where n is the number of weld ties. For the case when tension along the seam controlled, Eqs. (6-47) and (6-56) again applied. Summing moments about the west

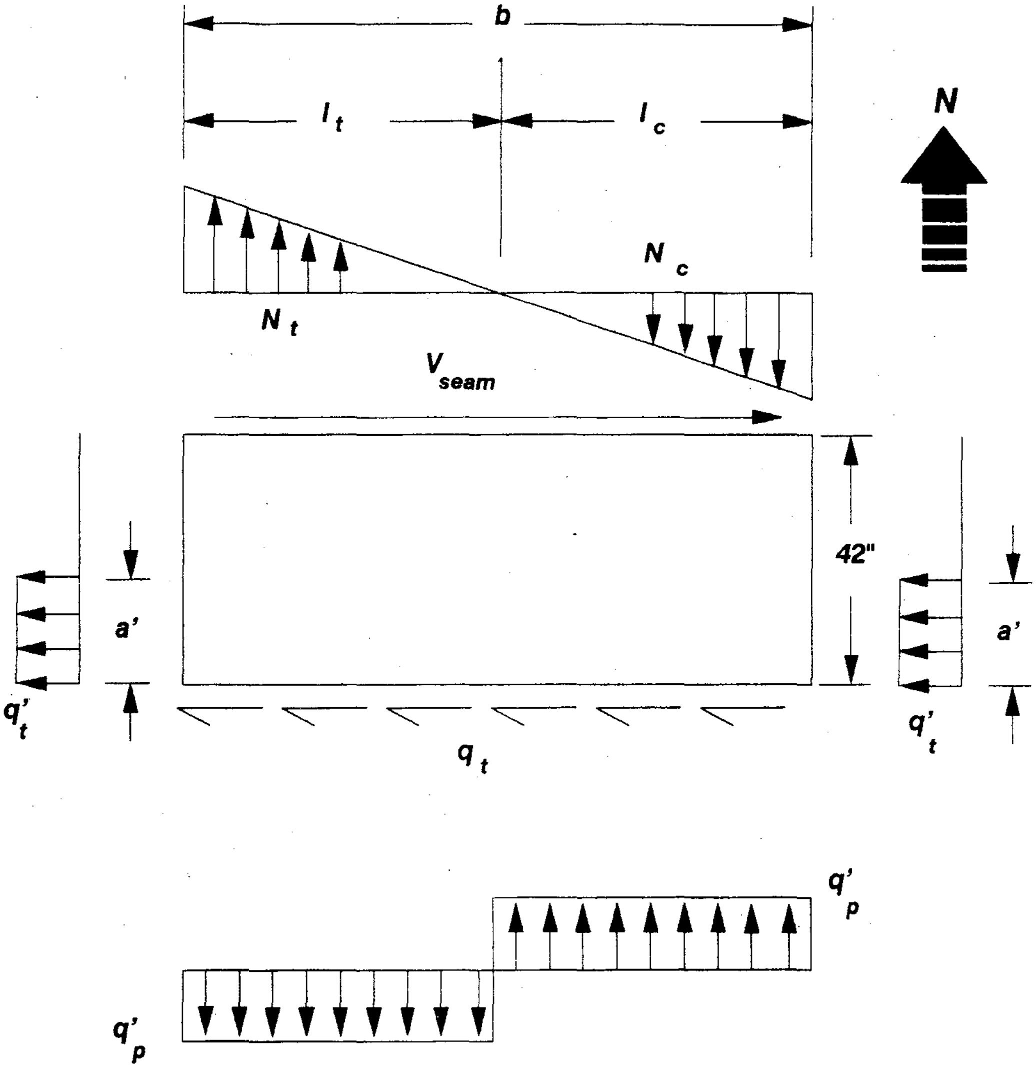

Figure 122. Limit state force distribution on south plank for tensile-bond failure

edge beam at the south seam (see Figure 123) and substituting from these equations gave

$$V^{p}_{ls} = (3b - l_c - l_t)\ N_c \ /\ ((84 - 2a' + 42b)\ /\ (b + l_t') + (b^2/4 - 42b)) \qquad (6\text{-}59)$$

The predicted limit state shear strength, V^{p}_{ls}, was the smaller of that given by Eqs. (6-58) and (6-59).

6.3.3.5 FME and Limit State Prediction for Diagonal Tension Failure

The diagonal tension failure represented an upper limit for a concrete diaphragm. This failure occurred for only one of the untopped hollow-core diaphragm tests. Diagonal tension failure calculations were based on Equation (11-32) from the American Concrete Institute 318-83 code,

$$V_c = 3.3\ f'^{.5}_{c}\ b\ d + N_{cp}\ d/(4 l_w) \qquad (6\text{-}60)$$

where

V_c = diagonal shear capacity of the concrete.
f'_c = plank concrete compressive strength, psi.
b = diaphragm width, in.
d = effective plank depth, in.
N_{cp} = normal compressive force (prestressing), lb.
l_w = 0.8 b

The determination of the effective plank depth, d, was very critical in this equation. The shear force flow was assumed to follow that described in Figure 123. This shear force applied at the loading beam was transferred into the diaphragm through the edge zone. The following areas were assumed non-effective in resisting the in-plane force: the tension zone of the top wythe (if one existed), and the majority of the core web zone, excluding parabolic regions into each of the lower and upper webs.

In order to compute the extent of the non-effective tensile zone of the top wythe, fiber stresses in the top and bottom were determined, based on a linear stress distribution:

$$f^{t}_{fog} = -P_i/A + P_i\ e\ y_t/I - M_o\ y_t/I$$

$$f^{b}_{fog} = -P_i/A - P_i\ e\ y_b/I - M_o\ y_b/I \qquad (6\text{-}61)$$

where

f^{t}_{fog} = top fiber stress, psi.
f^{b}_{fog} = bottom fiber stress, psi.
P_i = compressive prestressing force (after relaxation losses), lb.
A = cross sectional area of plank, in^2.
e = eccentricity of the strands with respect to the plank neutral axis, in.
y_t = distance from neutral axis to the top fiber, in
y_b = distance from neutral axis to bottom fiber, in.

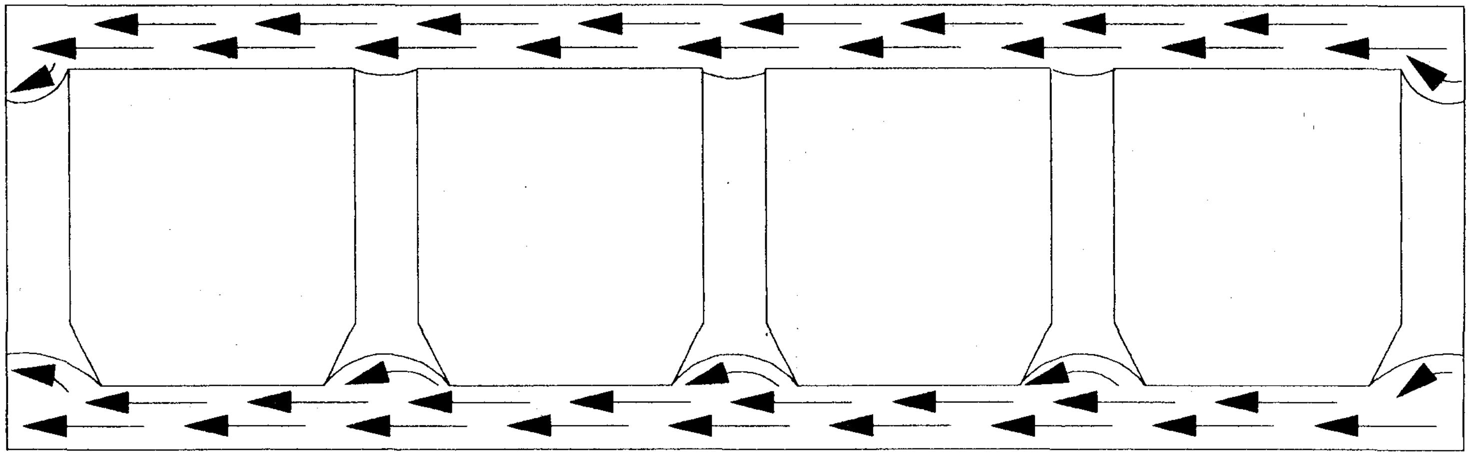

Figure 123. Proposed shear force transfer system

M_o = dead load moment, lbs. in.

When the top fiber was subjected to tension, a modification due to the effect of in-plane shear was considered. The shear stress was computed using

$$v = V Q / (I_d t) \tag{6-62}$$

where

v = shear stress at specified location, psi
V = shear on plank applied at loading beam, lbs.
Q = first moment of area of the diaphragm, in^3.
I_d = moment of inertia of diaphragm, in^4.
t = average cross-sectional area divided by plank width, in.

Mohr's circle was utilized as shown in Figure 124 to determine this modified tensile stress:

$$f'^{t}_{f0g} = f^{t}_{f0g}/2 + (f^{t}_{f0g}/2)^2 + v^2)^{0.5} \tag{6-63}$$

where

f'^{t}_{f0g} = modified tensile stress, psi.

The effective zone of the top wythe subjected to compression, d^{t}_{eff}, was

$$d^{t}_{eff} = -1.25\ f^{b}_{f0g}/(f^{t}_{f0g} - f^{b}_{f0g}) \tag{6-64}$$

The shear forces were assumed to transfer partially into parabolic regions of the webs between the cores. The following relationship describes this second degree curve:

$$y_f = a_g\ x_c^{2} \tag{6-65}$$

where

y_f = vertical shear flow limit
a_g = web shear flow gradient
x_c = core-to-core spacing.

The effective depth which acted to resist the shearing force was computed as follows:

$$d = d^{b}_{eff} + d^{t}_{eff} + d^{p}_{eff} \tag{6-66}$$

where

d^{b}_{eff} = the effective zone of the bottom wythe subjected to compression, in.
d^{p}_{eff} = the effective zone of the parabolic region actively transferring in-plane shear forces, in.

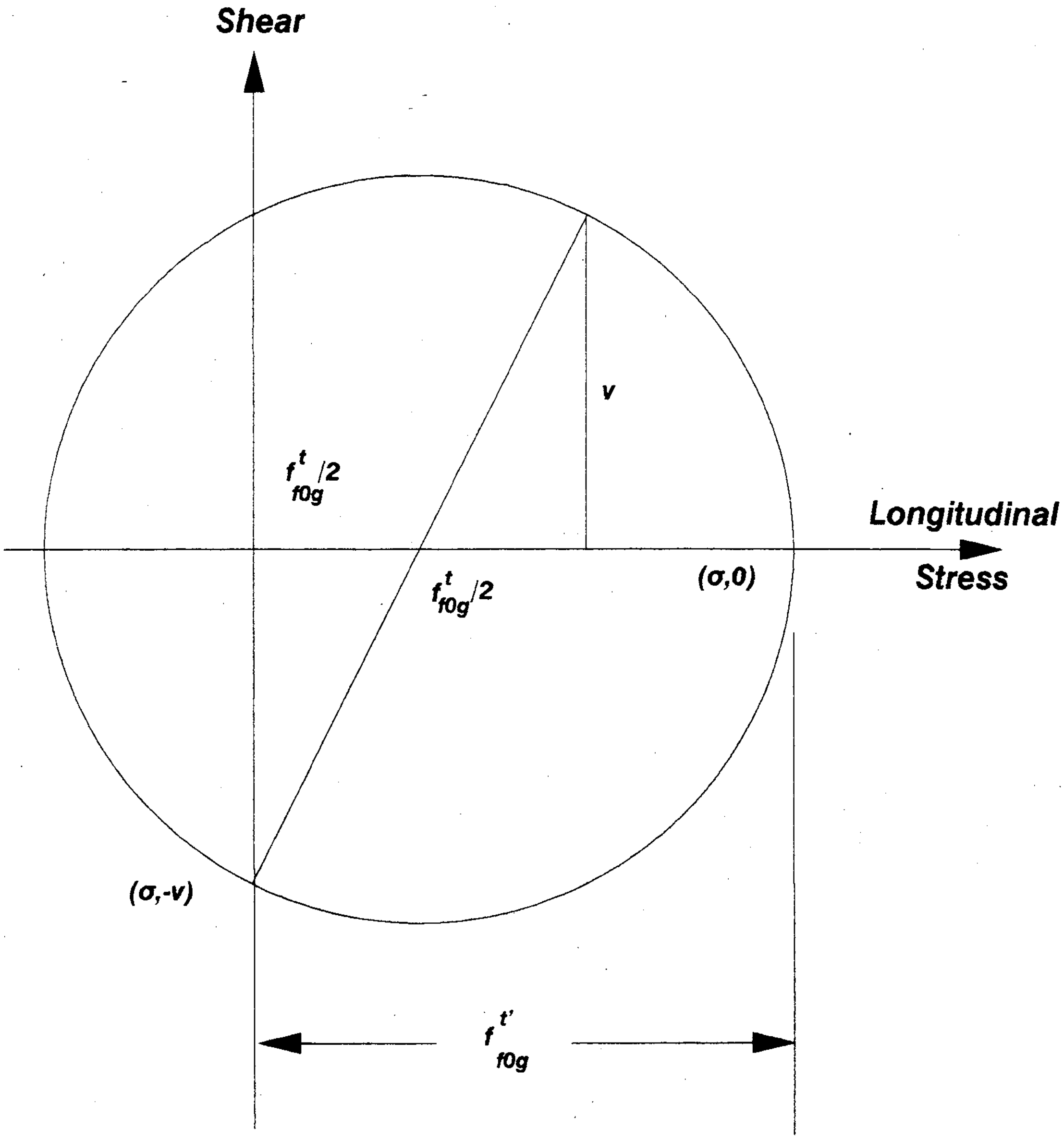

Figure 124. Principal tensile stresses using Mohr's circle

Figured 125 demonstrate graphically the effective depths for four cases:

- a) 6-inch planks with 4 strands.
- b) 12-inch planks with 6 strands.
- c) 8-inch planks with 4 strands.
- d) 8-inch planks with 6 strands.

The diagonal shear strength calculated in Eq. (6-61), representing the predicted FME strength, had an internal factor of safety. This factor of safety was approximately 1.15 for concrete with a compressive strength of 8300 psi. The numerical strength results for the diagonal tension mode to be presented in Section 6.4.2 reflect the extraction of this factor of safety.

6.3.4 Hysteretic Model Formulation

After the initial stiffness and the limit state strength had been calculated, the hysteretic model was formulated. The LPM model best represented the actual hysteretic curves formed during testing as discussed in Section 6.1.2. The majority of the following formulation of the LPM model was taken from References 14 and 15. Development of the LPM model follows a series of steps (which correspond to linear segments on the curve as shown in Figure 13). In the formulation of the hysteretic model, these line segments are referenced.

Initial loading follows the skeleton curve up to the desired displacement. The skeleton curve consists of a second order function and two linear segments as discussed in Chapter 2. For this development the displacement at peak strength was empirically chosen as 0.2 inches for shear and tension bond failure and 0.3 for diagonal tension (as shown in Figure 126 for the three failure modes). This value was obtained from the mean experimental displacement rounded to the nearest increment of the displacement for the actual test. The maximum displacement was determined from both experimental and analytical information. A linear regression was performed on the receding slope of the experimental data (0.5 inches to the maximum displacement value). This regression resulted in a 35% difference in slopes between tests oriented transverse (shear-bond failure mode) and parallel to the applied shear load (tensile-bond failure mode) as shown in Figure 127. This inconsistency in receding slope can be experimentally verified by noting that the test oriented parallel to the loading beam lost strength early in the test and maintained a reduced value thereafter. The opposite orientation, on the other hand, revealed a more constant, gradual decline in strength. These observations can, in turn, be attributed to the large strength decrease associated with the failure of the weld ties in the parallel orientation. Once these units were no longer functional, frictional forces caused the continuous residual force. In the other orientation, the normal, and consequently the frictional forces, were more consistent throughout the test resulting in a gradual decline in load. A maximum displacement value of five inches was selected for the parallel orientation to reflect the concavity in the receding slope of the experimental data. A maximum displacement value of three inches was established for the transverse orientation.

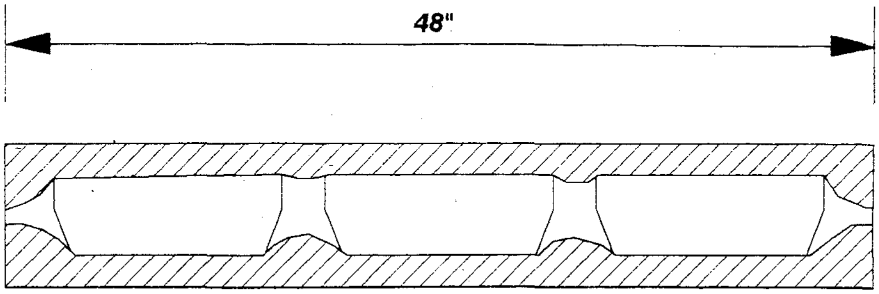

6-inch plank

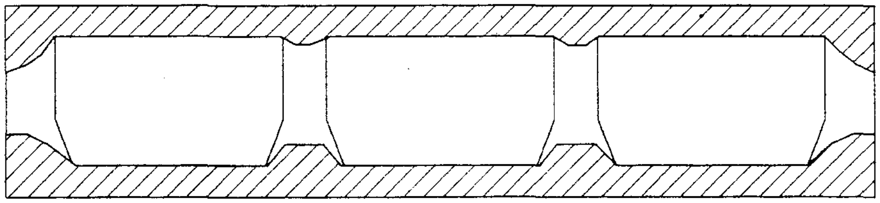

8-inch plank

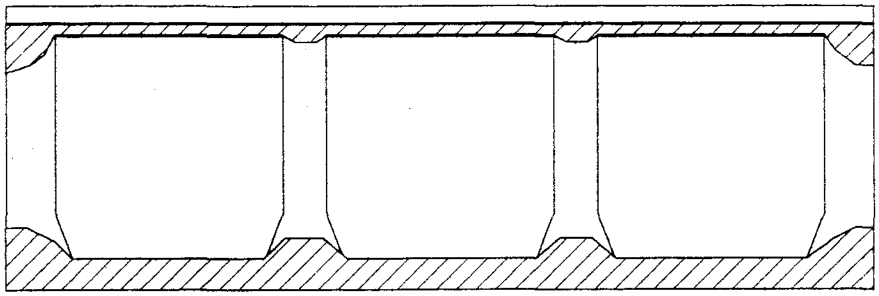

12-inch plank

▨ Effective area of concrete

Figure 125. Effective area for 6-, 8-, and 12-inch planks

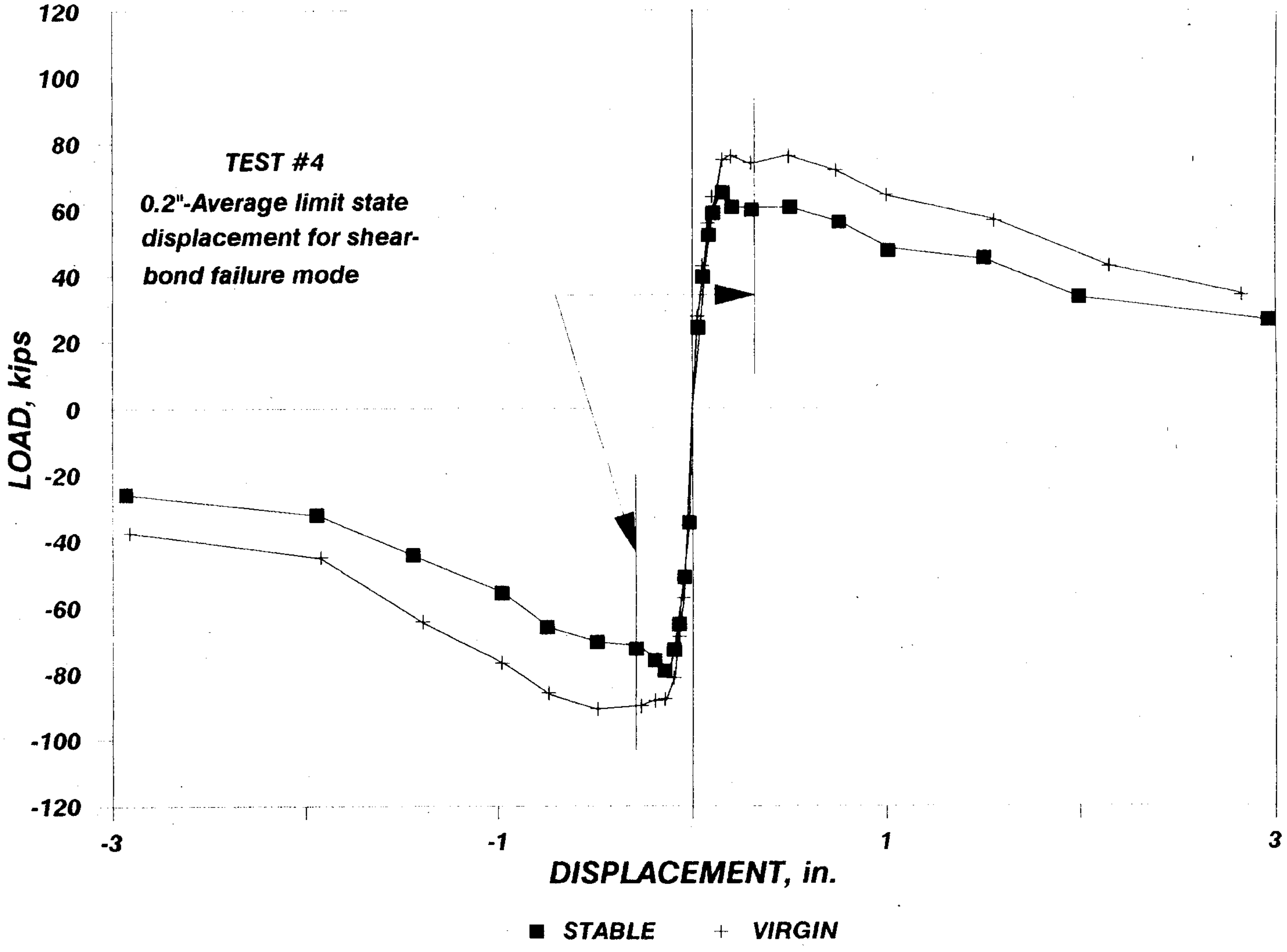

Figure 126a. Peak strength displacement for shear-bond failure mode

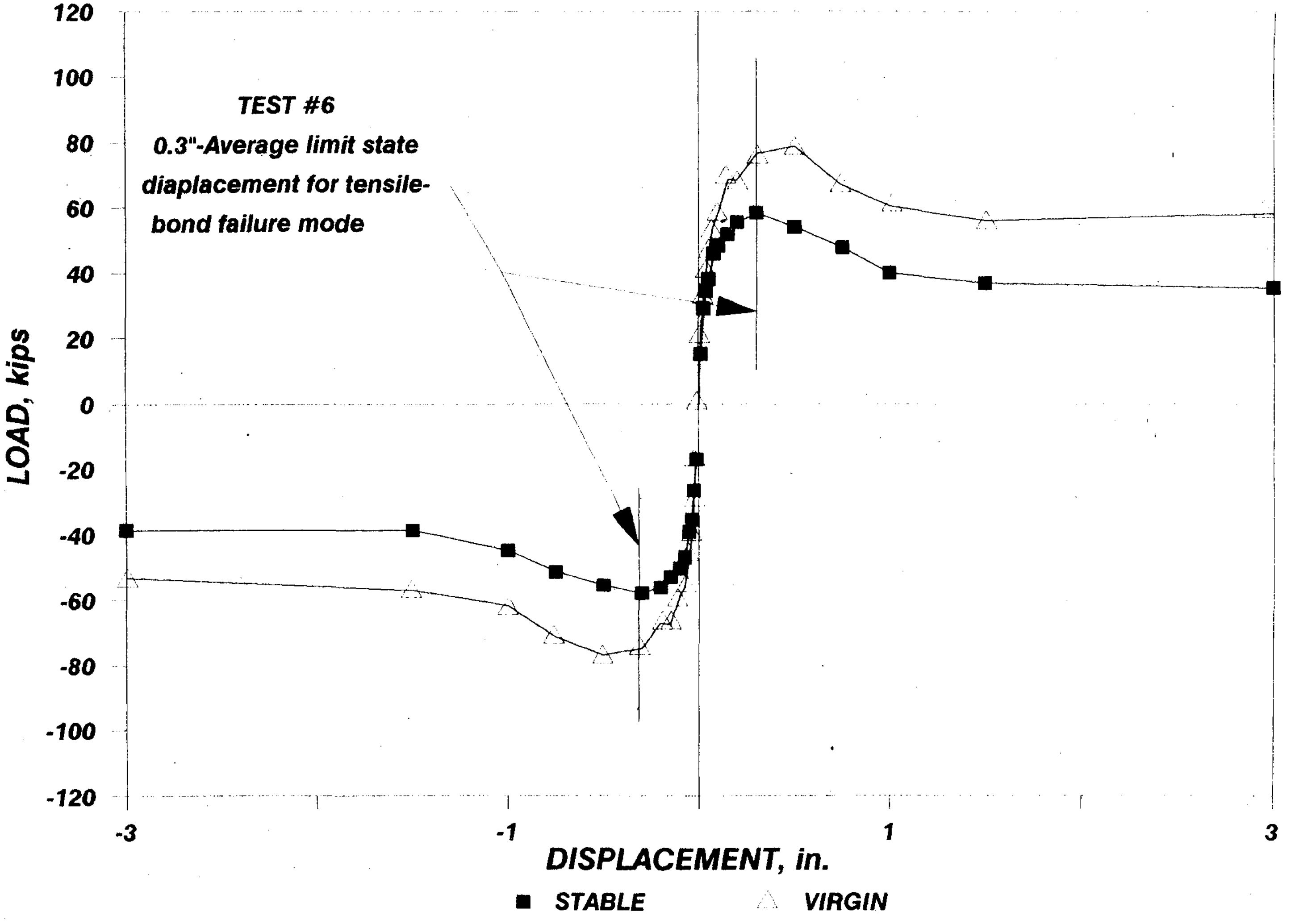

Figure 126b. Peak strength displacement for tensile-bond failure mode

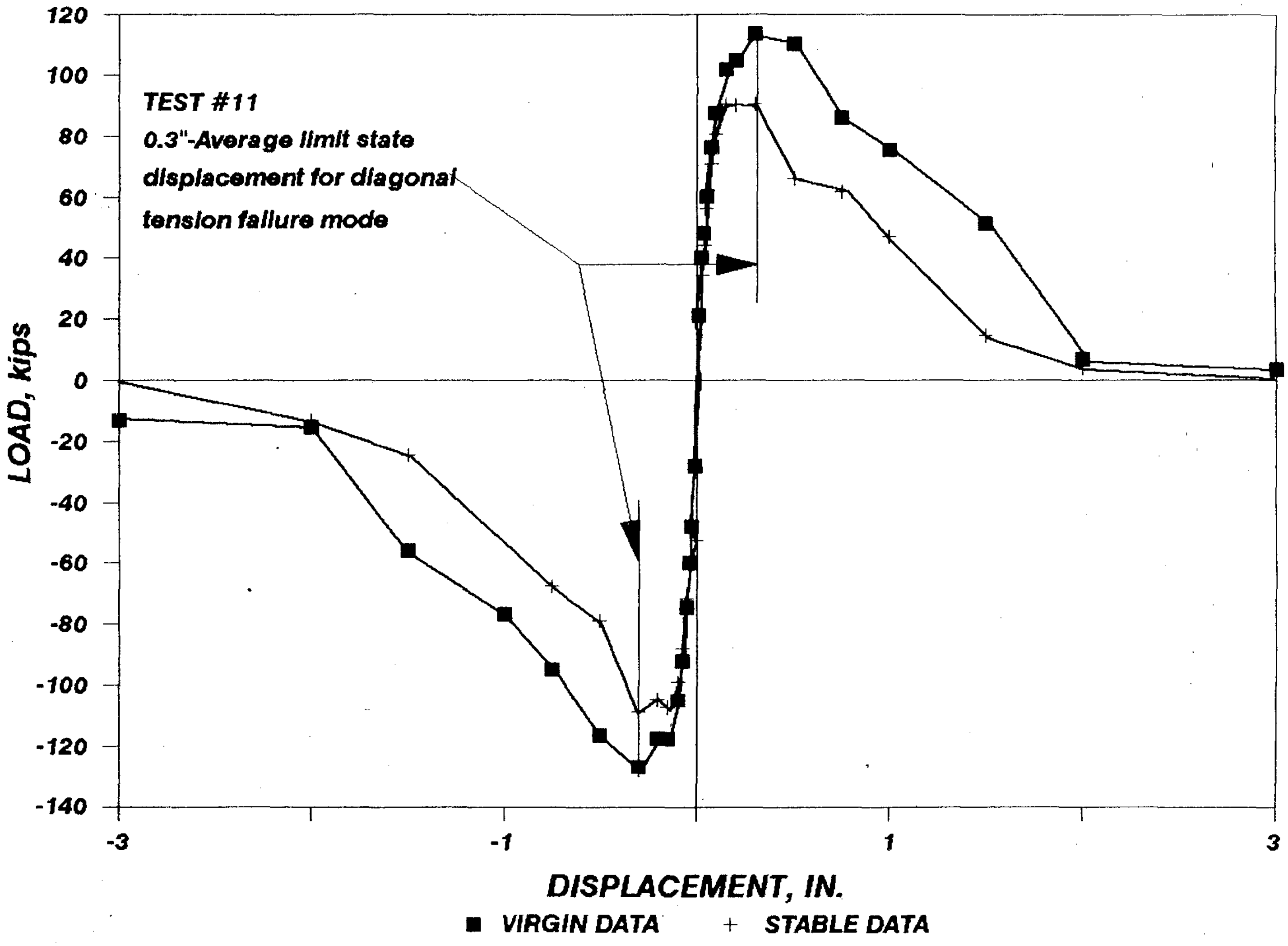

Figure 126c. Peak strength displacement for diagonal tension failure mode

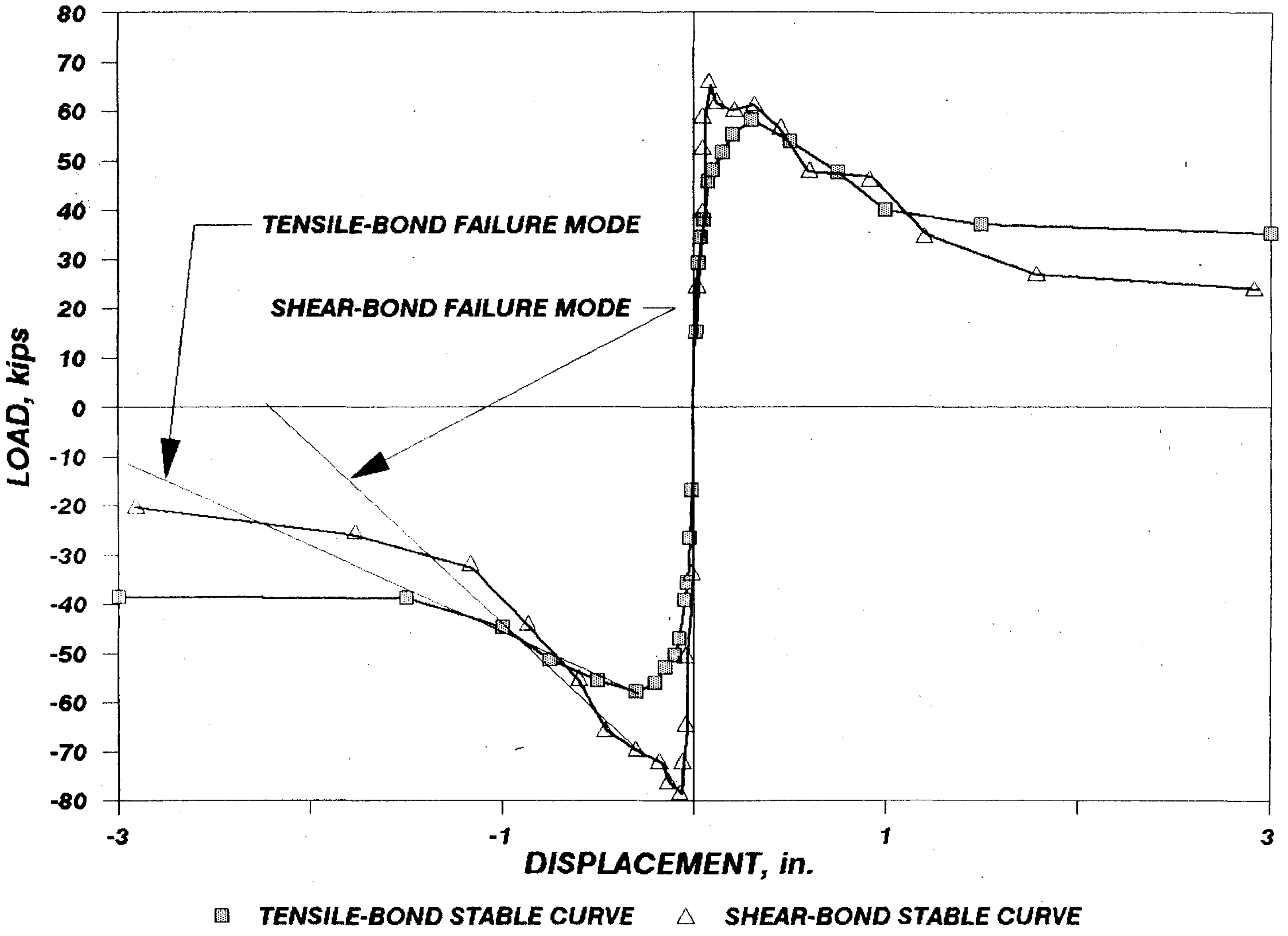

Figure 127. Differing receding slopes for stabilized envelope curves with shear-bond and tensile-bond failures

In the skeleton curve development, the peak strength was assumed to coincide with the ultimate spring capacity. These values were predicted with the stabilized peak strength for the experimental models. For the analytical models, the peak strength varied depending on the failure mode. For tests which exhibited shear-bond seam failure, the peak strength was taken as the FME strength. For tests with tensile-bond seam failure, the peak strength was selected as the limit state strength. The selection criteria for these assumptions reflected the shape of the skeleton curve with respect to the FME and limit state strength points.

6.4 Comparison of Experimental and Analytical Results

The purpose of the analytical work was to develop predictive equations for the initial stiffness, FME strength and limit state strength and to formulate a hysteretic model for a hollow-core concrete diaphragm. The following section discusses the application of the equations described in the previous sections and compares the results with those from the experimental investigation.

6.4.1 Initial Stiffness

The predicted initial stiffness was calculated according to Eq. (6-37) and the results are summarized in Table 7. The values used in this equation were as follows. The bending stiffness component was calculated with Eq. (6-4). In order to determine the modulus of elasticity for use in this equation, the strength of the concrete was required. The plank system consisted of three different concrete mixes: the plank concrete, the grout in the seams and the grout in the cores. Since the grout in the seams maintained the weakest compressive strength, this value was used in the computations for bending and shear stiffnesses. The shear stiffness component was predicted according to Eq. (6-5) and the edge zone component was calculated according to Eq. (6-32). The stud spacing variable was assumed to reflect the outer two studs and equal spacing between the remaining studs. Thus for Test #4, during which the diaphragm was not connected along the side beams, the spacing factor for the side beams was the full span, or 192". For an unsymmetrically connected specimen, such as Test #7, the average stud spacing for both sides was used. The compressive concrete strength used in the edge zone calculations was the lesser of either the Span-Deck plank strength or the core grout strength (grout around the studs). In most diaphragm tests, the core grout strength controlled. The final component of the stiffness equation was the axial flexibility of the edge beam abutment connections. An experimentally derived value of 10,000 kips/in. was used as stated in Reference 9.

Table 7 lists the intermediate calculated stiffnesses as well as the total predicted stiffness for each of the diaphragm tests. As discussed in Chapter 4, the actual experimental values were computed using data from the initial increment of loading beam displacement. The summation of the loads attained from both the east and west displacements were divided by the total absolute movement. These values, K_{act}, are listed in the final column.

Table 7. Initial Stiffness Results

Test	K_b (Kips/in)	K_s (Kips/in)	K_z (Kips/in)	K_f (Kips/in)	K_{tot} (Kips/in)	K_{act} (Kips/in)
1	9668	8293	1797	10000	1136	1375
2	8112	7637	1775	10000	1090	675
3	1724	4147	1013	10000	524	250
4	9807	8501	1861	10000	1167	1281
5	7846	7184	8090	10000	2040	2005
6	8377	8088	7268	10000	2081	1376
7	9114	8358	6075	10000	2024	1647
8	9891	8627	1760	10000	1670	716
9	9325	7780	1793	10000	1119	1486
10	7752	7025	6500	10000	1904	2734
11	11497	11029	1799	10000	1200	2144
12	12396	12375	1586	10000	1125	1596
13	10556	11798	6671	10000	2329	2698
14	10414	11555	6081	10000	2237	3288
15	8377	8088	6672	10000	2029	2518
8B	12363	12325	1771	10000	1210	1003

The experimental stiffness for Test #2 may have been inaccurate due to the lack of adequate diaphragm connections. The actual initial stiffness for Test #6 and #8 may have also been altered due to the initial false starts in the testing procedure. Values for Test #11 differed somewhat due to the sensitivity of the seam grout compressive strengths. In general, the predicted stiffness values were quite acceptable.

6.4.2 FME and Limit State Strength Calculations

The edge zone force distribution discussed in Section 6.3.2. was used to determine the predicted strength values. The procedure for these calculations was discussed in Sections 6.3.3., 6.3.4., and 6.3.5. In the diagonal tension failure mode calculations, the web shear flow gradient limit, a_g, was selected to be 0.2 based on a visual interpretation of the flow area. Table 8 summarizes the analytical and experimental results for the FME and Limit State loads for all the failure modes. The predicted values were quite close in most cases.

During the process of calculating the strength values, all failure modes were considered and the controlling factor (lowest value) was selected. For most of the diaphragm tests, the values were in close agreement. Test #10 was an exception. Clearly the actual FME load, 82 kips, was closer in magnitude to the shear bond seam failure range. Based on the previous tests, a tensile bond failure was anticipated. Since the test was fastened on all perimeter edges, perhaps this configuration had the potential to fail in either shear-bond or tension-bond. The predicted value for Test #11, on the other hand, served to verify that this diaphragm failed in diagonal tension.

The calculations also provided evidence to support the theory proposed in Chapter 4. This hypothesis stated that the diaphragms oriented parallel to the applied shear load cracked at the seams under tensile loads, whereas those systems oriented transverse to the loading beam cracked under shear. The FME calculations demonstrated that Tests #6, #7, and #8 (which were all oriented parallel to the applied shear load) failed in tension.

6.4.3 Hysteretic Model

Hysteretic models were formulated for some of the diaphragms tests according the LPM element EKEH model as discussed in Section 6.3.5. The completed model for Test #5 is shown in Figure 128. The skeleton curve was formed according to Eq. (6-67). These curves, and the actual virgin and stabilized experimental curves, have been plotted in Figure 129. This figure contains two plot; the upper figure is a plot of the experimental data in the LPM model and the lower plot is the predicted data in the model. These figures are both given in order to facilitate comparison of error in the LPM model and the predicted model. Additional comparisons concerning the adequacy of these models can be found in a comparison of the cumulative energy as shown in Table 9. A complete discussion and comparison of the hysteretic modeling is included under Task 2.4a of the TCCMAR research project. In general, the LPM model predictions were quite acceptable.

Table 8. FME and Limit State Strength Results

Test No.	Failure Mode	Predicted Load FME (kips)	Predicted Load Limit State (kips)	Experimental Load FME (Kips)	Experimental Load Limit State (Kips)
1	Shear Bond	80	68	70	83
2	Tension Bond	21	58	58	58
3	Rigid Body Motion	61	14	22	22
4	Shear Bond	89	86	88	79
5	Shear Bond	83	71	84	85
6	Tension Bond	22	58	32	58
7	Tension Bond	19	50	20	62
8	Tension Bond	26	61	19	27
8B	Tension Bond	57	57	43	39
9	Shear Bond	66	59	78	68
10	Tension Bond	18	49	82	84
11	Diagonal Tension	104	104	118	108
12	Diagonal Tension	139	200	127	120
13	Diagonal Tension	138	213	230	246
14	Diagonal Tension	146	100	261	264
15	Shear Bond	84	120	98	221

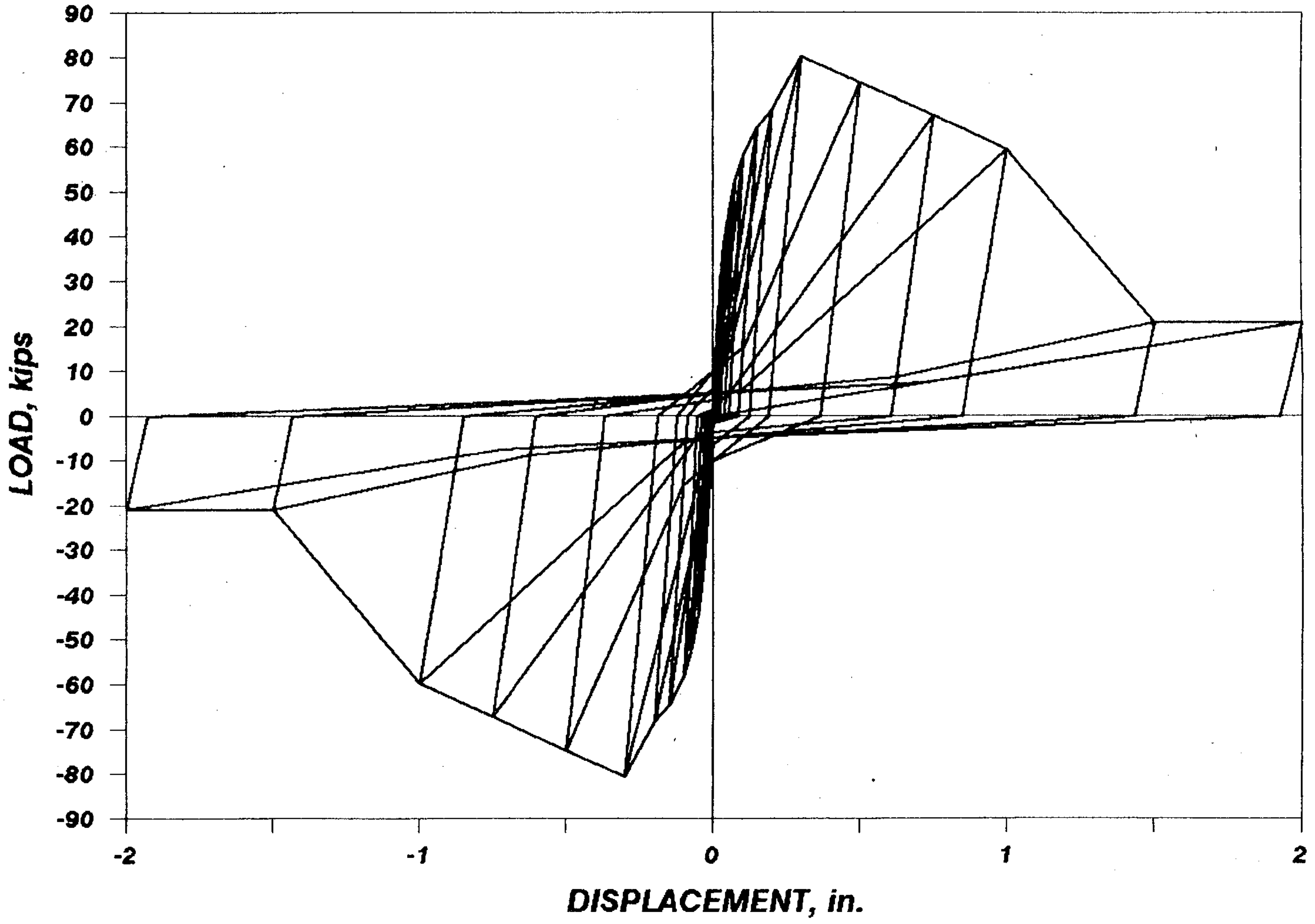

Figure 128. Complete hysteretic model for Test #5

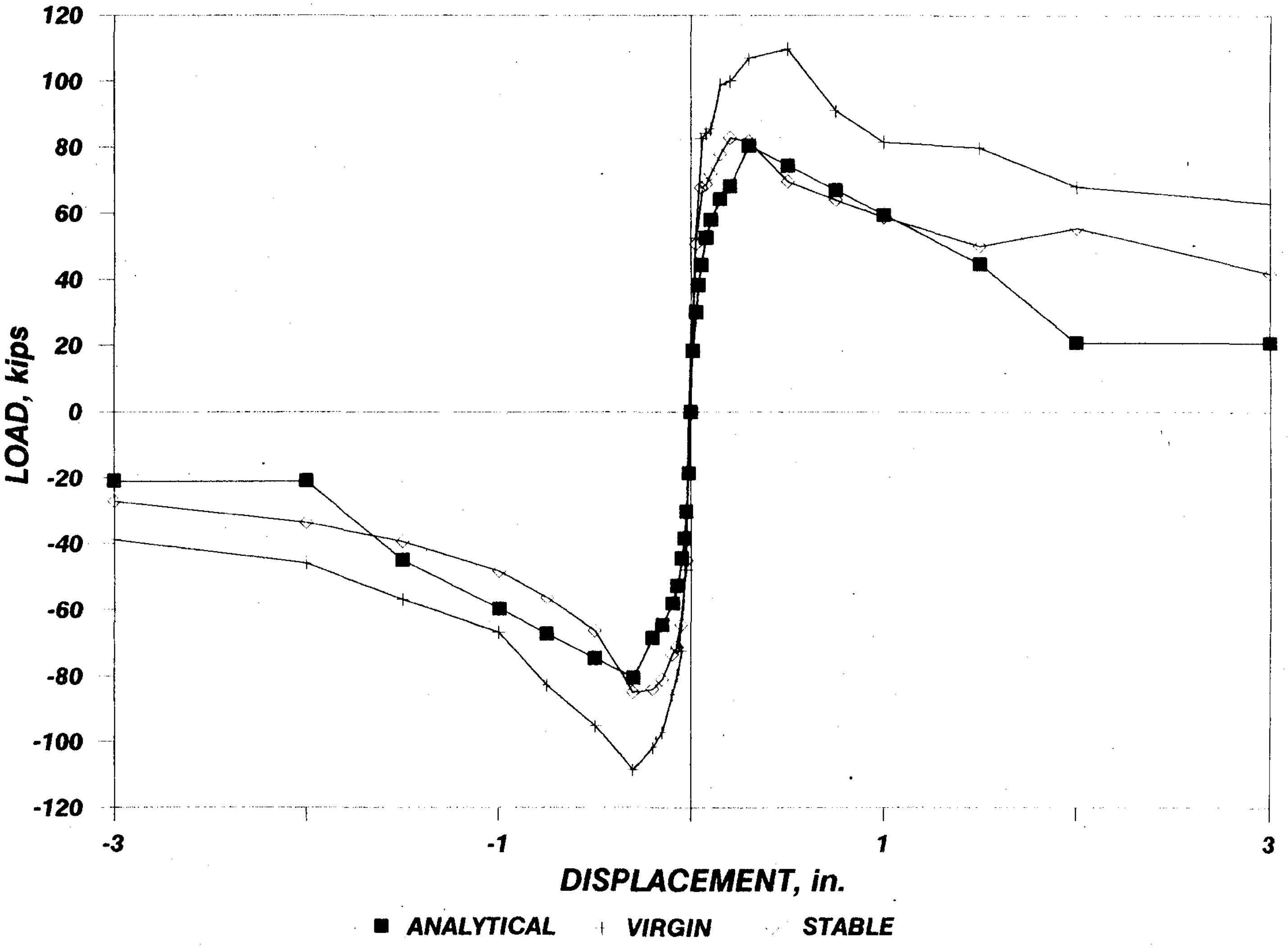

Figure 129. Sample LPM model comparison with experimental results

Table 9. Cumulative Hysteretic Model Energy

Test No.	Cumulative % Error Through 1.0"		Cumulative % Error Through 1.5"	
	Analytical	Experimental	Analytical	Experimental
4	15.8	9.1	12.1	5.1
5	3.5	2.4	2.9	2.1
6	3.8	0.4	8.2	7.1
7	21.1	45.6	14.4	39.4
8	32.3	27.0	36.6	31.4
9	4.2	18.4	4.1	19.0
10	18.7	1.4	15.3	4.7
11	1.6	31.0	18.2	21.6

7. SUMMARY, CONCLUSIONS AND RECOMMENDATIONS

7.1. Summary

This investigation on the behavioral characteristics of hollow-core planks subjected to in-plane loading was part of the overall Masonry Building Research Program being conducted by the Technical Coordinating Committee on Masonry Research (TCCMAR). The project was divided into four phases: loading of full-scale diaphragms into their limit state, testing elemental tension and shear specimens to determine seam characteristics, compilation of data, and development of a analytical model with accompanying initial stiffness and strength calculations. The purpose of this study was to ascertain the behavioral characteristics of the concrete plank diaphragms subjected to horizontal (in-plane) shear loading.

Sixteen full-scale diaphragm tests and sixty-six elemental tension and shear tests have been completed as part of this investigation. Predictive equations describing the initial stiffness for the plank diaphragms were examined, based on the edge zone concept. From the initial and ultimate force distributions, a static analysis yielded predictive equations for the FME and limit state strengths. A hysteretic model was utilized in order to attain a predicted seismic response for the diaphragm system. Energies of the predicted model were compared to those generated during the experimental testing.

7.2. Conclusions

The following conclusions were based on the investigation summarized above:

7.2.1. Experimental Full-Scale Diaphragm Conclusions

1) Three failure modes were identified for the untopped diaphragms: seam shear-bond, seam tension-bond, and diagonal tension failure.
2) For untopped diaphragm tests oriented with seams transverse to the applied shear load, the shear-bond failure mode dominated.
3) For untopped diaphragm tests oriented with seams parallel to the applied shear load, the tensile-bond failure mode controlled.
4) For topped diaphragm tests, the diagonal tension failure mode governed.
5) The diagonal tension failure mode exhibited "low" strength capacities at high displacements due to the extensive cracks through the plank.
6) A study of the stiffness, FME and limit state strengths, and the dissipated energy confirm a definite correlation between the number of sides connected and the amount of diaphragm action achieved. Diaphragms with three and four sides connected achieve higher diaphragm capacity.
7) The greatest amount of diaphragm action is achieved by orienting the planks transverse to the applied shear load.
8) Generally, the greater the diaphragm depth, the greater the strength and stiffness for the given orientation. The greater depth

diaphragm system of Test #6 yielded a somewhat smaller limit state strength capacity than Test #10, contrary to expectations.

9) Increasing the plank depth increased the peak load. However, the ductility was adversely affected.

10) Weld ties provided a means of extending the total displacement capability of the diaphragm system by restructuring seam slippage and separation. This ductility served to enhance the energy absorption characteristics of the diaphragm systems after the FME and prior to the limit state condition in each case.

11) The increase of the number of seam fasteners, increases the diaphragm strength for untopped diaphragms. This parameter also leads to a change in the failure mode as observed in Test #15 where the failure mode changed from shear-bond to diagonal tension.

12) The highest initial stiffness achieved for the untopped diaphragm tests was 2734 Kips/in corresponding to Test #10. The highest for the topped diaphragms was 3288 Kips/in corresponding to Test #14.

13) The maximum load achieved for the untopped diaphragms was 221 Kips corresponding to Test #15. The maximum load for the topped diaphragms was 264 Kips corresponding to Test #14.

14) The testing arrangements of Test #2 is unsuitable for developing diaphragm action, since using an insufficient number of plank segments, produce simple rigid body motion.

15) In general, the displacement associated with the limit state strength of the untopped diaphragm (peak of the stabilized envelope curve) was associated with the failure of the first weld tie during a test.

7.2.2. Elemental Test Conclusions

1) From the elemental test data, the average ultimate shear strength of a grouted seam was approximately 98 psi and the average ultimate tensile stress was around 70 psi.

2) Grout strength significantly increased the limit state strength of a seam due to the frictional and confining forces the grout introduced. The grout appeared to serve as the major strength developing agent and the weld ties produced a ductile failure.

3) The average limit state capacity of a weld tie in shear was 5,500 lbs.

4) Modification of the elemental shear test stresses to account for the non-uniform stress distribution associated with low length/width ratios for the testing configuration resulted in more accurate stresses.

5) Favorable results were obtained after the elemental shear and tensile test stresses were adjusted by using an elliptical interaction curve, which reduced these values.

6) Weld ties provided means of maintaining close to 100% of the peak strength through 0.75" displacement. Thus, weld ties greatly enhanced ductility.

7.2.3. Conclusions From Analysis

1) The edge zone concept was found to be valid and was utilized as the basis for calculating the initial and ultimate force distribution systems.
2) From the elastic distribution, the initial stiffness were determined. Comparisons with the experimental results were favorable.
3) For the seam shear-bond and tensile-bond failure modes, FME and limit state loads were computed based on states of the initial and ultimate force distribution systems, respectively.
4) The predictive strength for the diagonal tension mode was determined to be a function of the effective plank depth that resisted the in-plane shear forces. The effective area transformed to the effective depth consisted of the plank compression zone, excluding an interior portion of the web.

7.2.4. Hysteretic Model Conclusions

1) The LPM was selected as the type of hysteretic model best describing the behavior of the plank diaphragm system. It predicted the actual hysteretic behavior quite well during the early stages of the tests.
2) For design, the more conservative stabilized envelope was selected as the skeleton curve to be modeled.
3) During the latter stages of the event, the LPM model does not accurately portray the sudden drop in energy or unsymmetric behavior associated with several of the tests.
4) Two methods of verifying the model accuracy were employed: a visual interpretation of the hysteretic model versus the virgin and stabilized curves and a method comparing the energy of the model to that of the experimental stabilized energy. Results of the model were generally in very close agreement to that of the experimental test data.

7.3. Recommendations for Continued Study

1) Develop an analysis technique to accurately predict, from the movement of the stud connectors, the shear forces in the plank seams.
2) Determine the effects of superimposed vertical load on the overall diaphragm behavior.
3) Determine the effect of utilizing actual reinforced masonry units by replacing the steel frame under the diaphragm with small masonry walls. This set-up would more closely model the actual connections used in practice (Task 5.3 of TCCMAR research).
4) Investigate the hysteretic purpose of the plank diaphragm subjected to pseudo-dynamic loading.
5) Complete a three-dimensional finite element analysis in order to determine the effect of in-plane forces and to verify the experimentally confirmed calculations on the overall system.

6) Determine the effect of various testing arrangements, configurations and additional spans on diaphragm behavior.
7) Strengthen plank joints between seams by either modifying the plank edge profile or developing a better weld tie.
8) Perform additional diaphragm tests on other types of hollow-core slabs to verify that the results obtained are representative for the entire precast industry.
9) Prepare a set of design recommendations and a design procedure based on the three predictive failure modes for hollow-core plank diaphragms.

ACKNOWLEDGEMENT

This investigation was sponsored by the National Science Foundation, Grant No. CES-8517028 (Formerly Grant No. ECE-8517028). The work is part of the United States - Japan Coordinated Program for Masonry Building research program conducted under the auspices of the Panel on Wind and Seismic Effects of the U.S.-Japan Natural Resources Development Program (UNJR).

The planks material for the research was provided by Prestressed Concrete Operation, a division of Wheeler Consolidated. The shear studs, and the stud welding gun were donated by the Nelson Stud Welding Division of TRW. The weld ties were furnished by Central Pre-mix Concrete Company. The experimental work was conducted in the Structural Engineering Laboratory.

The authors are greatly appreciative of the work of Messrs. Paul M. Tremel and Ronald J. Meyer who conducted all the laboratory experiments and laid the foundation work for this report. We would also like to acknowledge the many hourly employees in the laboratory who helped take the readings and set up the tests. Acknowledgement is also due to Dr. Carl Ekberg, who helped us through the four phases of the project. Thanks are also due the TCCMAR committee members for their input on testing and specimen selection.

REFERENCES

1. ASTM Standard E455-76, "Standard Methods for Static Load Testing of Framed Floor or Roof Diaphragm Constructions for Buildings.", ASTM Standards, Philadelphia, PA, 1976.

2. Buettner, D. R. and R. J. Becker, Manual for the Design of Hollow-Core Slabs. Prestressed Concrete Institute, Chicago, Illinois, 1985.

3. Chow, L., et al. "Stresses in Deep Beams." Trans. of the American Society of Civil Engineers. Vol. 118 (1953), pp. 686.

4. Clough, D. P. "Considerations in the Design of Precast Concrete Diaphragms for Earthquake Loads.", Proc. of a Workshop on the Design of Prefabricated Concrete Buildings for Earthquake Loads. Applied Technology Council, Berkeley, Calif., 1981.

5. Clough, D. P. "Design of Connections for Precast, Prestressed Concrete Buildings for the Effects of Earthquakes." Prestressed Concrete Institute, Tech. Report 5, Chicago, Illinois, March, 1985.

6. Concrete Technology Associates. "Shear Diaphragm Capacity of Precast Floor Systems." Technical Bulletin 73-B6, Concrete Technology Associates, Tacoma, Washington, June, 1973.

7. Concrete Technology Associates. "Shear Diaphragm Capacity of Untopped Hollow-Core Floor Systems." Technical Bulletin 80-B3, Concrete Technology Associates, Tacoma, Washington, August, 1981.

8. DeSilva, C., Dynamic Testing and Seismic Qualification Practice., Lexington Books, 1983.

9. Dodd, S. M. "Effect of Edge Fasteners on Seismic Resistance of Composite Floor Systems." Unpublished Master's Thesis, Iowa State University, Ames, Iowa, 1986.

10. Easterling, W. S. "Analysis and Design of Steel-Deck-Reinforced Concrete Diaphragms." Unpublished Doctoral Dissertation, Iowa State University, Ames, Iowa, 1987.

11. Elsesser, Eric, "Analytical Modeling Problems of Precast Diaphragms.", Proc. of a Workshop on the Design of Prefabricated Concrete Buildings for Earthquake Loads. Applied Technology Council, Berkeley, Calif., 1981.

12. Emori, K. and W. C. Schnobrich. Analysis of Reinforced Concrete Frame-wall Structures for Strong Motion Earthquakes. Univ. of Illinois, Urbana-Champaign, Structural Research Series #4. Univ. of Illinois Press, Champaign, Illinois, 1978.

13. Engineering Testing Laboratories, Inc. "Reports on Horizontal Shear Tests of Span-Deck Grouted Edge Joints." Prepared by Tanner Prestressed and Architectural Concrete Co., Inc., Phoenix, Arizona, March, 1973.

14. Ewing, R. D., et al. LPM/1 - A Computer Program for the Nonlinear, Dynamic Analysis of Lumped Parameter Models. National Science Foundation, Tech. Rep. 2.3-1, August, 1987.

15. Ewing, R. D., et al. "Seismic Analysis of Wood Diaphragms in Masonry Buildings." Proc. of a Workshop on Design of Horizontal Wood Diaphragms. Applied Technology Council, Berkeley, Calif., Nov. 1980.

16. Hawkins, N. M. "State of the Art Report on Seismic Resistance of Prestressed and Precast Concrete Structures, Part I." Journal of Prestressed Concrete Institute. 22, No. 6 (Nov.-Dec. 1978) pp. 80-110.

17. Iwan, I. D. "The Response of Simple Stiffness Degrading Structures." Proc. of the Sixth World Conference on Earthquake Engineering. Volume II. Meerut, India: Sarita Prakashan, January 1977.

18. Jennings, P. C. "Periodic Response of a General Yielding Structure." Journal of Engineering Mechanics Division. 90, No. EM2 (April, 1964), pp. 131-166.

19. Leffler, R. E., "Stresses in Floors of Staggered-Truss Buildings: Precast Prestressed Concrete Floor Plank.", United Steel Technical Report: 46.019-400(5), December, 1983.

20. Martin, L. D. and W. J. Korkosz. Connections for Prestressed Concrete Buildings Including Earthquake Resistance. Prestressed Concrete Institute, Chicago, Illinois, 1985.

21. National Bureau of Standards. Description of Stress-Strain curves by Three Parameters. By W. Ramberg and W. Osgood. Washington, D.C., GPO, July, 1943.

22. Nakashima, M., et al. "Effect of Diaphragm Flexibility on Seismic Response of Building Structures." Proc. of Eighth World Conference on Earthquake Engineering. Prentice Hall, Englewood Cliffs, New Jersey, 1984.

23. Neilson, M. K. "Effects of Gravity Load on Composite Floor Diaphragm Behavior." Unpublished Master's Thesis, Iowa State University, Ames, Iowa, 1983.

24. Nelson Stud Welding Division. Nelson Embedment Properties of Headed Studs Catalog. n.p., 1984.

25. Noland, J. L. "U.S. Research Plan." U.S.-Japan Coordinated Program for Masonry Research. Typescript, Atkinson-Noland and Associates, Boulder, Colorado, 1984, Revised 1985.

26. Otani, S. "Hysteresis Models of Reinforced Concrete for Earthquake Response Analysis." Proc. of the Eighth World Conference on Earthquake Engineering. Englewood Cliffs, New Jersey: Prentice Hall, 1984.

27. Pauley, T., R. Park, and M. H. Philips, "Horizontal Construction Joints in Cast-in-Place Reinforced Concrete." American Concrete Institute - SP 42-27, (1974): 599-616.

28. Phillips, W. R. and D. A. Sheppard, Plant cast, precast, and prestressed Concrete: A Design Guide. Second Edition, Prestressed Concrete Manufactures Association of California, Nappa Valley, California, 1980.

29. Porter, M. L. "The Behavior and Analysis of Two-way Simply Supported Concrete Composite Floor Slabs Constructed with Cold-formed Steel Decking." Unpublished Doctoral Dissertation, Iowa State University, Ames, Iowa, 1974.

30. Porter, M. L. and L. F. Greimann. "Seismic Resistance of Composite Resistance of Composite Floor Diaphragms." Engineering Research Institute, Iowa State University, Final Report ERI-80133, May, 1980.

31. Porter, M. L. and P. M. Tremel. "Sequential Phase Displacement." U. S. Japan Coordinated Program for Masonry Building Research, Task 5.1. Typescript, Iowa State University, Ames, Iowa, 1987.

32. Prestressed Concrete Operations, Prestressed Span-Deck Catalog. Iowa Falls, Iowa, ca.1985.

33. Prestressed Concrete Institute. PCI Design Handbook for Precast and Prestressed Concrete. Third Edition., Prestressed Concrete Institute, Chicago, Illinois, 1985.

34. Prins, M. D. "Elemental Tests for the Seismic Resistance of Composite Floor Diaphragms." Unpublished Master's Thesis. Iowa State University, Ames, Iowa, 1985.

35. Riddell, R. and M. N. Newmark, "Force Deflection Models for Nonlinear Analysis." Journal of Structural Engineering 105 (1979): 2773-2778.

36. Reinhardt, H. W. "Length Influence on Bond Shear Strength of Joints in Composite Precast Concrete Structures." International Journal of Cement Composites and Lightweight Concrete. 4, No. 3 (August, 1982) pp. 139-143.

37. Roark, R. J. and W. C. Young. Formulas for Stress and Strain. McGraw-Hill Book Company, N. Y., New York, 1975.

38. Saiidi, M. and M. A. Sozen. Simple and Complex Models for Nonlinear Seismic Response of Reinforced Concrete Structures. University of Illinois, Urbana-Champaign, Structurtal Research Series #4. University of Illinois Press, Chambaign, Illinois, 1979.

39. Saatcuglu, M., et al. "Modeling Hysteretic Behavior of Coupled Walls for Dynamic Analysis." Earthquake Engineering and Structural Dynamics. 11 (1983), pp. 711-726.

40. "Seismic Design for Buildings." Technical Manual TM 5-809-10, Departments of the Army, the Navy, and the Air Force, Washington D.C., February 1982.

41. Sozen, M. A. "Hysteresis in Structural Elements." Applied Mechanics in Earthquake Engineering. (1974), pp. 63-98.

42. Stanton, J., et al., "Connections in Precast Concrete Structures." Concrete International Design and Construction. Vol. 9, No. 11 (1987) pp. 49-53.

43. Stanton, J., et al. "Moment Resistant Connections and Simple Connections.", Prestressed Concrete Institute, Research Project No. 1/4, Chicago, Illinois, 1986.

44. Takayanagi, T. and W. C. Schnobrich, Computed Behavior of Reinforced Conrete Coupled Shear Walls. University of Illinois, Urbana-Champaign, Structurtal Research Series #4. University of Illinois Press, Chambaign, Illinois, 1976.

45. Ugural, A. C. and S. K. Fenster. Advanced Strength and Applied Elasticity. Elsevier Publishing, N. Y., New York, 1975.

46. Umeura, H. and H. Takizawa. Structural Engineering Documents. International Association for Bridge and Structural Engineers, Zurich, Switzerland, 1982.

47. Velkov, M., et al. "Experimental and Analytical Investigation of Prefabricated Large Panel Systems to be Constructed in Seismic Regions." Proc. of Eighth World Conference on Earthquake Engineering. Prentice Hall, Englewood Cliffs, New Jersey, 1984.

48. Walker, H. C., "Summary of Basic Information on Precast Concrete Connections. ", Journal of Prestressed Concrete Institute. 14, No. 6 (1969), pp. 14-58.

49. Wakabayashi, M. Design of Earthquake-Resistant Buildings. New York: McGraw-Hill Book Company, 1986.

50. Clough, R. W., and S. B. Johnston. "Effect of Stiffness Degradation on Earthquake Ductility Requirements." Proc. at Second Japan Earthquake Engineering Symposium. Tokyo: 1966. 227-232.

51. Takeda, T., M. A. Sozen, and N. N. Nielsen. "Reinforced Concrete Response to Simulated Earthquakes." Proc., ASCE, Journal of the Structural Division 96, ST12 (Dec. 1970): 2557-2573.

52. Tanabashi, R., and K. Kaneta. "On the Relation Between the Restoring Force Characteristics of Structures and the Pattern of Earthquake Ground Motions." Proc. First Japan Earthquake Engineering Symposium. Tokyo: 1962. 57-62.

53. Iwan, W. D. "The Steady State Response of the Double Bilinear Hysteretic Model." Trans. ASME, Journal of Applied Mechanics 32 (1965): 921-925.

54. Tremel, P. M. "Boundary Conditions and Orientation Behavioral Characteristics for Hollow-Core Planks." Unpublished Master's Thesis, Iowa State University. Ames, Iowa, 1988.

55. Meyer, R. J. "Effect of Plank Depth Parameter on Seismic Resistance of Precast Hollow-Core Plank Diaphragms." Unpublished Master's Thesis, Iowa State University. Ames, Iowa, 1988.